MULTI-AXIAL REAL-TIME HYBRID SIMULATION FRAMEWORK FOR TESTING NONLINEAR STRUCTURE SYSTEMS WITH MULTIPLE BOUNDARY INTERFACES

BY

MIR AMIRALI NAJAFI

DISSERTATION

Submitted in partial fulfillment of the requirements
for the degree of Doctor of Philosophy in Civil Engineering
in the Graduate College of the
University of Illinois at Urbana-Champaign, 2021

Urbana, Illinois

Doctoral Committee:

Professor Billie F. Spencer Jr., Chair and Director of Research
Professor Emeritus Lawrence A. Bergman
Professor Larry A. Fahnestock
Professor Shirley J. Dyke, Purdue University
Professor Oh-Sung Kwon, University of Toronto

ABSTRACT

Hybrid simulation is a widely accepted laboratory testing approach that partitions a proposed structure into numerical and physical substructures, for a space- and cost-effective testing method. Structural elements that are expected to remain in the linear elastic range are usually modeled numerically, while computationally intractable nonlinear elements are tested physically. The loads and conditions at the boundaries between the numerical and physical substructures are imposed by servo-hydraulic actuators, with the responses measured by loadcells and displacement transducers. Traditionally, these actuators impose boundary condition displacements at slow speeds, while damping and inertial components for the physical specimen are numerically calculated. This slow application of the boundary conditions neglects rate-dependent behavior of the physical specimen. Real-time hybrid simulation (RTHS) is an alternative to slow speed hybrid simulation approach, where the responses of numerical substructure are calculated and imposed on the physical substructure at real world natural hazard excitation speeds. Damping, inertia, and rate-dependent material effects are incorporated in the physical substructure as a result of real-time testing.

For a general substructure, the boundary interface has six degrees-of-freedom (DOF); therefore, an actuation system that can apply multi-axial loads is required. In these experiments, the boundary conditions at the interface between the physical and numerical substructures are imposed by two or more actuators. Significant dynamic coupling can be present between the actuators in such setups. Kinematic transformations are required for operation of each actuator to achieve desired boundary conditions. Furthermore, each actuator possesses inherent dynamics that needs appropriate compensation to ensure an accurate and stable operation.

Most existing RTHS applications to date have involved the substructuring of the reference structures into numerical and physical components at a single interface with a one-DOF boundary condition and force imposed and measured. Multi-DOF boundary conditions have been explored in a few applications; however a general six-DOF stable implementation has never been achieved. A major research gap in the RTHS domain is the development of a multi-axial RTHS framework capable of handling six DOF boundary conditions and forces, as well as presence of multiple physical specimen and numerical-to-physical interfaces.

In this dissertation, a multi-axial real-time hybrid simulation (maRTHS) framework is developed for realistic nonlinear dynamic assessment of structures under natural hazard excitation. The framework is comprised of numerical and physical substructures, actuator-dynamics compensation, and kinematic transformations between Cartesian and actuator/transducer coordinates. The numerical substructure is compiled on a real-time embedded system, comprised of a microcontroller setup, with onboard memory and processing, that computes the response of finite element models of the structural system, which are then communicated with the hardware setup via the input-output peripherals. The physical substructure is composed of a multi-actuator boundary condition box, loadcells, displacement transducers, and one or more physical specimens. The proposed compensation is a model-based strategy based on the linearized identified models of individual actuators. The concepts of the model-based compensation approach are first validated in a shake table study, and then applied to single and multi-axis RTHS developments.

The capabilities of the proposed maRTHS framework are demonstrated via the multi-axial load and boundary condition boxes (LBCBs) at the University of Illinois Urbana-Champaign, via two illustrative examples. First, the maRTHS algorithm including the decoupled controller, and kinematic transformation processes are validated. In this study, a moment frame structure is partitioned into numerical beam-column finite element model, and a physical column with an LBCB boundary condition. This experiment is comprised of six DOFs and excitation is only applied in the plane of the moment frame. Next, the maRTHS framework is subjected to a more sophisticated testing environment involving a multi-span curved bridge structure. In this second example, two LBCBs are utilized for testing of two physical piers, and excitation is applied bi-directionally. Results from the illustrative examples are verified against numerical simulations. The results demonstrate the accuracy and promising nature of the proposed state-of-the-art framework for maRTHS for nonlinear dynamic testing of structural systems using multiple boundary points.

To my parents,

who have given me invaluable educational opportunities.

Acknowledgements

I would like to thank my graduate research advisor, Dr. Billie F. Spencer, Jr., for the opportunities he has given me over the last 5 years, including his guidance, mentorship, and support. He created a friendly and collaborative research environment, supported by exposure to many conferences and educational workshops, where I felt confident to work independently and to take on a leadership role in my own research. I learned countless professional and personal skills through the example he set.

I appreciate my dissertation committee, Dr. Lawrence A. Bergman, Dr. Shirley J. Dyke, Dr. Oh-Sung Kwon, and Dr. Larry A. Fahnestock, whose breadths of research expertise and experiences were invaluable sources. Their availability and feedback helped me greatly improve my dissertation research.

I sincerely thank all my colleagues at the Smart Structures and Technology Laboratory (SSTL), including Dr. Yuguang Fu, Dr. Vedhus Hoskere, Dr. Yasutaka Narazaki, Dr. Han Qin, Dr. Jian-xiao Mao, Tu Hoang, Koji Tsuchimoto, Shaik Althaf Veluthedath Shajihan, and Bolaji Lawal. Particular acknowledgement and appreciation to Dr. Gaston A. Fermandois for all his support and assistance in the theoretical and experimental constructs of this dissertation.

Finally, I would like to thank my family for their love, support, and encouragement throughout my doctoral program.

CONTENTS

CHAPTER 1 INTRODUCTION

1.1 Motivation

In the past 20 years, natural hazards mitigation has experienced increased focus and investment. In 2004, the National Science Foundation (NSF) instituted the George E. Brown Jr. Network for Earthquake Engineering Simulation (NEES) to develop innovative solutions and enhance the design and construction practices for minimizing earthquake- and tsunami-induced damages. NEES stretched over 15 facilities across the U.S., in laboratories well-equipped with shake tables, a tsunami wave basin, geotechnical centrifuges, and a variety of field-testing equipment. During the 10-year operation of NEES, earthquake engineering education and research saw huge strides and generated large volumes of literature. Following the conclusion of NEES, the natural hazards engineering community looked for new programs, research funding opportunities, and a broader research focus via inclusion of other forms of natural hazards. In the years since, the Natural Hazards Engineering Research Infrastructure (NHERI) was founded as the national research infrastructure with multiple focuses (e.g., earthquake and wind research).

With the looming consequences of climate change, threats of natural hazards in major urban centers, energy issues, current global recession, the need to develop new strategies to rehabilitate and rebuild our aging civil infrastructure is more important than ever before. The goal of new infrastructure efforts should be the creation of resilient and sustainable communities. Traditional civil infrastructure approaches should be complemented with multi-hazard considerations focusing on mitigation and resilience.

Historically, engineers have relied on numerical (e.g., finite element) modeling, quasi-static (cyclic), and shake table testing for assessment of element and system level interactions. Numerical modeling has seen rapid growth in the recent years. With advances in computational hardware, parallel computing, and increases in affordability and availability of supercomputers, engineers and researchers have the unprecedented ability to develop sophisticated finite element models. However, predictions of numerical models are only as good as the assumptions on which they are based, and although numerical modeling can be extremely accurate for elastic systems, nonlinear predictions are often inaccurate. Therefore, physical testing is often desired for exploration of the non-trivial phenomena in structures and materials.

1.2 Experimental Testing

From early verifications of the Hooke’s law, to identification of the most sophisticated material constitutive models and structural behaviors, experimental testing is deeply interwoven in the science of structures. Not only are experiments useful in uncovering new physical phenomena and validating existing theories, but also serve in establishing reliability metrics and building confidence in engineering solutions. Experimental vibration testing of structural systems can be classified into two main categories: (i) *field testing*, and (ii) *laboratory testing*.

Field vibration testing strategies can be classified as forced and unforced vibration tests. Forced testing involves installation of a vibration generator (e.g., shaking machine or actuators) for providing prescribed excitations to a structure of interest (Chopra 2011). Unforced strategies rely on naturally induced vibrations (e.g., ambient, wind and vehicular). The relationships between the input forces and the sensors provide a basis for evaluation of a variety of structural parameters, including damping and natural frequencies (Juang and Pappa 1985; Peeters and Roeck 1999). The fundamental limitation of field vibration testing is that structures cannot be pushed beyond the elastic range. In addition, occupants and owners of structures (e.g., municipalities) are often reluctant to have properties vibration tested, as operations may be affected by testing.

Laboratory tests are often more desirable as they provide a more controlled environment for experimental testing. For nonlinear performance assessments useful for earthquake and wind engineering, structures are tested at either:

i. slow speeds (e.g., quasi-static testing), or
ii. fast speeds (e.g., shake table and fast cyclic testing),

with slow speed testing intended to suppress inertial effects and focus only on restoring forces.

In *quasi-static* or slow cyclic testing, an actuator imposes a predefined displacement or force history on a structural element of interest. The performance of the structure is assessed under cyclic load reversals and amplitude variations. Quasi-static testing is a popular method for identifying the nonlinear backbone curves and hysteretic behaviors of structures and materials, and the slow nature of the method allows researchers to observe the damage propagate on the specimen. The obvious limitation of the quasi-static method is that inertial effects are ignored, and materials and structures with high degrees of rate-dependence must be tested using alternative methods. Fast cyclic testing is an alternative, where the cyclic loading is fast enough to engage inertial (acceleration) effects. Some literature is devoted to exploring the dependence of common building materials (e.g., steel and concrete) to the rate of loading (Chae et al. 2017; Malvar and Ross 1998; Murray et al. 2014). Another limitation of the quasi-static test method is that structural elements are tested independently, and system level interactions are not considered, as shown in Fig. 1.1. In addition, the cyclic loading of the structure bears no resemblance to forces sustained by the structure under natural hazard excitation.

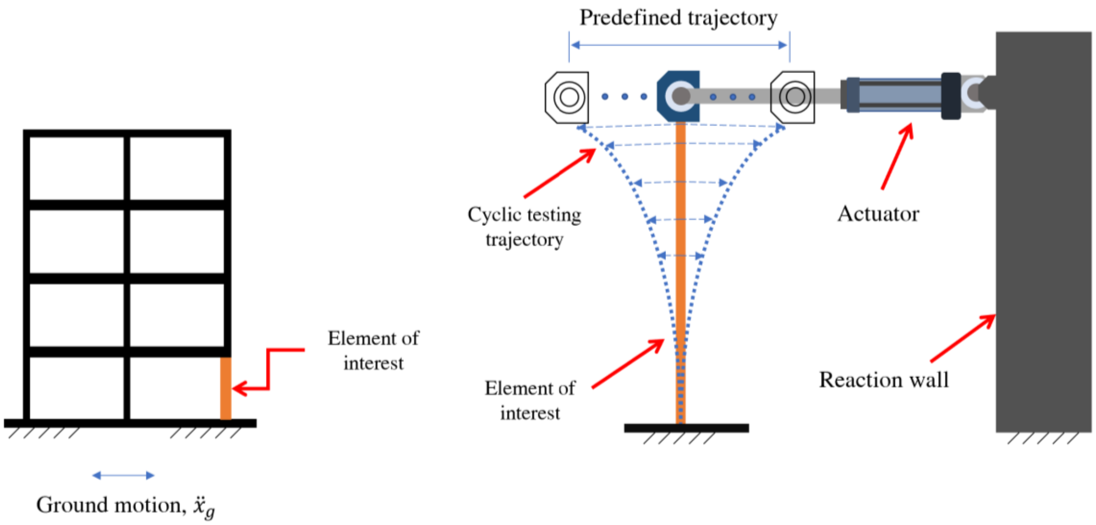

(a) Reference structure (b) Quasi-static testing

Figure 1.1 Quasi-static testing subject to predefined cyclic displacement trajectory

Understanding and engineering structures to withstand natural hazards requires researchers to have the dynamic experimental tools necessary to replicate recorded excitations. Researchers typically use *shake table test* to subject structures to synthetic and historical earthquakes as a basis for assessing structural performance (Luco et al. 2010; Reinhorn et al. 2004). The earliest form of a shake table was a hand-powered device built in Japan in the 1890s (Severn 2011). Until the first ever ground motion was recorded (i.e., Long Beach – 1933), shake tables were mostly simple mechanical devices that imposed simple cyclic displacements to the base of a structure (Severn et al. 2012). With the advent of strong motion seismometers, electromechanical and servo-hydraulic shake tables were developed to reproduce synthetic and pre-recorded earthquakes. Shake tables were developed for scaled- and full-sized structures. Significant developments were made in the form of the $7.6\ m \times 12\ m$ shake table in San Diego and the $20\ m \times 15\ m$ E-Defense shake table in Japan, both capable of testing full-scale structures (Luco et al. 2010; Ohtani et al. 2004).

Shake table actuators have physical characteristics such as friction, frequency-dependence, nonlinearities (Rea et al. 1977), and more sophisticated phenomena like control-structure interaction (CSI), which refers to the dynamic coupling between actuators and test structure (Dyke et al. 1995; Zhao et al. 2005). A wide body of literature is available discussing the different control strategies for compensation of shake table dynamics to ensure accurate replication of pre-recorded ground motions (Fletcher 1990; Gao et al. 2011; Phillips et al. 2014; Spencer and Yang 1998; Stoten and Shimizu 2007; Twitchell and Symans 2003).

Although shake table testing is the most complete and accurate method for assessment of seismic behavior of structures, the method faces many challenges and limitations:

i. large shake tables are few, expensive to build and operate, and inaccessible to most researchers and engineers,
ii. small shake tables are limited to small specimens, which must be designed using complex similitude laws and results may not extrapolate to results of equivalent full-scale tests,
iii. shake table actuators have their own dynamics which need to be compensated in order to accurately replicate historical ground motions, and
iv. although one or few structural elements may be of interest, the entire structure must be built and tested as shown in Fig. 1.2.

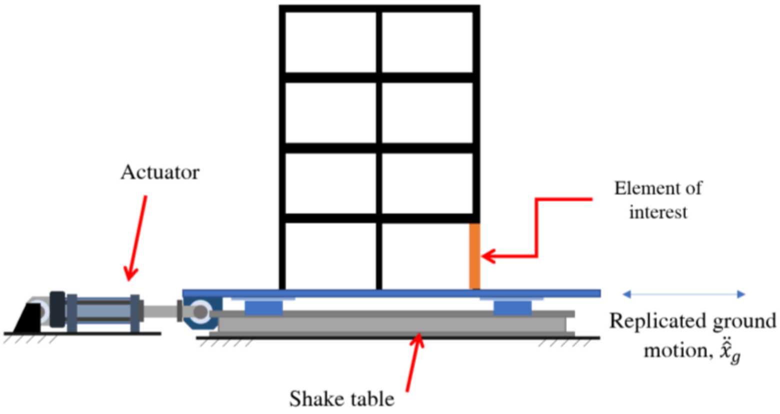

Figure 1.2 Shake table testing replicating historical earthquake

From the discussion on the traditional testing techniques so far, it is evident that material rate-dependent phenomena are primary reasons why fast testing techniques are desirable in some instances. The next section discusses the physics of rate-dependence.

1.3 Material rate-dependence

In general, the hysteretic behaviors of materials and structural systems tend to vary between quasi-static and dynamic load scenarios. Experimental evidence has demonstrated that under dynamic loading, the elastic modulus remains largely the same, while the load capacity (i.e., height of the hysteresis) tends to grow (Campbell 1954; Cristescu 1967; Goldsmith 1960). The loading rate is often described by the measure of strain rate experienced by the structures and materials.

For hybrid simulation applications, the challenge in classifying material strain rate-dependence is twofold: (i) if the rate-sensitive load capacity increase happens at typical loading frequencies of natural hazard excitations, and (ii) whether the rate-dependence makes a significant enough difference to run experiments at real-time speeds, instead of slow speeds. Real-time testing poses additional experimental challenges, which may not be desirable if rate-dependence is insignificant. Nevertheless, strain rate dependence is an important consideration for both theoretical and experimental constructs.

Strain rate dependence of commonly used structural materials include steel, concrete, and masonry have been widely studied. Chang and Lee (1987) studies the A36 structural steel under monotonic and cyclic loading conditions with strain rate range of 10^{-1}/sec to 10^{-6}/sec. Faster strain rates corresponded to increased yield capacity and longer plastic plateaus. Strain rate effects were found to be more significant under monotonic loading than for cyclic loading. Chang et al. (1989) applies the endochronic plasticity model for evaluation of strain-rate effects on inelastic behavior of structural steel under earthquake loading. At extreme strain rates of $> 10^{-6}$/sec, such as impact loading scenarios, mild steel was found to have yield strengths of around 2000 MPa (Singh et al. 2008). When a ball projectile is impacted with a steel plate, the depth of surface penetration is correlated with the yield strength of the steel. The yield strength was demonstrated to be sensitive to the velocity of the ball projectile. Murray et al. (2014) highlight the yield and ultimate strength increase in steel reinforcement bars for A572-50 and A992 steels. A572-50 exhibits yield strength increases of up to 35% and ultimate strengths of up to 20%. A992 steel exhibits yield strength increases of up to 45% and ultimate strengths increases of up to 20%. Thereby, high strain rates have been shown to drastically change the yield capacity of structural steel.

Concrete materials have also been the subject of several material rate-dependence studies. Malvar and Ross (1998) offers a literature review on the effects of strain rate on tensile strength of concrete. A bilinear function of the strain rate is improved to describe dynamic amplification data based on Comité Euro-International du Béton Model Code report. Zhou and Hao (2008) compares numerical models and experimental results for compressive behavior of concrete. Strain rate effects result in capacity amplifications described via the dynamic increase factor (DIF) of compressive capacities for strain rates of < 200/sec. A secondary amplification is also suggested to be induced by inertial confinement effects at strain rates of > 1000/sec. Chen et al. (2013) suggests that although DIF is observed in flexural strength, the direct tensile strength of concrete is more sensitive to increases in strain rate than flexural strength. Ghannoum et al. (2012) performs cyclic testing on reinforced concrete columns at slow and fast speeds. Cyclic speeds of up to 1,016 mm/s were investigated, with higher cyclic loads resulting in lateral load capacity increases of up to 33%.

Few literatures in the hybrid simulation are also devoted to exploration of the material rate-dependence. Shing and Mahin (1988) developed a single degree-of-freedom (DOF) numerical model for hybrid simulation to study the effects of DIF in the strength of seismically excited structures. The maximum strain rate sustained by the structure is 0.1/sec, which translated to a monotonic DIF of 40%. This value seems too high given the small strain rate. Nevertheless, two significant parameters are highlighted pertaining to rate-dependence of materials: (i) natural frequency of structure, and (ii) characteristics of the excitation. A multi-DOF structure with high natural frequencies coupled with a high frequency excitation may result in strain rate induced increases in capacity. Chae et al. (2017) studied the rate dependency of reinforced concrete piers subject to slow speed and real-time hybrid simulation tests. Small increases in capacity were exhibited along with increases energy dissipation. The bridge structure considered in these hybrid simulation tests experienced an average reduction of 5% in the maximum displacements.

Although countless studies have illustrated rate-dependence of steel and reinforced concrete building materials, the discussion on the significance of such phenomena under seismic and wind loads is not a settled one. Existing studies and literature are few and limited in scope. In addition, available results fail to demonstrate significant rate-dependence at seismic and wind loading rates, and their repeatability is not verified.

On the other hand, high performance structural systems such as seismic isolation devices, passive energy dissipation devices, and semi-active and active control systems possess significant rate-dependent physics. Seismic isolation devices include elastomeric and rubber bearings and sliding friction pendulums devices. Passive energy dissipation devices include metallic, friction, viscoelastic, tuned mass, tuned liquid dampers. Semi-active and active control systems involve active mass dampers and bracing systems, variable stiffness or damping systems, MR dampers and smart materials. Because these systems are rate-dependent, real-time testing may be a more suitable testing method.

Another time-dependent material behavior is the stress relaxation phenomenon. Stress relaxation describes the decrease in the structural stress levels while a constant strain is maintained. In slow speed testing, hold-ramp-hold algorithms impose displacements on the physical specimen (Carrion and Spencer, Jr. 2007). Because the extended timescale of conventional slow speed testing, and the potentially long durations of hold, stress relaxation may occur in the physical specimen. Stress relaxation calculations may vary for different materials, but generally speaking, it follows a logarithmic pattern with most of the relaxation happening immediately. Temperature and stress levels also affect the relaxation process (Ashter 2014).

Stress relaxation was reported in Chang and Lee (1987) for 10-minute holds. This relaxation was less significant in the strain-hardening zone as compared to the plastic plateau range. In addition, with changing strain rates, a unique stress-strain curve was not identified. This may be attributed to stress relaxation under slowly changing strains. Mosqueda et al. (2004) observed force/stress relaxation for 5-second holds. Continuous testing was proposed as an alternative to ramp-hold testing to avoid relaxation.

1.4 Single-axis Hybrid Simulation

Hybrid simulation is an alternative to the quasi-static and shake table test methods, for examining the response of structures. A hybrid test is typically comprised of both numerical (e.g., finite element analysis) and physical substructures. The objective of the hybrid simulation method is to overcome the limitations of quasi-static testing in incorporating system-level interactions into the experiment and need to test a complete structure in the shake table method.

The first hybrid simulation tests were developed in 1969 by Hakuno et al. (1969). A single-degree-of-freedom (SDOF) equation of motion was programmed into an analog computer and a physical specimen was tied to an electromagnetic actuator. The analog computer solves the equation of motion and the restoring forces generated from the physical specimen are used in the next time step. Takanashi et al. (1975) utilizes a digital computer with a magnetic drum to solve the equation of motion and the loading task (e.g., servo-hydraulics). Servo-hydraulic actuators are moved slowly in small increments to achieve good tracking between target and executed displacements. Computers were still quite primitive at the time and establishing the first hybrid simulation took 2 years of development (Nakashima 2020). In the U.S., work on hybrid simulation begin in the 1980s with Hanson and McClamroch (1984). Mahin and Shing (1985) implemented full-scale hybrid simulation test and validated results via comparisons with analytical studies.

A major challenge with hybrid simulation is ensuring that the actuators accurately tracked the target boundary conditions. Small errors can accumulate, propagate into inaccurate hybrid simulation results (Shing and Mahin 1983). The first form of online compensation method for ensuring actuators correctly and accurately tracked boundary conditions is introduced in Nakashima and Kato (1987). The earliest attempts made at developing implicit and explicit numerical integration schemes for ensuring an accurate and stable hybrid simulation came next (Dermitzakis and Mahin 1985; Nakashima et al. 1990; Shing et al. 1991).

The basic procedure for executing a hybrid simulation experiment for a structure subject to earthquake loading is shown in Fig. 1.3, and can be summarized in four steps:

1. At each time step, the ground motion excites the numerical substructure.
2. Within the numerical substructure, the displacements at the boundary condition with the physical specimen are computed.
3. A control algorithm ensures that the physical boundary condition can be achieved with sufficient accuracy.
4. Physical execution is complete via actuators, and restoring forces are recorded and returned to the numerical model for the next time step.

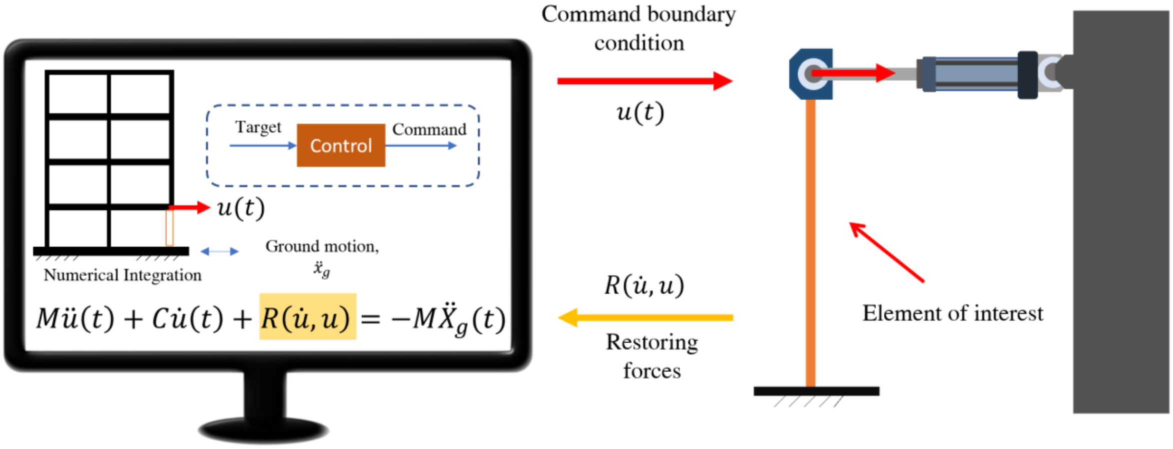

(a) Numerical substructure and controller (b) Physical substructure

Figure 1.3 Hybrid simulation of the reference structure

Hybrid simulation is typically executed at slow speeds with a ramp-hold loading procedure. Many developments allowed for the flexibility to pause and resume the loading during the simulation. The advantage of such capability is for researchers to closely observe the damage and structural behavior. Naturally, slow rate of loading results in dynamic structural behaviors to be ignored. Hybrid simulation is not an appropriate method for materials with significant rate-dependent hysteresis. Many studies have noted small rate-dependence in common structural materials like steel and concrete (Fan et al. 2014; Ghannoum et al. 2012; Li and Li 2012). Therefore, hybrid simulation may be sufficient for steel and concrete.

The next wave of developments came in the form of fast and real-time hybrid simulation (RTHS). Early efforts to capture rate-dependence, resulted in increases in the speed of hybrid simulation to one-fifth of the speed of the actual earthquake (Takanashi and Ohi 1983). The actuator and velocity-control capacities at the time did not yet allow for a real-time test. RTHS requires rapid discrete-time implementation of embedded and data acquisition systems, numerical integration and actuator execution. The first successful RTHS test was demonstrated in Nakashima et al. (1992) for a base isolated structure with a viscous damper. Velocity and acceleration physics of the specimen were automatically incorporated as a result of the real-time testing.

The consequence of the real-time implementation is that stability of the RTHS may be jeopardized when the closed-loop delay is too large. Experimental time delays in RTHS typically translate into negative damping. Although, Moni et al. (2020) discovered that if only inertial forces develop due to actuation, control delays lead to positive damping. This is due to the 180° phase shift between stiffness and inertial forces. When the closed-loop system does not possess sufficient damping and friction to turn the overall system damping positive, instability can occur. Delays in RTHS experiments stem from actuator dynamics, computation, and communication processes. Actuators are complex electro-mechanical devices that possess many unwanted behaviors. Computational delays are due to the effort necessary for time-stepping integration algorithms. Communication delays are associated with the digital and analog signal processing, and exchange of signals between different machines and hardware. Unless a controller is designed to compensate for these closed-loop delays, instability and performance issues are likely to occur. A controller receives the target boundary conditions (e.g., displacements or accelerations) and sends command signals to actuators for execution.

Hybrid simulation to this point was conducted by imposing a displacement target boundary condition. Another type of hybrid simulation that is performed in real-time is the *effective force testing* (ETF) method. The computed inertial force introduced as a result of the relative acceleration of the mass with the ground in the numerical model, is imposed by the actuator. Therefore, the traditional displacement control is not necessary for this method and force control is preferred (Dimig et al. 1999; Thewalt and Mahin 1987; Zhao et al. 2005).

Researchers have adopted RTHS testing for a variety of structural engineering research applications. Horiuchi et al. (1996) performs RTHS on an energy absorber physical specimen and compares results with the shake table method. Polynomial extrapolation techniques are used for actuator compensation. The limitation of this approach is that the order of the proposed polynomial and the overshoot of the actuators when tracking high velocity contents. Carrion et al. (2009) studies a semi-actively controlled structure with a magnetorheological (MR) damper, using the RTHS method. The MR damper and a single servo-hydraulic actuator makes up the physical substructure in this development. A viscous damper is physically tested in Chae et al. (2013). The adaptive time series (ATS) compensator is proposed, where the coefficients of a second-order compensator are updated using a least-square algorithm to minimize closed-loop time delays. This is a time domain compensator and does not provide the predictability of frequency-domain compensators. Additionally, guarantees of parameter convergence and robustness of design are not provided. Asai et al. (2013) proposes a smart outrigger system for tall buildings using clipped optimal semi-actively controlled MR dampers. A feedforward controller is used for compensation. Ou et al. (2015) performs RTHS on an MR damper as well. An H_∞ controller is used for the compensation action. H_∞ controllers are best utilized when closed-loop uncertainties are quantifiable. Measurements of uncertainty are not readily available when physical experiments are involved. Ashasi-Sorkhabi et al. (2015) utilizes a tuned liquid damper for RTHS testing and compares the results of shake table and substructured configurations. Zhang et al. (2017) partitions a 15-story building structure into a 9-story numerical and 5-story physical substructures. An inter-story isolation layer is introduced in the 10th floor along with an MR damper device for vibration reduction. A model-based compensation techniques, based on Phillips et al. (2014), is incorporated for dynamic compensation of the actuators. For further reading on single-axis RTHS applications, reader can see Ahmadizadeh et al. (2008), Chen and Ricles (2010), Gao et al. (2011), Jung et al. (2007), Maghareh et al. (2013), Mercan and Ricles (2009), Nakata et al. (2019), Reinhorn et al. (2003), Shao et al. (2011), Wu et al. (2006), and Zhu et al. (2017).

1.5 Multi-axis Hybrid Simulation

Three-dimensional (3D) and multi-axis tests are important for realistic evaluation of structures and materials. In the context of hybrid simulation, 3D numerical models interact with multi-axial boundary devices (actuator assemblies) to deform the physical specimens. The corresponding 3D feedback forces are then returned to the numerical model. The Load and Boundary Condition Box (LBCB) at the University of Illinois Urbana-Champaign, shown in Fig. 1.4, is an example of a multi-axial boundary device designed for multi-axial hybrid simulation applications.

Figure 1.4 Load and Boundary Condition Box (LBCB)

Multi-axial hybrid simulation has been explored over the last 15 years and is realized typically through one or more multi-actuator boundary interfaces. A physical specimen is equipped with several individual actuators or a rigid multi-axial boundary device (e.g., LBCB), as shown in Fig. 1.5. The Multi-Axial Subassemblage Testing (MAST) system at the University of Minnesota is another multi-axial boundary device that has key quasi-static capabilities (French et al. 2004). Elnashai et al. (2005) introduces the hybrid simulation capabilities at the Newmark Civil Engineering Laboratory at the University of Illinois, and describes examples for use of the large- and small-scale LBCBs of the multi-axial full-scale substructured testing and simulation (MUST-SIM) facility. Frankie et al. (2013) implements hybrid simulation on a curved four-span bridge using the MUST-SIM facility, where the piers of the bridge are physically tested, and the deck is numerically evaluated. The results from the curved bridge simulation are compared to analytical simulations for verification. Murray and Sasani (2016) performs hybrid simulation on a reinforced concrete frame structure under pulse type ground motions. This study evaluated shear failures in pre-1970s RC frame structures. A 10-story structure was considered, and despite immediate failure of the physically tested columns, the building structure did not undergo collapse. Stathas et al. (2017)

introduces hybrid simulation for bridge pier uplifting under transverse seismic loading conditions. A two-span bridge is considered, where the pier is physical and the decks are numerically evaluated. Hashemi et al. (2017) introduces the MAST system at the Swinburne University and its 6-DOF application to an RC column. Carbon fiber reinforcement polymers (CFRP) are used to repair the column. A comparative study of the undamaged and damaged columns concludes that CFRP repair of damaged columns can restore the resistance capacity and ductility of earthquake-damaged columns. Sadeghian et al. (2017) performs multi-axial hybrid simulation of a shear-critical reinforced concrete frame. Modeling of such RC columns for accurate reproduction of damage patterns are discussed. A vast body of literature is designated to the multi-axial and multi-actuator hybrid simulation framework. This framework is however unable to reproduce real-time results because loads are imposed at slow speeds.

The multi-axial real-time hybrid simulation (maRTHS) adds complications involving actuator coupling and dynamics. Unless appropriate steps are taken toward decoupling and control of the multi-actuator system, inaccuracies and instabilities may result. Blakeborough et al. (2001) is the first example of RTHS with a coupled two-actuators system, used for a 2-DOF RTHS experiment. Darby et al. (2002) used the same two-actuator configuration and introduced a polynomial extrapolation algorithm for actuator compensation. In both developments, actuators are compensated independently.

Other literatures in this domain explore increases in the number of DOFs and use of more sophisticated controllers for actuator dynamics and coupling compensation. Wallace et al. (2005) proposes an adaptive polynomial forward prediction algorithm for multi-actuator RTHS. Jung et al. (2007) performs maRTHS using two actuators (e.g., 2-DOF) and explores discrete feedforward and phase lead compensation. Bonnet et al. (2007) investigates the effects of highly stiff actuator coupling. A stiff 3-DOF mass-spring system is studied with actuators installed at either ends. The stiffer the mass-spring system is, the harder the job of controlling the actuators. A minimal control synthesis with a modified demand compensator is introduced, with adaptive feedforward and feedback gains. Phillips and Spencer (2013) proposes a coupled model-based controller for an experimental setup with three actuators. Coupled and decoupled control of the experimental setup are evaluated. Chae et al. (2014) implements a multi-DOF ATS compensator.

Many of the presented developments have involved individually attached actuators to a common physical specimen, as shown in Fig. 1.5(b), instead of a multi-axial boundary device, per Fig. 1.5(a). Control and manipulation of a multi-axial boundary device requires a framework that considers the kinematic transformations necessary between actuator and Cartesian frames of reference. Actuators bound by a rigid link tend to have dynamic coupling, where the movement of one actuator resulting in the movement of other actuators.

Fermandois and Spencer (2017) introduces an maRTHS framework as a tool for addressing rigid boundary condition devices like the LBCB and the MAST. The general architecture for this maRTHS framework involves directing target displacement obtained from a numerical substructure through an outer-loop controller, to computer control signal for LBCB execution. Feedback forces from the physical execution of the boundary device are returned to the microcontroller responsible for the numerical computations, thus closing the overall RTHS loop.

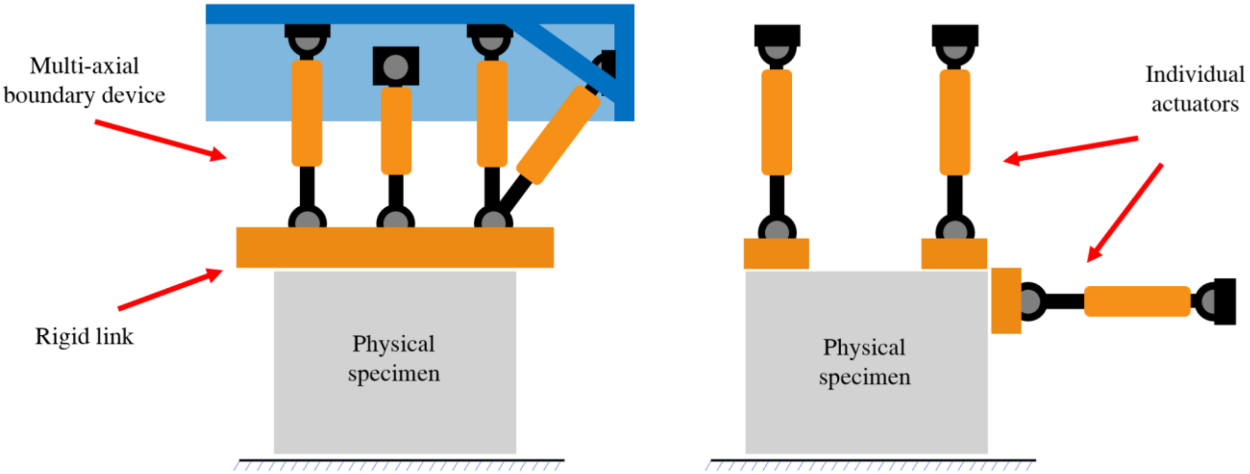

(a) Multi-axial boundary device (b) Several individual actuators

Figure 1.5 Multi-actuator setups

A model-based outer-loop controller is proposed for this framework which addresses the dynamic coupling that exists between the LBCB actuators. Following system identification of the actuators, transfer function models of the individual actuator channels are developed. Through kinematic transformations, the actuator transfer function models are converted to Cartesian coordinate transfer models. Next, feedforward and feedback controllers are designed according to the model-based controller architecture proposed in Phillips and Spencer (2013).

Data acquisition is conducted through the onboard loadcells, which are installed in the axis of each actuator, and external potentiometers that monitor the moving platform of the LBCB. Linear Variable Differential Transformers (LVDT) use can result in inaccurate measurements when LBCB casing and reaction wall undergo elastic deformations. External potentiometers are used instead of the onboard LVDTs. Fig. 1.6, illustrates the small-scale LBCBs and the external potentiometers used in the Fermandois and Spencer (2017) study.

Kinematic transformations are necessary when dealing with multi-axial boundary points. In the maRTHS framework, external potentiometer measurements are converted from potentiometer to Cartesian coordinates. The transformation from axial to Cartesian coordinates is obtained through forward kinematic transformation. By converting the potentiometer measurements to Cartesian coordinates, direct comparison is made between prescribed Cartesian displacements and rotations computed from the numerical model. Since the reference and measured displacements are in Cartesian coordinates, the corresponding outer-loop control task is performed in Cartesian coordinates. Because of the significant coupling that exists in the Cartesian frame of reference, the Cartesian compensator described in the maRTHS procedure is a multi-input multi-output (MIMO) coupled controller.

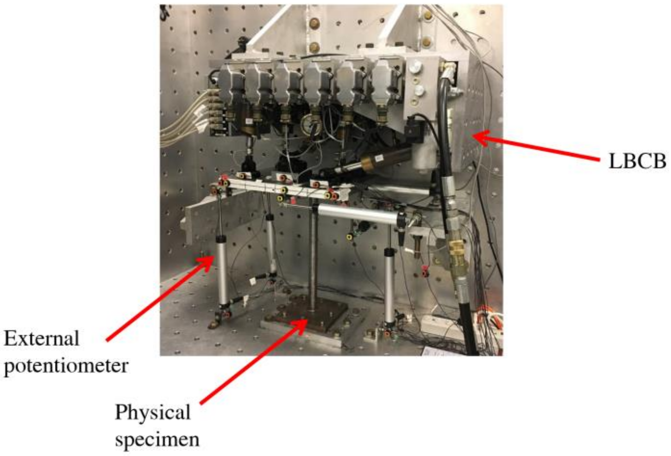

Figure 1.6 Small-scale LBCB and external potentiometers

The illustrative example in Fig. 1.7 is provided, which entails a moment frame with one column substructured physically and the remainder substructured numerically. Only the translational DOF of the inertial mass is considered in this experiment. Earlier studies on the release of the rotational DOFs were found to cause instability problems. It was later discovered that the MIMO controller used for the dynamic compensation of the LBCB was not authoritative and robust enough. Tuning and optimization of MIMO controllers is a challenging task.

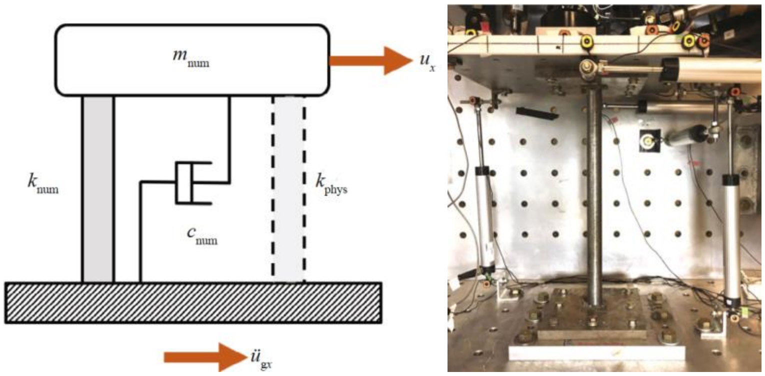

(a) Numerical substructure (b) Physical substructure

Figure 1.7 Multi-axis RTHS of a moment frame

1.6 Actuator compensation

Simulating natural hazard excitations in laboratories require actuators capable of reproducing dynamic behaviors. Accurate replication of prescribed trajectories is desirable for purposes of repeatability and comparison with numerical studies. Shake table testing and real-time hybrid simulation are experimental methods where accurate replications of prescribed trajectories are critical. Both testing methods take advantage of electro-mechanical or servo-hydraulic actuators for imposing forces or movements. Actuator dynamics, however, result in undesirable phase shifts and amplitude variations in the experimental response. Therefore, compensation techniques have been proposed throughout the literature to cancel out some of the dynamics from actuators. System or actuator dynamics in the control theory context is often referred to as a *plant* dynamic.

1.6.1 Shake table compensation

Researchers use shake tables to subject structures to synthetic and historical records as a basis for assessing structural performance (Luco et al. 2010; Ohtani et al. 2004; Reinhorn et al. 2004). Shake tables and structures have a combined dynamic that is coupled and referred to herein as the *shake table-structure dynamics*. Unless appropriate compensation is provided for the shake table-structure dynamics, the shake table will not be able to sufficiently reproduce the prescribed motion accurately.

The process of manipulating an acceleration signal to compensate for unwanted effects of shake table-structure dynamics is referred to as *acceleration tracking*. The *Transfer Function Iteration* (TFI) is a commonly used control method built using an inverse model of the shake table-structure dynamics, that augments the original acceleration time-history with an error signal iteratively, resulting in improved tracking of the reference acceleration signal (Fletcher 1990; Spencer and Yang 1998). Small amplitude time-histories are used for iterative tuning of the TFI controller. Thereby, this method is well-suited when the dynamics of the shake table remains linear. When nonlinearities exist in the dynamics of the onboard structure, the shake table dynamics will also be nonlinear due to the ongoing coupling that exists with the onboard structure. In addition, the TFI method may not be able to compensate for the changing dynamics of the shake table.

Early model-based controllers used the inverse of the nominal model of a shake table, to create a feedforward filter, for prefiltering of acceleration time-histories. Operation of a model-based controller is typically conducted by first obtaining a model of the coupled shake table-structure dynamics. There are numerous system identification tools including frequency-domain identification methods that generate accurate and predictable models of the shake tables. Twitchell and Symans (2003) proposes inverting the actuator model into a feedforward filter and prefiltering the reference signal to tackle both displacement and acceleration tracking problems. This approach is sensitive to structural nonlinearities and failures.

Online model-based controllers can better compensate in acceleration tracking even when nonlinearities are present. Model-based controllers make use of feedforward and feedback controllers for trajectory control of shake tables. Stoten and Shimizu (2007) uses minimal control synthesis (MCS) for adaptive identification of feedforward control parameters. The tracking performance of the MCS is not clearly established. Gao et al. (2012) proposes an H_∞ control approach for actuator displacement tracking. This method requires a high level of accuracy in identification of the plant model and uncertainties. Esparza et al. (2013) introduces model reference adaptive controller (MRAC) for position tracking of a two-axis shake table. This development was only applied to displacement signals, and acceleration tracking was not assessed. Application of MRAC to acceleration tracking is challenging, as the adaptive controller generates low frequency feedback signal, which translates into large drifts for acceleration tracking implementations. Nakata (2010) proposed an acceleration trajectory tracking controller (ATTC) based on the acceleration feedforward control concept, coupled with a displacement feedback and a time delay filter, to ensure displacement feedback does not interfere in the acceleration tracking. The shake table was tested without an onboard structure in this study and the effects of shake table-structure interaction were thus ignored. Phillips et al. (2014) applied a similar architecture for acceleration tracking of a single-axis shake table, called the Model-Based Controller (MBC). Several different feedback configurations were studied, including feedbacks on acceleration, displacement and the combined. With this method, as the control authority is increased to achieve better tracking, stability of the shake table is jeopardized. On the contrary, as the stability is enhanced, the tracking becomes sluggish. In addition, the tracking performance of the MBC often deteriorates as changes take place in the shake table-structure dynamics, resulting in poor tracking robustness. The MBC is used for development of a new controller with enhanced tracking robustness and serves as one of the baseline control techniques used for comparison herein.

1.6.2 Real-time hybrid simulation compensation

The typical RTHS experiment involves numerical simulation of the linear components and physical testing on the components expected to behave in the nonlinear range of the structure using an actuation device. In the experimental partition, actuator dynamics along with computation and communication delays result in phase shifts and amplitude variations which need to be compensated. Some early compensation approaches involved polynomial extrapolation methods (Darby et al. 2002; Horiuchi et al. 1996). The major limitation of these approaches is the order of the proposed polynomial in relationship to the velocity content of the reference signal. Lower order polynomials result in overshoot when tracking high frequency contents and higher order polynomials result in oscillations when tracking low frequency contents. CSI is another phenomenon that has major impact on the performance of actuated systems, which time domain extrapolation methods fail to account for.

Frequency-domain controllers have proven successful for dealing with CSI. Feedforward inverse transfer function methods were the earliest frequency-domain approaches, which stemmed from system identification of a linear system, followed by offline feedforward filtering of the reference signal. Feedforward controllers have improved tracking of both displacement and acceleration reference record (Twitchell and Symans 2003). In real-time applications, inclusion of a feedback controller is necessary to deal with impulse-like behavior and disturbance attenuation.

Next, Model-based techniques came about and made use of feedforward and feedback concepts to produce fast tracking controllers. A displacement tracking MBC combined feedforward and feedback controller was introduced in Carrion et al. (2009) to compensate for experimental dynamics and attenuate disturbances. An additional Linear Quadratic Gaussian (LQG) feedback loop for acceleration tracking was proposed, for improved multi-metric tracking (Phillips and Spencer 2013). The MBC algorithm has been used in operation of single and multi-axis RTHS experiments (Fermandois and Spencer 2017). Tracking accuracy of these controllers is largely dependent on the goodness of the identified plant model. As plant nonlinearities increase and modeling uncertainties develop, these linear controllers may lose robustness and lead to instability. Thus, some later developments shifted focus to robust and adaptive approaches to overcome the listed limitations of linear controllers.

Adaptive control is an approach where the controller adapts itself to the changing dynamics of the plant, hence expanding the successful operational horizon of the controller. The Adaptive Inverse Compensation method is based on displacement tracking where the focus of the adaptation is on the time-varying actuator delays (Chen and Ricles 2010). A discrete-time transfer function is formed with proportional-integral adaptive law based on the tracking indicator (TI) proposed in (Mercan and Ricles 2009). The Adaptive Time Series compensator is another proposed method where the coefficients of a second-order compensator are updated using a least-square algorithm to minimize the system delay (Chae et al. 2013). An advantage of this method is that there are no adaptive gains and the disadvantage is that this method was developed in the time domain, lacks predictability, and does not guarantee parameter convergence. An adaptive scheme was next proposed for the MBC with a projection adaptive law (Chen et al. 2015). The feedforward controller proposed is limited to a third-order transfer function and this poses a constraint when dealing with higher-order systems.

1.7 Research Objective

The objective of this research is to address several of the main limitations of existing hybrid simulation methods for assessment of structural behavior under natural hazard loading. These limitations can be summarized as follows:

i. inability to capture dynamic and rate-dependent behavior of materials,
ii. ineffective means to represent complex three-dimensional interactions at substructure boundaries,
iii. inaccurate target tracking in the nonlinear range,
iv. restriction to a single substructuring interface, and
v. cost burdens.

This research is expected to advance multi-axial real-time hybrid simulation (maRTHS) technology, including multiple boundary interfaces, as a natural extension to many of the existing contributions, namely Carrion et al. (2009), Phillips and Spencer (2013), and Fermandois and Spencer (2017).

1.8 Outline of the Chapters

The chapters in this dissertation will introduce the fundamental concepts and algorithms necessary for successful actuator and shake table operations, single-axis RTHS, and multi-axial RTHS.

Chapter 2 will discuss topics fundamental towards this hybrid simulation research. A generalized equation of motion for modeling of dynamic systems will be presented. A background on control of dynamic systems will be introduced, because many compensation algorithms shall be discussed herein. The governing equations of motion describing the dynamics of servo-hydraulic actuators will be described next, with an in-depth discussion on the servo valve mechanisms. Then, methods for system identification of single-input single-output (SISO) systems are presented. System identification is crucial in design and development of model-based controllers. Because multi-actuator boundary devices are useful for multi-axial testing, fundamentals of kinematic transformations will be presented. Lastly, several commonly used numerical integration schemes will be listed.

Chapter 3 will focus on actuator dynamics and compensation. The natural dynamics of actuators inhibits them from tracking a prescribed trajectory in an accurately and timely manner. A modified actuator compensator based on the model-based controller class of actuator compensators will be discussed. The modified compensator will be comprised of feedforward and feedback LQG controllers. An adaptive expansion will also be proposed for the modified compensator. The application involving the ground motion acceleration tracking of a shake table will also be explored as a verification study.

Chapter 4 will discuss the fundamentals of single-axis model-based RTHS. Model-based frameworks utilize system identified models of actuator and physical specimen dynamics. Several model-based applications will be studied, including: (i) RTHS for lightly-damped and highly-nonlinear structure, (ii) RTHS of bridge vibration mitigation strategy using an MR damper, and (iii) virtual RTHS with adaptive compensation of a three-story steel frame. Once the success of the single-axis model-based strategy is demonstrated, the stage will be set for a multi-axial expansion of the model-based RTHS strategy.

Chapter 5 will introduce the major contribution of this dissertation in the form of the multi-axial RTHS. Requirements for the successful execution of multi-axial RTHS will be listed, including kinematic transformations, actuator compensation, multi-axis load and boundary devices, and computational and input-output peripherals. A simple steel moment structure will be excited with a ground acceleration and used for a validation study. A single physical specimen will be tested in this study. Out-of-plane vibrations will be ignored.

Chapter 6 will consider maRTHS with multiple boundary points and physical specimens. Incorporation of multiple interfaces will expand the existing applications of the RTHS methodology. A validation study involving a multi-span curved bridge structure will be considered where two of the bridge piers will be physically tested while the remainder of the structure is numerically modeled. The behavior of the bridge tested via the maRTHS method will first be compared to numerical simulation results. Next, the test specimen will be pushed into the inelastic range to demonstrate that the proposed framework is capable of nonlinear dynamic testing of structures. In this validation study, out-of-plane capability of the maRTHS framework will be demonstrated.

Lastly, **Chapter 7** will provide concluding remarks regarding the developments in this dissertation and discuss future studies and research directions that the hybrid simulation community can consider exploring.

CHAPTER 2 CONCEPTS IN HYBRID SIMULATION

2.1 Introduction

This chapter provides the prerequisites for the technical concepts described later in this dissertation. The goal of this chapter is twofold: (i) breaking down real-time hybrid simulation (RTHS) framework into smaller subcomponents for ease of understanding, and (ii) insisting on some preliminary aspects, which would otherwise be overlooked. As an example, reference tracking and stabilization of a dynamical systems, like actuators, are possible only when certain conditions of observability and controllability are satisfied.

2.2 Equation of Motion

Consider an *n*-story *reference structure* subject to some arbitrary external force $f(t)$ and ground motion acceleration $\ddot{x}_g(t)$, shown in Fig. 2.1(a). This is representative of a 2-dimensional building structure subject to dynamic forces and accelerations. This *n*-story structure is idealized as an *n*-DOF discretized finite element model (FEM) in Fig. 2.1(b). An FEM model may have any number of DOFs for added complexity and realism, but for the sake of establishing the abstract concept of substructuring of an equation of motion, only the lateral DOFs are presented.

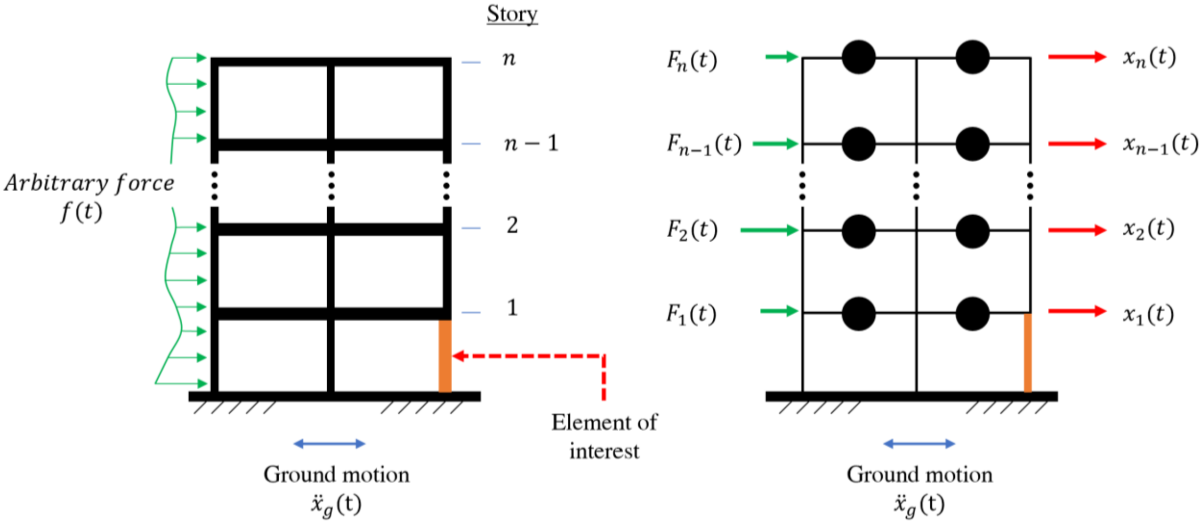

(a) 2-dimensional building structure (b) Idealized building structure

Figure 2.1 Reference structure

The equation of motion for the reference structure can be described as a second-order differential equation, given by

$$\boldsymbol{M}\ddot{\boldsymbol{x}}(t) + \boldsymbol{C}\dot{\boldsymbol{x}}(t) + \boldsymbol{R}(t) = -\boldsymbol{M}\boldsymbol{\iota}\ddot{x}_g(t) + \boldsymbol{F}(t) \tag{2.1}$$

where $\boldsymbol{R}(t) \in \mathcal{R}^n$, $\boldsymbol{C} \in \mathcal{R}^{n\times n}$, and $\boldsymbol{M} \in \mathcal{R}^{n\times n}$ are restoring force, and the positive semi-definite damping and mass matrices for the reference structure. For the elastic case, $\boldsymbol{R}(t) = \boldsymbol{K}\boldsymbol{x}(t)$ with $\boldsymbol{K} \in \mathcal{R}^{n\times n}$ as the stiffness matrix. $\boldsymbol{x}(t) = [x_1(t), x_2(t), \ldots x_{n-1}(t), x_n(t)]^T$, $\dot{\boldsymbol{x}}(t)$, and $\ddot{\boldsymbol{x}}(t)$ are vectors of displacement, velocity, and acceleration value for the DOFs as a function of time t. The ground acceleration is described as $\ddot{x}_g(t)$ and $\boldsymbol{\iota} \in \mathcal{R}^n$ is an influence vector indicating the direction of the inertial forces. All lateral externally applied forces are described in vector form as $\boldsymbol{F}(t) = [F_1(t), F_2(t), \ldots, F_{n-1}(t), F_n(t)]^T$.

The damping matrix is representative of the various friction and dissipative mechanisms that exist in structures. Because damping is a difficult phenomenon to model, it is customary to assume the damping matrix as proportion of the mass and stiffness matrices (i.e., Rayleigh damping).

$$\boldsymbol{C} = a_1\boldsymbol{M} + a_2\boldsymbol{K} \tag{2.2}$$

where a_1 and a_2 are positive coefficients that are fit to predefined modal damping values of the structures under consideration. Modal damping is another approach for estimating the damping matrix, where a specific damping ratio ζ is assigned to each mode individually (Chopra 2011).

The governing equation for the reference structure is next partitioned into numerical and physical substructures by breaking down the property matrices per:

$$\boldsymbol{R} = \boldsymbol{R}_N + \boldsymbol{R}_P\,, \qquad \boldsymbol{C} = \boldsymbol{C}_N + \boldsymbol{C}_P\,, \qquad \boldsymbol{M} = \boldsymbol{M}_N + \boldsymbol{M}_P \tag{2.3}$$

where the subscripts N and P refer to numerical and physical substructures. The property matrices of the numerical and physical substructures should ideally add up to the property matrices of the reference structure. The new governing equations for the numerical and physical substructures are given by:

$$\boldsymbol{M}_N\ddot{\boldsymbol{x}}_N(t) + \boldsymbol{C}_N\dot{\boldsymbol{x}}_N(t) + \boldsymbol{R}_N(t) = -\boldsymbol{M}_N\boldsymbol{\iota}\ddot{x}_g(t) + \boldsymbol{F}(t) - \boldsymbol{F}_R(t) \tag{2.4}$$

$$\boldsymbol{M}_P\ddot{\boldsymbol{x}}_P(t) + \boldsymbol{C}_P\dot{\boldsymbol{x}}_P(t) + \boldsymbol{R}_P(t) = \boldsymbol{F}_R(t) \tag{2.5}$$

where $\boldsymbol{F}_R$(t) are the feedback forces from the physical specimen to the numerical substructure. The numerical substructure is typically modelled as completely elastic. Therefore, the numerical restoring force is simplified to just the elastic stiffness element, $\boldsymbol{R}_N(t) = \boldsymbol{K}_N\boldsymbol{x}_N(t)$.

A structural element of interest is selected for physical substructuring in the reference structure in Fig. 2.1. The boundary point between the physical and numerical substructures is indicated with the red circle in Fig. 2.2. Within the numerical substructure, the states (e.g., displacements and rotations) associated with the boundary condition with the physical substructure are denoted as $\boldsymbol{x}_N^{BC}(t) \subset \boldsymbol{x}_N(t)$. In an ideal world, the calculated boundary conditions are perfectly replicated in the physical substructure, with $\boldsymbol{x}_N^{BC}(t) = \boldsymbol{x}_P^{BC}(t)$. Upon excitation of the physical substructure with boundary point states (i.e., conditions), specimen forces are measured and applied back to the numerical substructure at the location of the boundary condition.

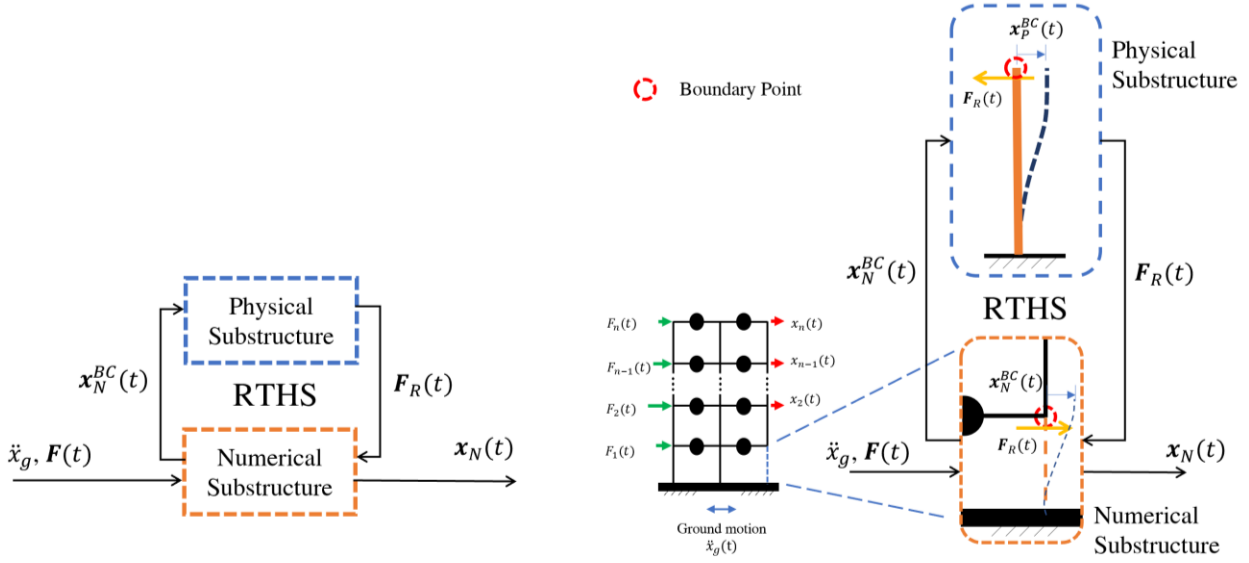

(a) Closed-loop architecture of RTHS (b) Application of RTHS to reference structure

Figure 2.2 Real-time hybrid simulation of the reference structure

It follows that in reality a perfect match between the numerical and physical boundary conditions is very difficult to achieve, due to the unwanted dynamics that exist in servo-hydraulic actuators. Control algorithms are incorporated into the closed-loop architecture to ensure that the error between the numerical and physical boundary conditions at time t is minimized to less than some finite value ϵ, otherwise instability can occur.

$$|\boldsymbol{x}_N^{BC}(t) - \boldsymbol{x}_P^{BC}(t)| < \epsilon \tag{2.6}$$

2.3 Dynamic System Control

The job of control theory in engineering is to alter and modify the responses of dynamic systems or plants. The behavior of a plant may be linear or nonlinear, and deterministic or stochastic. The plant inputs, outputs, and states are described by the vectors $\boldsymbol{u}(t)$, $\boldsymbol{y}(t)$, and $\boldsymbol{x}(t)$, respectively. The control objective is summarized as manipulation of the input signal $\boldsymbol{u}(t)$ to ensure that the output signal $\boldsymbol{y}(t)$ follows a prescribed trajectory and physical performance requirement.

Given a linearized n-DOF building structure in Fig. 2.1, a general form for the governing equation can be written as

$$\boldsymbol{M}\ddot{\boldsymbol{x}}(t) + \boldsymbol{C}\dot{\boldsymbol{x}}(t) + \boldsymbol{K}\boldsymbol{x}(t) = \boldsymbol{F}(t) \tag{2.7}$$

where the input to the building structure or plant is the force vector $\boldsymbol{F}(t) \in \mathcal{R}^n$. The outputs from the system can be defined as the story-level accelerations $\ddot{\boldsymbol{x}}(t) \in \mathcal{R}^n$, since displacement and velocity data are harder to detect via data acquisition sensors from a building structure.

The second-order differential equation in Eq. (2.7) is next re-written as set of first-order differential equations, via the introduction of a new state variable $\boldsymbol{z}(t) = \begin{bmatrix} \boldsymbol{x}^T(t) & \dot{\boldsymbol{x}}^T(t) \end{bmatrix}^T$. Following a series of arithmetic manipulations, the governing equation can be written as a state-space formulation, given by

$$\begin{aligned} \dot{\boldsymbol{z}}(t) &= \boldsymbol{A}_s\boldsymbol{z}(t) + \boldsymbol{B}_s\boldsymbol{F}(t) \\ \boldsymbol{y}(t) &= \boldsymbol{C}_s\boldsymbol{z}(t) + \boldsymbol{D}_s\boldsymbol{F}(t) \end{aligned} \tag{2.8}$$

$$\boldsymbol{A}_s = \begin{bmatrix} \boldsymbol{0} & \boldsymbol{I} \\ -\boldsymbol{M}^{-1}\boldsymbol{K} & -\boldsymbol{M}^{-1}\boldsymbol{C} \end{bmatrix}, \quad \boldsymbol{B}_S = \begin{bmatrix} \boldsymbol{0} \\ \boldsymbol{M}^{-1} \end{bmatrix}, \quad \boldsymbol{C}_s = [-\boldsymbol{M}^{-1}\boldsymbol{K} \quad -\boldsymbol{M}^{-1}\boldsymbol{C}], \quad \boldsymbol{D}_s = [\boldsymbol{0}] \tag{2.9}$$

where $\boldsymbol{A}_s \in \mathcal{R}^{2n\times 2n}$, $\boldsymbol{B}_s \in \mathcal{R}^{2n\times n}$, $\boldsymbol{C}_s \in \mathcal{R}^{n\times 2n}$, and $\boldsymbol{D}_s \in \mathcal{R}^{n\times n}$ are state, input, output, and throughput matrices, respectively. $\boldsymbol{y}(t) \in \mathcal{R}^n$ is a vector of outputs (i.e., story-level absolute accelerations). In the state-space matrices provided in Eq. (2.9), $\boldsymbol{I} \in \mathcal{R}^{n\times n}$ and $\boldsymbol{0} \in \mathcal{R}^{n\times n}$ are identity and zero matrices.

The eigenvalues and eigenvectors of the state matrix $\boldsymbol{A}_s$, are described by $\boldsymbol{\Lambda} \in \mathcal{R}^{2n\times 2n}$ and $\boldsymbol{V} \in \mathcal{R}^{2n\times 2n}$ respectively. An n-DOF system has n eigenvalues which can be obtained through $\boldsymbol{\Lambda} = \boldsymbol{V}\boldsymbol{A}_s\boldsymbol{V}^{-1} = diag[\lambda_1, \lambda_2, \dots, \lambda_{2n-1}, \lambda_{2n}]$. A linear time-invariant (LTI) system is said to be *stable* when $Re(\lambda_i) \leq 0$ for $i = \{1,2,\dots,2n-1,2n\}$. For nonlinear systems, the Lyapunov direct method may be used for proof of stability (Chen 1999). The analytical expression for the states of the system in Eq. (2.8) is computed via:

$$\boldsymbol{z}(t) = \boldsymbol{\phi}(t)\boldsymbol{z}_0 + \int_0^t \boldsymbol{\phi}(t-\tau)\boldsymbol{B}_s\boldsymbol{F}(\tau)d\tau \tag{2.10}$$

where $\boldsymbol{z}_0 = \boldsymbol{z}(0) \in \mathcal{R}^{2n}$ are the initial conditions for the system states, and $\boldsymbol{\phi}(t) \coloneqq e^{\boldsymbol{\Lambda}t} = diag\left[e^{\lambda_1 t}, e^{\lambda_2 t}, \dots, e^{\lambda_{2n-1} t}, e^{\lambda_{2n} t}\right]$.

Sometimes dynamical systems are converted from time domain to Laplace domain (or frequency domain). In frequency-domain differential operations are converted to algebraic operations, resulting in computational efficiency. Laplace transform is a one-sided improper integral given by:

$$P(s) = \int_0^\infty p(t)e^{-st}dt \tag{2.11}$$

with s as the Laplace variable. $P(s)$ and $p(t)$ are a Laplace pair (i.e., Laplace and time domain manifestations of the same function). A linear time-invariant dynamical system can be described in the Laplace domain as a transfer function. The equation of motion in Eq. (2.7) for a single-DOF system, given an input force $F(t)$ and output acceleration $\ddot{x}(t)$ is written as:

$$\boldsymbol{G}_{\ddot{x}F}(s) = \frac{\ddot{X}(s)}{F(s)} = \frac{s^2}{ms^2 + cs + k} \tag{2.12}$$

where k, c, and m are the stiffness, damping, and mass parameters for the single-DOF system. The subscripts of the transfer function $\boldsymbol{G}_{\ddot{x}F}(s)$ describe the output-input pair, respectively. The transfer function for the n-DOF can be obtained by converting the state-space to a transfer function formulation:

$$\boldsymbol{G}_{\ddot{x}\boldsymbol{F}}(s) = \frac{\ddot{\boldsymbol{X}}(s)}{\boldsymbol{F}(s)} = \boldsymbol{C}_s(s\boldsymbol{I} - \boldsymbol{A}_s)^{-1}\boldsymbol{B}_s + \boldsymbol{D}_s \tag{2.13}$$

The state-transition matrix in Laplace domain is defined as $\boldsymbol{\Phi}(s) = (s\boldsymbol{I} - \boldsymbol{A}_s)^{-1} = \mathcal{L}\big(\boldsymbol{\phi}(t)\big)$, with $\mathcal{L}$ indicating a Laplace transform. Even before solving the differential equation, a transfer function can provide valuable information about the system characteristics. The numerator and denominator of a transfer function can be written in factored form:

$$\boldsymbol{G}(s) = \frac{N(s)}{D(s)} = \frac{K(s - z_1)(s - z_2)\ldots(s - z_{a-1})(s - z_a)}{(s - p_1)(s - p_2)\ldots(s - p_{b-1})(s - p_b)} \tag{2.14}$$

where $N(s)$ and $D(s)$ are numerator and denominator polynomials. The roots of the numerator and denominator, z_j for $j = \{1,2,\ldots,a\}$ and p_k for $k = \{1,2,\ldots,b\}$ and K, are termed as the *zeros*, *poles*, *and gain* of the transfer function, respectively. All zeros and poles are either purely real valued $p_k = \sigma_k$, or appear in complex conjugate pairs $p_k = \sigma_k \pm i\omega_k$. For a stable system, all the poles must have negative real parts, otherwise the output of the system increases without bounds, resulting in instability.

2.3.1 Controllability and observability

A system of linear algebraic equations has unique solutions if and only if the rank of the system is equal to the number of variables in that system. *Controllability* and *observability* are important tests for the LTI systems that involve ranking testing of state-space matrix combinations. Controllability describes whether a system can be manipulated with a control input, in a finite time. Observability describes whether the states of a system are observable given the available knowledge from the system inputs and outputs, in a finite time. These concepts are later on tied to controllers and estimators.

For the n-DOF system in Eq. (2.1), the controllability matrix is given by:

$$\boldsymbol{\mathcal{C}} = [\boldsymbol{B}_s \quad \boldsymbol{A}_s\boldsymbol{B}_s \quad \boldsymbol{A}_s^2\boldsymbol{B}_s \quad \ldots \quad \boldsymbol{A}_s^{2n-1}\boldsymbol{B}_s] \tag{2.15}$$

and if the rank of the controllability matrix is equal to the rank of the system, $rank(\boldsymbol{\mathcal{C}}) = 2n$, the dynamical system is controllable. Similarly, an observability matrix is written as:

$$\boldsymbol{\mathcal{O}} = [\boldsymbol{C}_s \quad \boldsymbol{C}_s\boldsymbol{A}_s \quad \boldsymbol{C}_s\boldsymbol{A}_s^2 \quad \ldots \quad \boldsymbol{C}_s\boldsymbol{A}_s^{2n-1}]^T \tag{2.16}$$

and if the rank of the observability matrix is equal to the rank of the system, $rank(\boldsymbol{\mathcal{O}}) = 2n$, the dynamical system is observable.

2.3.2 State feedback

A full-state feedback is the simplest form of control action, used to change how a dynamic system (plant) behaves by moving the poles of the system. A *state feedback* matrix $\boldsymbol{K} \in \mathcal{R}^{n\times 2n}$ scales the system states and typically gets added to the reference trajectory $\boldsymbol{r}(t)$ to produce a control signal $\boldsymbol{u}(t) = \boldsymbol{K}\boldsymbol{z}(t) +$

$\boldsymbol{r}(t)$. For the dynamic system in Eq. (2.1), the reference signal is $\boldsymbol{F}(t) = \boldsymbol{r}(t)$. The new closed-loop state-space system with the added state-feedback is demonstrated in Fig. 2.3, and also expressed in Eq. (2.17).

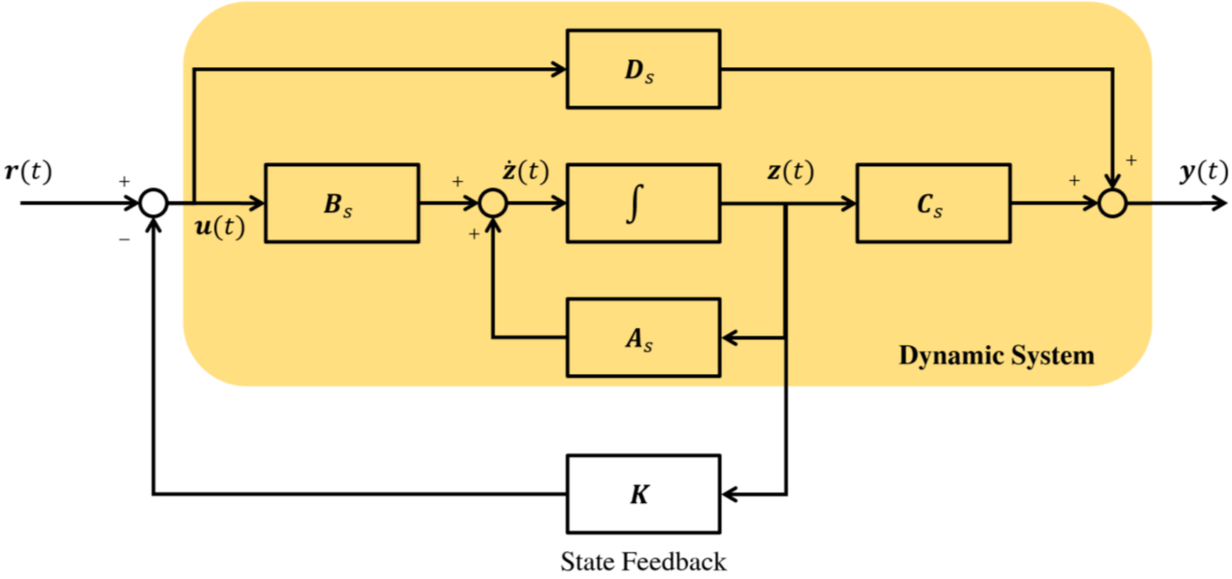

Figure 2.3 State-space system with full-state feedback

$$\dot{\boldsymbol{z}}(t) = (\boldsymbol{A}_s - \boldsymbol{B}_s\boldsymbol{K})\boldsymbol{z}(t) + \boldsymbol{B}_s\boldsymbol{r}(t) \tag{2.17}$$

Having established the concepts of controllability and stability and state-feedback, the following theorem needs to be stated: An LTI system is *stabilizable* if there exists a state feedback matrix $\boldsymbol{K}$ that can ensure $\boldsymbol{A}_s - \boldsymbol{B}_s\boldsymbol{K}$ is stable. All unstable modes need to be controllable for this condition.

2.3.3 State observer

The assumption so far has been that states of the dynamical system are available for feedback action. Measurements of states depend on availability and distribution of sensors. For instance, in the dynamical system in Eq. (2.1), installation of accelerometers results in the availability of the acceleration states. Other states like velocity and displacement are typically not available. A *state observer* or *estimator* will generate an estimate of the states of the plant, whether available or not. Development of state observers typically require advanced knowledge of the system and the availability of an estimate of the dynamical model. Assuming a perfect knowledge of the plant dynamics, the following state observer can be designed:

$$\dot{\hat{\boldsymbol{z}}}(t) = (\boldsymbol{A}_s - \boldsymbol{L}\boldsymbol{C}_s)\hat{\boldsymbol{z}}(t) + \boldsymbol{B}_s\boldsymbol{r}(t) + \boldsymbol{L}\boldsymbol{y}(t) \tag{2.18}$$

where $\hat{\boldsymbol{z}}(t)$ and $\dot{\hat{\boldsymbol{z}}}(t)$ are estimates of the system states and their derivatives. $\boldsymbol{L} \in \mathcal{R}^{2n\times n}$ is termed as the *observer gain*, and the main design objective in a state observer. A dynamic system is said to be detectable if there exists an observer gain $\boldsymbol{L}$ such that $\boldsymbol{A}_s - \boldsymbol{L}\boldsymbol{C}_s$ is stable. All unstable modes must be observable for this condition (Tsai and Gu 2014).

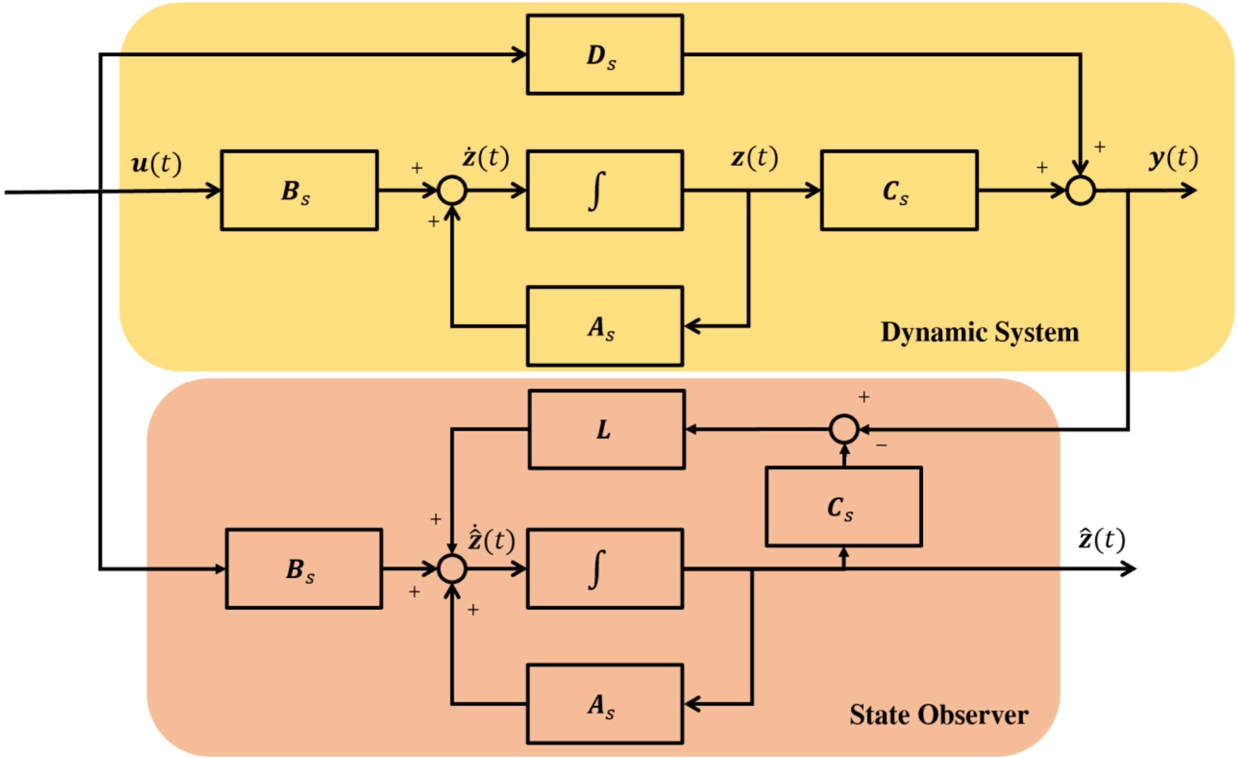

Figure 2.4 State-space system with a state observer

A major share of the discussions on dynamic system controls in this dissertation surrounds the control of servo-hydraulic actuators which are critical to experimental testing of structures – in particular, the physical testing component of RTHS.

2.3.4 PID control

The proportional-integral-derivative (PID) controller is a popular control algorithm that is often used as an inner stabilizing controller for many research and industrial control applications. Simplicity and ease-of-design have made PID a popular choice. The error between a reference and measured executed signal are computed and subjected to *proportional*, *integral*, and *derivative* gains (the three gains).

The design objective for a PID controller is summarized in the optimization of the three gains G_P, G_I, and G_D. Proportional gain reduces rise-time and the steady-state errors between the reference and measured signals. However, it also results in overshoot and ripple effects (i.e., extended settling time). Derivative gain reduces the overshoot and ripple effects. The proportional gain can never fully remove steady-state error; thus, an Integral control is usually included. These gains are increased from a zero position gradually until the desired performance between the reference and measured signals $r(t)$ and $y(t)$ are met. The Ziegler -Nichols rule is an attempt at developing heuristic tuning steps for a PID controller.

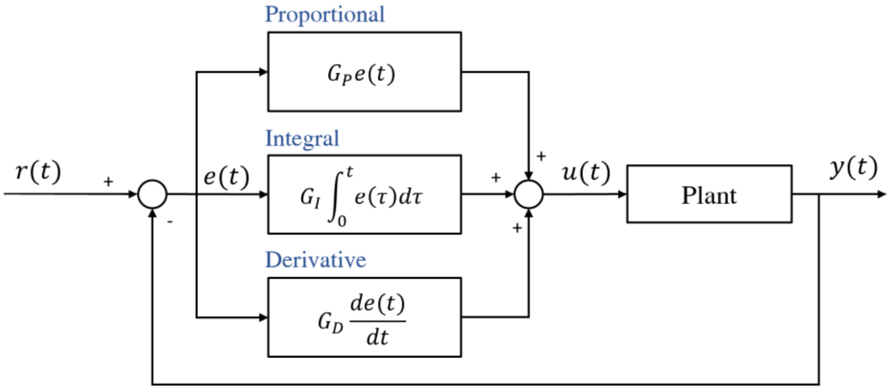

Figure 2.5 PID control architecture

The command signal $u(t) \in \mathcal{R}$ is the summation of the error terms multiplied by their corresponding PID gains

$$u(t) = G_P e(t) + G_I \int_0^t e(\tau)d\tau + G_D \frac{de(t)}{dt} \tag{2.19}$$

2.4 Servo-hydraulic Actuators

Servo-hydraulic actuators fulfil the important purpose of imposing boundary conditions on physical specimen(s) in an RTHS test. Actuators can operate individually or in tandem to actuate one or more Cartesian DOFs. The LBCB device shown in Fig. 1.4 for instance has six actuators and can impose motion in six DOFs. Based on the principles of incompressible flow, hydraulic fluid pressure provides the main energy source for a series of mechanical and electrical apparatuses that result in extension or retraction of an actuator arm. As the flow of the hydraulic fluid is stymied, pressure is built up.

The operation of a servo-hydraulic actuator begins with a hydraulic oil tank. An oil pump generates flow through the pressure pipe shown in blue in Fig. 2.6(a). A tank pipe, shown in red, returns the flow of oil into the oil tank, ensuring a closed-loop operation. A hydraulic actuator has two chambers: left and right as illustrated in Fig. 2.6(b).When oil flows into the right chamber, it is followed by pressure build up in the right chamber and a resultant pressure differential across the piston. This results in the extension of the piston rod. Similarly, oil flow into the left chamber corresponds to a retraction of the piston rod.

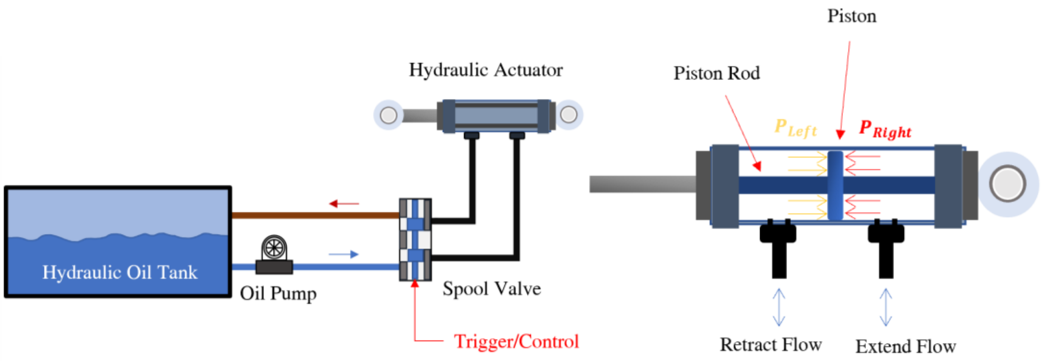

(a) Closed-loop hydraulic actuator (b) Chambers of a hydraulic actuator

Figure 2.6 Operation of a servo-hydraulic actuator

A spool valve controls the flow into each chamber of the actuator. Control and trigger of the spool valve are typically conducted in three ways: (i) manually, (ii) solenoids, and (iii) servo valves. A manual approach at triggering a spool valve is the simplest form but is not an option for real-time applications. Solenoids are inexpensive and easy to operate. High flow rates and high frequency operations are however not possible due to the physical limitations of solenoids. Electrohydraulic servo valves are another popular but more expensive options for operation of more powerful hydraulic actuators with a small electric signal.

2.4.1 Servo valve

The focus of the discussion herein is limited to two-staged electrohydraulic servo valves, similar to the types used in the experimental setups in later sections. These servo valves are able to convert low-powered electrical signals to high-precision control, high-power and low-speed hydraulic actuators (Changhai and Hongzhou 2014). The two-stages involved are: (i) flapper nozzle system, and (ii) spool valve. The servo valve receives high pressure hydraulic oil from a pump and an electrical signal. The job of a servo valve is to release hydraulic pressure to an actuator proportional to the electrical current provided (Merritt 1967).

The mechanisms involved in the operation of a two-staged servo valve are highly precise and repeatable. Fig. 2.7 provides a schematic of a two-staged servo valve. Hydraulic oil supplied from an oil pump enters through the supply pipe and rises in the spool valve (blue region) chamber in stage 2. When the hydraulic actuator is intended to be at an equilibrium position, no electrical signal is applied to the flapper in stage 1. Hence, the flapper stays in a vertical position and oil flow continues through the nozzles (yellow region) to leaves through the tank return pipe. In this configuration, the oil pressure in the vertical columns to the left and right of the spool remain equal, resulting in no pressure differential and movement.

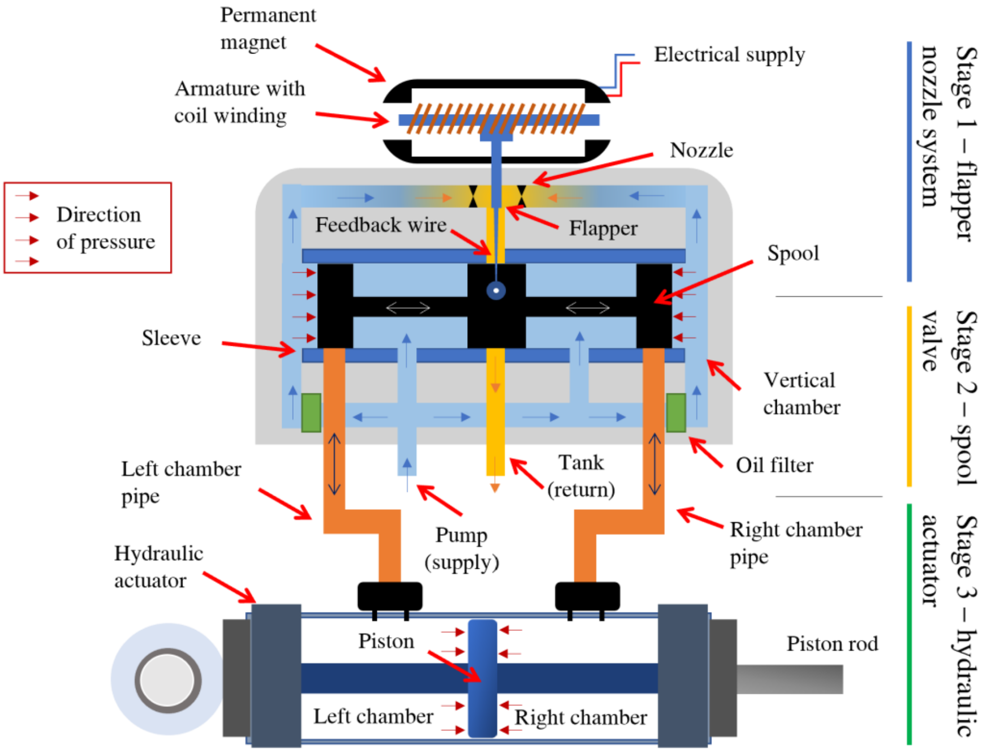

Figure 2.7 Two-stage servo valve and hydraulic actuator

Now suppose the objective is to extend the piston rod by increasing the pressure in the left chamber of the illustrated hydraulic actuator. An electrical signal is applied to the coil windings around the armature in stage 1. The coil generates an electromagnetic torque. The newly magnetized flapper reacts with the permanent magnets and deflects from the original position. The flapper moves horizontally, hindering the flow through one of the nozzles. The decrease in the flow of oil through one nozzle results in the accumulation of pressure in the vertical chamber. This is also associated with a reduction in the oil pressure in the opposing vertical chamber. As a result of the pressure differential at the ends, the spool begins to move releasing flow into the left chamber. Lastly, the pressure in the left chamber of the actuator increases and the piston rod extends.

A feedback mechanism exists that brings the servo valve back to equilibrium. The sliding of the spool results in displacement at the base of the feedback wire, which is fed back to the flapper. The feedback wire provides a spring force that opposes the direction of motion of the spool. This spring force increases until an equilibrium state is reached. The servo valve can therefore release oil flow proportional to the direction and the magnitude of the current applied to the armature.

2.4.2 Parametric modeling of hydraulic actuation

In developing a parametric model, the major components that form a hydraulic actuator system in series are separated and dynamic models of each are formulated. These components include the testing specimen, hydraulic actuator (cylinder), servo valve, and controller. A single-DOF physical specimen is considered by simplifying the system in Eq. (2.1). To move the physical specimen, a piston rod applies a force of f_p. This dynamic force engages the dynamic properties of both the actuator cylinder and the physical specimen.

$$m\ddot{x}(t) + c\dot{x}(t) + kx(t) = f_p(t) \tag{2.19}$$

where $m = m_s + m_p$, $c = c_s + c_p$, and $k = k_s$, with subscripts s and p referring to specimen and piston rod components of mass, damping and stiffness. The stiffness of the physical specimen here is expected to dominate the stiffness of the hydraulic actuator (Carrion and Spencer, Jr. 2007). The specimen is assumed to stay in the linear elastic range in Eq. (2.19). A transfer function model of the equation of motion is achieved by converting to Laplace domain

$$\boldsymbol{G}_{xf}(s) = \frac{X(s)}{F_p(s)} = \frac{1}{ms^2 + cs + k} \tag{2.20}$$

The physical principal behind deriving the dynamic equation for a hydraulic actuator is the flow continuity principle. Flow continuity is a form of the law of conservation of mass that of course appears in fluids. For a given volume of fluid with volume and density of V and ρ, and input and output flows q_{in} and q_{out} and densities ρ_{in} and ρ_{out} shown in Fig. 2.8(a) the following relationship is established

$$q_{in} - q_{out} = \frac{dV}{dt} + \frac{V}{\rho}\frac{d\rho}{dt} \tag{2.21}$$

Next, the bulk modulus of elasticity for fluids $\beta = \frac{dp}{\frac{d\rho}{\rho}}$ is considered, with dp defining a differential change in pressure, and $d\rho$, the differential change in density of the object, in order to remove the density terms in Eq. (2.21).

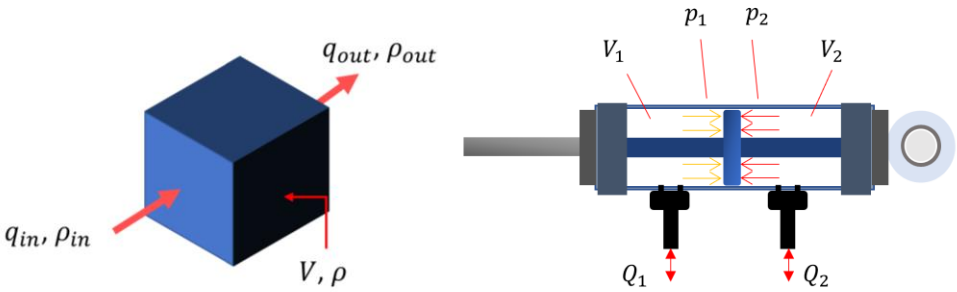

(a) Control volume for continuous flow (b) Hydraulic actuator

Figure 2.8 Schematics for continuity flow relationships

It is also important to incorporate the flow directions into relationship Eq. (2.21) as the extension/retraction behavior of hydraulic actuators matters. By considering actuator motion in one direction only, Eq. (2.21) simplifies to the given

$$q_i(t) = A_i v(t) + \frac{V_i}{\beta}\frac{dp_i(t)}{dt} \tag{2.22}$$

where A is the internal area of the piston, v is the fluid velocity, V is the volume of the chamber, and i specifies which chamber (e.g., 1 for left and 2 for right). So far, the continuity assumption has assumed a perfect flow without any leakage. However, leakages exist in the form of external leakage: from actuator lining to the drain, and internal leakage: across the piston. The total load flow, hence, includes volumetric flow, leakage flow, and compressibility. Combining equation Eq. (2.22) for $i = \{1,2\}$ and given that $V_t = V_1 + V_2$, the following relationship is arrived at

$$q_L(t) = A\dot{x}(t) + C_l p_L(t) + \frac{V_t}{4\beta}\dot{p}_L(t) \tag{2.23}$$

where $q_L = \frac{q_1+q_2}{2}$ is the total load flow, A is the area of the piston (assumed equal on both sides), $\dot{x}(t)$ is the velocity of the piston, C_l is the total leakage coefficient, and $p_L(t) = p_2(t) - p_1(t)$ is the load pressure (Merritt 1967). The force applied by the piston rod is $f_p(t) = Ap_L(t)$. Expressing the first-order dynamics in the Laplace domain

$$\boldsymbol{G}_{pq}(s) = \frac{P_L(s)}{Q_L(s) - AsX(s)} = \frac{1}{C_l + \frac{V_t}{4\beta}s} \tag{2.24}$$

The characteristics of a three-position four-way spool valve similar to those in Fig. 2.7 are considered next with the objective of expressing load flow as a function of load pressure and displacement of spool from the neutral position. A total of 11 nonlinear algebraic equations must be solved simultaneously, which can be tedious. By confining the operational horizon of the valve to the vicinity of the neutral position, a Taylor series expansion of the load flow equation approximated per

$$q_L(t) \coloneqq \frac{\partial q_L}{\partial x_v}x_v(t) + \frac{\partial q_L}{\partial p_L}p_L(t) \tag{2.25}$$

where the first partial derivative is defined as the flow gain $K_q' \coloneqq \frac{\partial q_L}{\partial x_v}$ and the second partial derivative is the flow-pressure coefficient $K_c' \coloneqq -\frac{\partial q_L}{\partial p_L}$.

The dynamics of a servo valve are quite difficult to model due to the complex physical geometry of the various spools and oil chambers. Pressure flow inside the chambers of a servo valve spool are inherently nonlinear (Mu and Li 2011). Many researchers have used first-order models for describing dynamics of servo valves (Carrion and Spencer, Jr. 2007; Qian et al. 2014). Merritt (1967) derived a third-order model, Kim and Tsau (2000) proposed a fifth-order model, and Changhai and Hongzhou (2014) proposed a seventh-order model. For the sake of simplicity, a first-order model of servo valve dynamics used

$$\boldsymbol{G}_{xi}(s) = \frac{K_{sv}}{1 + \tau s} \tag{2.26}$$

where K_{sv} is the servo valve gain, τ is the model time constant, and s is the Laplace variable.

The linearized dynamics of the physical specimen in Eq. (2.20), actuator pressure in Eq. (2.24), servo valve flow in Eq. (2.25), and spool valve motion in Eq. (2.26) are combined to formulate the closed-loop dynamics of the complete servo-hydraulic and specimen system in Fig. 2.9 and fourth-order system in Eqs. (2.27-2.32). A proportional controller with a gain of G_p is assigned to the error term $e(t)$ between the control and measured signals $u(t)$ and $x(t)$.

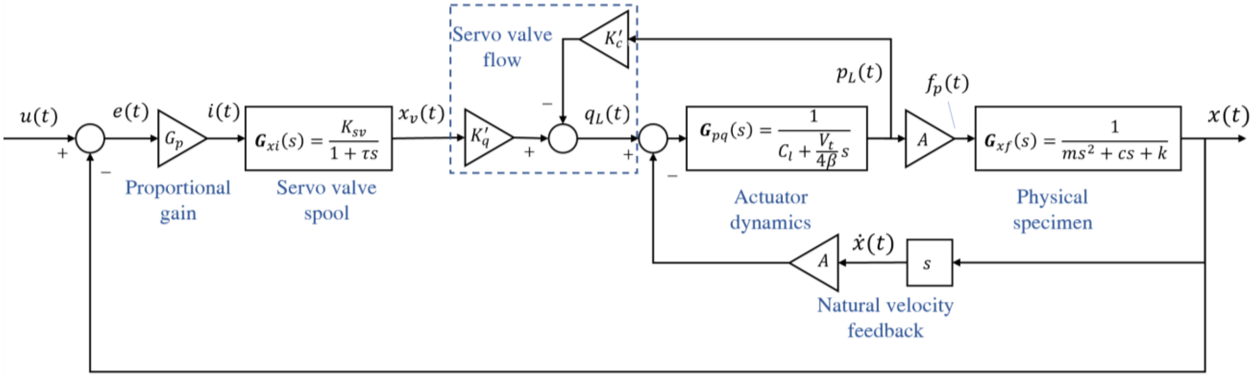

Figure 2.9 Closed-loop dynamics of servo-hydraulic and specimen system

$$\boldsymbol{G}_{xu} = \frac{a_1}{b_5 s^4 + b_4 s^3 + b_3 s^2 + b_2 s + b_1} \tag{2.27}$$

$$a_1 = 4\beta K_p K_q A \tag{2.28}$$

$$b_1 = 4\beta K_c k + 4\beta K_p K_q A \tag{2.29}$$

$$b_2 = 4\beta K_c + V_t k + 4\beta A^2 + 4\beta K_c k\tau \tag{2.30}$$

$$b_3 = 4\beta K_c m + V_T c + 4\beta A^2 \tau + 4\beta K_c c\tau + V_t k\tau \tag{2.31}$$

$$b_4 = V_t m + 4\beta K_c m\tau + V_t c\tau \tag{2.32}$$

$$b_5 = V_t m\tau \tag{2.33}$$

The dynamic coupling between the physical specimen and the actuator is described by a natural velocity feedback. This phenomenon is described as control-structure interaction in (Dyke et al. 1995). The parametric model identified in Eq. (2.27) is capable of capturing this phenomenon for a single-DOF specimen. With the introduction of system identification and nonparametric modeling in later sections, natural velocity feedback for higher-DOF structures are incorporated into the linearized model of the servo-hydraulic actuator and structure system.

A parametric model, also known as a *white-box model*, must be fit to a physical model. Manufacturer specifications provide accurate estimates of many of these parameters. Optimization algorithms for parameter identification may be used because of the finite-dimension of the parameter space (i.e., finite number of unknowns). The linear least-square approach is a simplest form of parameter estimator. Tidwell et al. (2009) uses a nonlinear least-square approach, and Qian et al. (2014) uses a genetic algorithm approach for identification of the parameters. The limitation of parametric modeling is that the exact structure of the dynamical system must be known.

2.4.3 Nonparametric modeling of hydraulic actuation

Nonparametric modeling differs from parametric in that input-output relationships for dynamical systems are not based on predetermined explanatory parameters (e.g., flow coefficients). These models are also termed *black-box* because the structure of the physical process is completely “black” or unknown. The benefit of nonparametric modeling is that it is applicable to the physical specimen with unknown performance. Important design and performance considerations for identification procedures include choice of excitation signals, data sampling, measurement and sensing, and pre-filtering and treatment of data. The modeling tool must be appropriate for the physical system (i.e., linear vs. nonlinear modeling).

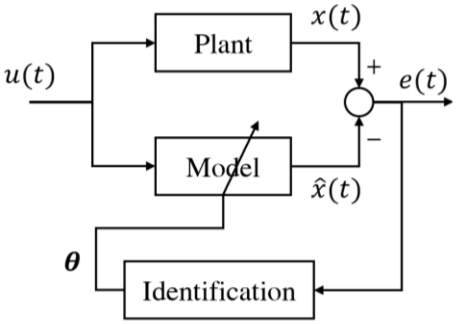

Figure 2.10 System identification of plant dynamics

Modeling of a dynamic process is a two-step process: i) choice of mathematical representation for the model, ii) choice of optimization tool to minimize the error between model output and measured signal. Given the control and measurement signals $u(t)$ and $x(t)$, a mathematical model of the plant dynamics is identified by minimizing the error between the actual and predicted measurement signals, $e(t) = x(t) - \hat{x}(t)$, as illustrated in Fig. 2.10.

Classical modeling approaches include polynomial fitting, autoregressive (ARX) models, state-space and frequency domain fitting. Kim et al. (2005) presents a modeling tool based on frequency domain experimental data and offers the graphical tool *MFDID*, shown in Fig. 2.11, for visualization of the fitted data. MFDID is used for system identification in later sections. The plant dynamics is idealized as a linear polynomial transfer function model and then optimized in three-steps:

1. estimation of plant model via the linear least-square method,
2. improvement using Steiglitz-McBridge method, and
3. final optimization via the Levenberg-Marquardt method.

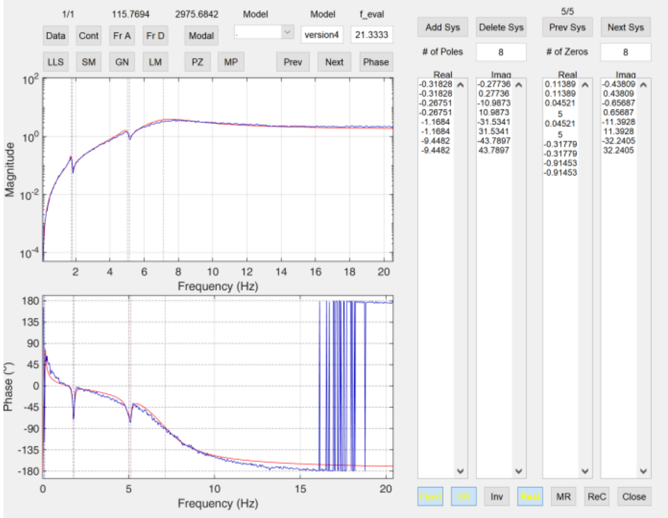

Model: version4

f_eval: 21.3333

# of Poles: 8

# of Zeros: 8

Poles, Real: -0.31828, -0.31828, -0.26751, -0.26751, -1.1684, -1.1684, -9.4482, -9.4482

Poles, Imag: -0.27736, 0.27736, -10.9873, 10.9873, -31.5341, 31.5341, -43.7897, 43.7897

Zeros, Real: 0.11389, 0.11389, 0.04521, 5, 0.04521, 5, -0.31779, -0.31779, -0.91453, -0.91453

Zeros, Imag: -0.43809, 0.43809, -0.65687, 0.65687, -11.3928, 11.3928, -32.2405, 32.2405

Figure 2.11 MFDID

Statistical identification tools like artificial neural networks and fuzzy models have also been proposed for describing the dynamics of actuator-structure systems (Jelali and Kroll 2004). He and Sepehri (1999) used neural networks for describing the dynamics of servo-hydraulic actuators with a mass attached to the piston rod. Neural networks were shown to accurately estimate the nonlinear behaviors of hydraulic actuators. Lastly, between black-box and white-box modeling, if there are any physical insights available into the plant dynamics, *gray-box* modeling techniques can be utilized.

2.5 Frequency domain System Identification

System identification is the process of developing mathematical models of a plant dynamics via measurements of input and output signals. For example, the table acceleration in a shake table test is the input signal and the story accelerations from the onboard structure are output signals. After post-processing of measurement data, a model of the structure is selected, and an optimization algorithm is applied to fit the response of the plant to the model. The final step of system identification is to verify the model against the actual plant.

In a dynamic system, the outputs at the current time are dependent on the instantaneous inputs, and all the past inputs and behaviors. Although many different system identification tools are available for developing dynamic models as discussed in the previous section, the focus of this section is on *frequency* *domain system identification*. As the name suggests, measurements in time domain must first be converted to the frequency domain. A time domain signal $h(t)$ is converted to frequency domain via Fourier transform as described by

$$\begin{aligned} H(\Omega) &= \mathcal{F}[h(t)] \\ &= \int_{-\infty}^{\infty} h(t) e^{-i\Omega t} dt \end{aligned} \tag{2.34}$$

for $-\infty < \Omega < \infty$, where $\Omega \coloneqq 2\pi f$ is the angular frequency, f is the harmonic frequency, and $\mathcal{F}$ indicates Fourier transforms. The inverse Fourier transform converts frequency domain signals back to time domain:

$$\begin{aligned} h(t) &= \mathcal{F}^{-1}[H(\Omega)] \\ &= \frac{1}{2\pi} \int_{-\infty}^{\infty} H(\Omega) e^{i\Omega t} d\Omega \end{aligned} \tag{2.35}$$

with Eqs. (2.34) and (2.35) termed as Fourier transform pairs. The Fourier transforms of signals are often used to find the power of a signal distributed with frequency. An *auto-spectral density function* (also called power spectral) is given by

$$S_{hh}(\Omega) = |H(\Omega)|^2 \tag{2.36}$$

Similarly, the cross-spectral density function is defined as

$$S_{hg}(\Omega) = |H^*(\Omega)G(\Omega)| \tag{2.37}$$

where the superscript $*$ signifies a complex conjugate.

2.5.1 Frequency response function

A *frequency response function* (FRF) conveys valuable information about the dynamics of a plant, including gain and phase as a function of frequency, resonant frequencies, and damping factors. The FRF of a plant is obtained using Fourier transforms of signals, spectral densities, and excitation. Random and sine-sweep excitations are popular options as they cover a whole bandwidth of frequencies. Other forms of excitations used for resonance analysis, like hammer impact testing, may also be used for acquiring the FRF. An FRF contains both gain and phase informations of the plant dynamics. Per Fig. 2.12, given an excitation $x(t)$ and a response $y(t)$, an FRF $\boldsymbol{H}(\Omega)$ is expressed by

$$X(\Omega) = \boldsymbol{H}(\Omega)Y(\Omega) \tag{2.38}$$

where $X(\Omega)$ and $Y(\Omega)$ are Fourier transforms of $x(t)$ and $y(t)$, respectively.

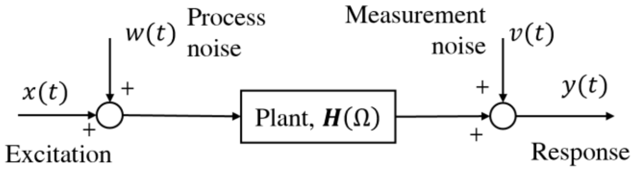

Figure 2.12 Plant response subject to excitation

Two commonly used methods for acquiring the FRFs of single-input single-output plants are the $\boldsymbol{H}_1(\Omega)$ and $\boldsymbol{H}_2(\Omega)$ methods. The $\boldsymbol{H}_1(\Omega)$ is an FRF estimation approach where the output is expected to be noisier than the input, $v(t) \gg w(t)$. The influence of uncorrelated noise in the output is reduced via averaging.

$$\boldsymbol{H}_1(\Omega) = \frac{S_{xy}(\Omega)}{S_{xx}(\Omega)} \tag{2.39}$$

The $\boldsymbol{H}_2(\Omega)$ is the second approach where the input is expected to be noisier than the output, $w(t) \gg v(t)$. The influence of uncorrelated noise in the input is reduced by averaging. The $\boldsymbol{H}_2(\Omega)$ is more commonly used, as it is subject to less resolution-bias errors.

$$\boldsymbol{H}_2(\Omega) = \frac{S_{yy}(\Omega)}{S_{yx}(\Omega)} \tag{2.40}$$

The *coherence function* measures the extent to which an optimum linear least-square relationship can predict the output $y(t)$ from the input $x(t)$. Mathematically, the coherence function is equivalent to the ratio between the cross-spectral density between the input and output signals, and the corresponding auto-spectral densities for each input and output term, given per

$$\gamma_{xy}(\Omega) = \frac{\left|S_{xy}(\Omega)\right|^2}{S_{xx}(\Omega)S_{yy}(\Omega)} \tag{2.41}$$

with γ_{xy} always satisfying $0 \leq \gamma_{xy} \leq 1$. When the value of the coherence function is one, the relationship between input and output signals are perfectly linear. Presence of noise, nonlinearities, and other inputs signals result in reduction in the value of coherence function. A coherence value of zero indicates that the two signals are completely unrelated (Berndat and Piersol 2010). Lastly, the system identification toolbox MFDID discussed in Section 2.4 is applied to the FRF data for fitting transfer function models.

2.6 Kinematic Transformation

Multi-axial boundary point devices are mechanical manipulators made up of several prismatic servo-hydraulic actuators and connected by rotational ball/swivel joints. The number of servo-hydraulic actuators are typically equal to the number of degrees of freedom that the boundary condition assembly can operate in (Tsai 1999). For instance, a 6-DOF boundary condition assembly has six actuators. Each prismatic actuator is a simple prismatic device that extends and retracts in 1-DOF. The actuators are driven by hydraulic fluid pressure described by mechanisms in Section 2.4. Actuators are pinned to a *fixed base* at one end, and a *moving platform* at the other end. The fixed base is typically attached to a rigid reaction wall, and the moving platform is attached to the physical specimen. Examples of multi-axial testing facilities with load and boundary devices are demonstrated in Figs. 2.13 and 2.14.

For hybrid simulation applications, the moving platform may be required to impose displacements and forces onto a physical specimen. The multi-axial boundary condition devices possess mechanical components and sensing devices that allow them to measure the displacements and forces as well, like displacement transducers and loadcells. Controllers are used for the operation of the hydraulic actuators. Inner control loops via PID control (see Section 2.3) ensure stability and outer model-based controllers improve the tracking accuracies. Computational hardware including single-tasking microcontrollers and host personal computers (PCs), provide the high-speed real-time computation and control commands necessary for successful operation of the multi-axial boundary devices.

(a) MAST at the University of Minnesota (b) MAST at the Swinburne University

Figure 2.13 Multi-axial testing facilities

Kinematics of boundary condition devices must be understood for successful use of these assemblies. Kinematics is the science of motion that deals with the geometry of position and force variables with respect to time. There are two types of kinematics transformations that are of importance in this dissertation: forward kinematics and inverse kinematics. *Forward kinematics* considers the strokes in each individual actuator and sensing device for deriving the position and orientation of the moving platform. *Inverse kinematics* uses the available desired positions of the moving platform to calculate what the strokes of individual actuators need to be to achieve the desired motion of the moving platform.

Figure 2.14 Load and Boundary Condition Boxes at the University of Illinois at Urbana-Champaign

2.6.1 Basics of kinematics

A Cartesian coordinate system is employed for studying the kinematics of boundary condition boxes, where every point in a 3D space is described via a three-axis frame of reference (i.e., x, y, and z). The frame of reference is termed *fixed frame* and *moving frame*, when in the original position and orientation and when moved, respectively. Because boundary condition boxes are typically very stiff, the scope of the motions described herein are limited to rigid body motion, which include translation and rotation. A vector $\boldsymbol{v} = \left[v_x, v_y, v_z\right]^T$ describes the motion of the fixed frame origin O to a new position O'. A second vector $\boldsymbol{b} = \left[b_x, b_y, b_z\right]^T$ defines the relative location of the point of interest P to the moving frame origin O'.

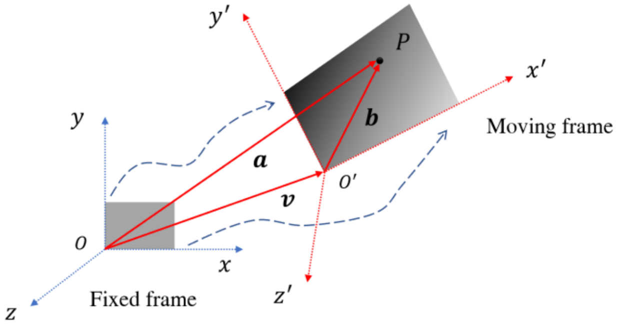

Figure 2.15 3D Cartesian motion

Three moving frame rotations (roll, pitch, and yaw) are possible about the fixed frame. Rotations around the x, y, and z axes are represented by Euler angles and are termed θ_x, θ_y, and θ_z. The counter-clock-wise direction around each axis is the positive rotation. The action of each rigid body rotation is presented mathematically as a matrix. $\boldsymbol{A}_{\theta_x}$, $\boldsymbol{A}_{\theta_y}$, and $\boldsymbol{A}_{\theta_z}$ are three successive rotation matrices about the reference frame. These matrices are multiplied to create a combined rotational matrix $\boldsymbol{A}\left(\theta_x, \theta_y, \theta_z\right) = \boldsymbol{A}_{\theta_x}\boldsymbol{A}_{\theta_y}\boldsymbol{A}_{\theta_z}$.

$$\boldsymbol{A}_{\theta_x} = \begin{bmatrix} 1 & 0 & 0 \\ 0 & c\theta_x & -s\theta_x \\ 0 & s\theta_x & c\theta_x \end{bmatrix}, \quad \boldsymbol{A}_{\theta_y} = \begin{bmatrix} c\theta_y & 0 & s\theta_y \\ 0 & 1 & 0 \\ -s\theta_y & 0 & c\theta_y \end{bmatrix}, \quad \boldsymbol{A}_{\theta_z} = \begin{bmatrix} c\theta_z & -s\theta_z & 0 \\ s\theta_z & c\theta_z & 0 \\ 0 & 0 & 1 \end{bmatrix} \tag{2.42}$$

where c and s are cosine and sine operators. The matrix $\boldsymbol{A}$ contains 9 terms, but rotation can be described by three rotational DOFs. The matrix multiplication in Eq. (2.42) is not commutative, and the order of operation is important. The relationship between the position vectors and rotation matrix help describe the position of the point P with reference with the fixed frame

$$\boldsymbol{a} = \boldsymbol{v} + \boldsymbol{A}\boldsymbol{b} \tag{2.43}$$

where $\boldsymbol{a} = \left[a_x, a_y, a_z\right]^T$. The rigid motions can be represented in a single *homogeneous transformation* matrix with the form given by

$$\boldsymbol{H} = \begin{bmatrix} \boldsymbol{A} & \boldsymbol{v} \\ \boldsymbol{0} & 1 \end{bmatrix} \tag{2.43}$$

where $\boldsymbol{0} = [0 \quad 0 \quad 0]^T$. In addition, the vectors $\boldsymbol{a}$ and $\boldsymbol{b}$ are augmented to the form

$$\boldsymbol{a}' = \begin{bmatrix} \boldsymbol{a} \\ 1 \end{bmatrix} \qquad \boldsymbol{b}' = \begin{bmatrix} \boldsymbol{b} \\ 1 \end{bmatrix} \tag{2.44}$$

2.6.2 Serial manipulators

Serial manipulators are a class of open-loop robots with a series of actuated joints extending from a fixed base to a moving platform or end effector. The relative motion for each actuator (e.g., motor) is controlled individually to achieve a prescribed final position for the end effector. Fig. 2.16 illustrates an n-DOF serial manipulator with a fixed base and an end effector. The frame of reference at the fixed base is referred to as the fixed frame, and each actuator has its own moving frame.

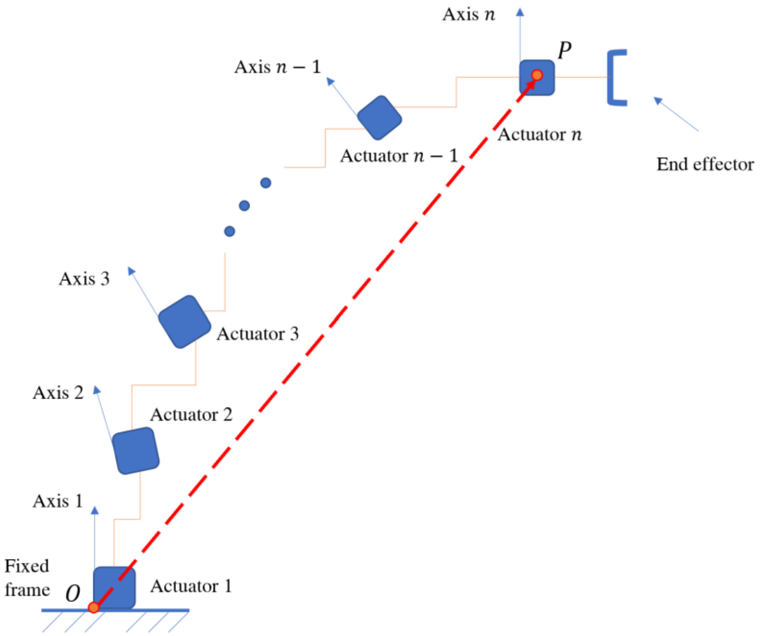

Figure 2.16 n-DOF serial manipulator

The forward kinematics path in a serial manipulator involves user specified strokes in prismatic actuators and rotations in revolute actuators, to achieve some final end effector position. Most actuators are either prismatic or revolute. Hence, a joint variable is considered as input into the homogeneous transformation matrix:

$$q_i = \begin{cases} \theta_i & : \text{revolute actuators} \\ v_i & : \text{prismatic actuators} \end{cases} \tag{2.45}$$

and since most actuators are either prismatic or revolute the homogeneous transformation matrix becomes a function of a single joint variable $\boldsymbol{H}_i = \boldsymbol{H}_i(q_i)$. Note, that the matrix $\boldsymbol{H}_i$ is not a constant and is updated at each time instant for a moving end effector (Spong et al. 2005). The homogeneous transformation matrices are next multiplied to achieve a *transformation matrix* denoted by T_{ij}, given by

$$\begin{aligned} &\boldsymbol{T}_{ij} = \boldsymbol{H}_{i+1}\boldsymbol{H}_{i+2} \dots \boldsymbol{H}_{j-1}\boldsymbol{H}_j \quad \text{if} \quad \mathrm{i} < \mathrm{j} \\ &\boldsymbol{T}_{ij} = \boldsymbol{I} \quad \text{if } \mathrm{i} = \mathrm{j} \\ &\boldsymbol{T}_{ij} = \left(\boldsymbol{T}_{ij}\right)^{-1} \quad \text{if} \quad \mathrm{j} > \mathrm{i} \end{aligned} \tag{2.46}$$

The transformation matrix between the fixed frame and the end effector summarizes the forward kinematics in serial manipulators and is described by

$$\boldsymbol{T}_{0n} = \boldsymbol{T}_1\boldsymbol{T}_2 \dots \boldsymbol{T}_{n-1}\boldsymbol{T}_n \tag{2.47}$$

The matrix $\boldsymbol{T}_{0n} = t_{ij}$ for $i = \{1{,}2{,}3\}$ and $j = \{1 \dots 4\}$, has 12 entries which are nonlinear trigonometric equations. Because the forward kinematic relationships are non-trivial and complex nonlinear functions of joint variables, inverting the kinematics problem is a challenging task. The inverse kinematic problem for a serial manipulator involves solving for the closed-form relationship

$$q_k = f_k(t_{11}, \dots, t_{34}) \quad \text{for } i = 1, \dots, n \tag{2.48}$$

In instances when finding a closed-form solution is computationally expensive and not manageable within a finite time, numerical approximations are possible. In a serial manipulator, forward kinematics is fairly straightforward and inverse kinematics is very tricky to solve. For applications of RTHS, iterative numerical approximations are often not appropriate. Next, several solutions may exist for inverse kinematics problems. Physical laws need to be considered to rule out unfeasible and unrealistic solutions.

2.6.3 Parallel manipulators

Parallel manipulators are a class of closed-loop robots with multiple actuator arms controlling a single moving platform. Because the loads experienced by the moving platform are shared between the actuators, parallel manipulators have large load-carrying capacities. This quality is very attractive for experimental testing applications in structural engineering where high load capacity boundary devices are desired. The boundary condition devices illustrated in Fig. 2.13 and Fig. 2.14 are both examples of parallel manipulators.

A schematic of a generalized parallel manipulator is presented in Fig. 2.17. A Cartesian fixed frame of reference is selected in arbitrary position, and a moving frame is selected on the moving platform. For RTHS applications, the location choice for the moving frame should fall at the centroid of the attachment with the physical specimen. The linear strokes of the prismatic limbs (e.g. actuators) result in displacement and rotation of the moving platforms. For some prescribed Cartesian motion at the moving frame, an inverse kinematic transformation can calculate the necessary stroke of each actuator. A translation vector $\boldsymbol{v}$ describes the motion of the moving frame relative to the fixed frame. The vectors $\boldsymbol{a}_i$ and $\boldsymbol{b}_i \in \mathcal{R}^3$, denoting the fixed and moving joint locations of the i-th actuator, respectively, are drawn from the frames of reference to the center of rotation of each spherical joint.

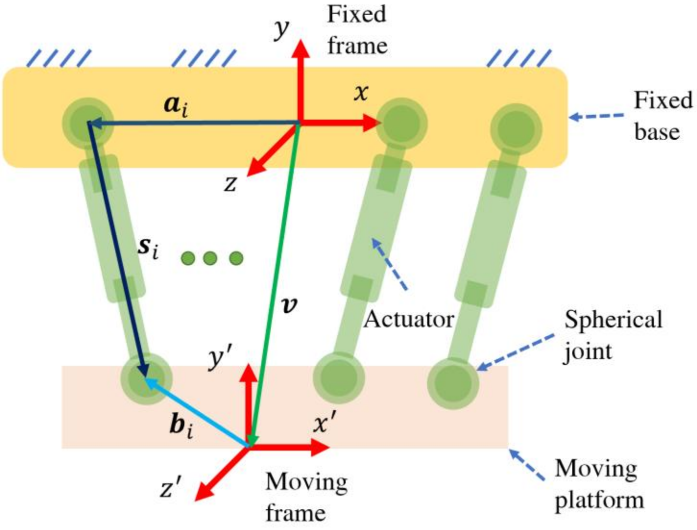

Figure 2.17 n-DOF parallel manipulator

Three rotational matrices from Eq. (2.42), describe the rotational motion of the moving platform. Through the matrix multiplication $\boldsymbol{A}(\theta_x, \theta_y, \theta_z) = \boldsymbol{A}_{\theta_x}\boldsymbol{A}_{\theta_y}\boldsymbol{A}_{\theta_z}$, the combined rotational matrix is obtained. The Cartesian motion is described via the vector $\boldsymbol{w} = \{u_x, u_y, u_z, \theta_x, \theta_y, \theta_z\}^T$. Through addition and subtraction of vectors, the below formulation is formed

$$\begin{gathered} \boldsymbol{s}_i = \boldsymbol{v} + \boldsymbol{A}\boldsymbol{b}_i - \boldsymbol{a}_i \\ \lambda_i = |\boldsymbol{s}_i| = f_i(\boldsymbol{w}) \end{gathered} \tag{2.49}$$

where $\boldsymbol{s}_i$ is the vector representation of the actuator length, λ_i is the total length of the actuator for some prescribed Cartesian motion at the moving base, and f_i is a nonlinear function describing the relationship between λ_i and $\boldsymbol{w}$.

The forward kinematic transformation is the process through which actuator measurements are used to calculate the Cartesian motion in the moving platform. This process is described by implicit equations, which must be solved through iterations until convergence is achieved. In parallel manipulators, the inverse kinematics is a straightforward and the forward kinematics is a challenging transformation. Solutions to forward kinematic problems are typically approximated via linearization around a stationary operation position. A first-order Taylor expansion of Eq. (2.49) around the equilibrium point, $\boldsymbol{w} = \boldsymbol{0}$, results in

$$\dot{\boldsymbol{\lambda}} = \boldsymbol{J}\dot{\boldsymbol{w}} \tag{2.50}$$

where $\boldsymbol{J} \in \mathcal{R}^{n \times n}$ is the Jacobian matrix and $\dot{\boldsymbol{\lambda}} \in \mathcal{R}^{n \times 1}$ and $\dot{\boldsymbol{w}} \in \mathcal{R}^{n \times 1}$ are derivatives of the earlier described terms. The Jacobian describes the relationship between incremental changes in the actuator lengths and incremental changes in Cartesian motion. Next, a linearized forward kinematics is formulated via a discrete-time solution to Eq. (2.50). This approximation is generally more accurate for smooth Cartesian motions and during operations closer to the equilibrium position. For an n-DOF parallel manipulator:

$$\boldsymbol{J} = \begin{bmatrix} \frac{\partial \lambda_1}{\partial w_1} & \cdots & \frac{\partial \lambda_1}{\partial w_n} \\ \vdots & \ddots & \vdots \\ \frac{\partial \lambda_n}{\partial w_1} & \cdots & \frac{\partial \lambda_n}{\partial w_n} \end{bmatrix} \tag{2.51}$$

$$\boldsymbol{w}_{k+1} = \boldsymbol{w}_k + \boldsymbol{J}^{-1}(\boldsymbol{\lambda}_{k+1} - \boldsymbol{\lambda}_k) \tag{2.52}$$

where k is the discrete time step.

2.7 Numerical Integration

A damped dynamical system with nonlinear restoring force behavior is described by the equation of motion

$$\boldsymbol{M}_N \ddot{\boldsymbol{x}}(t) + \boldsymbol{C}_N \dot{\boldsymbol{x}}(t) + \boldsymbol{R}_N(t) = \boldsymbol{F}(t) - \boldsymbol{F}_R(t) \tag{2.53}$$

where $\boldsymbol{M}_N$ is a positive definite mass matrix, $\boldsymbol{C}_N$ is a non-negative definite damping matrix, and $\boldsymbol{R}_N(t)$ is a vector of nonlinear restoring forces. Analytical solutions to equations of motion, which are second-order differential equations, are typically difficult to solve, instead numerical integration algorithms are employed for estimation of the responses of dynamical systems. Because dynamical systems are time-dependent systems, every point in time must be described by

$$t = t_{i+1} = dt(i+1) \tag{2.54}$$

where dt is a time increment.

Implicit and explicit schemes are two classifications of numerical integration methods. When the states $\boldsymbol{x}(t_{i+1})$ are estimated based on available quantities in former and current time steps, the integration is said to be *explicit*. When the states are embedded in a set of coupled equations, and iterative solutions are required, the integration is said to be *implicit*. Explicit methods are mostly conditionally stable, because when the time step is too large, numerical errors increase and instability may ensue. Implicit methods on the other hand tend to be unconditionally stable. For RTHS applications, explicit integration methods are preferred as implicit solutions are complex to program and require significantly more computational effort and time. The implications of choosing a numerical integration algorithm are felt in the accuracy and stability of the evaluations. Time steps are generally selected to be much smaller than the natural period of the dynamical system.

Consider the motion of a particle using Newton's law

$$\frac{dx}{dt} = v(t) \qquad \frac{dv}{dt} = a(t) \tag{2.55}$$

by utilizing the Taylor series expansion, the following relationships are achieved for $\boldsymbol{x}(t) = \boldsymbol{x}_{i+1}$ and $\boldsymbol{v}(t) = \boldsymbol{v}_{i+1}$

$$\boldsymbol{x}_{i+1} = \boldsymbol{x}(t_i + dt) = \boldsymbol{x}_i + \boldsymbol{v}_i dt + \frac{1}{2}\boldsymbol{a}_i dt^2 + \boldsymbol{O}(dt^3) \tag{2.56}$$

$$\boldsymbol{v}_{i+1} = \boldsymbol{v}(t_i + dt) = \boldsymbol{v}_i + \boldsymbol{a}_i dt + \boldsymbol{O}(dt^2) \tag{2.57}$$

where $\boldsymbol{O}(dt^2)$ and $\boldsymbol{O}(dt^3)$ are the higher-order terms.

2.7.1 Euler algorithm

The Euler algorithm is when only the first-order terms (e.g., $\boldsymbol{O}(dt)$) are considered. An algorithm is said to be of the n^{th} order when error term is of the order $\boldsymbol{O}(dt^n)$. This algorithm has limited accuracy and stability due to its simplistic form given by

$$\boldsymbol{x}_{i+1} = \boldsymbol{x}_i + \boldsymbol{v}_i dt \tag{2.58}$$

$$\boldsymbol{v}_{i+1} = \boldsymbol{v}_i + \boldsymbol{a}_i dt \tag{2.59}$$

2.7.2 Central difference algorithm

In the central difference algorithm, velocity term does not appear in the right-hand-side when integrating the equations of motion. This algorithm has been implemented for RTHS use in several studies (Carrion and Spencer, Jr. 2007; Horiuchi et al. 1999; Nakashima et al. 1992). The new approximations for the displacement and derivative terms are

$$\boldsymbol{v}_i \approx \frac{\boldsymbol{x}_{i+1} - \boldsymbol{x}_{i-1}}{2dt} \tag{2.60}$$

$$\boldsymbol{a}_i \approx \frac{\boldsymbol{x}_{i+1} - 2\boldsymbol{x}_i + \boldsymbol{x}_{i-1}}{dt^2} \tag{2.61}$$

$$\boldsymbol{x}_{i+1} = \left(\frac{1}{dt^2}\boldsymbol{M}_N + \frac{1}{2dt}\boldsymbol{C}_N\right)^{-1}\left\{\frac{2}{dt^2}\boldsymbol{M}_N\boldsymbol{x}_i + \left(-\frac{1}{dt^2}\boldsymbol{M}_N + \frac{1}{2dt}\boldsymbol{C}_N\right)\boldsymbol{x}_{i-1} - \boldsymbol{R}_N - \boldsymbol{F}_R + \boldsymbol{F}\right\} \tag{2.62}$$

The step-by-step procedure begins with mass, damping, and stiffness matrices formulated for the numerical substructure. The displacement, velocity, and acceleration values are then initialized $\{x_0, v_0, a_0\}$. Relationships Eqs. (2.60) – (2.62) are incorporated to compute time steps 1 through n. Nakashima et al. (1992) used a forward difference methodology, which Wu et al. (2006) incorporated to produce the operator-splitting algorithm.

2.7.3 Newmark-β algorithm

The Newmark-β method is a more generalized finite difference method, where for a selection of β and γ parameters, the performance of the approximation is altered. For a linear structure, some force vector $\boldsymbol{P}_0 = \boldsymbol{F}_0 - \boldsymbol{R}_{N,0} - \boldsymbol{F}_{R,0}$, and initial conditions $\boldsymbol{x}_0$ and $\boldsymbol{v}_0$

$$\boldsymbol{a}_0 = \frac{\boldsymbol{P}_0 - \boldsymbol{C}_N \boldsymbol{v}_0 - \boldsymbol{K}_N \boldsymbol{x}_0}{\boldsymbol{M}_N} \tag{2.63}$$

$$\begin{gathered} \boldsymbol{b}_1 = \frac{1}{\beta dt^2}\boldsymbol{M}_N + \frac{\gamma}{\beta dt}\boldsymbol{C}_N \quad \boldsymbol{b}_2 = \frac{1}{\beta dt}\boldsymbol{M}_N + \left(\frac{\gamma}{\beta} - 1\right)\boldsymbol{C}_N \\ \boldsymbol{b}_3 = \left(\frac{1}{2\beta} - 1\right)\boldsymbol{M}_N + dt\left(\frac{\gamma}{2\beta} - 1\right)\boldsymbol{C}_N \end{gathered} \tag{2.64}$$

Calculations at each time step ($i = 0, 1, 2 \ldots$) follow

$$\widehat{\boldsymbol{P}}_{i+1} = \boldsymbol{P}_{i+1} + \boldsymbol{b}_1 \boldsymbol{x}_i + \boldsymbol{b}_2 \boldsymbol{v}_i + \boldsymbol{b}_3 \boldsymbol{a}_i \tag{2.65}$$

$$\boldsymbol{x}_{i+1} = \frac{\widehat{\boldsymbol{P}}_{i+1}}{\boldsymbol{K}_N + \boldsymbol{b}_1} \tag{2.66}$$

$$\boldsymbol{v}_{i+1} = \frac{\gamma}{\beta dt}(\boldsymbol{x}_{i+1} - \boldsymbol{x}_i) + \left(1 - \frac{\gamma}{\beta}\right)\boldsymbol{v}_i + dt\left(1 - \frac{\gamma}{2\beta}\right)\boldsymbol{a}_i \tag{2.67}$$

$$\boldsymbol{a}_{i+1} = \frac{1}{\beta dt^2}(\boldsymbol{x}_{i+1} - \boldsymbol{x}_i) - \frac{1}{\beta dt}\boldsymbol{v}_i - \left(\frac{1}{2\beta} - 1\right)\boldsymbol{a}_i \tag{2.68}$$

Special cases of the Newmark-β method involve when $\gamma = \frac{1}{2}$ and $\beta = \frac{1}{4}$, for the constant average acceleration methods, and $\gamma = \frac{1}{2}$ and $\beta = \frac{1}{6}$, for the linear acceleration method. The Newmark method is similar to the explicit central difference method when $\gamma = \frac{1}{2}$ and $\beta = 0$. Mahin and Shing (1985) demonstrates that in some cases the Newmark algorithm is less sensitive to experimental error than the central difference algorithm for a hybrid simulation example. For nonlinear systems, this method is augmented with additional features per (Chopra 2011).

2.7.4 HHT-α algorithm

The Hilber-Hughes-Taylor-α (HHT-α) is an implicit method that allows for second-order convergence and energy dissipation through numerical damping. The finite difference equations in Eqs. (2.66) and (2.67) are adopted and the equation of motion is modified with a parameter α, which describes numerical lag in damping, restoring forces and external forces.

$$\begin{aligned} \boldsymbol{M}_N a_{i+1} + (1+\alpha)\boldsymbol{C}_N \boldsymbol{v}_{i+1} - \alpha \boldsymbol{C}_N \boldsymbol{v}_i + (1+\alpha)\left\{\boldsymbol{F}_{R,i+1} + \boldsymbol{R}_{N,i+1}\right\} - \alpha\left\{\boldsymbol{F}_{R,i} + \boldsymbol{R}_{N,i}\right\} \\ = (1+\alpha)\boldsymbol{F}_{i+1} - \alpha \boldsymbol{F}_i \end{aligned} \tag{2.69}$$

where α is a damping parameter. The three parameters α, β,and γ used as inputs for the HHT-α algorithm are computed per

$$\alpha \in \left[-\frac{1}{3}, 0\right], \qquad \beta = \frac{(1-\alpha)^2}{4}, \qquad \gamma = \frac{1}{2} - \alpha \tag{2.70}$$

For nonlinear systems, Newton-type iterative procedures are added to the HHT-α method to solve the equation of motion. Jung et al. (2007) proposed a modified Newton approach using the initial structural stiffness to compile hybrid simulation with the HHT-α method.

2.7.5 Runge-Kutta algorithm

The Runge-Kutta algorithms are a class of implicit and explicit numerical integration methods. A first-order Runge-Kutta algorithm is defined for a first-order differential equation given by

$$\dot{y}(t) = f\big(t, y(t)\big) \tag{2.71}$$

for which the time-stepping is procedure is the Euler algorithm presented earlier or

$$k_i^I = f\big(t_i, y(t_i)\big) \tag{2.72}$$

$$y(t_{i+1}) = y(t_i) + k_i^I dt \tag{2.73}$$

A second-order Runge-Kutta (or mid-point) algorithm begins with Eq. (2.72) to estimate the derivative at $t = t_0$. Next, Eq. (2.73) is modified for the intermediate estimate of the time function at $t = t_0 + \frac{dt}{2}$, per

$$y_1\left(t_0 + \frac{dt}{2}\right) = y(t_0) + k_0^I \frac{dt}{2} \tag{2.74}$$

$$k_i^{II} = f\left(y_i\left(t_i + \frac{dt}{2}\right), t_i + \frac{dt}{2}\right) \tag{2.75}$$

$$y(t_{i+1}) = y(t_i) + K_i^{II} dt \tag{2.76}$$

with Eqs. (2.75) and (2.76) describing the general procedure for the second-order Runge-Kutta after the initial time step. The development of the fourth-order Runge-Kutta follows from the second-order procedure and is not covered in detail here.

$$\begin{gathered} k_i^I = f(y(t_i), t_i), \quad k_i^{II} = f\left(y(t_i) + k_i^I \frac{dt}{2}, t_i + \frac{dt}{2}\right), \\ k_i^{III} = f\left(y(t_i) + k_i^{II} \frac{dt}{2}, t_i + \frac{dt}{2}\right), \quad k_i^{IV} = f(y(t_i) + k_3 dt, t_i + dt) \end{gathered} \tag{2.77}$$

The fourth-order Runge-Kutta algorithm presented in Eq. (2.77) has been used extensively in hybrid simulation (Carrion et al. 2009; Carrion and Spencer 2007c; Drazin and Govindjee 2017; Fermandois and Spencer, Jr. 2018; Friedman et al. 2015; Phillips and Spencer 2013; Silva et al. 2020).

2.7.6 Dormand-Prince algorithm

The Dormand-Prince is an explicit numerical integration algorithm for solving equations of motion, and an expansion to the Runge-Kutta method (Dormand et al. 1987). Both Dormand-Prince and Runge-Kutta are applicable to nonlinear systems. The fifth- and eight-order Dormand-Prince algorithms are highly stable and use current values of states and their derivatives. The method uses multiple functions evaluations per step of integration. Dormand-Prince integration algorithms are widely popular for MATLAB users (MathWorks 2020). This algorithm has been implemented in several hybrid simulation applications (Chen et al. 2015; Najafi et al. 2020; Najafi and Spencer 2019).

2.8 Summary

The physical and mathematical tools for the ultimate objective of this dissertation, multi-axial RTHS testing, were outlined in this chapter. Modeling of dynamical systems requires an understanding of the mathematical representations necessary, in the form of an equation of motion. Manipulation of dynamical systems requires knowledge of control theory. Servo-hydraulic actuator and structural specimens are the primary dynamical systems of interest presented in this work. Frequency domain mathematics are presented as system identification is largely conducted in this domain throughout this literature. Kinematics of robotics and actuated systems were shown to be largely non-trivial to model and manipulate. Hence, the notion of kinematic transformation was developed and discussed. And lastly numerical integration algorithms were presented for solving the equations of motion.

CHAPTER 3 ACTUATOR COMPENSATION

3.1 Problem Statement

Actuator delays can result in instabilities in the closed-loop interaction between the numerical and physical substructures in RTHS experiments. Compensation strategies are an essential component of the RTHS methodology, in attempts to recover some of the actuator delays. Many compensation strategies have limitations in their abilities to sufficiently recover actuator delays, and thus performance and stability of the RTHS loop is compromised. In this chapter, an effort is made to develop compensation strategies that have excellent tracking and stability performance. The developments will later be incorporated in the multi-axial RTHS framework proposed in future chapters.

A modification is proposed to the MBC proposed by (Carrion et al. 2009). The new architecture is referred to as the *modified Model-Based Controller* (mMBC). Like its predecessor, the mMBC uses a feedback and an inverse model controller designed using the identified model of the actuator-structure system. When the control authority is increased to achieve better tracking, stability of the MBC is jeopardized. The new mMBC provides better tracking performance, tracking robustness, and stability predictability A stability condition is proposed for the model-based class of controllers to demonstrate the tracking robustness of the mMBC.

Next, an adaptive augmentation of the mMBC is introduced, and labeled as the *Adaptive Model Reference Control* (aMRC) with the objective of improving the tracking abilities of actuators through adaptation, while maintaining robustness. The proposed aMRC architecture is wrapped around the mMBC. The aMRC takes advantage of the model-reference idea to drive to track the desire performance embedded in the reference model. An adaptive projection algorithm is featured, with bounded output to prevent the adaptive parameter from drifting. At its core, the proposed adaptive algorithm is an integral controller, which ensures that steady-state errors induced by uncertainties and nonlinearities are dissipated.

3.2 Setpoint tracking

A setpoint is a desired target value to reach and maintain for a dynamic system. Two classes of setpoint problems in control theory include: (i) disturbance rejection, and (ii) reference tracking. In a *disturbance rejection* problem, the compensator attempts to maintain a constant equilibrium state while rejecting process disturbances and noise. In a *reference tracking* problem, the equilibrium state may be constantly evolving, and the goal of the compensator is to ensure that the plant follows the new equilibrium state. In reality, the job of the compensator is often both disturbance rejection and reference tracking.

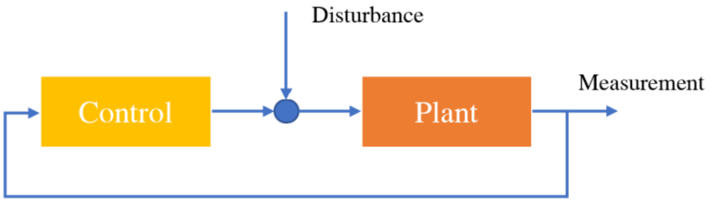

Figure 3.1 Disturbance rejection

Figure 3.2 Reference Tracking

Shake tables are used to replicate historic and synthetic ground accelerations, for experimental testing of onboard structures. In order to have repeatability and for comparison with numerical simulations, the shake table must accurately replicate a prescribed acceleration record. However, shake tables possess inherent dynamics which alter the desired characteristics of the acceleration records executed on the onboard structure. Reproducing an acceleration time-history thus necessitates real-time comparisons of the reference and measured accelerations and manipulation of control signals in what is commonly referred to as an *acceleration tracking* problem.

In real-time hybrid simulation, displacement and acceleration are often the preferred forms of imposing a boundary condition on a physical specimen (Zhang et al. 2017). Force tracking may be desired when imposing structural self-weighting on the physical specimen, or if the effective force testing method is used. In many applications, force and displacement tracking may be enforced simultaneously.

3.3 Modified Model-Based Control

The mMBC is developed using a linearized transfer function model of actuator-structure dynamics. The transfer function model should closely match the FRF of actuator-structure setup. In this section, the architecture of the mMBC is described for tracking of displacement and its derivatives (e.g., acceleration). The mMBC manipulates a prescribed reference signal and commands a control signal to an actuator for execution.

3.3.1 Feedforward control

Feedforward or inverse controllers are dynamical systems designed as the inverse of the nominal plant dynamics. The goal of this controller is to reconstruct the reference signal such that unwanted plant dynamics are cancelled out in the executed signal. The model used in the feedforward controller is determined from the nominal plant dynamics obtained through system identification. The amplitude and bandwidth of the excitation during system identification should reflect the experimental conditions and intended use of the model. The feedforward control employed is cascaded with a lowpass filter.

Since actuator-structure dynamics (i.e., plant) are described by strictly proper transfer functions, with more poles than zeros, as discussed in Section 2.4, the inverse must be an improper system. Multiplication with a lowpass filter will add the necessary poles for a proper and causal realization. Lowpass filters also serve in canceling high frequency dynamics which are often inaccurately identified in the nominal model. The inverse model is obtained per

$$\boldsymbol{F}(s) = \boldsymbol{P}^{-1}(s)\boldsymbol{L}(s) \tag{3.1}$$

where $\boldsymbol{P}(s)$ is the plant or actuator-structure dynamics, $\boldsymbol{L}(s)$ is the lowpass filter and $\boldsymbol{F}(s)$ is the feedforward controller. The cutoff frequency and order for the lowpass filter are the only two design considerations and vary depending on experimental setups. The lowpass filter must have enough poles to make the inverse controller proper. The multiplication of the plant and feedforward controller result in the lowpass filter, which will be referred to as an *augmented plant* in this dissertation.

3.3.2 Feedback control

Feedback control can further compensate for tracking errors and provide tracking robustness in the presence of nonlinearities and noise. Feedback control refers to a large class of controllers each with their own advantages, like the H_∞ (Ou et al. 2015). In this development, the LQG feedback controller is used. The proposed output feedback LQG is designed based on the augmented plant with and without noise

$$\boldsymbol{L}(s) = \frac{y(s)}{q(s)} = \boldsymbol{P}(s)\boldsymbol{F}(s) = \boldsymbol{C}_L(s\boldsymbol{I} - \boldsymbol{A}_L)^{-1}\boldsymbol{B}_L + \boldsymbol{D}_L \tag{3.2}$$

$$\begin{aligned} \dot{\boldsymbol{x}}(t) &= \boldsymbol{A}_L\boldsymbol{x}(t) + \boldsymbol{B}_L q(t) + \boldsymbol{F}w(t) \\ y(t) &= \boldsymbol{C}_L\boldsymbol{x}(t) + v(t) \end{aligned} \tag{3.3}$$

where $\boldsymbol{A}_L$, $\boldsymbol{B}_L$, $\boldsymbol{C}_L$ and $\boldsymbol{D}_L$ are the state-space realizations of the lowpass filter or augmented plant, $q(s)$ in Laplace-domain or $q(t)$ in time domain is the sum of the feedback controller outputs added back to the reference signal. The system in Eq. (3.2) is the augmented plant without noise, and the system in Eq. (3.3) is the augmented plant with noise. The combined use of the feedforward control, plant dynamics, and feedback control are illustrated in Fig. 3.1. $\boldsymbol{x}(t)$ is a vector of state from the augmented plant and $w(t)$ and $v(t)$ represent process and observation noise. The reference and measured signals are denoted as $r(t)$ and $y(t)$, respectively, and the control signal sent to the plant for execution is labeled as $u(t)$. The feedforward control served in prefiltering the reference signal in the previous MBC development, but has been moved into the feedback loop in this modified development.

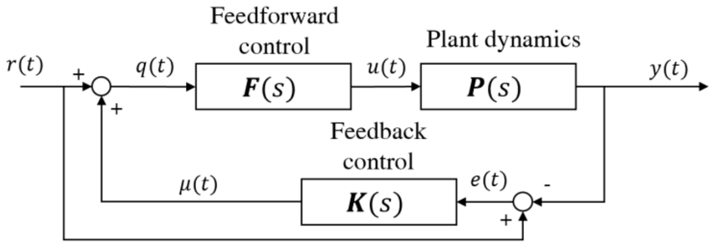

Figure 3.3 mMBC architecture

Considering the augmented plant in Eq. (3.3) to be both controllable and observable, the proposed mMBC utilizes an LQG controller, which minimizes the expected value of a quadratic cost function, weighting the signal $q(t)$ and states $\boldsymbol{x}(t)$.

$$J_{LQG} = \mathbb{E}\left\{\int_0^\infty \left(\boldsymbol{x}^T(t)\boldsymbol{Q}\boldsymbol{x}(t) + q^T(t)Rq(t)\right)dt\right\} \tag{3.4}$$

where $\mathbb{E}$ denotes expected value, and $\boldsymbol{Q}$ and R are weighting parameters, which are positive semidefinite and positive definite, respectively. The LQG controller assumes that the process and observation noises are Gaussian, white, zero-mean and stationary processes, and covariance matrices $\boldsymbol{W}$ and $\boldsymbol{V}$ are positive definite (Datta 2003).

$$\mathbb{E}[w(t)w^T(t)] = \boldsymbol{W}\delta(t-\tau) \qquad \mathbb{E}[v(t)v^T(t)] = \boldsymbol{V}\delta(t-\tau) \tag{3.5}$$

where $\delta(t-\tau)$ is the Dirac Delta function as a function of time. In stochastic systems where the process and observation noise are Gaussian, the optimal feedback solution is separable into a linear quadratic estimator (LQE) or Kalman estimator and a linear quadratic regulator (LQR):

1. Linear quadratic regulator – obtain the matrix feedback $\boldsymbol{K}_{LQR}$

$$\boldsymbol{K}_{LQR} = R^{-1}\boldsymbol{B}_L^T\boldsymbol{X}_{LQR} \tag{3.6}$$

where $\boldsymbol{X}_{LQR}$ is the solution to the following algebraic Riccati equation

$$\boldsymbol{X}_{LQR}\boldsymbol{A}_L + \boldsymbol{A}_L^T\boldsymbol{X}_{LQR} + \boldsymbol{Q} - \boldsymbol{X}_{LQR}\boldsymbol{B}_L R^{-1}\boldsymbol{B}_L^T\boldsymbol{X}_{LQR} = 0 \tag{3.7}$$

2. Linear quadratic estimator – obtain the observer gain $\boldsymbol{L}_{LQE}$

$$\dot{\hat{\boldsymbol{x}}}(t) = \left(\boldsymbol{A}_L - \boldsymbol{L}_{LQE}\boldsymbol{C}_L\right)\hat{\boldsymbol{x}}(t) + \boldsymbol{B}_L q(t) + \boldsymbol{L}_{LQE}e(t) \tag{3.8}$$

where the observer gain is calculated by $\boldsymbol{L}_{LQE} = \boldsymbol{X}_{LQE}\boldsymbol{C}_L^T\boldsymbol{V}^{-1}$, with $\boldsymbol{X}_{LQE}$ as the solution to the following algebraic Riccati equation

$$\boldsymbol{A}_L\boldsymbol{X}_{LQE} + \boldsymbol{X}_{LQE}\boldsymbol{A}_L^T - \boldsymbol{X}_{LQE}\boldsymbol{C}_L^T\boldsymbol{V}^{-1}\boldsymbol{C}_L\boldsymbol{X}_{LQE} + \boldsymbol{F}\boldsymbol{W}\boldsymbol{F}^T = 0 \tag{3.9}$$

Taking advantage of the separation principle and the regulator and estimator matrices, the following feedback controller is obtained

$$\begin{aligned} \dot{\hat{\boldsymbol{x}}}(t) &= \left(\boldsymbol{A}_L - \boldsymbol{B}_L\boldsymbol{K}_{LQR} - \boldsymbol{L}_{LQE}\boldsymbol{C}_L\right)\hat{\boldsymbol{x}}(t) + \boldsymbol{L}_{LQE}e(t) \\ \mu(t) &= -\boldsymbol{K}_{LQR}\hat{\boldsymbol{x}}(t) \end{aligned} \tag{3.10}$$

The transfer function of the feedback controller can be written as

$$\boldsymbol{K}(s) = \frac{\mu(s)}{e(s)} = -\boldsymbol{K}_{LQR}\left(s\boldsymbol{I} - \boldsymbol{A}_L + \boldsymbol{B}_L\boldsymbol{K}_{LQR} + \boldsymbol{L}_{LQE}\boldsymbol{C}_L\right)^{-1}\boldsymbol{L}_{LQE} \tag{3.11}$$

The dynamics of the LQG system are dependent on the plant it controls. First, a state estimator based on the augmented plant is obtained and applied to the error signal, to estimate the states of the augmented plant. Next, the estimated states are multiplied by the optimal LQR gain $\boldsymbol{K}_{LQR}$ to obtain the feedback signal $\mu(t)$. For optimization of the feedback controller, the weighting terms $\boldsymbol{Q}$ and R are gradually adjusted until the error between the reference and measured signals is minimized.

3.4 Modified Architecture

The architecture difference between the MBC and mMBC is distinguishable in how the inverse model and feedback controllers are assembled. The output of the inverse model and feedback controllers are summed to formulate the control signal under the original architecture. In the mMBC, the output of the feedback controller is added back to the reference signal, per Figure 3.4. The feedback filter is designed on the basis of the inverse model and plant forming a combined augmented plant, idealized as a lowpass filter. This difference has important implications on the tracking robustness of the mMBC.

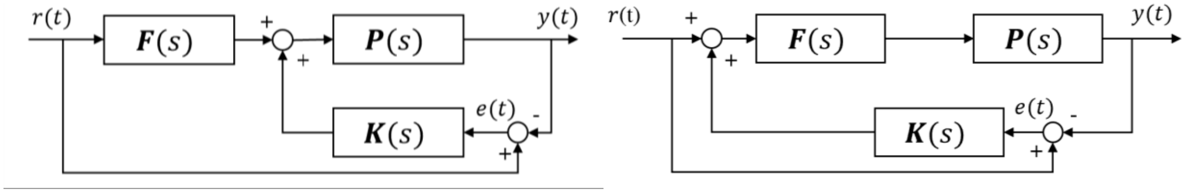

(a) MBC (b) mMBC

Figure 3.4 Original and modified model-based architectures

$$\boldsymbol{G}_{MBC}(s) = \frac{Y(s)}{R(s)} = \frac{\boldsymbol{P}(s)\big(\boldsymbol{F}(s) + \boldsymbol{K}(s)\big)}{1 + \boldsymbol{P}(s)\boldsymbol{K}(s)} \tag{3.12}$$

$$\boldsymbol{G}_{mMBC}(s) = \frac{Y(s)}{R(s)} = \frac{\boldsymbol{P}(s)\boldsymbol{F}(s)\big(1 + \boldsymbol{K}(s)\big)}{1 + \boldsymbol{P}(s)\boldsymbol{F}(s)\boldsymbol{K}(s)} \tag{3.13}$$

For a reference signal, $r(t)$, and a measurement signal, $y(t)$, the closed-loop system is denoted as $\boldsymbol{G}(s)$. $y(s)$ and $r(s)$ are Laplace representations of the reference and measurement signals. For some stable $\boldsymbol{P}(s)$, $\boldsymbol{K}(s)$ and $\boldsymbol{F}(s)$, the internal stability of the closed-loop system depends on the denominator or left-half plane closed-loop poles. The difference between the architectures of MBC and mMBC is demonstrated in the denominators of the closed-loop transfer functions in Eqs. (3.12) and (3.13), respectively.

3.4.1 Stability condition

The closed-loop stability is evaluated in this section, by assessing the denominator of the transfer functions in Eqs. (3.12) and (3.13). Let $\boldsymbol{T}$ serve as a stable operator and $\boldsymbol{K}$ be a stable feedback controller, where $\|\boldsymbol{K}\|_\infty \leq 1$. Then, $(\boldsymbol{I}+\boldsymbol{TK})^{-1}$is non-singular if $\|\boldsymbol{T}\|_\infty < 1$. In other words, if $\|\boldsymbol{TK}\|_\infty \leq \|\boldsymbol{T}\|_\infty \|\boldsymbol{K}\|_\infty < 1$, then $(\boldsymbol{I}+\boldsymbol{TK})$ is invertible. The mathematical backgrounds for these conditions are discussed in Dullerud and Paganini (2000).

The stability condition for the MBC is the existence of a non-singular $\left(1+\boldsymbol{P}(s)\boldsymbol{K}(s)\right)^{-1}$. Similarly, the stability condition for the mMBC is the existence of a non-singular $\left(1+\boldsymbol{L}(s)\boldsymbol{K}(s)\right)^{-1}$. The re-routing of the feedback signal has resulted in the presence of the inverse model controller as an additional stabilizing module in the denominator of the closed-loop transfer function.

Applying the norm conditions to Eq. (3.13), as discussed in the appendix, for some feedback controller, where $\|\boldsymbol{K}(s)\|_\infty \leq 1$, the mMBC closed-loop characteristic equation $\left(1+\boldsymbol{L}(s)\boldsymbol{K}(s)\right)^{-1}$is non-singular when $\|\boldsymbol{L}(s)\boldsymbol{K}(s)\|_\infty \leq \|\boldsymbol{L}(s)\|_\infty \|\boldsymbol{K}(s)\|_\infty < 1$. Since $\|\boldsymbol{L}(s)\|_\infty = 1$, the mMBC guarantees stability. Additional conditions for this stability are: (i) the specified bound on the infinity norm for the feedback controller, and (ii) assumption on lack of plant model uncertainty. Applying the norm condition to Eq. (3.12) with $\|\boldsymbol{K}(s)\|_\infty \leq 1$, $\|\boldsymbol{P}(s)\|_\infty$ may have any arbitrary gain. Hence, the stability condition $\|\boldsymbol{P}(s)\|_\infty \|\boldsymbol{K}(s)\|_\infty < 1$ cannot be guaranteed. Therefore, certainties in the robustness of the MBC system don't exist.

These norm bounds formulate a sufficient stability condition. Necessary conditions are exact and dependent on numerous physical parameters including the reachability of desired states. Due to the sufficient only nature of the stability condition discussed in this paper, the controller may remain stable even when the stability norm threshold is exceeded.

3.5 Adaptive Model Reference Control

The proposed aMRC controller is an augmentation on the mMBC controller discussed in Section 3.2. A reference model $\boldsymbol{M}(s)$ is introduced, loaded with the intended behavior of the plant. An adaptive law $\boldsymbol{A}(s)$, is used to calculate an adaptive variable $\theta(t)$. Fig. 3.5 illustrates the complete aMRC loop. The aMRC is built on the $L1$ adaptive control architecture. The control law feature of the $L1$ is omitted to speed up the tracking performance. The assumptions, theorems, and proofs relevant to the response of the $L1$ are provided in (Cao and Hovakimyan 2009).

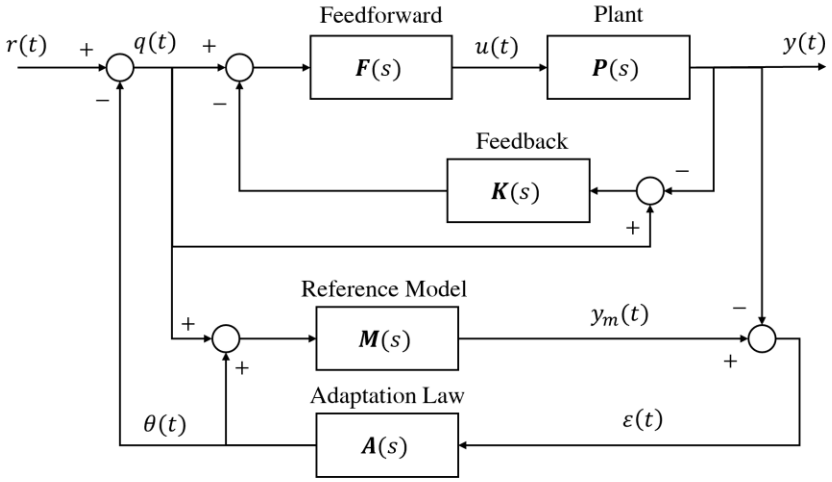

Figure 3.5 aMRC architecture

3.5.1 Reference model

The reference model developed in this adaptive scheme serves to drive the performance of the plant along the trajectory set by the reference model. Upon successful adaptation, the output trajectory of the plant converges to the output of the reference model. An ideal reference system representing perfect tracking is a unity-gain zero-phase system. The implication of this ideal system is that the reference signal will match the output signal, both in amplitude and phase.

In reality, controlled actuator systems should perform as a lowpass filter, as high frequency attenuation is inevitable due to physical limitations. The cutoff frequency f_c (Hz) for the lowpass filter should be a realistic selection based on the performance limitations of the actuator. The reference model is hence represented as a first-order lowpass filter

$$\boldsymbol{M}(s) = \frac{2\pi f_c}{s + 2\pi f_c} \tag{3.14}$$

3.5.2 Adaptation law

The adaptation law herein is responsible for the adaptive estimate that is continuously updated to change the controller behavior. The objective of the adaptation law in the proposed algorithm is to minimize steady-state errors that emerge when plant nonlinearities or unmodeled dynamics exist. Integral controllers have proven effective in minimizing steady-state errors. The integral control concept is used here in the adaptation law for fast and smooth attenuation of the steady-state errors. Integral controllers however are prone to drifting problems, where the calculated control parameter grows unbounded. A projection algorithm is thus introduced which addresses the drifting problem by limiting the calculated adaptive parameter to a prescribed bound. The projection algorithm used, ensures a bounded and smooth adaptive parameter estimate (Cao and Hovakimyan 2009).

Let $f(\theta)$ be a convex smooth function, the subset

$$\Omega_0 \coloneqq \{\theta \in \mathcal{R}^n | f(\theta) < 0\} \tag{3.15}$$

is convex. $f(\theta)$ maps $\mathcal{R}^n$ to $\mathcal{R}$ and is defined as

$$f(\theta) = (\theta\text{^}T\ \theta - \theta\text{\_max }\text{^}2)/(\epsilon\theta\text{\_max }) \tag{3.16}$$

where θ_{max} the maximum bound set on θ and ϵ is the exceedance tolerance on the bound. θ is the adaptive estimate and the outcome of the adaptation law. $\varepsilon(t)$ is the error between the plant and the reference model outputs, $\varepsilon(t) = y(t) - y_m(t)$. For an adaptive gain Γ, the projection operator on ε is formulated per

$$\dot{\theta} = \Gamma Proj(\theta, \varepsilon) \coloneqq \begin{cases} \Gamma\varepsilon & \text{if } f(\theta) < 0, \\ \Gamma\varepsilon & \text{if } f(\theta) > 0, \text{and } \nabla f^T \varepsilon \leq 0, \\ \Gamma\varepsilon - \Gamma \dfrac{\nabla f}{\|\nabla f\|} \left\langle \dfrac{\nabla f}{\|\nabla f\|}, \varepsilon \right\rangle f(\theta) & \text{if } f(\theta) \geq 0, \text{and } \nabla f^T \varepsilon > 0. \end{cases} \tag{3.17}$$

The adaptive law is denoted by $\boldsymbol{A}(s)$ in Fig. 3.5. The projection algorithm of the adaptive law in Eq. (3.17) at its core is simply an integral controller when $f(\theta) < 0$. The projection operator subtracts a vector normal to the boundary of the convex set, such that a smooth transformation is obtained from the original vector $\varepsilon(t)$. When $f(\theta) \geq 0$, the normal component of ε is attenuated until the $Proj(\theta, \varepsilon)$ is tangential to the boundary. This ensures the estimated parameter remains smooth and bounded. By definition, the projection operator does not alter the integral action in formulating θ, unless the maximum bound set for the adaptive estimate is approached. Fig. 3.6 illustrates a convex set and the action of the projection operator.

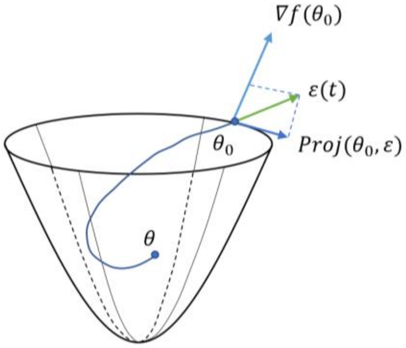

Figure 3.6 Projection operator

The reference model and the adaptation law are major components in the design of the aMRC algorithm. In the design of an aMRC compensator, if the cutoff frequency of the reference system is set too low, the controller tracking will be sluggish. If the cutoff frequency is too high, the adaptation law will not be able to compensate for high frequency contents appropriately and high frequency noise will appear in the output of the plant dynamics. While designing a reference model, a good practice is to start off with a moderately low cutoff frequency and increase gradually to optimize the tracking performance and ensure stability. Similarly, the adaptation gain should be gradually increased to enhance the tracking performance.

3.6 Numerical Evaluation

This section evaluates the proposed mMBC and aMRC compensation algorithms for a reference tracking problem. A second-order dynamical system is introduced, where the model of the system used for developing compensation strategies is perturbed. The discrepancy between the real plant and nominal (identified) model are intentionally created to evaluate each controller in the presence of modeling uncertainty. A 5-second chirp signal with a frequency bandwidth of 0 – 10 Hz is selected as the reference excitation. Four compensation techniques are evaluated as part of this analytical study: (i) feedforward, (ii) MBC, (iii) mMBC, and (iv) aMRC.

$$\boldsymbol{G}(s)=\frac{\omega_n^2}{s^2+2\zeta\omega_n s+\omega_n^2} \tag{3.18}$$

where ω_n and ζ are the natural frequency and damping ratio of the system, respectively. This second-order dynamic is representative of single-DOF dynamical system. The real plant is denoted as $\boldsymbol{P}(s)$ and the nominal model is denoted by $\widehat{\boldsymbol{P}}(s)$.

$$\boldsymbol{P}(s)=\{\boldsymbol{G}(s)|\omega_n=50,\zeta=0.5\} \tag{3.19}$$

$$\widehat{\boldsymbol{P}}(s)=\{\boldsymbol{G}(s)|\omega_n\sim U[45,50],\zeta\sim U[0.25,0.75]\} \tag{3.20}$$

where the parameters ω_n and ζ are distributed uniformly, with $U[a,b]$, and a and b as the lower and upper bounds for the parameter.

The numerical simulations are conducted for a duration of 5 seconds with the Dormand-Prince RK8 integration scheme (Dormand et al. 1987). The performance and feasibility of each compensator is assessed between reference and output signals $r(t)$ and $y(t)$ respectively, with the unitless root-mean-square error (*RMSE*) and maximum error (*MAXE*) evaluation criteria.

$$RMSE=\sqrt{\frac{\sum_{i=1}^{n}\left(r(i)-y(i)\right)^2}{\sum_{i=1}^{n}\left(r(i)\right)^2}} \tag{3.21}$$

$$MAXE=\frac{\max|r(i)-y(i)|}{\max|r(i)|} \tag{3.22}$$

where at step i, $r(i)$ and $y(i)$ are the reference and output (measured) signals respectively, and n is the total data point count.

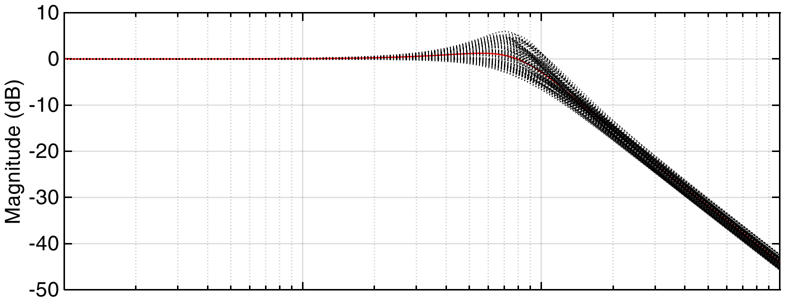

(a) Amplitude

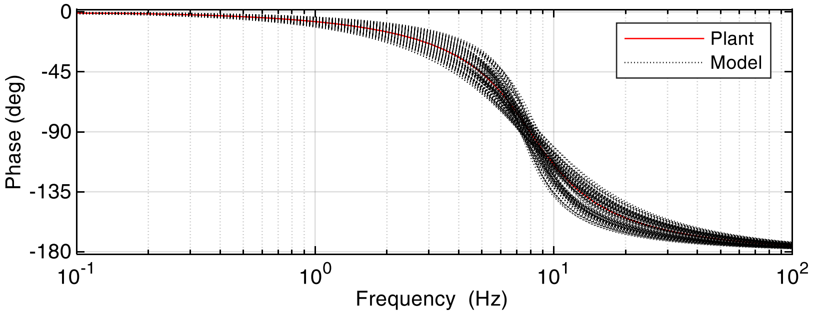

(b) Phase

Figure 3.7 FRF of the plant and 100 nominal models

A suite of 100 nominal models are obtained by randomizing the natural frequency and damping ratio per the upper and lower bounds provided in Eq. (3.20). This process creates variations or modeling uncertainties between the dynamics of the plant in Eq. (3.19) and nominal models in Eq. (3.20). The FRF of the plant and nominal model variations are presented in Fig. 3.5. A compensator which consistently produces good tracking performance under a wide degree of modeling uncertainties is said to have good tracking robustness.

Compensators require intricate tuning to optimize their performance. The general tuning procedure and control design for each of the compensators are presented below:

- Feedforward: nominal model in Eq. (3.20) is inverted and multiplied with a second-order lowpass filter with a cutoff frequency of 50 Hz.
- MBC: nominal model in Eq. (3.20) is used for design of a kalman state estimator and an LQR gain. The estimator and regulators are tuned until the error between the reference and measurement signals are minimized. The feedforward controller from earlier is then applied to complete the MBC compensator.
- mMBC: real plant in Eq. (3.19) and feedforward controller from earlier are cascaded to create an augmented plant. State estimator and feedback regulator are designed based on the augmented plant and tuned until the error between the reference and measurement signals are minimized.

- aMRC: the mMBC compensator is augmented with a reference model and an adaptive law. The cutoff frequency on the reference model is set to f_c =300 Hz and the gain on the adaptive law is set to $\Gamma = 200$.

The control-plant systems are next subject to the chirp signal in Fig. 3.8. This process is repeated for each of the 100 randomized nominal plants.

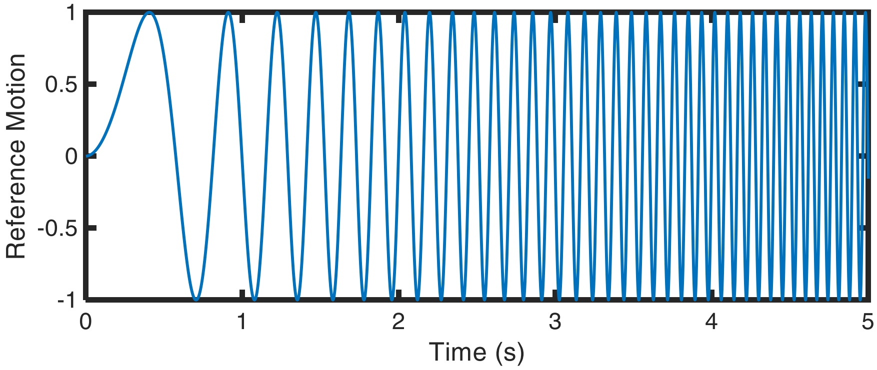

Figure 3.8 5-second chirp signal

Fig. 3.9 illustrates the synchronization plots for one simulation. A 1:1 diagonal line in a synchronization plot implies perfect tracking. As demonstrated, incorporation of feedforward and MBC compensators is not enough to cancel out the high frequency oscillations observed in the synchronization plots. The mMBC offers a more rigorous feedback action as noted by the major improvement in the tracking. Integration of the adaptive law in the form of the aMRC, bears no significant results however, when the tracking is already excellent.

The box plots in Fig. 3.10, Table 3.1, and 3.2 provide graphical and numerical results from the 100 simulations of the chirp signals for each compensator. The redlines and the bottom and top lines in the blue boxes indicate the median, 25th quartile and 75th quartile results respectively, for the *RMSE* and *MAXE* error indicators. The dashed lines extending from the box are whiskers of the box plot and indicate upper and lower extremes of the error data. The mMBC and aMRC compensators result in smaller errors compared to Feedforward and MBC algorithms. Note that although the improvements offered by the adaptive augmentation from the mMBC to the aMRC was not significant or observable for a single simulation in Fig. 3.9, the aMRC results in better tracking and more consistent (narrower box and whiskers) results. Therefore, the aMRC has the best tracking robustness followed by mMBC.

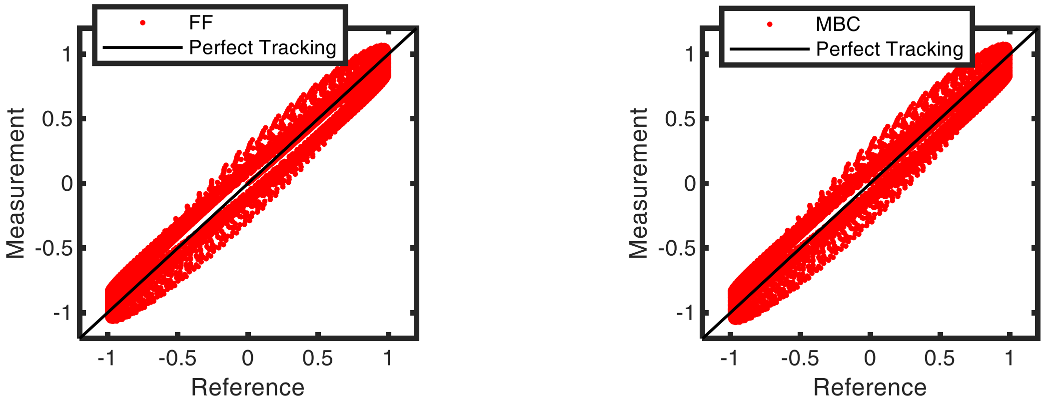

(a) Feedforward

(b) MBC

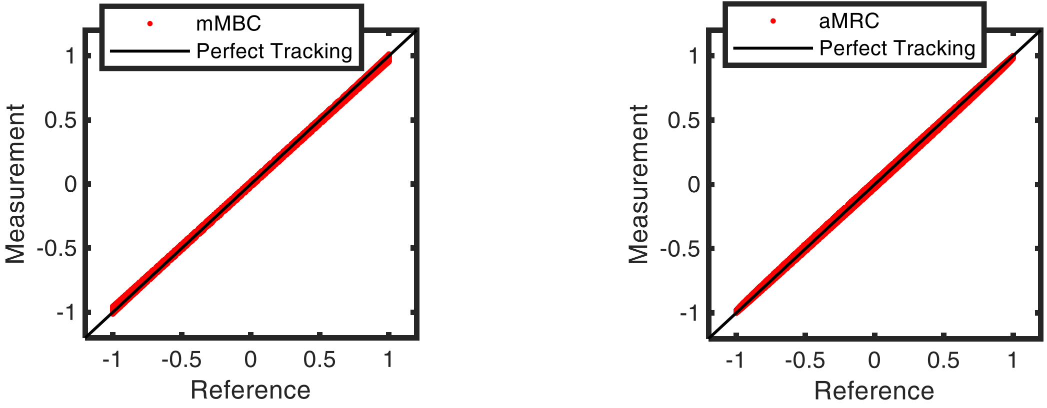

(c) mMBC

(d) aMRC

Figure 3.9 Synchronization plots

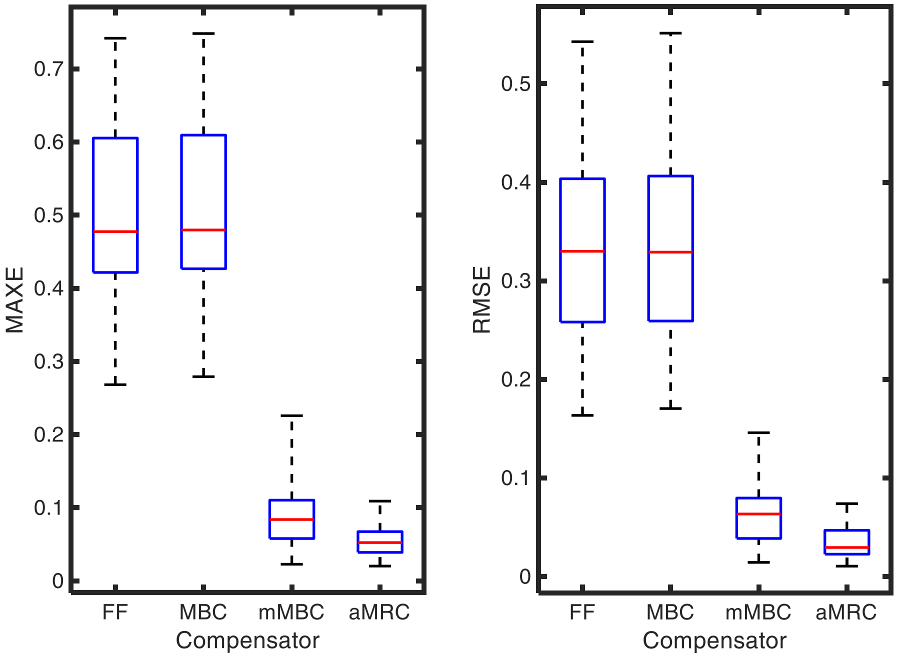

(a) *MAXE*

(b) *RMSE*

Figure 3.10 Box plots for the error indicators

Table 3.1 MAXE error variation

Compensator	Lower adjacent	25th percentile	Median	75th percentile	Upper adjacent
FF	0.274	0.406	0.490	0.610	0.724
MBC	0.275	0.406	0.495	0.617	0.731
mMBC	0.023	0.056	0.077	0.093	0.210
aMRCs	0.021	0.042	0.052	0.065	0.098

Table 3.2 RMSE error variation

Compensator	Lower adjacent	25th percentile	Median	75th percentile	Upper adjacent
FF	0.158	0.266	0.326	0.406	0.522
MBC	0.163	0.263	0.320	0.409	0.530
mMBC	0.012	0.041	0.056	0.072	0.131
aMRCs	0.010	0.023	0.029	0.040	0.068

3.7 Shake Table Control

For experimental validation of the tracking abilities of the proposed controllers, a shake table setup is selected with an onboard structure. The aim of this study is to provide acceleration tracking for the shake table. The aMRC compensator is not included in this study, as adaptive compensation results in low frequency control signals. A low frequency acceleration signal translates to large displacements, which exceed the stroke capacity of a shake table. Several ground motions are selected and the capabilities of the mMBC are compared to some of the existing compensation techniques.

3.7.1 Experimental setup

The experimental setup in this study consists of a 1-DOF Quanser II shake table, a 45 cm $\times$ 45 cm table operated on a linear ball bearing and powered by a 400 W DC Motor with an onboard 1000 LPR IP 40 relative encoder. The motor is operated with a Kollmorgan Silverline H-344-H-0600 amplifier. The operational frequency bandwidth of the shake table is $0-20$ Hz with a stroke length of $\pm$ 3”, (Dyke and Caicedo 2002). An NI CompactRIO 9073 controller is used along with the LabVIEW real-time module, to manage the controller programming. An 8-channel m+p VibPilot is used for data acquisition. Acceleration measurements are obtained with a PCB 3701G3FA3G capacitive accelerometer. The numerical and control interfaces are operated at a sampling frequency of 200 Hz.

Figure 3.11 Two-story structure onboard a shake table

To test the capabilities of the proposed controller, additional features are added to the shake table setup to achieve several phenomena including nonlinearity and modeling uncertainty. The two-story frame structure in Fig. 3.11 discussed in Wang et al. (2015) and Phillips et al. (2014) is mounted on the shake table throughout this experimental study. The structure's modes were experimentally identified to have natural frequencies of 1.73 Hz and 4.64 Hz with respective damping ratios of 0.4% and 0.2%. The identified mass and stiffness matrices are presented below:

$$\boldsymbol{M} = \begin{bmatrix} 25.11 & 0 \\ 0 & 23.40 \end{bmatrix} kg \qquad \boldsymbol{K} = \begin{bmatrix} 15400 & -8300 \\ -8300 & 8300 \end{bmatrix} N/m \tag{3.23}$$

3.7.2 System identification of a single-axis shake table

A bandlimited white noise (BLWN) with a frequency bandwidth of 0 – 30 Hz and an RMS value of 2 mm was used to excite the shake table and specimen. The RMS value for the BLWN should correspond to the expected RMS value of the actuator motion during the experiment. Fig. 3.12 presents the FRF from command signal to measured shake table acceleration for different proportional gains (p-gain). When p-gain is too high, distinct poles are formed resulting in harmonic behavior and sometimes instability. When p-gain is too low, the shake table becomes too slow for the acceleration tracking purposes. Established tuning approaches for PID controllers including the Ziegler-Nichols method, tend to predict smaller gains, leading to sluggish acceleration tracking performance. For the structure and shake table presented in Fig. 3.11, a p-gain value of 3 resulted in the best model for acceleration tracking. The small shake table used for system identification is unable to impose accelerations at low frequencies, as such accelerations correspond to high amplitude displacements. Therefore, the noise-to-signal ratio is quite high at low frequencies.

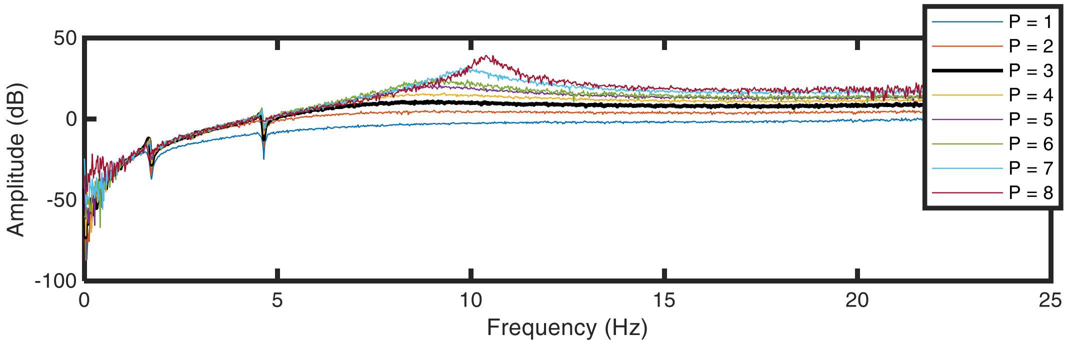

(a) Amplitude

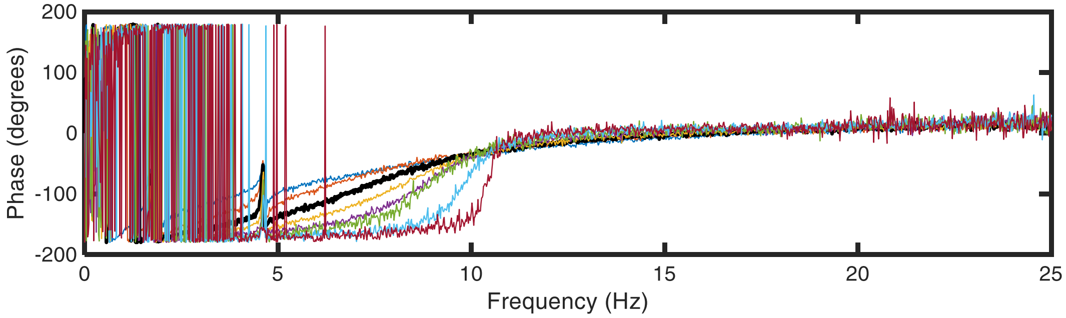

(b) Phase

Figure 3.12 FRF of shake table for different p-gains

Next, wooden braces are added to each story of the structure. System identification is then conducted to capture the added stiffness due to the wooden braces. The aim for adding these braces is to demonstrate how different controllers react to a physical change (i.e. wooden braces breaking). Braces are built from Balsa wood with a length of 9.5”, width of $^{1}/_{2}$", thickness of $^{3}/_{16}$”, and width of 3” at the supports. Presence of the braces implies greater stiffness in both floors, and higher natural frequencies of 1.89 Hz and 5.17 Hz for the two modes.

Following system identification, a linearized transfer function for input voltage and output acceleration is identified with 7 poles and 7 zeros, using the frequency domain identification tool MFDID, discussed in (Kim et al. 2005). This toolbox fits the FRF data with the closest matching transfer function model. All of the zeros reside in the left-hand plane or on the imaginery axis to ensure stability when the transfer function model of the shake table is inverted to produce an inverse model controller. The transfer function is presented in Eq. (3.24) and in graphical form in Fig. 3.13. The FRF for the setup with braces and without braces and the transfer function for the setup with braces are demonstrated in this figure. To ensure drifting is avoided due to the double integration in the inverse model implementation, input ground motions are highpass filtered to attenuate low frequency contents. A second-order butterworth highpass filter with a cutoff frequency of 0.25 Hz is used for prefiltering of earthquake time histories before experimenting.

$$\boldsymbol{P}(s) = \frac{1.667\,(s^2)(s+0.603)(s^2+0.577s+130)(s^2+1.609s+1041)}{(s+0.922)(s^2+0.511s+121.4)(s^2+2.106s+1000)(s^2+19.13s+2007)} \tag{3.24}$$

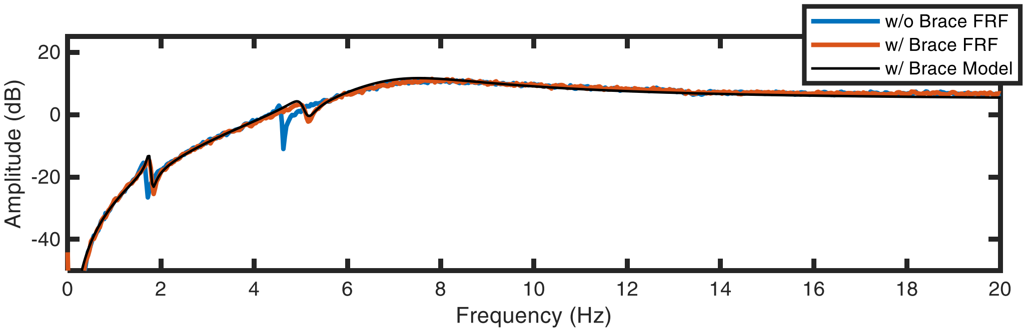

(a) Amplitude

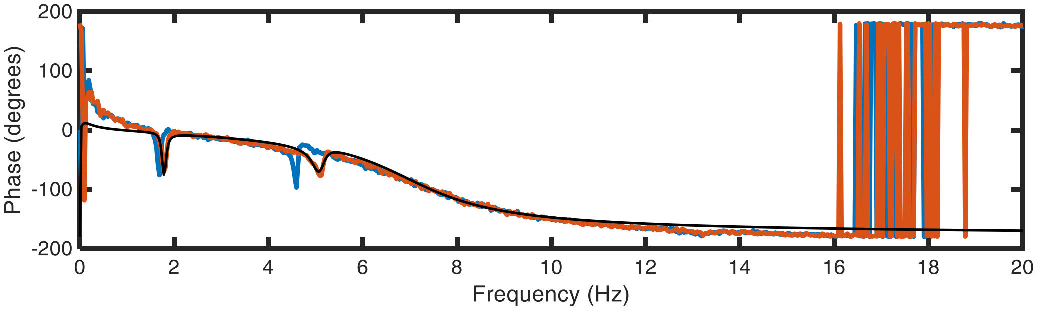

(b) Phase

Figure 3.13 FRF and transfer function models of shake table

3.7.3 Ground motion

Acceleration records from strong motion sensors are unique to the geography and individual site conditions. Assessing the performance of the shake table with different acceleration records offers different challenges to the control task. Many ground motions possess higher frequency contents but are shorter in duration, while others have lower frequency contents with higher durations. Three ground motions are selected and presented in Fig. 3.14, which include: (i) El Centro – 1940, (ii) Kobe – 1995, and (iii) Northridge – 1994. Due to limited stroke lengths of the shake table, the ground motion accelerations are scaled in amplitude and highpass filtered.

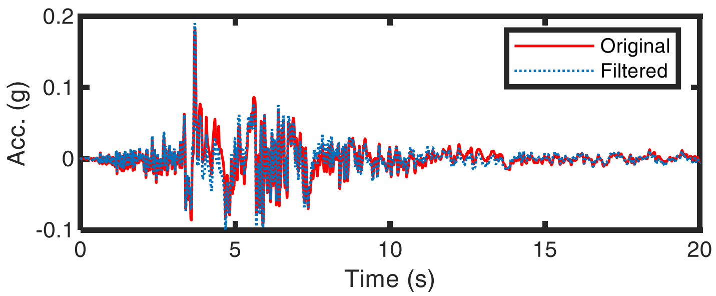

(a) El Centro 30%

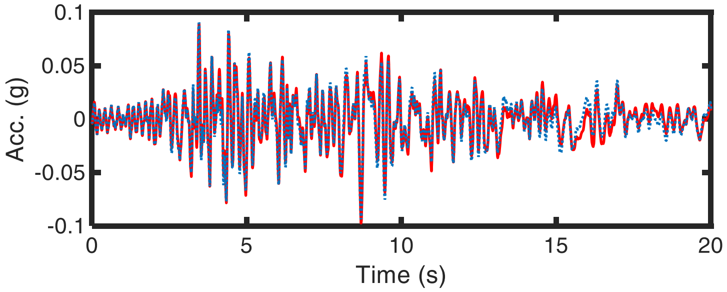

(b) Kobe 50%

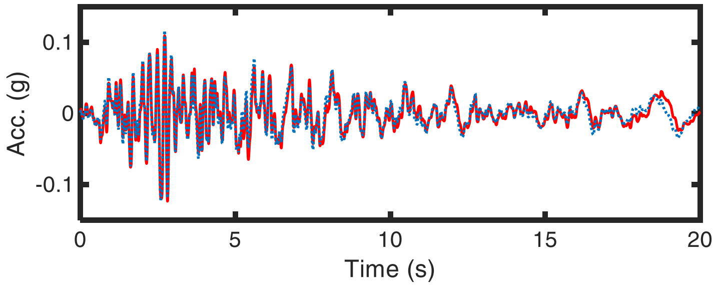

(c) Northridge 40%

Figure 3.14 Original and filtered ground motion accelerations

3.7.4 Tracking performance

Three different ground motion inputs are commanded to the shake table setup and reference-to-measurement signal tracking capabilities of the compensation techniques are evaluated. In this experimental study, the shake table is loaded with a two-story frame structure without the added braces, while the dynamic model used in the design of the controllers is derived from the identified two-story frame structure with the added braces. In addition, a roof-level Nonlinear Energy Sink (NES) device is mounted on the two-story frame, which adds nonlinearities to the shake table through CSI. The intent of this experiment is to test the controller behavior in the presence of nonlinearity and unmodeled dynamics.

Tracking performance of 4 controllers are evaluated via the RMSE and MAXE criteria between reference and output accelerations in both time and frequency domains. These include: (i) Feedforward, (ii)

TFI, (iii) MBC, and (iv) mMBC. The ideal controller is one which consistently realizes the smallest $RMSE$. Fig. 3.15 demonstrates the time domain acceleration tracking response for the El Centro earthquake PGA-scaled at 30%. Both reference and measured acceleration records have been post-processed with a 5th order lowpass filter with a cutoff frequency of 20 Hz, to reduce high frequency noise contents.

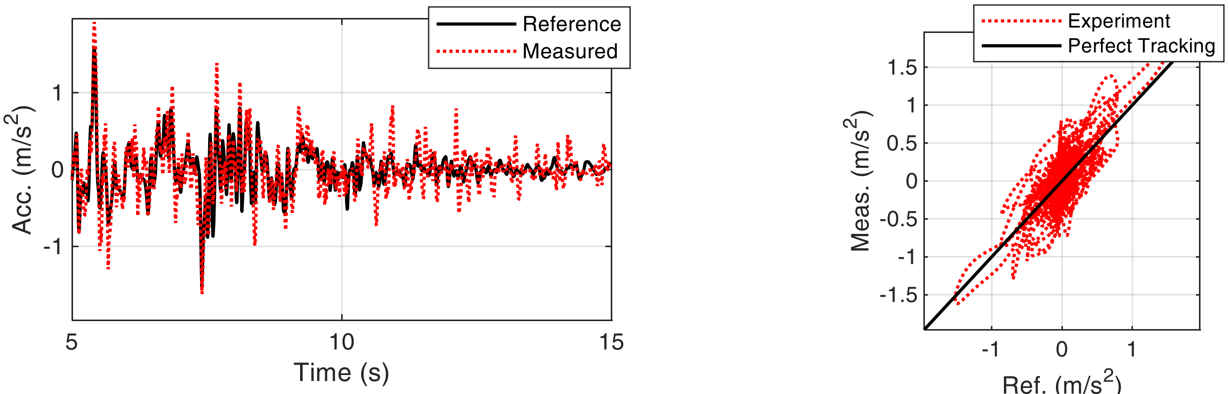

(a) Feedforward – time history

(b) Feedforward – synchronization plot

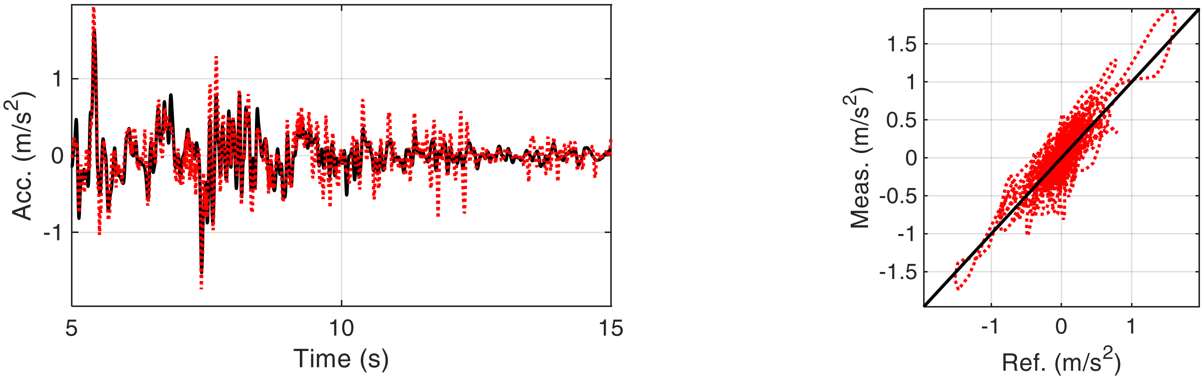

(c) TFI (3 iter.) – time history

(d) TFI (3 iter.) – synchronization plot

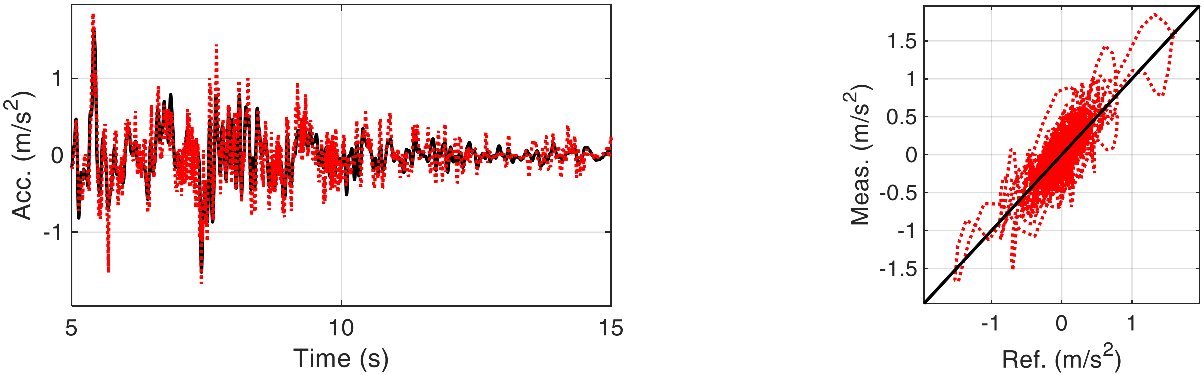

(e) TFI (6 iter.) – time history

(f) TFI (6 iter.) – synchronization plot

Figure 3.15 Acceleration tracking and synchronization plots for the 30% El Centro

Figure 3.15 (continued)

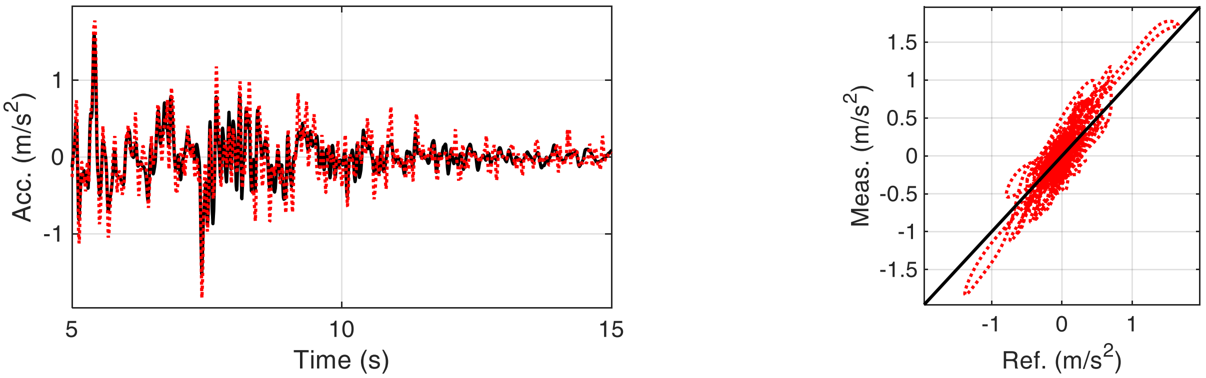

(g) MBC – time history (h) MBC – synchronization plot

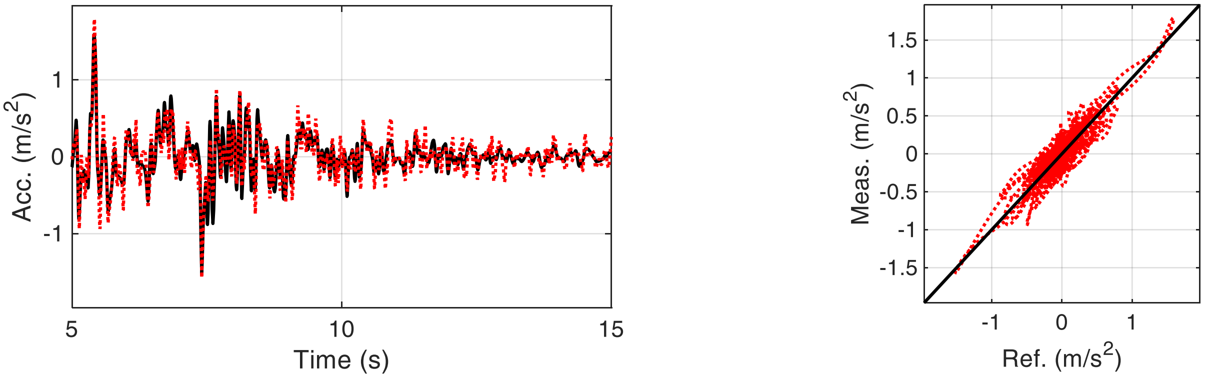

(i) mMBC – time history (j) mMBC – synchronization plot

The results of the *RMSE* and *MAXE* quantitative evaluation criteria in Eqs. (3.21) and (3.22), in time and frequency domain, are presented in Tables 3.3-3.5. Each tracking experiment is repeated three times and the performance criteria presented are for the average of the three performances. This is to account for the variability that may exist in these results. The feedback parameters of MBC and mMBC are optimized for the minimization of the tracking error. The results of the TFI technique are demonstrated for 3 iterations and 6 iterations. The iterative tuning of the TFI method amplifies high frequency contents as indicated by the results. The mMBC technique demonstrates the least overshoot in the output acceleration. This is attributed to the authoritative feedback design of the mMBC.

Table 3.3 Time domain RMSE performance for different ground motions

Controller Type	Time domain ***RMSE***		
	El Centro	Kobe	Northridge
Feedforward	0.930	1.242	0.945
TFI (3 iter.)	1.054	1.396	1.093
TFI (6 iter.)	1.160	1.332	1.169
MBC	0.870	1.376	0.951
mMBC	0.803	1.128	0.784

Table 3.4 Time domain MAXE for different ground motions

Controller Type	Time domain ***MAXE***		
	El Centro	Kobe	Northridge
Feedforward	0.550	0.786	0.611
TFI (3 iter.)	0.743	0.840	0.797
TFI (6 iter.)	0.790	0.843	0.791
MBC	0.432	0.843	0.665
mMBC	0.402	0.688	0.584

Table 3.5 Frequency domain RMSE performance for different ground motions

Controller Type	Frequency domain ***RMSE***		
	El Centro	Kobe	Northridge
Feedforward	1.121	1.386	1.004
TFI (3 iter.)	1.208	1.722	1.030
TFI (6 iter.)	1.154	1.392	1.001
MBC	1.101	1.731	0.957
mMBC	0.706	1.004	0.559

3.7.5 Tracking robustness

Tracking robustness is the evaluation of the tracking ability of a controller under changing dynamics of the plant. A controller that becomes unstable under changing plant dynamics will clearly lack tracking robustness. A tracking robustness study hence requires analysis of both the tracking and stability properties of a controller. The stability performance of a feedforward controller is arbitrary and easy to analyze. With a stable plant and a stable feedforward controller, this method needs no further stability analysis. TFI is an iterative expansion of the feedforward technique and its stability is dependent on the initial iteration. Therefore, in this section the focus of the stability performance is on the two model-based controllers. Addition of feedback control makes stability analysis difficult, particularly when changes in dynamics of the shake table are expected. The stability condition discussed earlier is further elaborated in this section.

Stability assessment of the discussed model-based controllers requires limiting feedback gains to $\|\boldsymbol{K}(s)\|_\infty \leq 1$. From an engineering perspective, an infinitely large feedback gain cannot be stabilizing. Thus, limiting the gain of the feedback controller for stability performance analysis is necessary. Having bounded the feedback gain, the limits that may exist on the plant gain must be studied. In the case of the MBC, the term plant refers to the coupled shake table and structure dynamics, and for the mMBC, refers to the cascaded use of the inverse model controller and the shake table and structure dynamics. A plant may have arbitrary gains over different frequency ranges and the amplitude of the gain is subject to change due to nonlinearities and changing plant dynamics. Understanding the operational frequency of the shake table helps determine what frequency range to study, when calculating the plant norm. In most shake tables, the frequency content of the input signal provides a good estimate of the operational frequency bandwidth of the shake table. Fig. 3.16 presents the power spectral densities (PSD) of three different ground motions. This PSD plot highlights the energy distribution at various frequencies. An important observation is that the majority of the energy of the listed ground motions is concentrated in the 0 – 10 Hz frequency range. Hence, stability conditions and norm calculations are assessed over this frequency bandwidth.

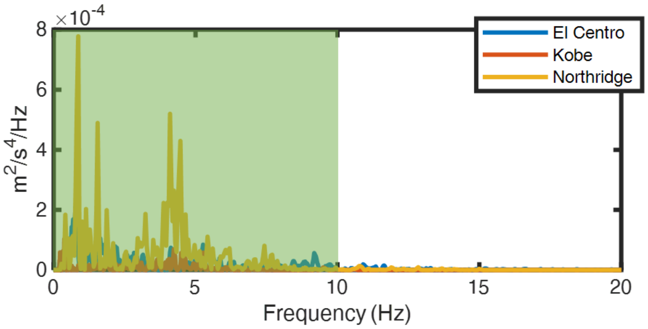

Figure 3.16 Power spectral density for ground motions

The goal of a feedback controller, particularly in tracking type problems, is to enhance the tracking abilities of the control system (i.e. amplitude and phase compensation). Feedback control induced instability happens when instead of observing improvements, by increasing the gain of the feedback the tracking abilities start to deteriorate and soon diverge into complete instabilities. Alternatively, instability may occur for a constant feedback gain, but with large nonlinearities or sudden changes of plant dynamics due to yielding or brittle failures of structural components onboard the shake table. The time domain performances of the shake table for the MBC and mMBC compensation methods are presented in Fig. 3.17, showing the tracking quality for increasing values of feedback gain. The El Centro ground motion was used in this robustness analysis.

With the MBC technique, the plant norm is calculated as $\|\boldsymbol{P}(s)\|_\infty = 3.84$ for the frequency range 0 – 10 Hz. Referring to the MBC stability plot, the RMSE value begins an upwards increase at $\|\boldsymbol{K}(s)\|_\infty \approx 0.3$. The stability norm condition $\|\boldsymbol{P}(s)\|_\infty \|\boldsymbol{K}(s)\|_\infty < 1$, derived mathematically is observed to be violated, in Fig. 3.17, roughly when this upward trend begins and tracking approaches instability. When the mMBC is used, the augmented plant norm is $\|\boldsymbol{L}(s)\|_\infty = 1$. For increasing values of $\|\boldsymbol{K}(s)\|_\infty$, not only is stability maintained, but the *RMSE* criterion decreases, which corresponds to a tracking enhancement.

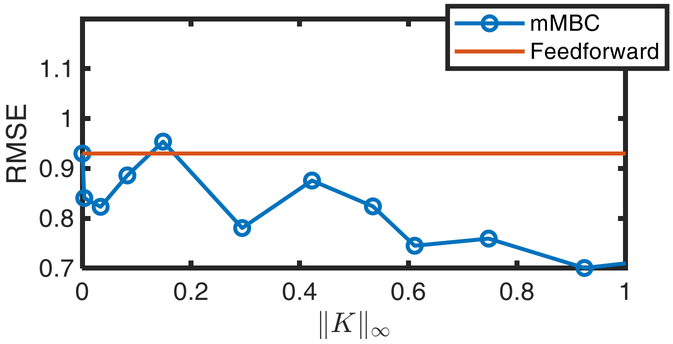

(a) MBC

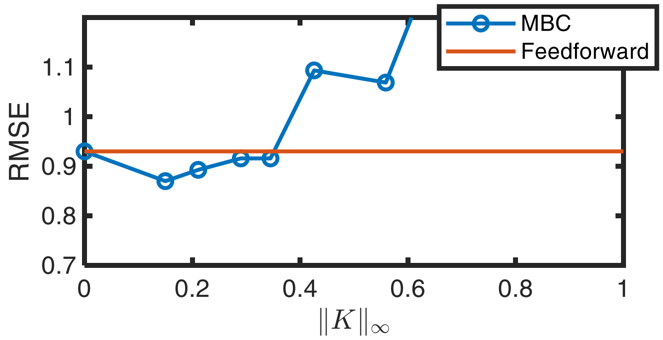

(b) mMBC

Figure 3.17 RMSE performance of model-based controllers vs. feedback gain for 30% El Centro

The mMBC achieves enhanced tracking for feedback gains satisfying $\|\boldsymbol{K}(s)\|_\infty \leq 1$, implying predictability in the stability performance of this control architecture. The MBC, however, does not have this predictive property. In the mMBC, the inverse model controller combines with the shake table dynamics in the stabilizing effort, while in the MBC, the entire stabilizing effort is burdened onto the shake table dynamics. The feedback controller in mMBC is designed based on a lowpass filter plant design, which typically results in fewer feedback states. However, in the feedback component of the MBC technique, there are at least as many states as there are in the presumed model of the shake table dynamics. Feedback on a smaller number of states is more stable and efficient from a computational perspective as well.

The tracking abilities of the discussed controllers are already demonstrated in the presence of unmodeled dynamics. The next step is to demonstrate the tracking robustness of the model-based controllers in the presence of sudden changes of dynamics during the test. This is achieved by installing Balsa wood braces, selecting a ground motion strong enough, and allowing the braces to break during the experiment. The El Centro ground motion, PGA-scaled to 70% was used for this purpose. An additional second-order Butterworth highpass filter with a cutoff frequency of 1.5 Hz is applied to ensure shake table stroke limit is not reached.

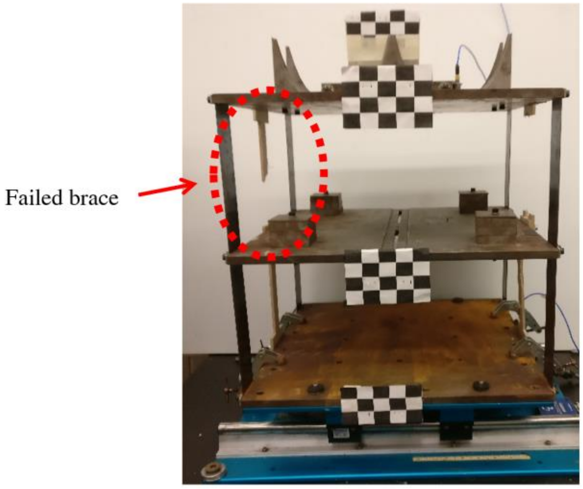

Figure 3.18 Two-story frame structure with failed braces

After the initial impulse at the 6 second mark, one or more braces failed, seen in Fig. 3.18, resulting in changes in the natural frequencies of the two-story frame. Since the response of the two-story frame is coupled with the response of the shake table through CSI, this change in natural frequency translates to a change in the dynamics of the shake table. Fig. 3.19 demonstrates the response of each model-based controller in the presence of brace failure. The MBC tends to unwind and is unable to bring the shake table acceleration to a zero equilibrium. The PSD for MBC output indicates a peak at around 5 Hz. The mMBC technique is capable of tracking the reference signal and stabilizing the new dynamics. The mMBC filters should be designed such that the stability norm condition is well below the stability condition threshold, to allow unmodeled behaviors to be accommodated throughout the experiments.

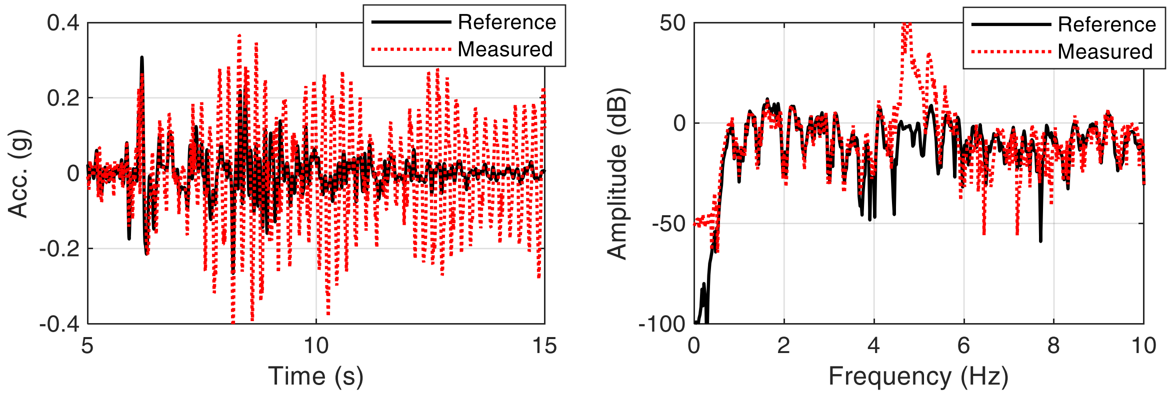

(a) MBC time domain (b) MBC frequency domain

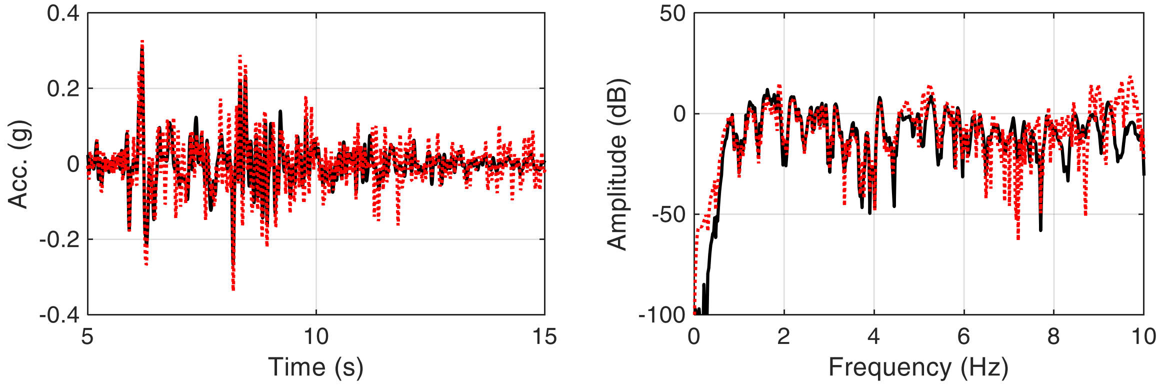

(c) mMBC time domain (d) mMBC frequency domain

Figure 3.19 Model-based controller responses to changing dynamics

The stability criterion for the mMBC algorithm is next schematically described, for before and after brace failure in Fig. 3.20. Under an elastic circumstance and prior to brace failure, the augmented plant behaves as a lowpass filter. Fig. 3.20(a) presents the lowpass filter $\boldsymbol{L}(s)$ along with the LQG feedback controller $\boldsymbol{K}(s)$. As mentioned earlier, stability can be guaranteed when $\left(1+\boldsymbol{L}(s)\boldsymbol{K}(s)\right)^{-1}$is nonsingular, which corresponds to $\|\boldsymbol{L}(s)\boldsymbol{K}(s)\|_{\infty} < 1$. This stability criterion is represented by the black dashed line in Fig. 3.20(a). When $\|\boldsymbol{L}(s)\boldsymbol{K}(s)\|_{\infty}$ is close to zero, the feedback action is minimal, and tracking is poor. When $\|\boldsymbol{L}(s)\boldsymbol{K}(s)\|_{\infty}$ is close to 1, the feedback action is strong, but the stability limit can be breached, if there are changes to the dynamics of the shake table and specimen. For particular feedback controller shown, the feedback gain was designed to be conservative to allow for changes in dynamics of the physical setup.

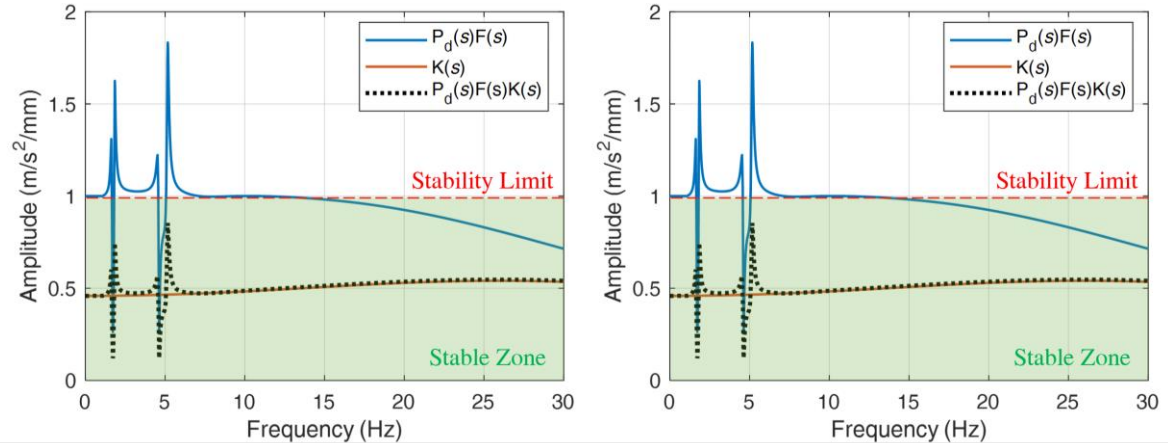

(a) Stability criterion before brace failure (b) Stability criterion after brace failure

Figure 3.20 Amplitude plots for the stability criterion

In Fig. 3.20(b), $\boldsymbol{P}_d(s)$ describes the dynamics of the system after braces are damaged. The new augmented plant is now described via $\boldsymbol{P}_d(s)\boldsymbol{F}(s)$. Due to the sudden failure in the brace elements, new peaks appear in the stability criterion (i.e., black dashed-line). The mMBC provides the foresight and predictability for the stability limit of the closed-loop dynamics. Designers can develop an mMBC controller with sufficient space between the stability limit and the stability criterion to allow for dynamic changes and, hence avoiding instabilities.

3.8 Summary

In this chapter, different control strategies were examined for compensation of unwanted actuator-structure dynamics. First, the concept of reference tracking for shake table and real-time hybrid simulation (RTHS) applications were described. Displacement, acceleration, and force are examples of reference tracking problems that were discussed. The modified Model-Based Control (mMBC) compensator was proposed as a modification to the Model-Based Control (MBC) already used in shake table and RTHS applications. The modified compensator has improved tracking performance, stability robustness, and stability predictability. An adaptive augmentation of the mMBC was proposed, called the adaptive Model Reference Control (aMRC). This algorithm is comprised of an adaptive law and a reference model. The adaptive law forces the plant to behave like the reference model. A projection algorithm is proposed for the adaptive law, which prevents adaptive parameter drifting.

The tracking abilities of the proposed mMBC and aMRC algorithms were next numerically and experimentally evaluated. A single-DOF numerical simulation compared four compensation strategies, determining that the mMBC and aMRC had the best tracking robustness. A shake table setup with an onboard structure was considered for acceleration tracking. The aMRC algorithm was excluded from the acceleration control problem, as the adaptive law generates low frequency contents which result in high amplitude displacements. Three other shake table compensation techniques were evaluated and the mMBC was determined to have the best tracking robustness and stability predictability.

CHAPTER 4 SINGLE-AXIS REAL-TIME HYBRID SIMULATION

4.1 Problem Statement

Real-time hybrid simulation (RTHS) is an alternative to the traditional hybrid simulation, which offers benefits of real-time testing (i.e., material rate-dependence can be accommodated) and substructuring (i.e., cost and space savings). Physical execution happens at real-world speeds and numerical integration is conducted explicitly at frequencies of 200 Hz or higher. The experimental capabilities and computational requirements are increased due to the rapid nature of the RTHS.

One of the challenges in RTHS is that researchers set higher than realistic (artificial) damping values to the numerical substructure to achieve stable execution. The stability and accuracy of an RTHS experiment are often jeopardized by the presence of unwanted actuator-structure dynamics, resulting in closed-loop delays. Model-based RTHS eliminates the need for the added artificial damping and results in a stable performance. This RTHS formulation addresses the challenges of unwanted actuator-structure behavior via model-based compensation methods (Carrion et al. 2009; Phillips and Spencer 2013; Zhang et al. 2017).

Another challenge with RTHS surrounds the question of the accuracy of the method. A number of publications in the recent years have investigated and compared the performances of shake table and various RTHS methods, as a means to validate the latter. Ashasi-Sorkhabi et al. (2015) studied the dynamic performance of a spring-mass system coupled to a tuned liquid damper. The displacement response of the full- and sub-structured test configurations were evaluated and demonstrated to be closely matching. Damping of the analytical substructure was set to a high value of 6.3%. Lamarche et al. (2010) conducted shake table and RTHS testing of a two-story reinforced concrete frame. Similar results were observed in the displacement response for the shake table and RTHS tests in both the linear- and nonlinear-range. However, validated methods for testing lightly-damped and highly-nonlinear structures don’t appear to be available. Nonlinear energy sink devices are examples of lightly-damped and highly nonlinear structural systems.

This section outlines the model-based RTHS method for single-axis testing, as a steppingstone for the multi-axial RTHS development to be described in later chapters. Several applications involving lightly-damped and highly-nonlinear structural systems are then explored.

4.2 Model-based Real-Time Hybrid Simulation

The RTHS method partitions the dynamics of a reference structure into two or more components. The fundamental components are typically numerical and physical substructures, and a boundary interface.

The numerical substructure is comprised of governing equations, state-space formulations, or more sophisticated finite element analysis (FEA) models. The physical substructure is the structural element of interest whose nonlinear hysteresis is the focus of the research. There exists a correspondence between the boundary conditions and forces in numerical and physical substructures, as if the entire experiment was one continuous reference structure. Since, it is impossible for a computer and a structural element to directly communicate the physical laws at the boundary conditions, actuators and sensors are utilized. The boundary point for a single-axis RTHS experiment is often enforced by just one servo-hydraulic actuator and one or more sensors, per Fig. 4.1.

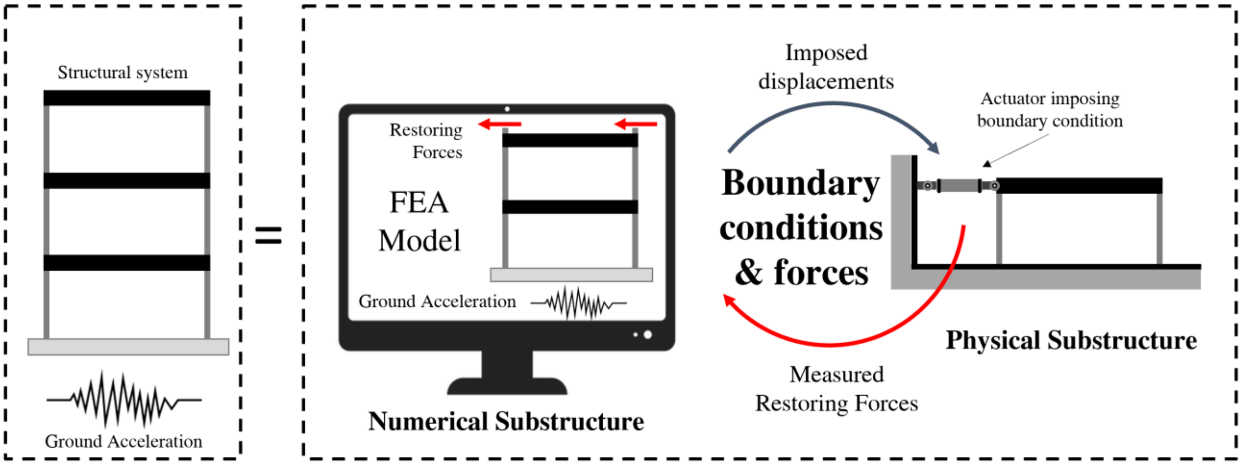

Figure 4.1 Schematic of a single-axis RTHS

The single-axis model-based RTHS framework presented herein employs the mMBC compensator developed by Najafi and Spencer (2020), which has excellent tracking and robustness capabilities, making it a suitable choice for RTHS applications. In setting up the framework, two types of model-based compensations are considered: (i) displacement tracking, and (ii) acceleration tracking, as shown in Fig. 4.2. The excitation considered here is an earthquake ground acceleration for demonstrative purposes. The choice of input excitation is arbitrary.

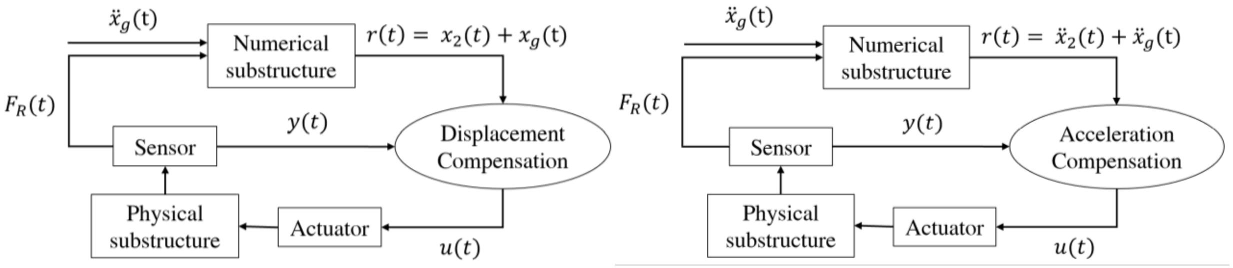

(a) RTHS with displacement tracking (b) RTHS with acceleration tracking

Figure 4.2 Model-based RTHS architecture

After excitation of the numerical substructure, displacements or accelerations at the boundary with the physical substructure are computed. The signal that exits the numerical substructure is referred to as the reference or target signal. The mMBC compensator may be used in both displacement and acceleration reference tracking problems. Output of the compensators is a control signal $u(t)$, sent for physical execution via an actuator. Once the physical substructure is deformed, onboard sensors including accelerometers, displacement transducers, and loadcells obtain the measurement signal $y(t)$ and feedback force $F_R(t)$.

Throughout this section, three applications of single-axis RTHS are explored. First, a validation study of model-based RTHS for a lightly-damped and highly-nonlinear structural system is presented, where the results of RTHS experiments are evaluated via comparisons to shake table tests. Next, an RTHS framework with the aMRC compensator is presented with application to the benchmark control problem discussed in Silva et al. (2020). Lastly, a study of magnetorheological dampers for mitigation of train-induced bridge vibrations is presented.

4.3 Model-based RTHS for lightly-damped and highly-nonlinear structure

With the objective of conducting model-based RTHS on a structural system with light damping and high degree of nonlinearity, the two-story structure from Section 3.7 is selected. The two-story frame shown in Fig. 4.3 behaves as a shear building, since the floor slabs are considerably stiffer than the columns. The structure is lightly damped, possessing damping ratios of 0.20% and 0.36% for the first two modes, respectively, when the NES is locked, the damping is 0.45% and 0.38% when the NES is unlocked.

Figure 4.3 Two-story steel frame with track NES

The NES mass, shown in Fig. 4.4, moves along a vertically nonlinear path described by the shape of the track $h(x_n)$, where x_n is the horizontal displacement of the mass. Due to this geometric nonlinearity, the restoring forces of the NES are identified per the nonlinear equation below and shown in Fig. 4.5.

$$\Gamma = \left([h'(x_n)]^2\ddot{x}_n + h'(x_n)h''(x_n)\dot{x}_n + h(x_n)\right)m_n \tag{4.1}$$

Figure 4.4 NES device

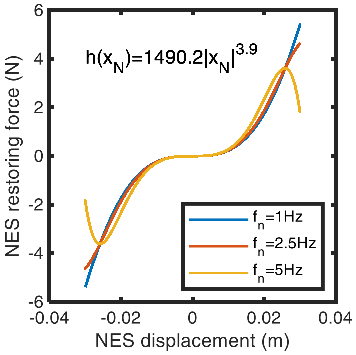

Figure 4.5 Track NES hysteretic relationship for different excitation frequencies

The two-story steel frame and NES are modeled with a three-DOF governing equation of motion with ground acceleration as the input excitation.

$$m_1\ddot{x}_1(t) + c_1\dot{x}_1(t) + c_2\left(\dot{x}_1(t) - \dot{x}_2(t)\right) + k_1x_1(t) + k_2\left(x_1(t) - x_2(t)\right) = -m_1\ddot{x}_g(t) \tag{4.2}$$

$$m_2\ddot{x}_2(t) + c_2\left(\dot{x}_2(t) - \dot{x}_1(t)\right) + k_2\left(x_2(t) - x_1(t)\right) - c_n\dot{x}_n(t) - \Gamma(\mathrm{t}) = m_2\ddot{x}_g(t) \tag{4.3}$$

$$m_n\ddot{x}_n(t) + c_n\dot{x}_n(t) + \Gamma(\mathrm{t}) = -m_n\left(\ddot{x}_2(t) + \ddot{x}_g(t)\right) \tag{4.4}$$

where m_i, c_i, and k_i are the mass, damping, and stiffness parameters, $\ddot{x}_i(t)$, $\dot{x}_i(t)$, and $x_i(t)$ are relative acceleration, velocity, and displacement terms of the i^{th} story, and c_n is the damping of the NES. m_n is the mass of the NES at 2.457 kg. $\ddot{x}_n(t)$ and $\dot{x}_n(t)$ describe the acceleration and velocity terms for the NES, relative to the second-floor mass. $\ddot{x}_g(t)$ is the ground acceleration. The schematic of the numerical realization for the two-story frame with the track NES device is presented in Fig. 4.6.

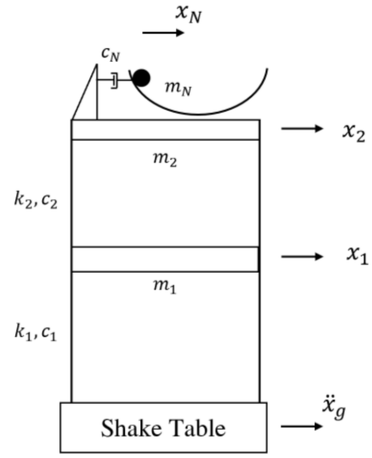

Figure 4.6 Shake table testing: two-story steel frame with a track NES device

4.3.1 Shake table testing result

The selected two-story steel frame with onboard track NES device is shake table tested as a benchmark for comparison with RTHS results in later sections. The proposed experimental study is conducted on a Quanser Shake Table II. An NI CompactRIO 9073 controller completes the task of stabilizing the shake table via a proportional-derivative controller. Numerical integration and compensation action are computed on a dSPACE DS1103PPC microcontroller with a sampling rate of 1kHz. A 4th-order Runge-Kutta integration algorithm is used. The development environment for the dSPACE controller consists of the Matlab/Simulink software suite and the ControlDesk program which converts algorithms to the C programming language and compiles them on the microcontroller.

Measurement of the horizontal displacements at the story levels in the discussed steel frame is a challenging task. Linear displacement measurement tools like linear variable differential transformers (LVDTs) possess small amounts of friction, which can offset experimental results. To solve this issue, vision-based displacement measurement techniques are incorporated.

A 60 frame-per-second camera is used to record the behavior of the building during the duration of a ground motion acceleration. Black and white square patterns are installed on the structural components for detection via a vision-based algorithm, per in Fig. 4.7. Base (i.e., shake table) displacement is measured via the onboard optical encoder.

PCB353B33 piezoelectric accelerometers are used for acceleration measurements. The accelerometers are installed at each story, on the NES, and on the shake table for acceleration feedback and compensation purposes. Following the data acquisition from the shake table testing procedure, results are synchronized and prepared for the model-based RTHS validation study.

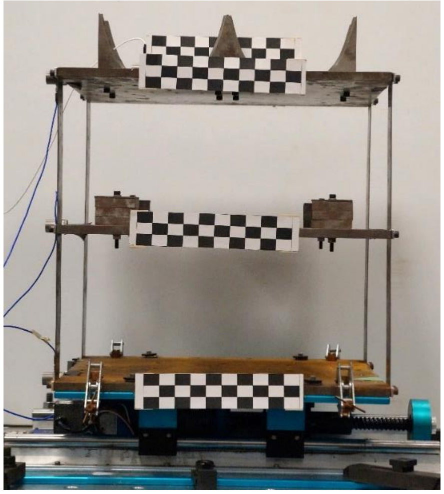

Figure 4.7 Two-story steel frame with track NES device

The two-story steel frame with the track NES device is excited with a PGA-scaled 30% 1940 El Centro earthquake, shown in Fig. 4.8. This original ground acceleration was sampled at a 100 Hz from recording station no. 6, was upsampled to 1000 Hz for this study. The mMBC is used for compensation during the shake table testing and provides better tracking than many existing methods. Details pertaining to tracking control and operation of the shake table and two-story steel frame are presented in Najafi and Spencer (2020).

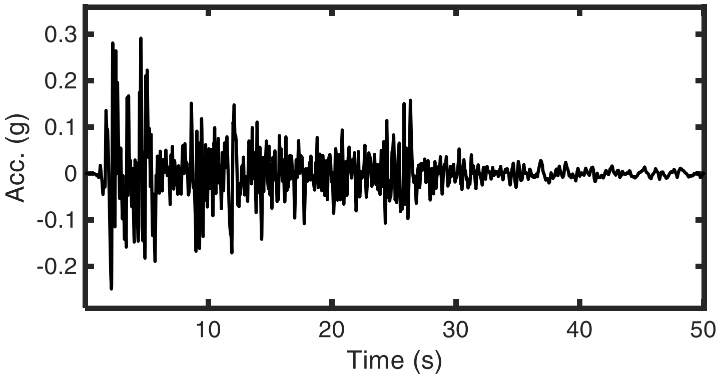

Figure 4.8 30% PGA-scaled 1940 El Centro earthquake

Nonlinearities in the dynamics of the shake table device result in small performance variations in every experiment. These variations are presented in Fig. 4.9, along with the minimum and maximum values. To study these variations, results for 10 experiments are presented. Next, the structure is partitioned and tested via the RTHS method.

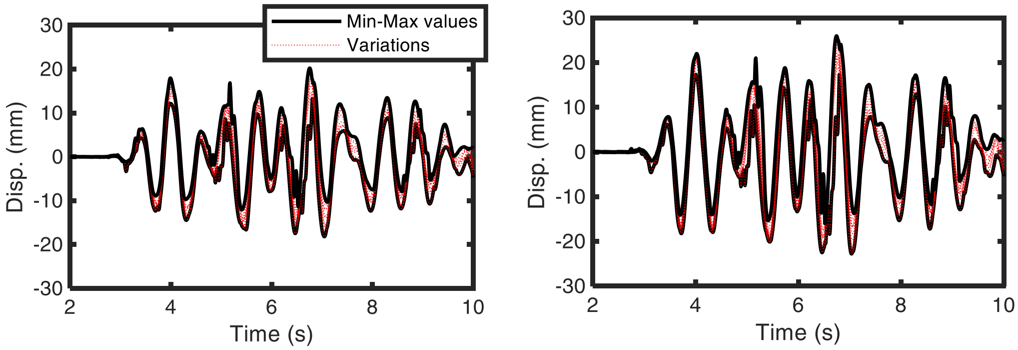

(a) First story displacement (b) Second story displacement

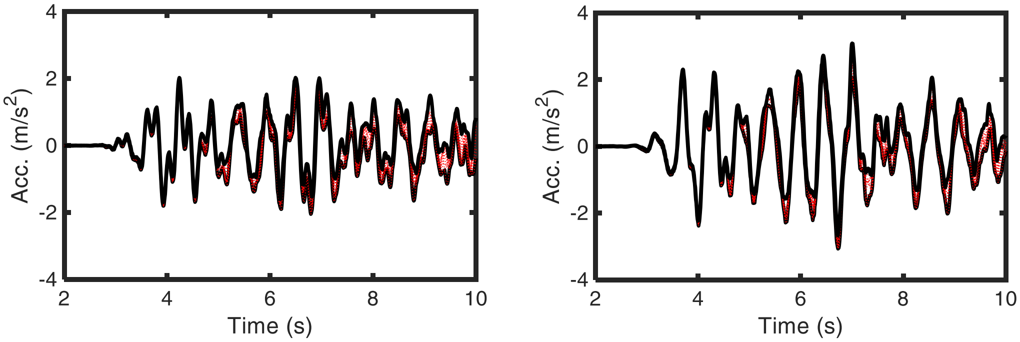

(c) First story acceleration (d) Second story acceleration

Figure 4.9 Variations in the displacement and acceleration responses for 10 repeated shake table tests

4.3.2 Real-time substructuring

Before conducting RTHS in the laboratory, the structure of interest is substructured and a numerical model identified. To this end, the two-story frame structure with NES is partitioned into two substructures. The two-story frame is numerically modeled while the NES device is physically tested. The proposed RTHS substructuring is demonstrated in Fig. 4.10.

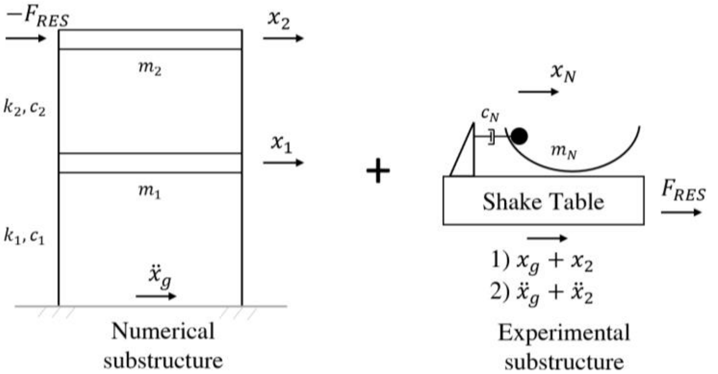

Figure 4.10 RTHS testing: substructuring of the two-story frame with track NES

$$\begin{bmatrix} m_1 & 0 \\ 0 & m_2 \end{bmatrix} \begin{Bmatrix} \ddot{x}_1(t) \\ \ddot{x}_2(t) \end{Bmatrix} + \begin{bmatrix} c_1 + c_2 & -c_2 \\ -c_2 & c_2 \end{bmatrix} \begin{Bmatrix} \dot{x}_1(t) \\ \dot{x}_2(t) \end{Bmatrix} + \begin{bmatrix} k_1 + k_2 & -k_2 \\ -k_2 & k_2 \end{bmatrix} \begin{Bmatrix} x_1(t) \\ x_2(t) \end{Bmatrix} \\ = -\begin{bmatrix} m_1 & 0 \\ 0 & m_2 \end{bmatrix} \begin{Bmatrix} 1 \\ 1 \end{Bmatrix} \ddot{x}_g(t) - \begin{Bmatrix} 0 \\ 1 \end{Bmatrix} F_R \tag{4.5}$$

where F_R is the hybrid simulation restoring force, estimated using the acceleration data from the track NES shown in Fig. 4.4, and given by

$$F_R = m_n \ddot{x}_{n,abs}(t) = m_n \left(\ddot{x}_n(t) + \ddot{x}_2(t) + \ddot{x}_g(t) \right) \tag{4.6}$$

The two-DOF equation of motion for the two-story frame is next converted to state-space format for simulation purposes

$$\begin{bmatrix} \dot{\boldsymbol{x}}_N(t) \\ \ddot{\boldsymbol{x}}_N(t) \end{bmatrix} = \begin{bmatrix} \boldsymbol{0} & \boldsymbol{I} \\ -\boldsymbol{M}^{-1}\boldsymbol{K} & -\boldsymbol{M}^{-1}\boldsymbol{C} \end{bmatrix} \begin{bmatrix} \boldsymbol{x}_N(t) \\ \dot{\boldsymbol{x}}_N(t) \end{bmatrix} + \boldsymbol{B}\ddot{x}_g(t) + \boldsymbol{G}F_R \tag{4.7}$$

$$y_1(t) = \begin{bmatrix} 0 & 1 & 0 & 0 \end{bmatrix} \begin{bmatrix} \boldsymbol{x}_N(t) \\ \dot{\boldsymbol{x}}_N(t) \end{bmatrix} + x_g(t) \tag{4.8}$$

$$y_2(t) = \begin{bmatrix} -\boldsymbol{M}^{-1}\boldsymbol{K}(:,2) & -\boldsymbol{M}^{-1}\boldsymbol{C}(:,2) \end{bmatrix} \begin{bmatrix} \boldsymbol{x}_N \\ \dot{\boldsymbol{x}}_N \end{bmatrix} \tag{4.9}$$

where M, C, and K are mass, damping, and stiffness matrices of the two-story frame and $x_N = [x_1 \quad x_2]^T$. Also, the input vectors are described as $\boldsymbol{B} = [0 \quad 0 \quad -1 \quad -1]^T$ and $\boldsymbol{G} = [0 \quad 0 \quad -[0 \quad 1]\boldsymbol{M}^T]^T$. The outputs of the numerical substructure are described as $y_1(t)$ and $y_2(t)$, which represent the second-story displacement and acceleration, respectively.

In the proposed setup, the boundary condition between the numerical and physical substructures is defined by the absolute motion of the second story. A shake table is used to actuate the physical substructure. By replicating the absolute motion of the second floor, the shake table ensures that the NES device undergoes the same inertial forces, as it would if the complete structure was tested. Actuator compensation is provided in the form of the mMBC for displacement and acceleration control.

The physics of the NES mass is largely determined by the inertial behavior of this device, as stiffness and damping properties are insignificant. Since the inertial behavior is directly proportional to the acceleration of the mass, it makes sense to control the acceleration behavior of the boundary condition, in order to ensure an accurate RTHS experiment.

A high-fidelity model of the two-story steel frame is next obtained via extraction of natural frequencies and mode shapes, and a particle swarm optimization (PSO) algorithm for model parameter optimization. The two-story frame structure (i.e., without the NES device), is installed on a shake table and excited with a BLWN voltage signal. Acceleration responses of the stories are recorded during this excitation. Time and frequency domain relationships between the input BLWN signal and recorded floor accelerations are used for the model identification. The process for modeling of the two-story steel frame involves the two steps: (i) parameter estimation, and (ii) parameter optimization.

The first steps for reasonably accurate parameter estimations are listed below:

1. Estimate the story masses and formulate mass matrix, $\boldsymbol{M}$.
2. Identify the natural frequencies $\boldsymbol{\Omega} = [\omega_1 \quad \omega_2]^T$, via a peak-picking strategy.
3. Use the FRF phase relationships to estimate the mode shapes, $\boldsymbol{\Phi} = [\boldsymbol{\Phi}_1 \quad \boldsymbol{\Phi}_2]$.
4. Calculate the diagonal modal mass and stiffness matrices, $\widehat{\boldsymbol{K}} = diag\{\hat{k}_1, \hat{k}_2\}$ and $\widehat{\boldsymbol{M}} = \boldsymbol{\Phi}^T \boldsymbol{M} \boldsymbol{\Phi} = diag\{\widehat{m}_1, \widehat{m}_2\}$, via $\hat{k}_i = \widehat{m}\omega_i^2$ for $i \in \{1,2\}$.
5. Convert the stiffness matrix from modal to general stiffness coordinates, $\boldsymbol{K}$.

$$\boldsymbol{K} = \boldsymbol{\Phi}^{-T} \widehat{\boldsymbol{K}} \boldsymbol{\Phi}^{-1} \tag{4.10}$$

6. Estimate the modal damping ratios ζ_i, for $i \in \{1,2\}$, by fitting the model to the peaks of the FRF plots.

In the next step, the parameter estimates identified earlier are optimized, such that the numerical model of the two-story frame more accurately resembles the real physical performance. PSO uses a nature-inspired swarming strategy (i.e., bird flocking) and uses primitive mathematical operators to create an inexpensive computational tool (Kennedy and Eberhart 1995). Optimizing a structural model requires evaluation of multiple parameters. The evolutionary programming of the PSO algorithm is suitable for handling combinatorial optimization problems.

The PSO model begins by assigning a swarm of a particles to each optimization variable. A population of d random particles with a uniform distribution between the two boundaries b_l and b_h , and a position $x_{i,j} \sim U[b_l, b_h]$, and a velocity $v_{i,j}$ for $i \in \{1, \dots, d\}$, where j is iteration count, are at first initialized for each variable. For the proposed structural model in Eq. (4.5), the optimization variables are selected as k_1, k_2, m_1, m_2, ζ_1, and ζ_2. Each particle moves iteratively in the search-space and remembers its own optimal position P_i^L. The best position amongst all swarm particles are next stored in P_i^G. During each iteration, the velocity is updated per:

$$v_{i,j+1} = IT_j + CT_j + ST_j \tag{4.11}$$

$$IT_j = w v_{i,j} \tag{4.12}$$

$$CT_j = c_1 r_1 \left(P_i^L - x_{i,j}\right) \tag{4.13}$$

$$ST_j = c_2 r_2 \left(P_i^G - x_{i,j}\right) \tag{4.14}$$

where IT_j is an inertial term, CT_j is a cognitive term, and ST_j is a social term. r_1 and r_2 are uniformly distributed random vectors $\sim U[0,1]$. w is the inertial weight, c_1 is the self-adjustment weight, and c_2 is the social-adjustment weight. The new position for each iteration is determined per below

$$x_{i,j+1} = x_{i,j} + v_{i,j+1} \tag{4.15}$$

Therefore, a particle can optimize its course based on the past experiences of itself and other swarm particles.

The standard deviation (SD) between the measured and numerically computed first and second story accelerations, a_{exp} and a_{num}, are used to develop the cost function in this optimizing algorithm. Minimizing this cost function results in a reduction of errors between measured and numerically calculated accelerations. The SD is formulated per

$$SD = \sqrt{\frac{\sum_{k=1}^{n}\left(a_{exp}(k) - a_{num}(k)\right)^2}{n}} \tag{4.16}$$

where n is the data point count.

The parameters of the two-DOF system described in Eq. (4.15) are next identified via the two-step process. The experimentally identified FRFs and fitted numerical models of the first and second story accelerations are shown in Fig. 4.11 and 4.12. The PSO in step 2 assists in improving the accuracy of the structural model.

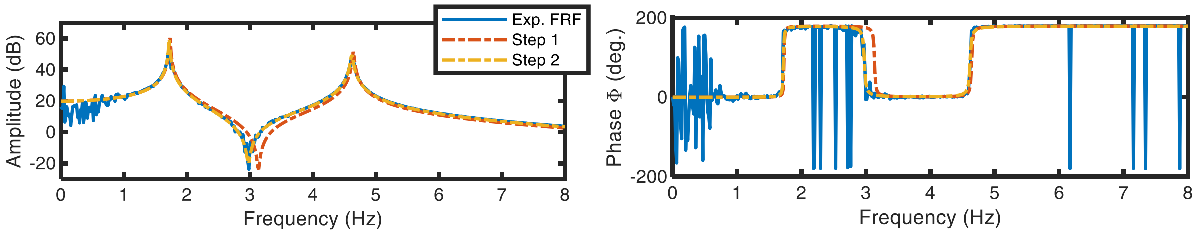

(a) Amplitude (b) Phase

Figure 4.11 First story acceleration FRF

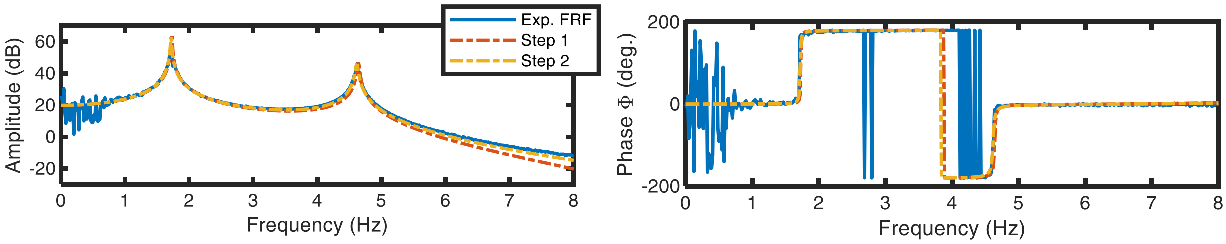

(a) Amplitude (b) Phase

Figure 4.12 Second story acceleration FRF

The acceleration and displacement responses of the numerical model subjected to the El Centro PGA-scaled at 30%, and are compared with the experimental results in Fig. 4.13.

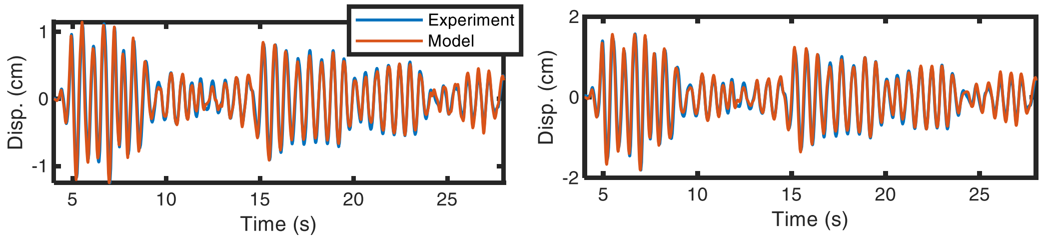

(a) First story displacement (b) Second story displacement

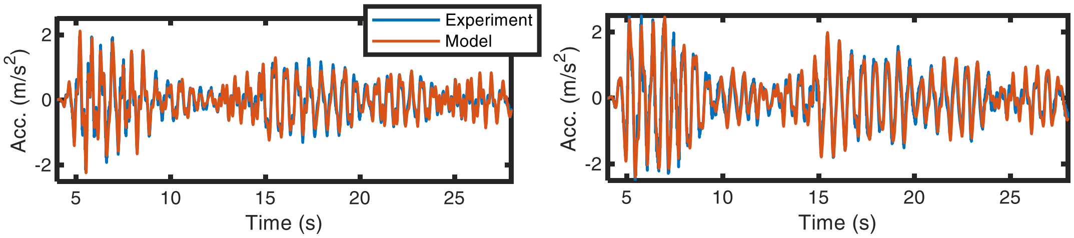

(c) First story acceleration (d) Second story acceleration

Figure 4.13 Time domain responses of the two-story structure – experimental and numerical results

The PSO algorithm is initialized with $d = 200$ swarm particles for each of the 6 structural parameters. Table 1 presents the predicted structural parameters after the estimation and optimization steps. This table also presents the lower and upper boundary values for the initialization of the swarm particles. The evolution of the swarm particles is demonstrated in Fig. 4.14, over the course of 15 iterations. These particles rarely converge to a single value due to the presence of an inertial term which ensures that their velocity is never converged to zero. Nevertheless, the position with the most optimal cost function is recorded and used.

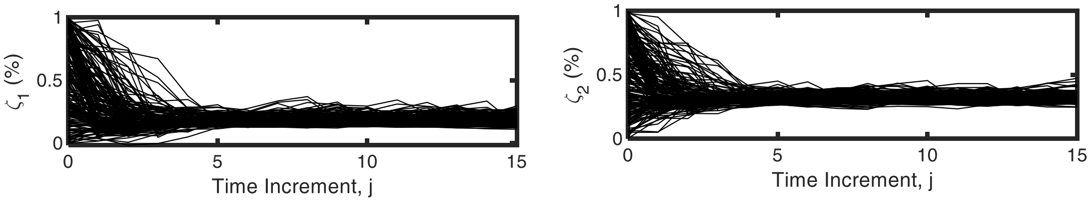

(a) ζ_1 (b) ζ_2

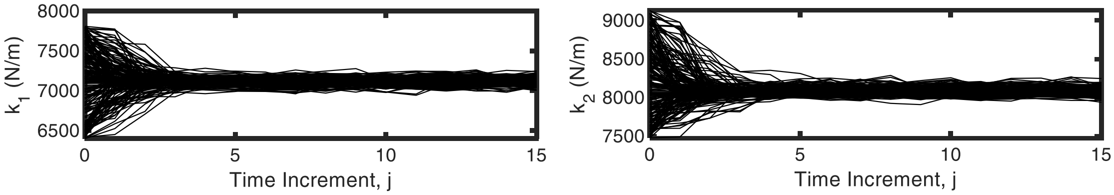

(c) k_1 (d) k_2

Figure 4.14 Evolution of the swarm particles assigned to each variable

Figure 4.14 (continued)

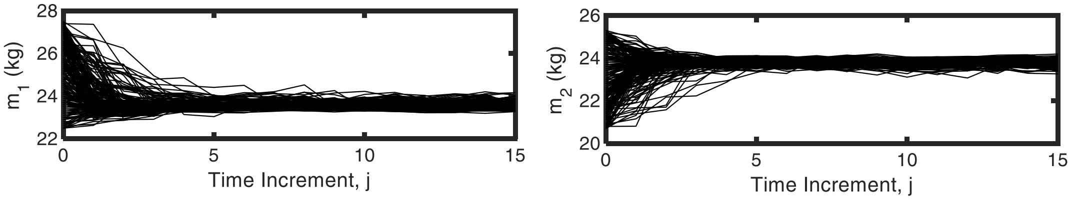

(e) m_1 (f) m_2

Table 4.1 Identified parameters for two-story steel frame

Parameters	Step 1 (Parameter estimation)	b_l	b_h	Step 2 (Parameter optimization)
$m_1\ (kg)$	25.1	22.5	27.5	24.98
$m_2\ (kg)$	23.4	20.7	25.3	24.31
$k_1\ (N/m)$	7100	6390	7810	7238
$k_2\ (N/m)$	8300	7470	9130	8236
ζ_1 (%)	0.250	0	1	0.196
ζ_2 (%)	0.250	0	1	0.359

4.3.3 Shake table and model-based RTHS comparison

The mMBC is developed using a linearized transfer function model of the shake table and structural system. The process for system identification, and frequency response function fitting are described in Section 3.7. Transfer function models of the shake table-structure interaction are used in the development of feedforward and feedback controllers.

System identification is conducted on the experimental substructure, which includes the shake table with the onboard NES device. A BLWN with a frequency range of 0 – 30 Hz and an RMS amplitude of 0.2 V is applied to the shake table and the realized displacements and accelerations are recorded.

Next, the time domain results are transformed to frequency domain to obtain FRFs for: (i) target displacement – measured displacement $\boldsymbol{P}_{dd}(s)$, and (ii) target displacement – measured acceleration $\boldsymbol{P}_{da}(s)$, transfer systems. The FRFs are fitted with transfer function models which are presented in Eqs. (4.17) and (4.18), per the process in Section 2.5. The bode plot of the experimental FRFs and identified transfer models are shown in Fig. 4.15 and 4.16.

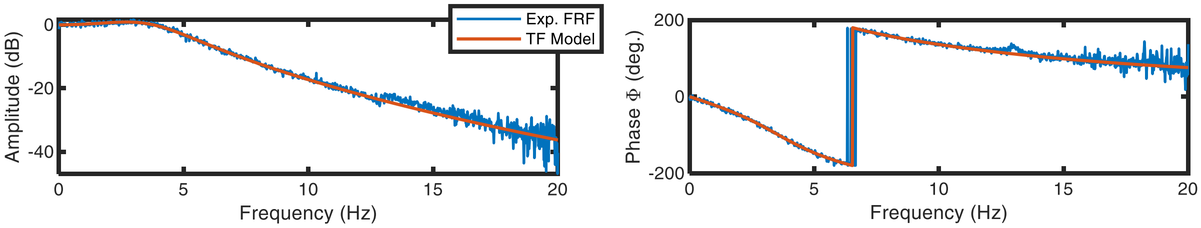

(a) Amplitude (b) Phase

Figure 4.15 $\boldsymbol{P}_{dd}(s)$ transfer system

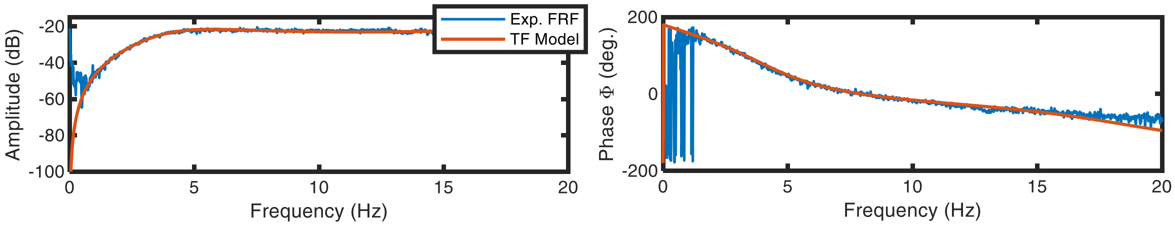

(a) Amplitude (b) Phase

Figure 4.16 $\boldsymbol{P}_{da}(s)$ transfer system

$$\boldsymbol{P}_{dd}(s) = \frac{d_{out}(s)}{d_{in}(s)} = \frac{4.67e6}{s^4 + 167s^3 + 1.14e4s^2 + 2.81e5s + 4.67e6} \tag{4.17}$$

$$\boldsymbol{P}_{da}(s) = \frac{a_{out}(s)}{a_{in}(s)} = \frac{1.18s^4 + 479.1s^3 + 4.83e4s^2}{s^4 + 126.6s^4 + 2.05e4s^3 + 1.09e6s^2 + 2.93e7s + 4.3e8} \tag{4.18}$$

The feedforward controller for displacement tracking is designed by cascading the inverse of the transfer system in Eq. (4.17) with a fourth-order Butterworth lowpass filter with a cutoff frequency of 50 Hz. The feedforward controller for acceleration tracking is designed by cascading the inverse model of Eq. (4.18) with first-order Butterworth lowpass filter with a cutoff frequency of 50 Hz.

Tracking performance results between the target and measured signals are evaluated next for displacement control and acceleration control mMBC RTHS schemes. The time histories of the reference and measurement signals are presented in Fig. 4.17 (a) and (c). Tracking is qualitatively assessed via the synchronization plots in Fig. 4.17 (b) and (d). This x-axis displays the target signal and y-axis refers to the measured output signal. Table 4.2 summarizes unitless $RMSE$ and $MAXE$ error indicators from Eqs. (3.21) and (3.22).

Table 4.2 Tracking performance for each control type

Control type	**Error index**	
	MAXE	*RMSE*
Displacement	0.1549	0.1587
Acceleration	0.3055	0.3432

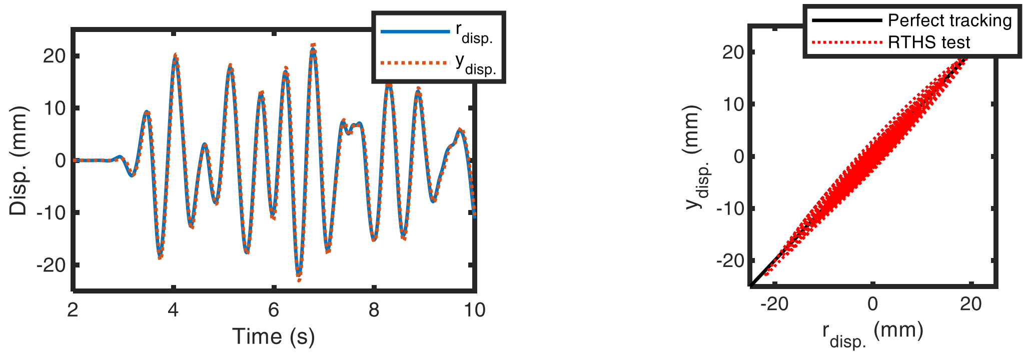

(a) Displacement control tracking (b) Displacement control synchronization

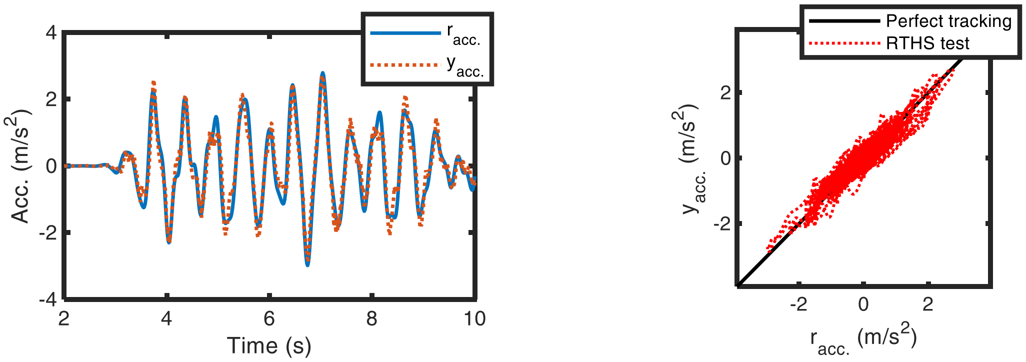

(c) Acceleration control tracking (d) Acceleration control synchronization

Figure 4.17 Tracking and synchronization plots of the proposed mMBC compensator

The performance and variations in the behavior of the two-story structure subject to a ground motion excitation are examined using both shake table testing and model-based RTHS in this section. The variables relevant to this study are the first and second story relative displacements and absolute accelerations. Particular attention is paid to the second story motions, as this floor formulates the boundary condition between the physical and numerical substructures.

Due to the nonlinear behavior of the actuator (i.e., shake table), variations exist in the performance of the RTHS experiments. Therefore 10 experiments are conducted for the evaluation of the displacement control RTHS and another 10 for the acceleration control RTHS. The RTHS experiments are next compared to the 10 shake table tests conducted earlier. Every shake table and RTHS experiment is cross evaluated using the RMSE criterion and the results are displayed in the RMSE bar charts in Fig. 4.18 and 4.19.

Experimental results are post-processed through synchronization and low and highpass filtering. In all experiments, the measured data are synchronized with their corresponding input ground motions. Since the ground motions are identical between all experiments, synchronization is conducted by matching the input ground motions. Next, measured data are post-processed with a second-order Butterworth lowpass filter with a cutoff frequency of 15 Hz, and a second-order Butterworth highpass filter with a cutoff frequency of 0.5 Hz.

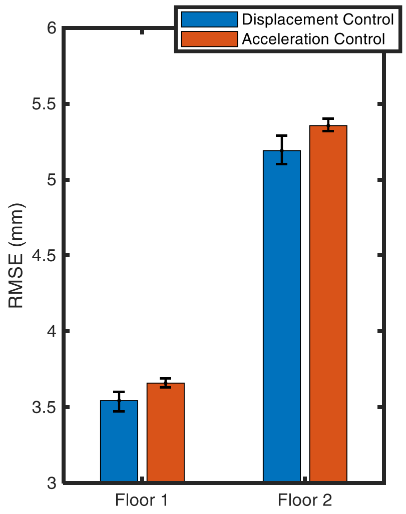

Figure 4.18 RMSE median and interquartile range for displacement results

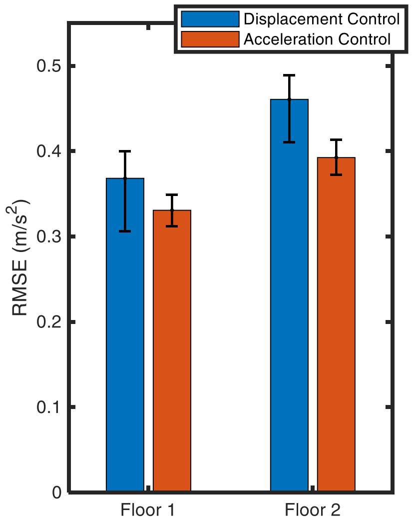

Figure 4.19 RMSE median and interquartile range for acceleration results

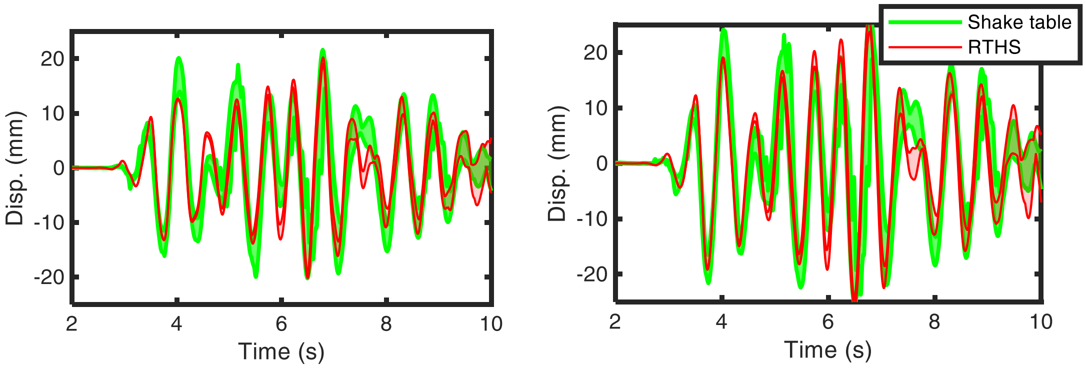

(a) First story displacement

(b) Second story displacement

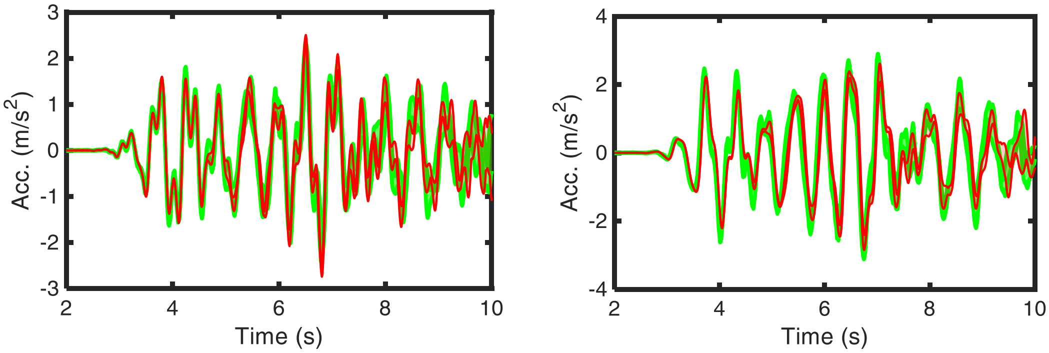

(c) First story acceleration

(d) Second story acceleration

Figure 4.20 Shake table and RTHS variational comparison – Displacement control

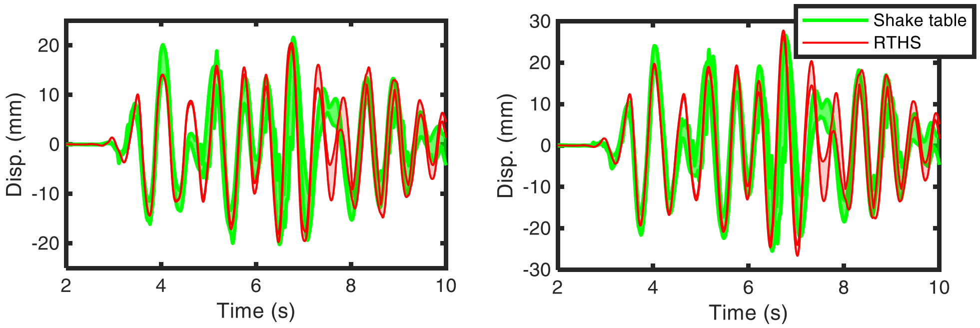

(a) First story displacement (b) Second story displacement

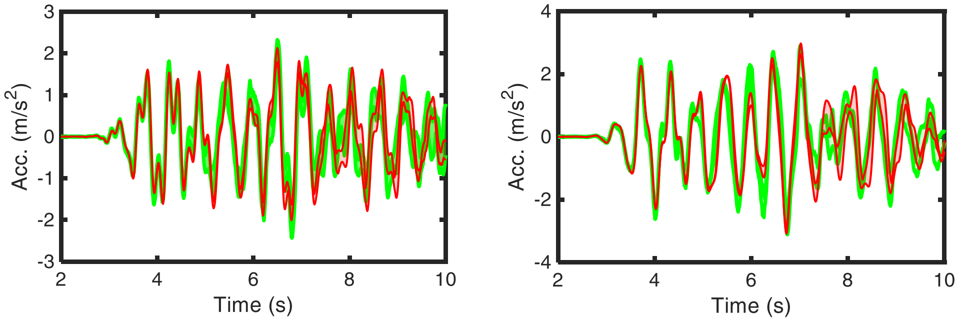

(c) First story acceleration (d) Second story acceleration

Figure 4.21 Shake table and RTHS variational comparison – Acceleration control

4.4 RTHS of bridge vibration mitigation using an MR damper

In general, high-speed railway bridges are expected to have a limited vibration performance, as excessive high frequency deflections may result in uncomfortable train rides for passengers, or even risk structural damage (Wang et al. 2003). Damping devices may be used for dissipation and vibration reduction. The major questions with damping devices are where and how to install them on existing and new bridges. In many bridges, the depth of the deck section is deep enough to create a large distance between the flange surface and neutral axis of the deck. In such bridges, installation of a diagonal damper between the abutment and the bottom flange of the deck can result in satisfactory damping performance, as a large neutral axis depth means noticeable horizontal movements in the bottom flange and engagement of the damping device.

A magnetorheological (MR) damper is a semi-active damping device comprised of a metal cylinder with a piston and rod, magnetorheological oil, an electromagnetic coil, and pressurized gas. As the piston rod is extended or retracted, the MR oil flows from one chamber of the cylinder to the other, across the damper piston. By applying an electric charge to the electromagnetic coil, the flow properties of the oil are across the piston are changed. In simple terms, with an increase in the current passing through the coil, the oil grows thicker, and thus the resistance of the flow across the piston increases. This is a useful property for a damper, as the friction characteristics of the damper may be altered in real-time for semi-active control purposes. In the study proposed in (Tell et al. 2019), an MR damper is used as a supplemental dissipation device for high-speed railway bridges. The RTHS method was selected for testing of the bridge-damper system, because real-time testing is necessary for understanding rate-dependent behaviors of dampers.

The model-based RTHS framework is applied for studying the behavior of a high-speed railway bridge with an added MR damper. The position of the MR damper is illustrated relative to the bridge deck in Fig. 4.22. In this study, the MR damper is physically substructured, and the bridge deck and train load are numerically modeled. A servo-hydraulic actuator and LVDT handle the boundary condition force-displacement.

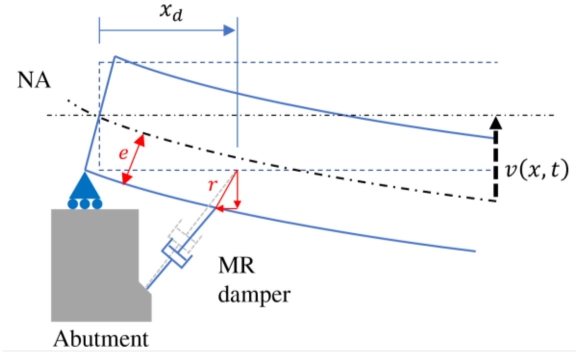

Figure 4.22 Simply supported bridge deck and damping device

A simply supported bridge deck is modeled with an Euler-Lagrange assumption. The governing equations of the system are modeled per

$$\frac{d}{dt}\frac{\partial \mathcal{T}}{\partial \dot{q}_i} - \frac{\partial \mathcal{T}}{\partial q_i} + \frac{\partial \mathcal{V}}{\partial q_i} = f_i(t) \tag{4.19}$$

where $\mathcal{T}$ and $\mathcal{V}$ are the kinetic and potential energy relationships (Craig and Kurdila 2006). q_i is the i^{th} generalized coordinate and f_i is the i^{th} generalized force. By assuming the general shape of the bridge modes, the transverse deflection of the deck is expressed as

$$v(x,t) = \sum_{i=1}^{N} \psi_i(x) q_i(t) \tag{4.20}$$

where ψ_i is the assumed i^{th} mode shape and N is the total number of modes considered. The equation of motion of the bridge deck using the assumed mode method simplifies to

$$\boldsymbol{M}\ddot{\boldsymbol{q}}(t) + \boldsymbol{C}\dot{\boldsymbol{q}}(t) + \boldsymbol{K}\boldsymbol{q}(t) = \boldsymbol{F}(t) \tag{4.21}$$

with $\boldsymbol{M} \in \mathcal{R}^{N\times N}$, $\boldsymbol{C} \in \mathcal{R}^{N\times N}$, and $\boldsymbol{K} \in \mathcal{R}^{N\times N}$ as the mass, damping, and stiffness matrices, and $\boldsymbol{F}(t) \in \mathcal{R}^{N}$ containing the external forces.

4.4.1 Real-time substructuring

The physical and numerical substructures are depicted in Fig. 4.23. As a highspeed train with a velocity of V passes over the bridge deck, a dynamic force of $\boldsymbol{F}(t)$ is exerted. The deformation of the bridge deck results in extension and retraction (stroke) of the MR damper rod. The stroke is computed as $r(t)$, and sent to the model-based compensator. The compensator sends a control signal $u(t)$ to servo-hydraulic actuator for execution. The LVDT onboard the hydraulic actuator records the measured stroke and reports back to the compensator for feedback action. The measured experimental force $F_R(t)$ is returned to the numerical substructure for a closed-loop RTHS.

The experimental setup is comprised of a double-ended servo-hydraulic actuator with load and stroke capacities of 556 kN and $\pm$ 152.4 mm. The hydraulic power supply is rated at 1000 psi in both directions. The actuator houses an onboard LVDT, a 445 kN-rated loadcell, and is supported by several rigid brackets to ensure accurate displacement measurement.

The servo-hydraulic actuator is operated with a Shore Western analog controller. The embedded system is comprised of a dSPACE DS1103PPC control board with onboard memory and processing of 1 GHz, input-output peripherals with 16-bit resolution, and the ControlDesk graphical user interface. Numerical models and compensation algorithms are developed on MATLAB/SIMULINK and converted into C source code for compilation on the dSPACE controller. A Topward 3303D power supply unit is used to command static voltage to the MR damper. Figure 4.24 provides a schematic of the experimental hardware.

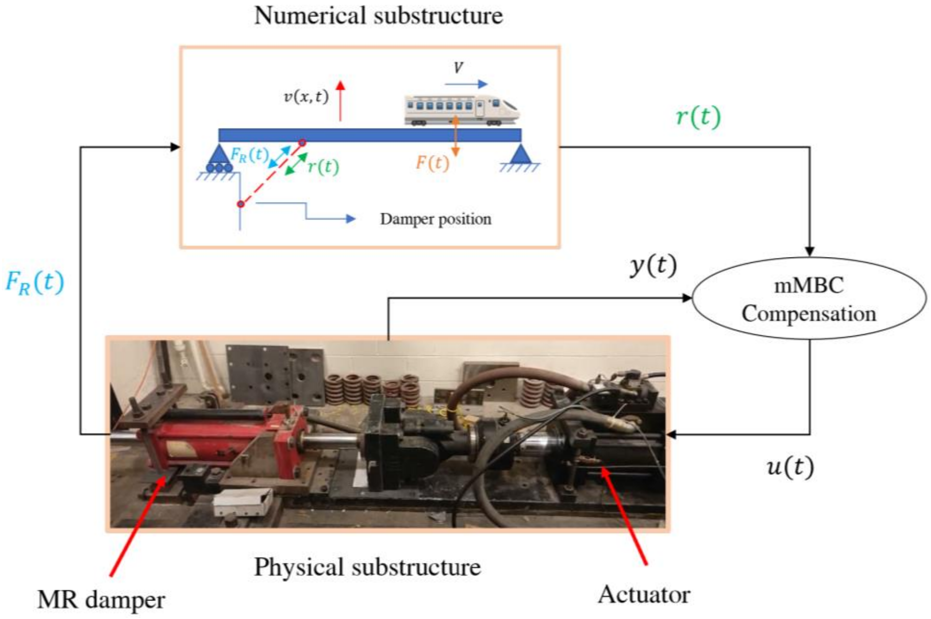

Figure 4.23 Model-based RTHS for rail-way bridge

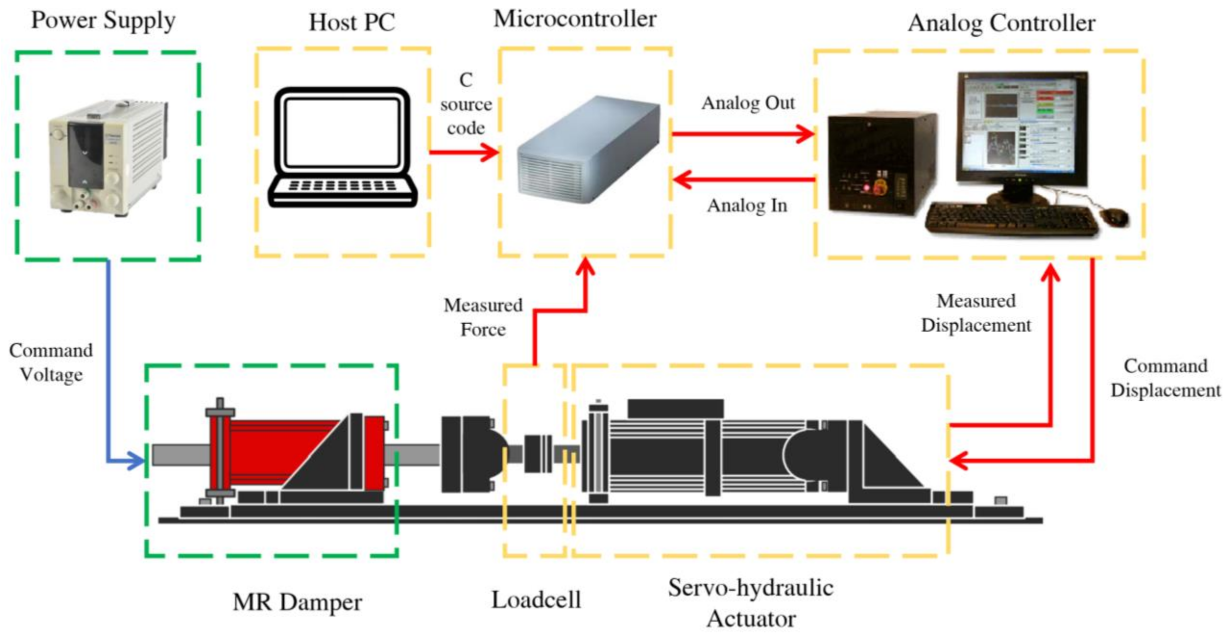

Figure 4.24 Experimental hardware and communication signals

4.4.2 System identification and tracking results

System identification of the actuator-MR damper setup is next conducted to develop a linearized nominal actuator model for use in the mMBC compensator. A bandlimited white noise with a frequency of 0 – 40 Hz ad RMS amplitudes of 0.1 V and 0.15 V are applied to the actuator. The current supply to the MR damper is also varied between 0 A to 2 A. The FRF between the reference and measured signals are displayed in Figure 4.25.

A 6-pole transfer function model of the actuator system is identified and used for the mMBC compensator:

$$\boldsymbol{P}(s) = \frac{y(s)}{r(s)} = \frac{2.414e13}{s^6 + 306.7s^5 + 1.495e5s^4 + 2.922e7s^3 + 5.429e9s^2 + 5.055e11s + 2.53e13} \tag{4.22}$$

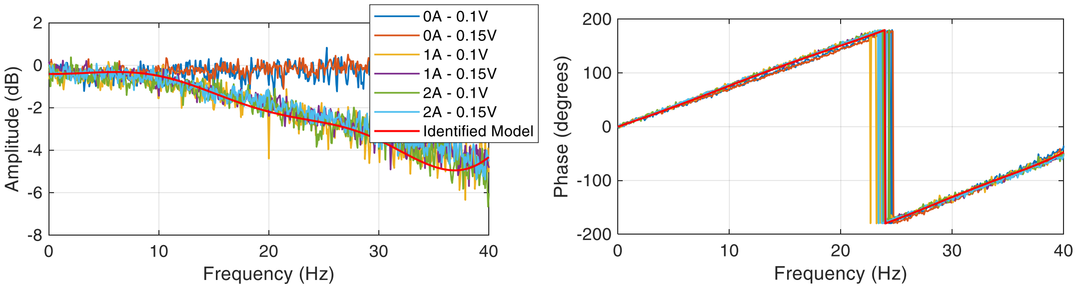

(a) Amplitude (b) Phase

Figure 4.25 Experimental FRF and identified nominal actuator model

For perfect displacement tracking between reference and measured signals, a 0 dB amplitude and 0 degree phase are desired. However, this is unachievable due to physical realities of actuation. The proposed mMBC algorithm reduces the phase slope (delay) and improves the amplitude tracking as demonstrated in Figure 4.26. Delay reduction results in less negative damping and a more stable and accurate RTHS (Horiuchi et al. 1996). Fig. 4.27 displays the hysteretic behavior of the MR damper subjected to a sinusoidal deformation.

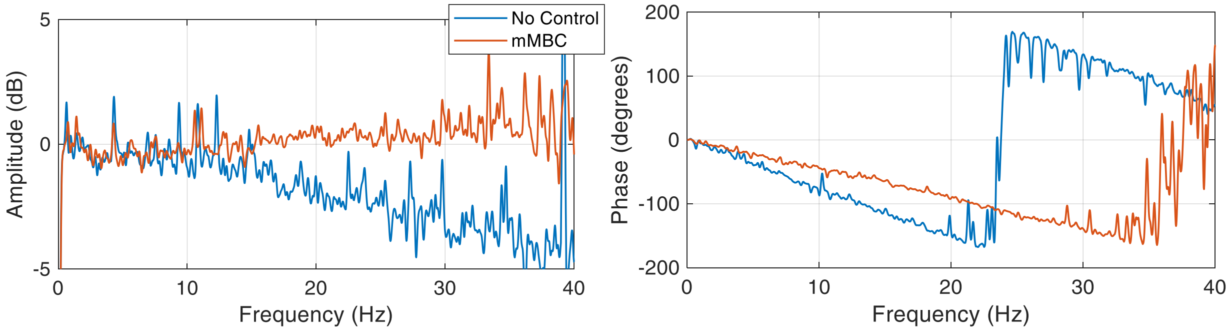

(a) amplitude (b) phase

Figure 4.26 Frequency response function with and without mMBC control

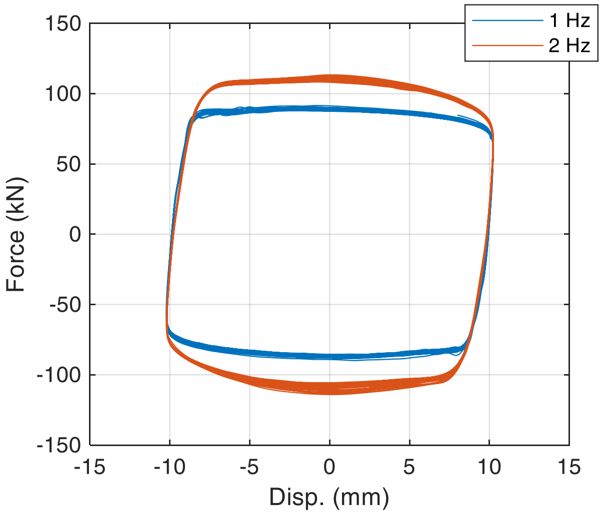

Figure 4.27 Sinusoidal hysteretic behavior of the MR damper

4.4.3 Vibration mitigation results

The Banafjäl bridge in Sweden is considered in this study. A finite element model of the bridge is developed as part of the numerical substructure of the experiment. The train loading applied on the bridge is based on the Eurocode High-Speed Load Models (HSLM). The HSLM-A4 is selected for simulation of a moving train load. The response of the bridge is considered for varying train velocities and current levels in the MR damper. Fig. 4.28 illustrates the maximum acceleration and displacements in the bridge, A_{max}

and D_{max}, as a function of the train velocity. As the current level is increased, the damping action in the MR damper becomes more rigorous. Therefore, a significant reduction is observed at the resonance speed of the bridge structure. Fig. 4.29 and 4.30 demonstrate the bridge performance for a train traveling at a velocity of 169 km/hr with an MR damper with current levels of 0.0 A and 2.0 A.

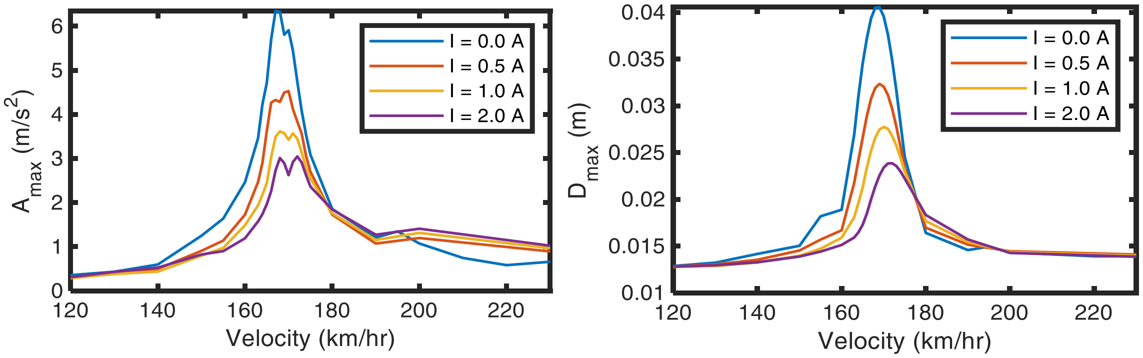

(a) Acceleration performance (b) Displacement performance

Figure 4.28 Maximum bridge acceleration and displacement as a function of train velocity

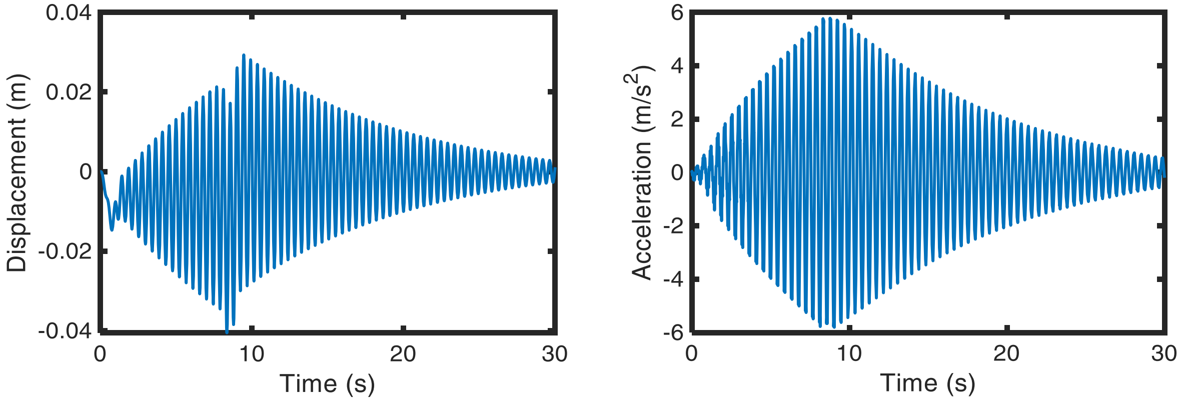

(a) Acceleration performance (b) Displacement performance

Figure 4.29 Mid-span bridge response with $I = 0.0\ A$ and $Velocity = 169\ km/hr$

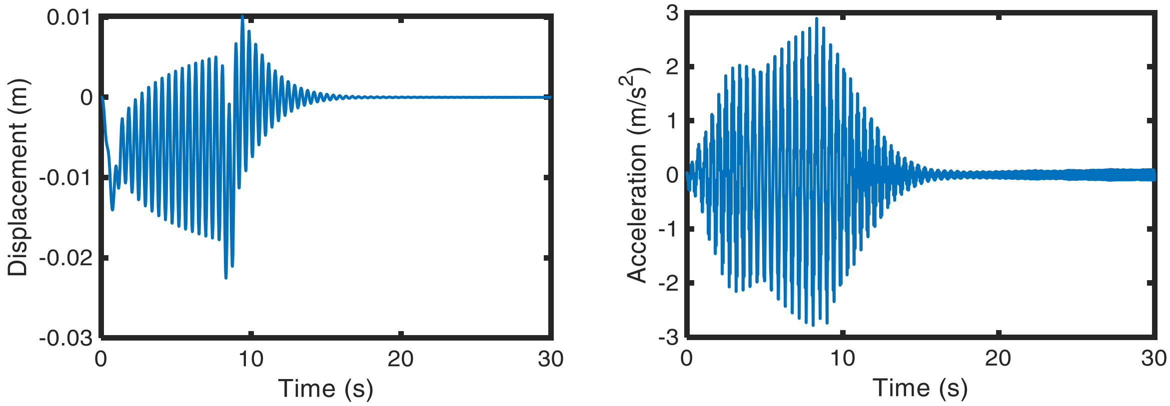

(a) Acceleration performance (b) Displacement performance

Figure 4.30 Mid-span bridge response with $I = 2.0\ A$ and Velocity $= 169\ km/hr$

4.5 Virtual RTHS with Adaptive Compensation

A virtual RTHS study is completed using the benchmark control problem for RTHS of the three-story steel frame defined in (Silva et al. 2020). The objective of the benchmark problem is to gather control techniques developed in the RTHS domain, for comparison and provide valuable lessons for future developments. The benchmark problem poses a three-story structure, which is seismically excited and evaluated using the RTHS technique. In this framework, a first-story moment frame is experimentally evaluated as the rest of the structure is numerically simulated. The physical component is attached to a hydraulic actuator and the combined transfer function is presented per

$$\boldsymbol{P}(s) = \frac{2.13e13}{29.12s^5 + 1.26e4s^4 + 8.42e6s^3 + 2.33e9s^2 + 5.44e11s + 2.17e13} \tag{4.23}$$

with $\boldsymbol{P}(s)$ as a 5-pole plant. For some control signal in Laplace domain $U(s)$, an output signal of $Y(s)$ is obtained. The plant is perturbed with a time-varying nonlinear signal $d(t) = f\big(t, y(t)\big)$, which contains all uncertainties and disturbances. The disturbance signal $D(s)$ is assumed to be continuous and bounded. The disturbance is assumed to be additive for the purpose of control design per below

$$Y(s) = \boldsymbol{P}(s)\big(U(s) + \mathrm{D}(s)\big) \tag{4.24}$$

A controller is next used to cancel out the unwanted dynamics due to actuator-structure interaction. In this analysis, three compensation techniques are studied: (i) PI control with a phase-lead compensator, (ii) MBC, and (iii) aMRC. The performances of these controllers are presented in terms of the evaluations criteria presented as part of the benchmark control problem.

4.5.1 Summary of the benchmark problem

The three-story steel frame reference structure in Fig. 4.31 is partitioned into numerical and physical substructures and evaluated with the RTHS technique. The new equation of motion for the three-story frame is presented below

$$\boldsymbol{M}_n\ddot{\boldsymbol{x}}_n(t) + \boldsymbol{C}_n\dot{\boldsymbol{x}}_n(t) + \boldsymbol{K}_n\boldsymbol{x}_n(t) = -\boldsymbol{M}_r\boldsymbol{\iota}\ddot{\boldsymbol{x}}_g(t) - \big(\boldsymbol{M}_p\ddot{\boldsymbol{x}}_p(t) + \boldsymbol{C}_p\dot{\boldsymbol{x}}_p(t) + \boldsymbol{K}_p\boldsymbol{x}_p(t)\big) \tag{4.24}$$

where $\boldsymbol{M}_n$, $\boldsymbol{C}_n$, and $\boldsymbol{K}_n$ are the numerical and $\boldsymbol{M}_p$, $\boldsymbol{C}_p$, and $\boldsymbol{K}_p$ are the physical mass, damping, and stiffness matrices. The states $\boldsymbol{x}_n(t)$ and $\boldsymbol{x}_p(t)$ belong to the numerical and physical substructures and M_r is the reference mass of the complete frame.

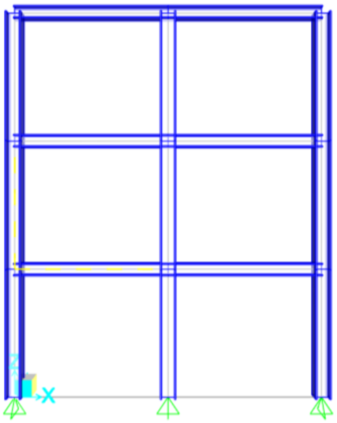

Figure 4.31 Three-story steel frame reference structure

To investigate the performance of the RTHS substructures, four variations on the substructuring configurations are considered. These configurations vary the choice of the reference floor mass and modal damping values. In addition to the nominal plant, several actuator and stiffness parameters are evaluated probabilistically to simulate modeling uncertainties and referred to as perturbation cases. Details on the substructuring configurations and perturbation cases are demonstrated in Fig. 4.32.

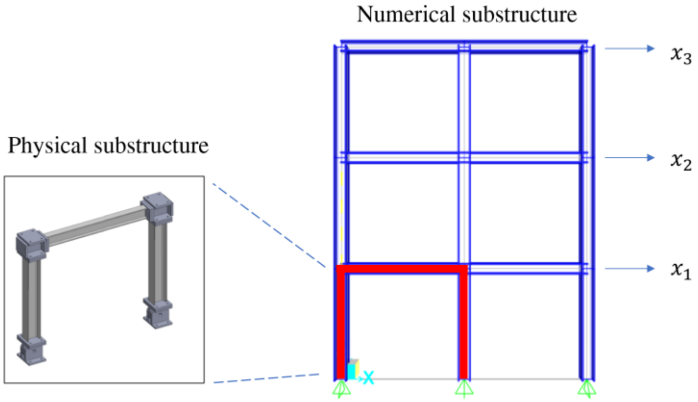

Figure 4.32 Substructuring of the three-story steel frame

4.5.2 Evaluation criteria

Per the companion paper, nine quantitative evaluation criteria are concerned to assess the performance of the proposed aMRC algorithm. Criteria $J_1 - J_3$ evaluate the input-output tracking ability of the controllers and $J_4 - J_9$ evaluate the performance accuracy of the RTHS relative to the reference structure.

As a brief summary, J_1 assesses the time delay (ms) between reference and measurement signals. J_2 evaluates the tracking error via the normalized root-mean-square (RMS). J_3 is a normalized peak tracking error measure. Next, $J_4 - J_6$ are the normalized RMS errors between the reference structure and substructured system floor displacements. Lastly, $J_7 - J_9$ are the normalized peak tracking errors between the reference structure and substructured system floor displacements. These criteria are evaluated for the three controllers described.

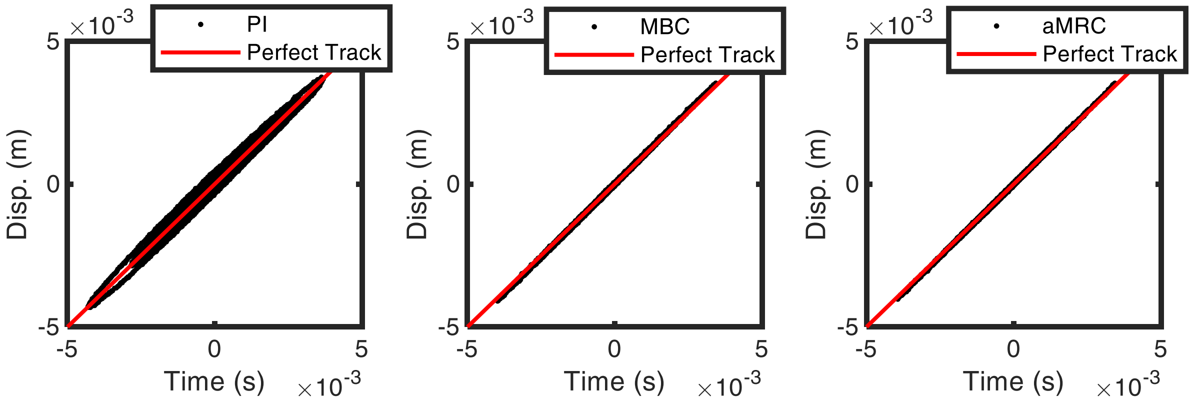

(a) PI + Phase-lead (b) MBC (c) aMRC

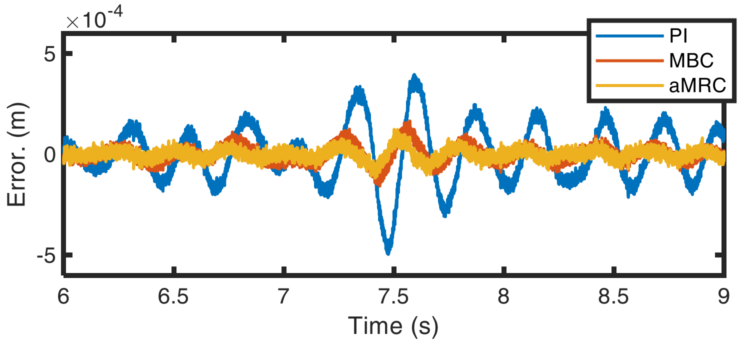

(d) Errors

Figure 4.33 Partition configuration 4: Control input-output tracking for the nominal plant

4.5.3 Virtual RTHS results

Next, the responses of the virtual RTHS and reference system simulations are compared and analyzed. For each controller, time histories of the floor displacements are visually inspected, and qualitative assessment is provided. The evaluation criteria are presented along with the performance of the controllers for each criterion.

Fig. 4.33 illustrates the tracking abilities for each controller along with the input-output errors. The phase-lead compensator feature of the PI controller amplifies high frequency contents, resulting in a noisy measurement. This controller demonstrates the largest steady-state error. Incorporation of the model-based filters into the RTHS, have resulted in enhanced tracking performance. The MBC has improved tracking relative to the PI compensator. The aMRC demonstrates the fastest tracking ability with the smallest noise feed-through. The choice of adaptive gain and cutoff frequency for reference model vary the tracking performance of the aMRC. A unity-gain zero-phase reference model is selected for the most rigorous feedback action in this case.

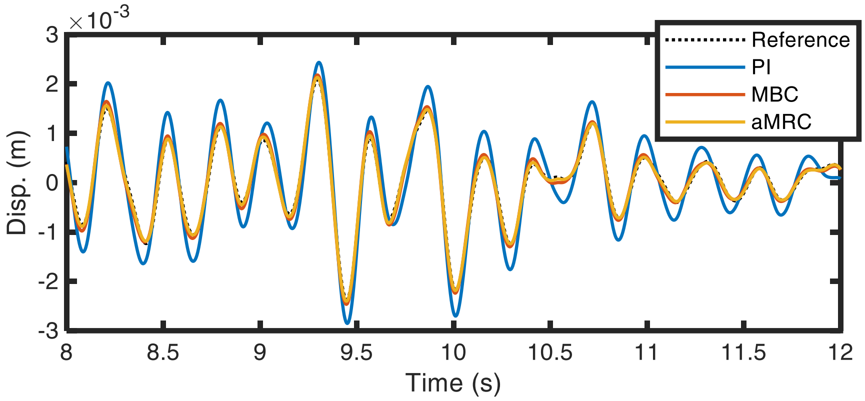

(a) Floor 1

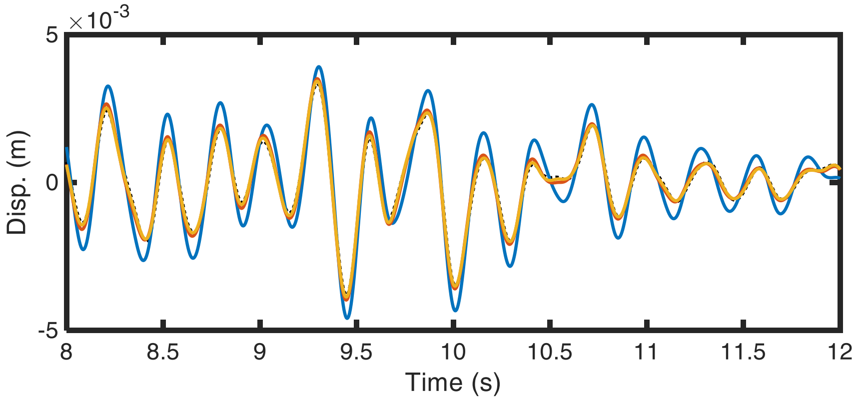

(b) Floor 2

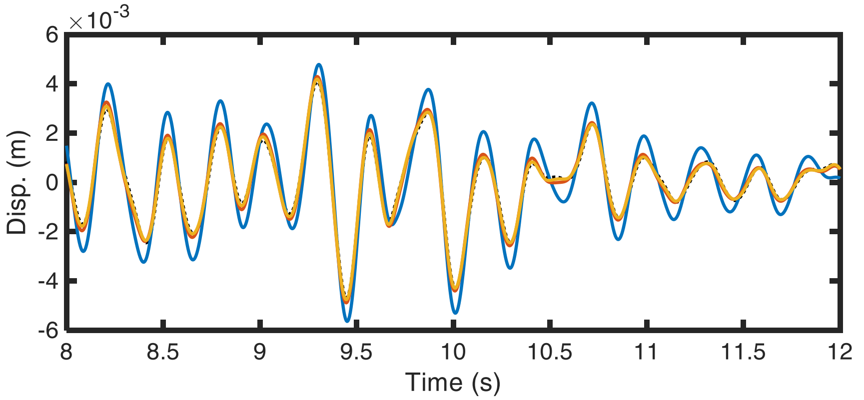

(c) Floor 3

Figure 4.34 Partition configuration 4: RTHS vs. reference displacements for the nominal plant

Fig. 4.34 compares the RTHS performance relative to the reference structure for each controller. Due to the larger phase lag produced by the PI technique, RTHS results have an inherent overshoot and produce larger displacement envelopes relative to the reference model. The aMRC however, closely tracks the reference behavior. The performance of the aMRC for configurations 1 – 3 is shown Fig. 4.35 – 4.37. The proposed controller demonstrates excellent tracking between the reference and RTHS formulations for all four configurations.

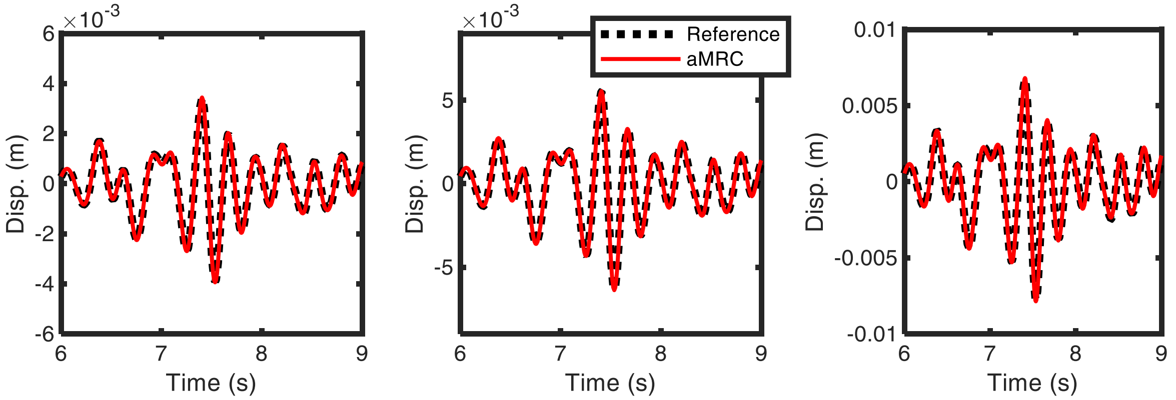

(a) Floor 1 (b) Floor 2 (c) Floor 3

Figure 4.35 Partition Configuration 1: RTHS vs. reference tracking for the nominal plant

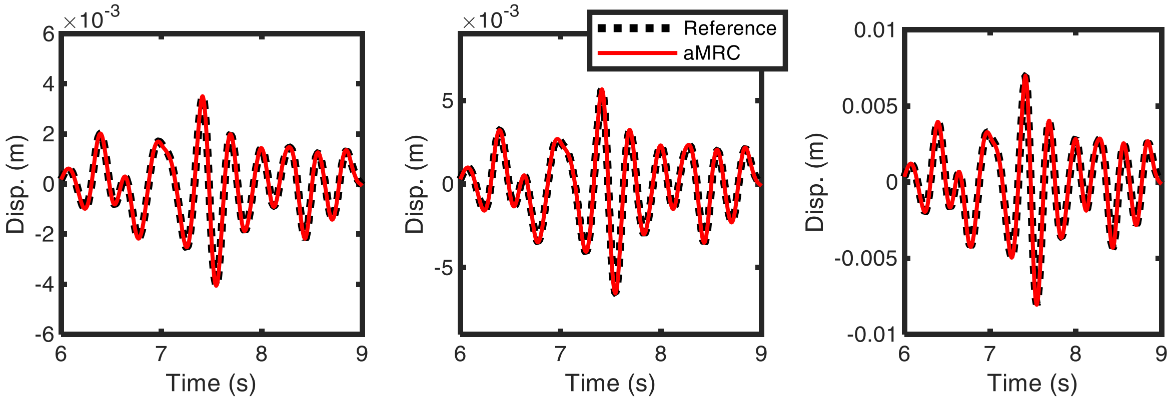

(a) Floor 1 (b) Floor 2 (c) Floor 3

Figure 4.36 Partition Configuration 2: RTHS vs. reference tracking for the nominal plant

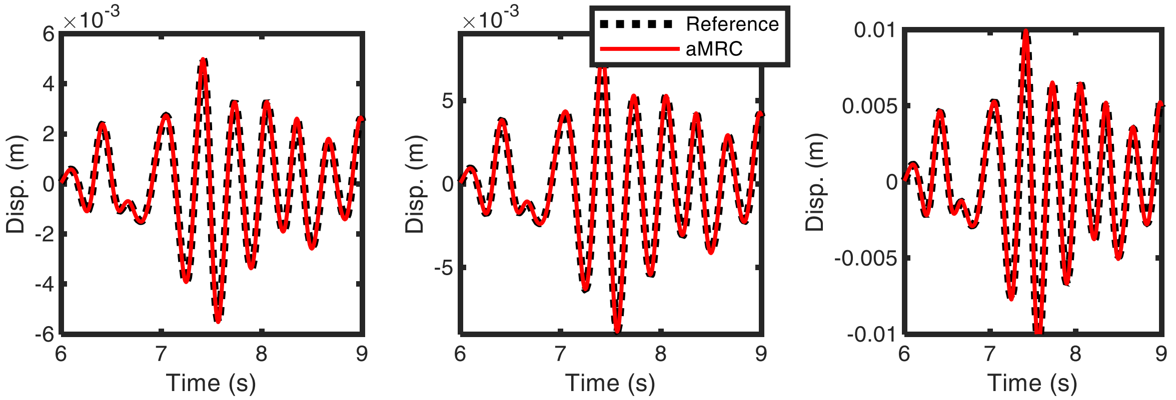

(a) Floor 1 (b) Floor 2 (c) Floor 3

Figure 4.37 Partition Configuration 3: RTHS vs. reference tracking for the nominal plant

The aMRC is shown in action in Fig. 4.38. The behavior of the adaptive parameter is demonstrated when the plant is perturbed. The adaptive action grows proportional to the steady-state error. For example, steady-state errors tend to be largest at peak displacement amplitudes and the adaptive parameter is amplified as well.

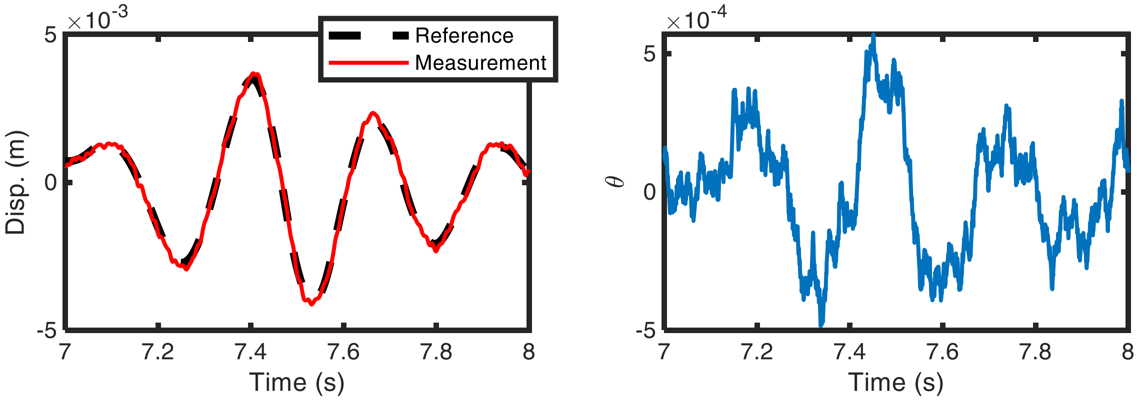

(a) Reference tracking (b) Adaptive parameter

Figure 4.38 Adaptive parameter for the perturbed configuration

Fig. 4.39 provides a visual illustration of the evaluation criteria introduced earlier. Tables 4.3 – 4.5 list the numerical values associated with the nine evaluation criteria. Table 4.2 provides a more direct comparison of the evaluation criteria for the partition configuration 1. From these results, the aMRC compensation offers the best tracking performance. The adaptation mechanism is quick in canceling out steady-state errors caused by modeling uncertainties. When the aMRC is used, there are no major increases in the evaluation criteria errors when perturbations are added to the plant. The PI and MBC controllers experience increased error quantities when the plant is perturbed, however. The aMRC method enhances tracking even in the presence of modeling uncertainties or perturbations, and therefore illustrates the best tracking robustness.

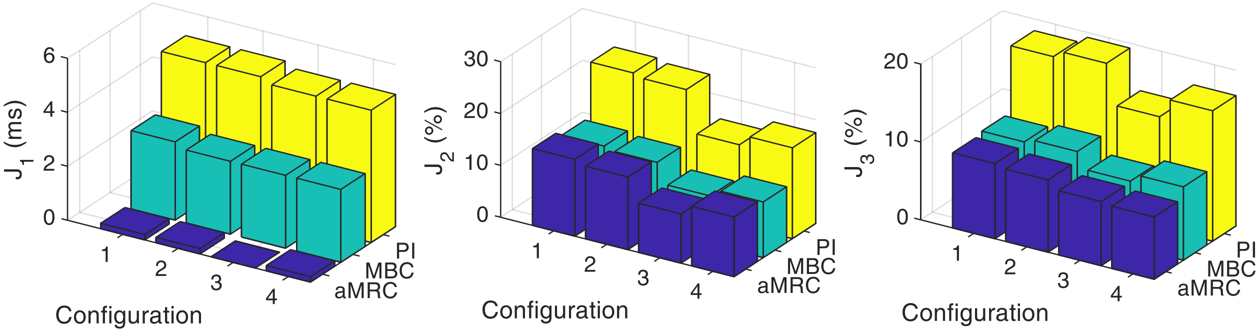

(a) J_1 (b) J_2 (c) J_3

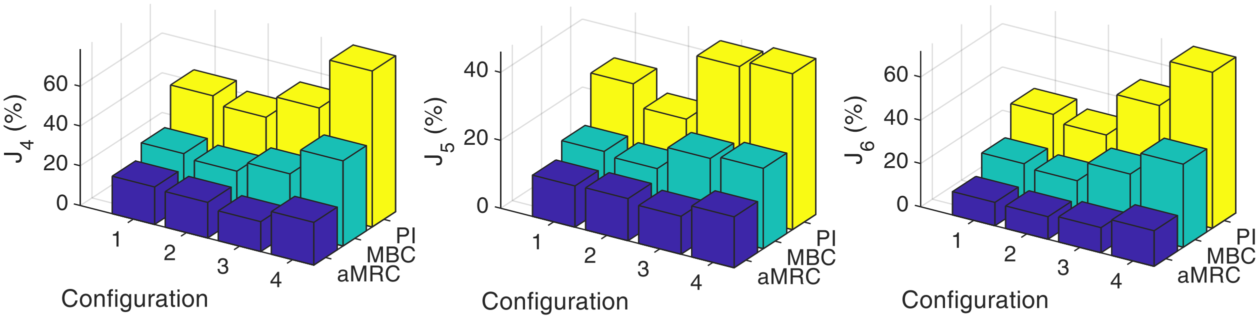

(a) J_4 (b) J_5 (c) J_6

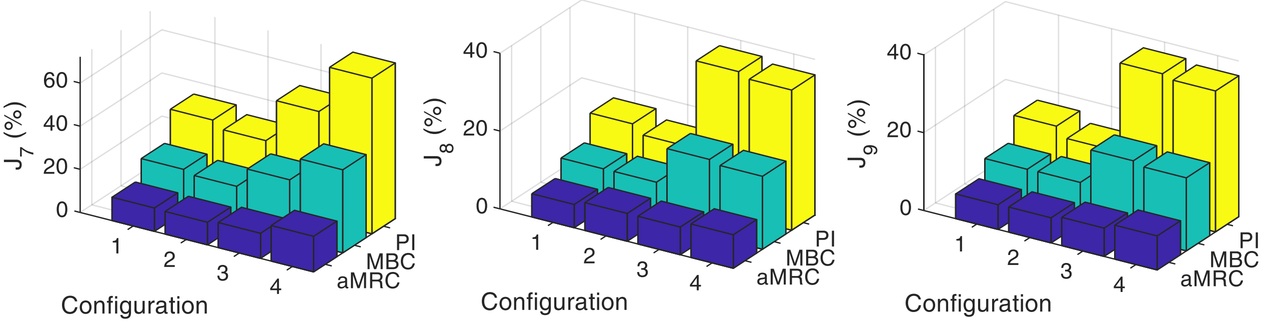

(a) J_7 (b) J_8 (c) J_9

Figure 4.39 Evaluation Criteria

Table 4.3 Partition configuration 1: evaluation criteria for nominal case

	Controller		
Evaluation Criteria	PI	MBC	aMRC
J_1	4.6	0.7	0
J_2	10.38	3.9	3.23
J_3	11.54	4.17	3.17
J_4	36.08	9.68	5.98
J_5	19.01	6.01	4.81
J_6	32.26	8.09	4.21
J_7	32.38	8.12	4.23
J_8	14.85	4.23	2.27
J_9	14.78	4.22	2.31

Table 4.4 PI evaluation criteria

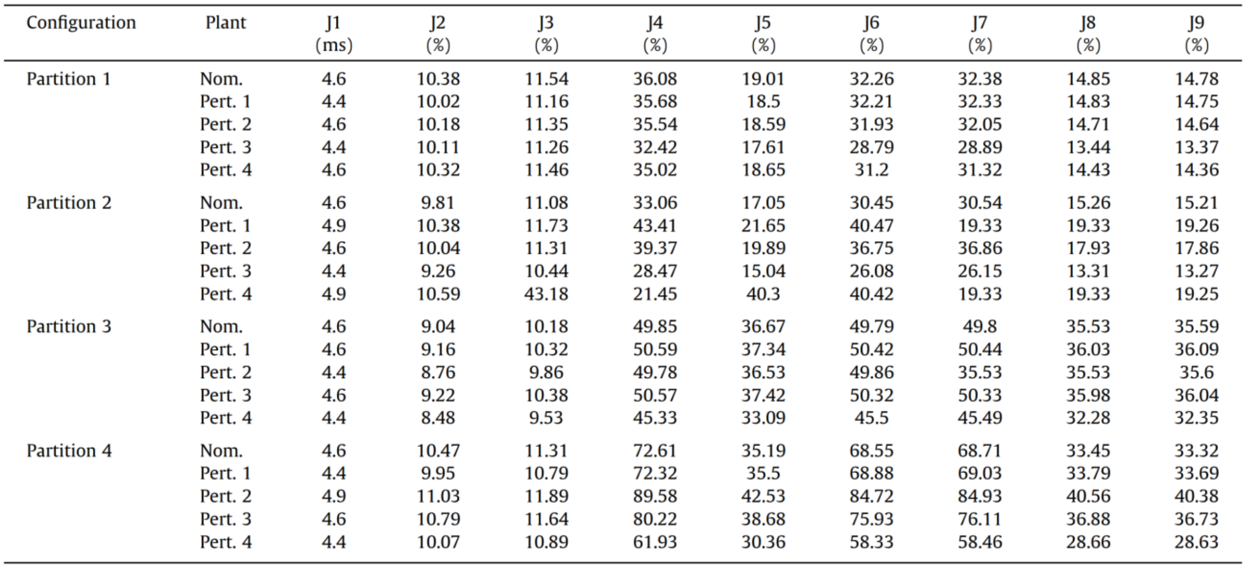

Configuration	Plant	J1 (ms)	J2 (%)	J3 (%)	J4 (%)	J5 (%)	J6 (%)	J7 (%)	J8 (%)	J9 (%)
Partition 1	Nom.	4.6	10.38	11.54	36.08	19.01	32.26	32.38	14.85	14.78
	Pert. 1	4.4	10.02	11.16	35.68	18.5	32.21	32.33	14.83	14.75
	Pert. 2	4.6	10.18	11.35	35.54	18.59	31.93	32.05	14.71	14.64
	Pert. 3	4.4	10.11	11.26	32.42	17.61	28.79	28.89	13.44	13.37
	Pert. 4	4.6	10.32	11.46	35.02	18.65	31.2	31.32	14.43	14.36
Partition 2	Nom.	4.6	9.81	11.08	33.06	17.05	30.45	30.54	15.26	15.21
	Pert. 1	4.9	10.38	11.73	43.41	21.65	40.47	19.33	19.33	19.26
	Pert. 2	4.6	10.04	11.31	39.37	19.89	36.75	36.86	17.93	17.86
	Pert. 3	4.4	9.26	10.44	28.47	15.04	26.08	26.15	13.31	13.27
	Pert. 4	4.9	10.59	43.18	21.45	40.3	40.42	19.33	19.33	19.25
Partition 3	Nom.	4.6	9.04	10.18	49.85	36.67	49.79	49.8	35.53	35.59
	Pert. 1	4.6	9.16	10.32	50.59	37.34	50.42	50.44	36.03	36.09
	Pert. 2	4.4	8.76	9.86	49.78	36.53	49.86	35.53	35.53	35.6
	Pert. 3	4.6	9.22	10.38	50.57	37.42	50.32	50.33	35.98	36.04
	Pert. 4	4.4	8.48	9.53	45.33	33.09	45.5	45.49	32.28	32.35
Partition 4	Nom.	4.6	10.47	11.31	72.61	35.19	68.55	68.71	33.45	33.32
	Pert. 1	4.4	9.95	10.79	72.32	35.5	68.88	69.03	33.79	33.69
	Pert. 2	4.9	11.03	11.89	89.58	42.53	84.72	84.93	40.56	40.38
	Pert. 3	4.6	10.79	11.64	80.22	38.68	75.93	76.11	36.88	36.73
	Pert. 4	4.4	10.07	10.89	61.93	30.36	58.33	58.46	28.66	28.63

Table 4.5 MBC evaluation criteria

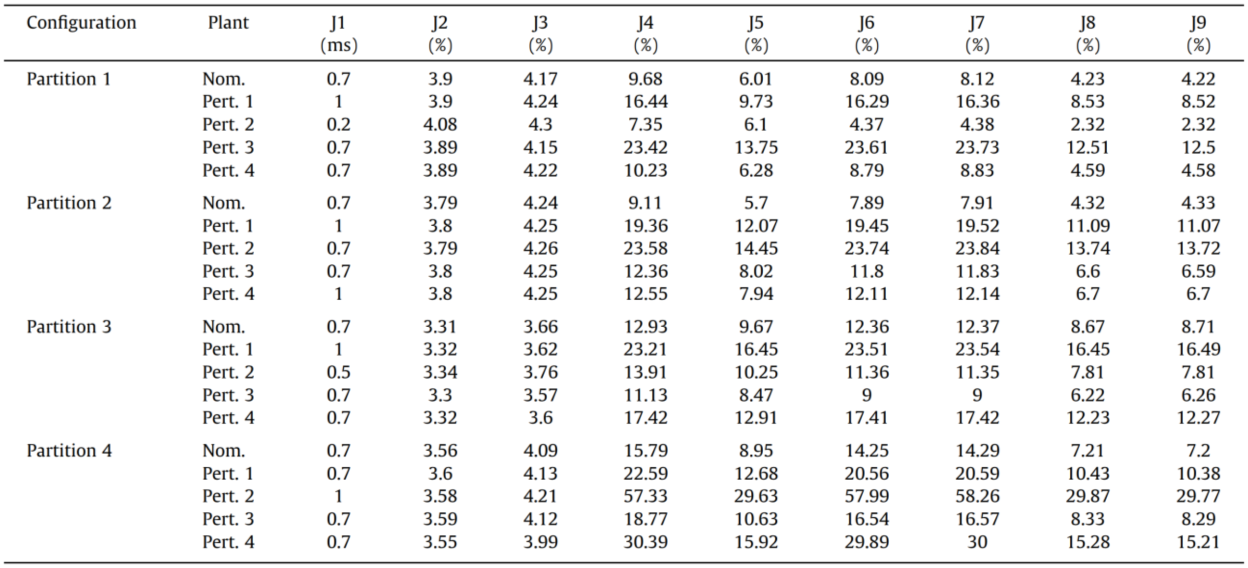

Configuration	Plant	J1 (ms)	J2 (%)	J3 (%)	J4 (%)	J5 (%)	J6 (%)	J7 (%)	J8 (%)	J9 (%)
Partition 1	Nom.	0.7	3.9	4.17	9.68	6.01	8.09	8.12	4.23	4.22
	Pert. 1	1	3.9	4.24	16.44	9.73	16.29	16.36	8.53	8.52
	Pert. 2	0.2	4.08	4.3	7.35	6.1	4.37	4.38	2.32	2.32
	Pert. 3	0.7	3.89	4.15	23.42	13.75	23.61	23.73	12.51	12.5
	Pert. 4	0.7	3.89	4.22	10.23	6.28	8.79	8.83	4.59	4.58
Partition 2	Nom.	0.7	3.79	4.24	9.11	5.7	7.89	7.91	4.32	4.33
	Pert. 1	1	3.8	4.25	19.36	12.07	19.45	19.52	11.09	11.07
	Pert. 2	0.7	3.79	4.26	23.58	14.45	23.74	23.84	13.74	13.72
	Pert. 3	0.7	3.8	4.25	12.36	8.02	11.8	11.83	6.6	6.59
	Pert. 4	1	3.8	4.25	12.55	7.94	12.11	12.14	6.7	6.7
Partition 3	Nom.	0.7	3.31	3.66	12.93	9.67	12.36	12.37	8.67	8.71
	Pert. 1	1	3.32	3.62	23.21	16.45	23.51	23.54	16.45	16.49
	Pert. 2	0.5	3.34	3.76	13.91	10.25	11.36	11.35	7.81	7.81
	Pert. 3	0.7	3.3	3.57	11.13	8.47	9	9	6.22	6.26
	Pert. 4	0.7	3.32	3.6	17.42	12.91	17.41	17.42	12.23	12.27
Partition 4	Nom.	0.7	3.56	4.09	15.79	8.95	14.25	14.29	7.21	7.2
	Pert. 1	0.7	3.6	4.13	22.59	12.68	20.56	20.59	10.43	10.38
	Pert. 2	1	3.58	4.21	57.33	29.63	57.99	58.26	29.87	29.77
	Pert. 3	0.7	3.59	4.12	18.77	10.63	16.54	16.57	8.33	8.29
	Pert. 4	0.7	3.55	3.99	30.39	15.92	29.89	30	15.28	15.21

Table 4.6 aMRC evaluation criteria

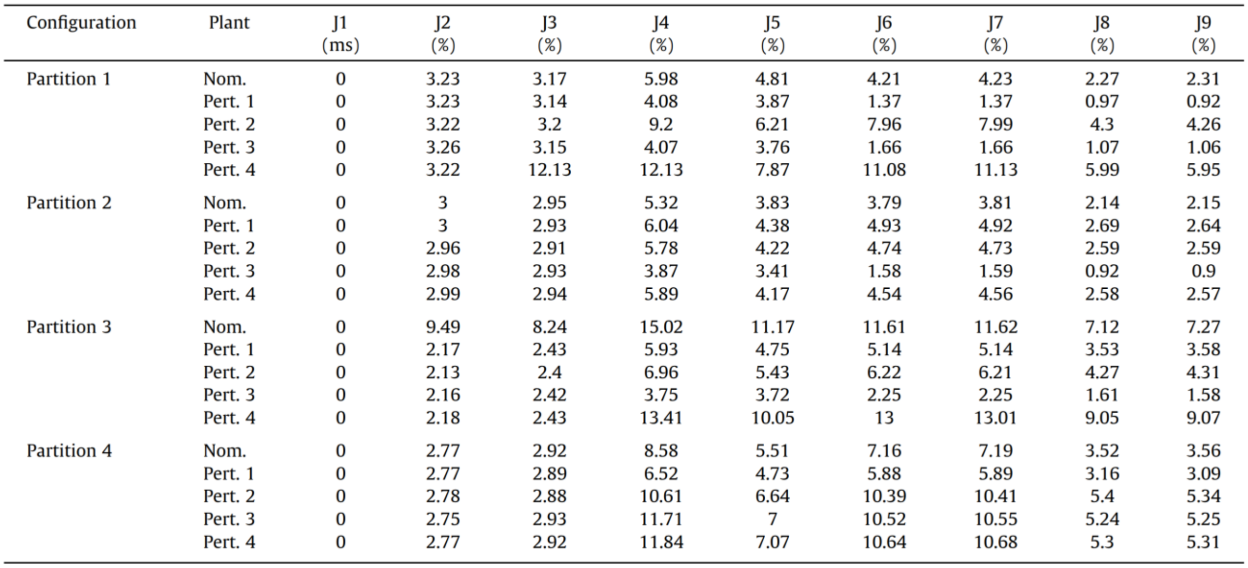

Configuration	Plant	J1 (ms)	J2 (%)	J3 (%)	J4 (%)	J5 (%)	J6 (%)	J7 (%)	J8 (%)	J9 (%)
Partition 1	Nom.	0	3.23	3.17	5.98	4.81	4.21	4.23	2.27	2.31
	Pert. 1	0	3.23	3.14	4.08	3.87	1.37	1.37	0.97	0.92
	Pert. 2	0	3.22	3.2	9.2	6.21	7.96	7.99	4.3	4.26
	Pert. 3	0	3.26	3.15	4.07	3.76	1.66	1.66	1.07	1.06
	Pert. 4	0	3.22	12.13	12.13	7.87	11.08	11.13	5.99	5.95
Partition 2	Nom.	0	3	2.95	5.32	3.83	3.79	3.81	2.14	2.15
	Pert. 1	0	3	2.93	6.04	4.38	4.93	4.92	2.69	2.64
	Pert. 2	0	2.96	2.91	5.78	4.22	4.74	4.73	2.59	2.59
	Pert. 3	0	2.98	2.93	3.87	3.41	1.58	1.59	0.92	0.9
	Pert. 4	0	2.99	2.94	5.89	4.17	4.54	4.56	2.58	2.57
Partition 3	Nom.	0	9.49	8.24	15.02	11.17	11.61	11.62	7.12	7.27
	Pert. 1	0	2.17	2.43	5.93	4.75	5.14	5.14	3.53	3.58
	Pert. 2	0	2.13	2.4	6.96	5.43	6.22	6.21	4.27	4.31
	Pert. 3	0	2.16	2.42	3.75	3.72	2.25	2.25	1.61	1.58
	Pert. 4	0	2.18	2.43	13.41	10.05	13	13.01	9.05	9.07
Partition 4	Nom.	0	2.77	2.92	8.58	5.51	7.16	7.19	3.52	3.56
	Pert. 1	0	2.77	2.89	6.52	4.73	5.88	5.89	3.16	3.09
	Pert. 2	0	2.78	2.88	10.61	6.64	10.39	10.41	5.4	5.34
	Pert. 3	0	2.75	2.93	11.71	7	10.52	10.55	5.24	5.25
	Pert. 4	0	2.77	2.92	11.84	7.07	10.64	10.68	5.3	5.31

4.6 Summary

This chapter introduced a single-axis model-based real-time hybrid simulation (RTHS) framework. Concepts of numerical and physical substructuring and boundary condition were discussed along with two types of tracking compensators: displacement and acceleration. The modified Model-Based Controller (mMBC) and adaptive Model Reference Controller (aMRC) were proposed for compensation action of actuator-structure dynamics. Three applications for single-axis model-based RTHS were presented:

1. Lightly-damped and highly-nonlinear structures
2. Vibration mitigation of high-speed railway bridges
3. Virtual RTHS for a control benchmark problem

When the reference signal from the numerical substructure is a displacement signal, both the mMBC and aMRC are applicable for compensation action. When the reference signal is acceleration, only the mMBC is applicable, as the aMRC for acceleration tracking can result in large actuator strokes. Results demonstrate the successful application of the model-based RTHS method in accurately reproducing the behavior of a reference structure.

CHAPTER 5 MULTI-AXIAL REAL-TIME HYBRID SIMULATION

5.1 Problem Statement

In this chapter, a multi-axial RTHS (maRTHS) framework is introduced for realistic and three-dimensional assessment of structural performance under dynamic loading. The framework is comprised of numerical and physical substructures, along with kinematic transformation layers and an actuator compensation scheme based on the mMBC. At each time step, the target motion of the boundary interface is calculated by the numerical substructure and enforced via an boundary condition device. When the physical specimen deforms, restoring forces are measured via the loadcells onboard the LBCB, and returned to the numerical substructure. The compensation task herein is performed in actuator coordinates as a means to overcome the limitations of Cartesian control seen the previous maRTHS development. To demonstrate and verify the capabilities of the new maRTHS framework in overcoming the earlier challenges, an illustrative example consisting of a steel moment frame is provided. In this example, one column is tested physically while other elements are computed numerically.

5.2 Multi-Axial RTHS Framework

The dynamic response of a reference structure may be represented via a second-order equation of motion (EOM)

$$\boldsymbol{M}\ddot{\boldsymbol{x}}(t) + \boldsymbol{C}\dot{\boldsymbol{x}}(t) + \boldsymbol{f}(\boldsymbol{x}, \dot{\boldsymbol{x}}) = \boldsymbol{F}(t) \tag{5.1}$$

where t is time, $\ddot{\boldsymbol{x}}(t)$, $\dot{\boldsymbol{x}}(t)$, and $\boldsymbol{x}(t)$ are the acceleration, velocity and displacement vectors, and $\boldsymbol{M}$ and $\boldsymbol{C}$ are matrices representing the mass and damping properties of the reference structure, and $\boldsymbol{f}$ represents the linear and nonlinear restoring forces properties of the reference structure, respectively. In this formulation, $\boldsymbol{F}(t)$ represent the external forces imposed on the reference structure, like inertial forces induced by earthquake accelerations.

Instead of testing structural systems as a whole, only components of interest are physically tested, and the remaining components are built into computational models. The physical and numerical components are linked via actuators which enforce the desired displacements calculated by the numerical model, and sensors which measure the feedback forces. The EOM for the numerical model is given by

$$\boldsymbol{M}_N\ddot{\boldsymbol{x}}_N(t) + \boldsymbol{C}_N\dot{\boldsymbol{x}}_N(t) + \boldsymbol{f}_N(\boldsymbol{x}, \dot{\boldsymbol{x}}) = \boldsymbol{F}(t) - \boldsymbol{F}_R(t) \tag{5.2}$$

where the subscript “N” describes the parameters of the numerical substructure. $\boldsymbol{F}_R$(t) represents a vector of measured feedback forces from the loadcells in physical substructure. Alternatively, feedback forces may be estimated from the dynamical parameters of the physical substructure.

The displacement-based maRTHS framework proposed herein is divided into four components: (i) numerical substructure, (ii) numerical to physical (N2P) transformation, (iii) physical substructure, and (iv) physical to numerical (P2N) transformation. The architecture of the maRTHS loop is illustrated in Fig. 5.1.

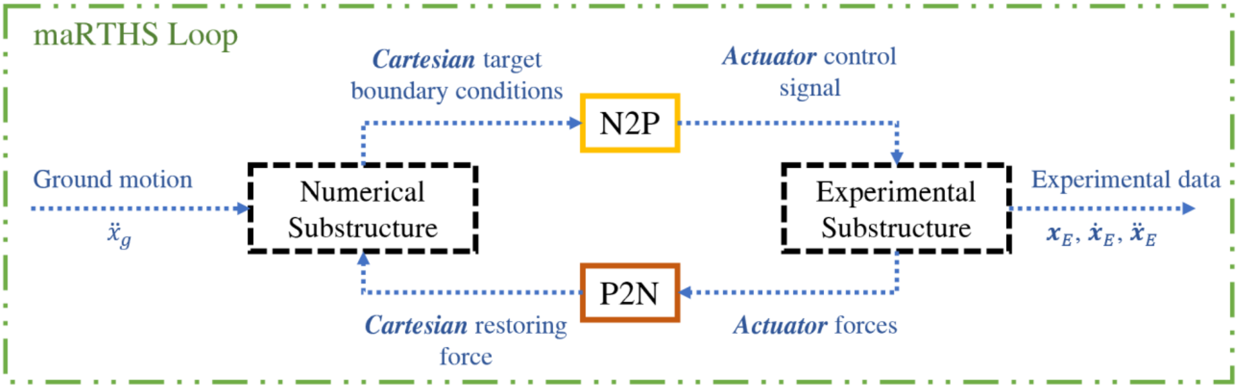

Figure 5.1 Proposed maRTHS framework

At each time step, the numerical substructure is excited by the ground acceleration, $\ddot{x}_g$, and produces the Cartesian target boundary conditions. The $N2P$ transformation converts target boundary conditions in Cartesian coordinates to actuator control signals for the experimental substructure to execute. The experimental substructure is comprised of the physical specimen, the LBCB and all onboard sensors. The experimental data which may include displacement, velocity, and acceleration behaviors of the physical specimen, denoted by $\boldsymbol{x}_E$, $\dot{\boldsymbol{x}}_E$, and $\ddot{\boldsymbol{x}}_E$, respectively, which are either directly measured or estimated. The $P2N$ transformation converts measured actuator forces to Cartesian restoring forces, which are returned to the numerical substructure to close the maRTHS loop.

5.2.1 Load and Boundary Condition Boxes at the University of Illinois

To demonstrate the capabilities of the proposed maRTHS algorithm, an LBCB device is used for experimental validation in this study. The LBCB, shown in Fig. 5.2, is a loading platform consisting of six hydraulic actuators, two in the X-direction, 3 in the Y-direction and one in the Z-direction, each equipped with inline loadcells and linear variable differential transducers (LVDT). The Multi-Axial Full-Scale Sub-Structuring Testing and Simulation (MUST-SIM) facility at the University of Illinois at Urbana-Champaign offers multiple LBCB devices capable of imposing loading and boundary conditions in 6-DOFs on structural specimens (Elnashai et al. 2005). Multiple LBCBs can be used together for the evaluation of the same specimen in different configurations for investigation of more complex structures. The LBCB is particularly useful for hybrid simulation testing due to its modularity and 6-DOF loading at the connection point with the physical specimen.

The MUST-SIM facility also offers 1/5th-scale LBCBs, shown in Fig. 5.2(b), for small-scale and proof-of-concept studies prior to testing in the large-scale facility. A 1/5th-scale LBCB is used for the experimental validation in this study. The actuators are supported by low-friction swivel bearing on both sides and housed by a rigid box frame that can be attached to the ground or a reaction wall in different orientations. The rigidity of the box frame is important for accurate assessment of specimen deformation. The extension and retraction capacities and stroke limits in each direction are listed in Table 1 for a rated pressure of 3000 psi for the hydraulic power supply (HPS).

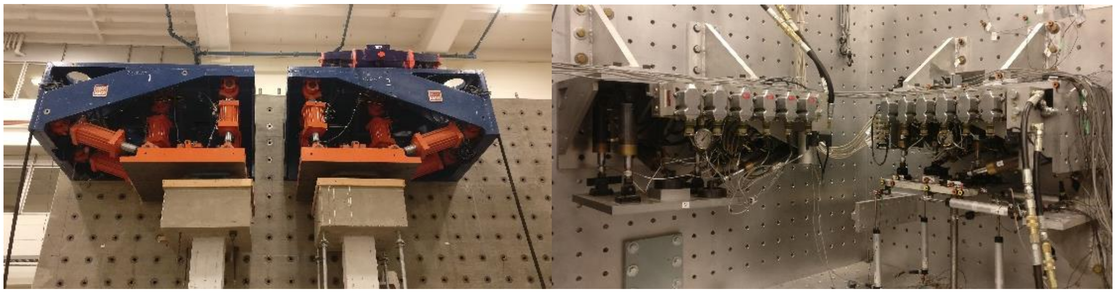

(a) Full-scale LBCBs (b) 1/5th-scale LBCBs

Figure 5.2 LBCB devices at the MUST-SIM facility

Table 5.1 Force and stroke capacities of the 1/5th-scale LBCB

Actuator Direction	X		Y		Z	
Retraction Force	18.9 kN	4.2 kip	28.0 kN	6.3 kip	9.3 kN	2.1 kip
Extension Force	31.1 kN	7.0 kip	46.7 kN	10.5 kip	15.6 kN	3.5 kip
Displacement	± 53.0 mm	± 2.09 in	± 25.4 mm	± 1.00 in	± 25.4 mm	± 1.00 in

The LBCBs were designed for quasi-static, cyclic and slow-speed hybrid simulation testing. In addition, recent developments have focused on slow-speed hybrid simulation implementations on the LBCBs ((Kim et al. 2011; Kwon et al. 2005; Mahmoud et al. 2013; Nakata et al. 2010)). The intended use of the LBCBs for real-time implementation as described by this paper, requires development and use of appropriate actuator compensation and kinematic transformations to address the dynamics of the LBCB.

5.2.2 Kinematic transformation

For completeness, this section briefly reviews the kinematic transformations that are employed to control the LBCBs. The states of a parallel manipulator like an LBCB can be specified either in: (i) actuator coordinates; or (ii) Cartesian coordinates. Fig. 5.3(a) presents a schematic of the relationship between the stroke of the *i*th actuator and Cartesian motion of the moving platform onboard an LBCB. A Cartesian reference frame is selected on the fixed based, denoted by $\boldsymbol{R_f}$, and another is selected on the moving platform, denoted by $\boldsymbol{R_m}$. The location of the $\boldsymbol{R_m}$ corresponds to the location of the attachment with the center of the physical specimen. The linear strokes of the prismatic limbs result in displacement and rotation of the moving platform. For some prescribed Cartesian motion at $\boldsymbol{R_m}$, an Inverse Kinematic Transformation (IKT) calculates the necessary stroke of each actuator. A translational vector $\boldsymbol{v} = \{u_x, u_y, u_z\} \in \mathbb{R}^3$ describes the motion at $\boldsymbol{R_m}$ with reference to $\boldsymbol{R_f}$. The vectors $\boldsymbol{a}_i \in \mathcal{R}^3$ and $\boldsymbol{b}_i \in \mathcal{R}^3$, denoting the fixed and moving joint locations of the i-th actuator, respectively, are drawn from the Cartesian reference frames to the center of rotation of each spherical joint. The actuators and their labels are demonstrated in Fig. 5.3(b).

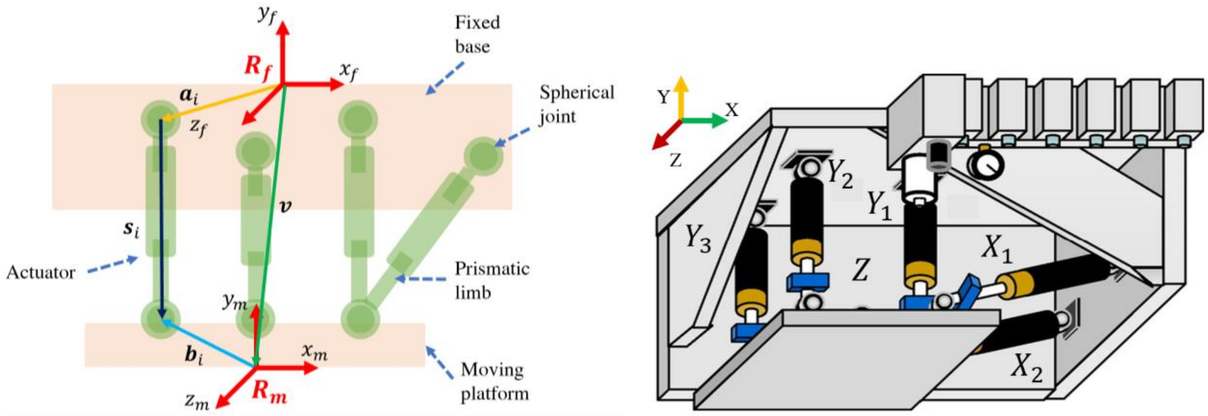

(a) Kinematics (b) Actuator orientations

Figure 5.3 Actuator kinematics for an LBCB

The Cartesian motion is described via the vector $\boldsymbol{w} = \{u_x, u_y, u_z, \theta_x, \theta_y, \theta_z\}^T$. Through addition and subtraction of vectors, the below formulation is formed

$$\boldsymbol{s}_i = \boldsymbol{v} + \boldsymbol{A}\boldsymbol{b}_i - \boldsymbol{a}_i \tag{5.3}$$

$$\lambda_i = |\boldsymbol{s}_i| = f_i\,(\boldsymbol{w}) \tag{5.4}$$

The Forward Kinematic Transformation (FKT) reverses the formulation in Eqs. (5.3) and (5.4), by using actuator measurements to calculate the Cartesian motion in the moving platform. A linearized forward kinematics is presented in discrete time in Eqs. (5.5) and (5.6). For an LBCB

$$\boldsymbol{J} = \begin{bmatrix} \dfrac{\partial \lambda_1}{\partial w_1} & \cdots & \dfrac{\partial \lambda_1}{\partial w_6} \\ \vdots & \ddots & \vdots \\ \dfrac{\partial \lambda_6}{\partial w_1} & \cdots & \dfrac{\partial \lambda_6}{\partial w_6} \end{bmatrix} \tag{5.5}$$

$$\boldsymbol{w}_{k+1} = \boldsymbol{w}_k + \boldsymbol{J}^{-1}(\boldsymbol{\lambda}_{k+1} - \boldsymbol{\lambda}_k) \tag{5.6}$$

where k is the discrete-time step.

5.2.3 N2P and P2N transformations

The $N2P$ block shown in the Fig. 5.1 is described in more detail in Fig. 5.4. This transformation receives Cartesian target and measured external potentiometer signals and calculates the actuator control signals. The inverse kinematic transformation for target signals, *Target IKT*, converts these displacements to actuator coordinate target signals, $\boldsymbol{r}(t) = \{r_{X_1}, r_{X_2}, r_Z, r_{Y_1}, r_{Y_2}, r_{Y_3}\}^T$. External potentiometers are used for displacement measurements of the moving platform of the LBCB. These measurements are transformed via a $Potentiometer\ FKT$ process to obtain Cartesian measurements and an $Actuator\ IKT$ to obtain actuator coordinate displacement measurements, $\boldsymbol{y}(t) = \{y_{X_1}, y_{X_2}, y_Z, y_{Y_1}, y_{Y_2}, y_{Y_3}\}^T$.

Next, a decoupled controller provides the necessary compensation for each of the six actuators independently. The term decoupled highlights the mMBC compensation in action in each actuator independent of other actuator channels. Actuator control signals are lastly transmitted to the LBCB for execution. The decoupled control concept is a unique aspect of the proposed maRTHS scheme, as it empowers the use of single-input single-output (SISO) type controllers which are easy to design and typically have performance guarantees. In the previously developed maRTHS scheme, actuators were compensated in Cartesian coordinates using a multi-input multi-output (MIMO) controller, which is hard to tune and stabilize. The requirement for MIMO controllers stemmed from the large degree of coupling between the actuators in Cartesian coordinates. By switching to actuator coordinate controls, the proposed framework aims to solve the challenges of MIMO Cartesian control, namely, the tuning and stability challenges.

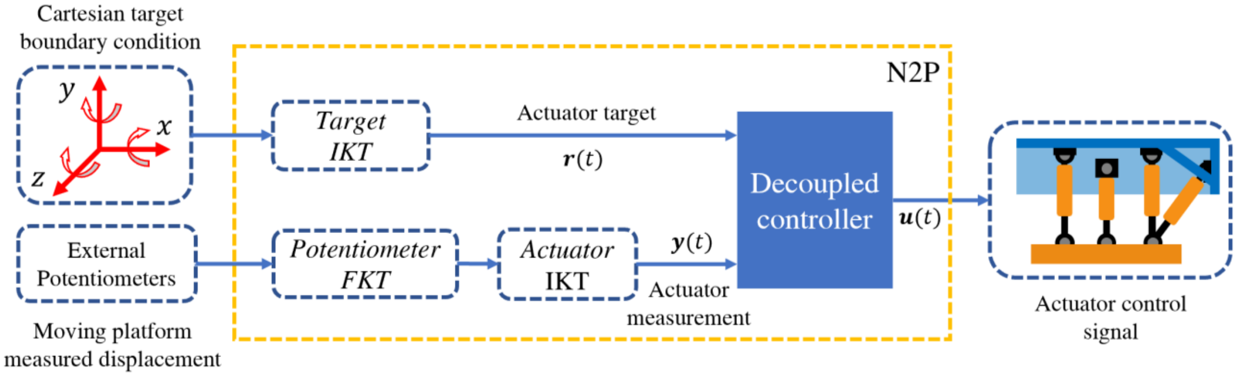

Figure 5.4 Numerical to physical (N2P) transformation

Meanwhile, the P2N block transforms actuator forces, measured from the onboard loadcells in-line with the actuators, to Cartesian restoring forces. This process is completed via the *Force Transform* block, shown in Fig. 5.5. Force transformation assumes a static equilibrium between internal actuator forces and external specimen forces. The static equilibrium is solved through the principle of virtual work. The Jacobian matrix $\boldsymbol{J}_1$ is required in this formulation to build a linearized kinematic relationship between

Cartesian and actuator coordinates. Next, loadcell measurements $\boldsymbol{F}_{act}(t)$ are transformed to Cartesian forces $\boldsymbol{F}_{crt}(t)$ via the force Jacobian $\boldsymbol{J}_1^T$ per below:

$$\boldsymbol{F}_{crt}(t) = \boldsymbol{J}_1^T \boldsymbol{F}_{act}(t) \tag{5.7}$$

where $\boldsymbol{F}_{crt}(t) = \{F_x, F_y, F_z, M_x, M_y, M_z\}^T$ are the measured forces in Cartesian coordinates. The measured Cartesian forces are in fact the feedback forces that are returned to the numerical substructure, thereby $\boldsymbol{F}_R(t) = \boldsymbol{P}_{crt}(t)$.

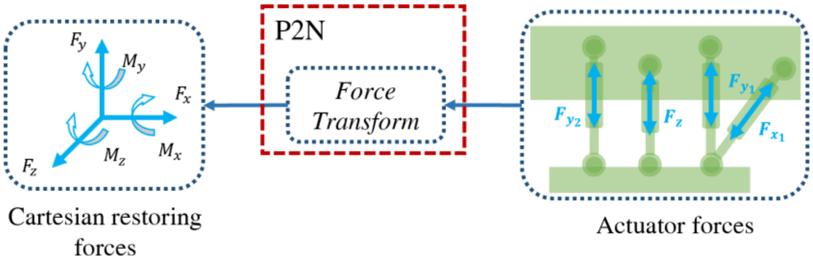

Figure 5.5 Physical to numerical (P2N) transformation

5.2.4 Decoupled controller: actuator dynamic compensation

The dynamics of actuators introduce significant lag in the RTHS system, which may result in loss of accuracy, as well as potential instability. Thus, controllers used in RTHS experiments must be designed specifically to compensate for the amplitude and phase discrepancies between target and measured signals. In this paper, a decoupled control technique is introduced for compensation of the actuator dynamics, per Fig 5.4. The term "decoupled" implies that each actuator onboard the LBCB is compensated independent of other actuators, as shown in Fig. 5.6.

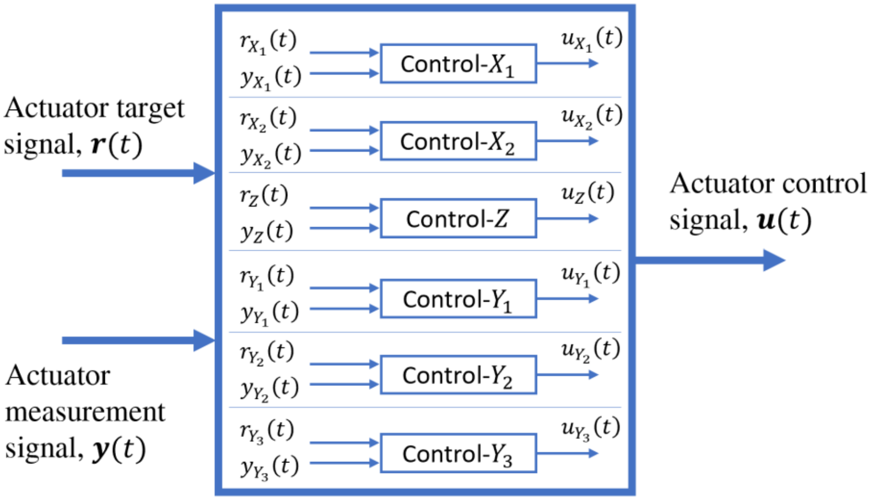

Figure 5.6 Architecture of the decoupled controller

The mMBC is the actuator compensation technique of choice for this decoupled strategy. The architecture of this controller provides specifications for the use of feedforward and feedback filters to ensure the controller has good tracking and robustness properties. The mMBC is applied to each actuator channel independently, as shown in Fig. 5.6. When designing a linear controller for a nonlinear process, the linear controller must be designed to sufficiently account for modeling errors and process nonlinearities. The performance of the proposed controller must be evaluated for small and high amplitude actuator displacements to ensure satisfactory performance. Najafi and Spencer, Jr. (2020) provide more extensive discussions on this controller and its tracking and robustness properties.

In this development, the $N2P$ and $P2N$ transformations are introduced for the operation of an LBCB device for an maRTHS experiment. The $N2P$ transformation converts Cartesian target signals to actuator target signals and the mMBC controller compensates for each actuator channel independently to create actuator control signals. Independent control of actuators is aimed at overcoming the challenges of Cartesian actuator control discovered in the previous maRTHS development (Fermandois and Spencer 2017). Next, the $P2N$ blocks transform actuator coordinate forces to Cartesian restoring forces. The $N2P$ and $P2N$ blocks combined, formulate the links between the numerical and physical substructures.

5.3 Experimental Setup

To verify the proposed maRTHS framework, an experimental study is envisioned involving a small-scale LBCB and a steel moment frame. This section describes the physical setups for the verification study. A three-DOF dynamical model is used to represent the steel moment frame, with two rotational and one translational DOFs, as shown in Fig. 5.7. This model assumes axial deformations are negligible. The moment frame is partitioned into a physical column and remaining components are numerically modeled. The physical column is designed from a 31.75 mm round steel section with a height of 457 mm. The natural frequencies of the complete structure are 1.58, 3.63, and 10.95 Hz. The mass and stiffness properties of the numerical substructure are provided below:

$$\boldsymbol{M}_N = \frac{EI}{h}\begin{bmatrix} 12 & 0 & 6h \\ 0 & h^2 & h^2/2 \\ 6h & h^2/2 & 5h^2 \end{bmatrix} \qquad \boldsymbol{K}_N = \frac{mh}{420}\begin{bmatrix} 1836 & 0 & 22h \\ 0 & 64h^2 & -48h^2 \\ 22h & -48h^2 & 68h^2 \end{bmatrix} \tag{5.7}$$

where $E = 200{,}000$ MPa, $I = 102{,}354$ mm^4, $h = 457$ mm and $m = 0.0091$ kg/mm. The natural frequencies of the numerical substructure are 1.09, 2.65, and 10.50 Hz. A nominal proportional damping ratio of 5% is assumed for this model. The 1940 El Centro acceleration record with two intensity measures (PGA-scaled at 10% and 30%) are considered to excite the moment frame structure in the elastic and nonlinear ranges, respectively. The 30% PGA-scaled El Centro earthquake is shown in Fig. 4.8. The feedback force and moment at DOFs 1 and 2 are denoted by F_x and M_z, and the displacement and rotation are denoted by U_x and R_z, respectively, in Fig. 5.7.

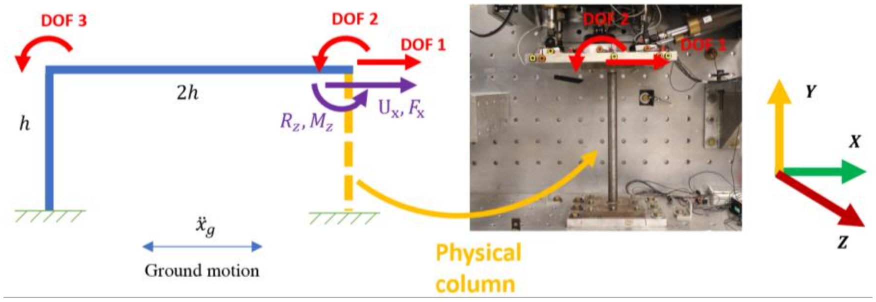

(a) Numerical substructure (b) Physical substructure

Figure 5.7 Numerical and physical substructuring of the steel moment frame

5.3.1 Experimental setup

A Shore Western computer manages the servo-control of the hydraulic actuators. The HSP has a capacity of 10 gallons per minute. A dSPACE microcontroller comprised of a DS1103 PPC controller board with an onboard PPC 70GX processor clocking at 1 GHz, which offers 20 analog input and 8 analog output channels with a 16-bit resolution, is used for compilation of numerical models and communication with external devices. Numerical models, control techniques and integration algorithms are developed on the MATLAB/SIMULINK platform on a separate host PC and compiled into a C source code and uploaded onto the dSPACE microcontroller. The management of the maRTHS experiments are carried out via the ControlDesk software.

External potentiometers are attached to the moving platform of the LBCB for accurate measurements of the executed boundary conditions. External potentiometers are preferred over the onboard LVDTs as reactional wall deflections can introduce errors to LVDT measurements (Chang et al. 2014). Fig. 5.8 provides a schematic of the proposed experimental setup.

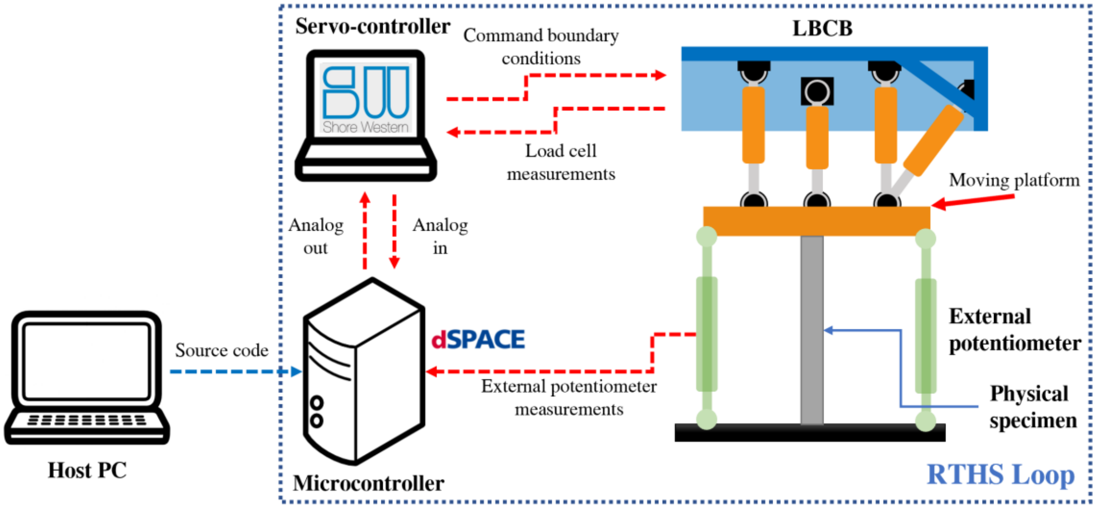

Figure 5.8 maRTHS hardware and physical setup

5.3.2 System identification and kinematic assembly

System identification is necessary for this framework, because of the use of the model-based compensation technique. The experimental substructure, which includes the LBCB attached to the physical specimen, is system identified. This process is initiated by commanding a BLWN to individual actuators and measuring their respective displacements. The six actuators onboard the LBCB device are labeled as X_1, X_2, Z, Y_1, Y_2 and Y_3, corresponding to the primary direction of the actuator in Cartesian space. The BLWN signals have a frequency bandwidth of 0 – 50 Hz and a root-mean-square (rms) amplitude of 5 mm in the X and Z axes and 2 mm in the Y axis. The rms amplitude of the bandlimited white noise must reflect the intended use of the actuator. The physical specimen is attached to the LBCB during the system identification. The effects of control-structure interaction are captured in this process, as the physical specimen is constrained by the LBCB. Thus, a natural velocity feedback from the specimen will cause a change in the dynamical properties of every actuator on the LBCB.

The target and measured results are next transformed from time to frequency domain. The sampling frequency, NFFT and window type are set to 1000Hz, 8192 and Hanning with 50% overlap, respectively. A system of six-by-six FRFs, where row "i" pertains to the target signal in actuator "i" and zero command in all the other actuators. Column "j" describes the FRF of the measured displacement of actuator "j", due to the target in actuator "i". The experimentally obtained FRFs of the LBCB actuators are fitted with a transfer matrix model. A linear time-invariant transfer function with 6 poles and zeros at infinity create the best fit for the diagonal terms of the transfer matrix:

$$\boldsymbol{P}_i(s) = \frac{\alpha_{0,i}}{s^6 + \beta_{5,i}s^5 + \beta_{4,i}s^4 + \beta_{3,i}s^3 + \beta_{2,i}s^2 + \beta_{1,i}s + \beta_{0,i}} \tag{5.8}$$

where $\alpha_{k,i}$ and $\beta_{k,i}$ are the numerator and denominator coefficient of the transfer function models. The six-by-six system of FRFs and the corresponding transfer matrix model are presented in Fig. 5.9. The off-diagonal terms are indicative of the dynamic coupling that exists between different actuators onboard an LBCB device.

From Fig. 5.9(a), the off-diagonal terms are deemed negligible due to the sufficient amplitude reduction between the target and measured displacement signals. In Fig. 5.9(b), off-diagonal phases often have a low signal-to-noise ratio, indicating the weak correlation between the target and measured displacement signals. Thereby, system identification is only conducted for on-diagonal terms. The important implication of this assumption in the design of the proposed maRTHS framework is that target and measured signals, and compensation are handled in actuator coordinate since dynamic coupling is weak in this frame of reference. SISO compensators are suitable for decoupled and weakly coupled systems. On the other hand, dynamic coupling tends to be significant when addressing multi-actuator loading assemblies in a Cartesian reference frame as was done in (Fermandois and Spencer, Jr. 2018). The proposed framework is applicable to multi-axial boundary conditions where the dynamic coupling in actuator coordinates is light.

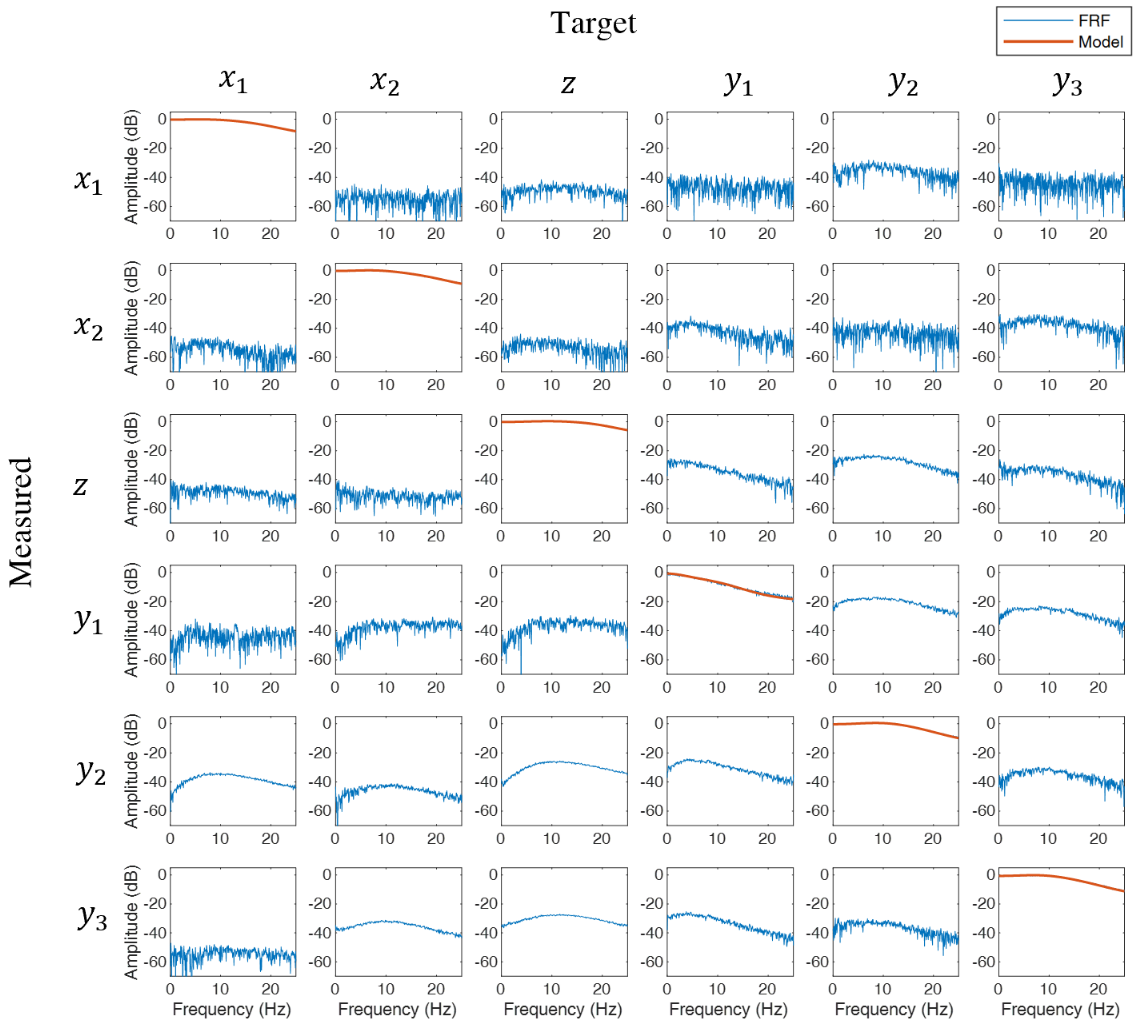

(a) FRF Amplitudes

Figure 5.9 System of FRFs for an LBCB device

Figure 5.9 (continued)

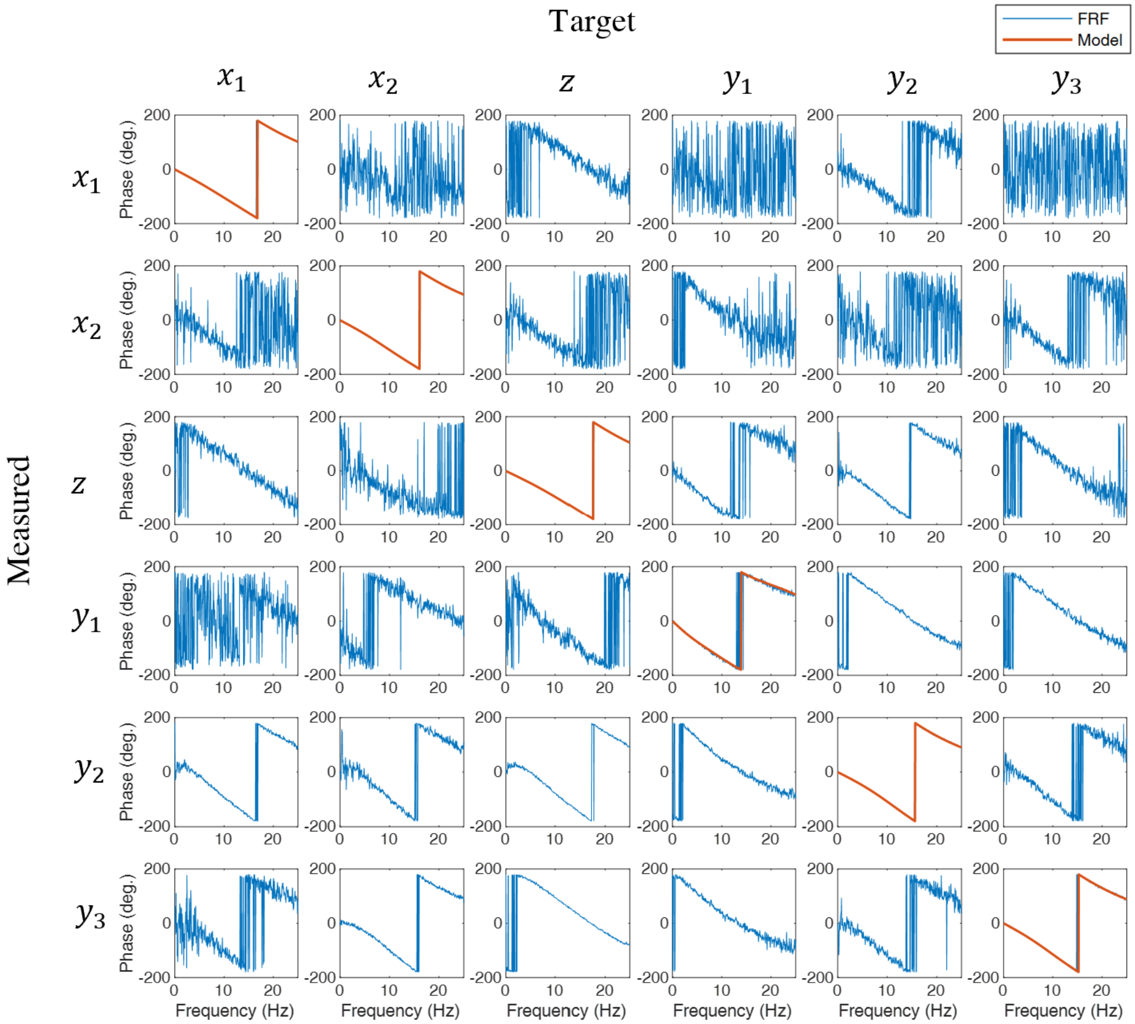

(b) FRF phases

Identification of the kinematic relationships is another important component of an maRTHS experiment. Determining the vectors in Eq. (5.4) and the Jacobian in Eq. (5.6) requires acquisition of accurate geometric quantities (i.e., dimensions) of the LBCB device and physical specimen. The Jacobian matrix associated with the *Potentiometer FKT* process is labeled $\boldsymbol{J}_2$. To obtain this Jacobian matrix, first the three-dimensional vectors in Eq. (5.3) need to be calculated between a potentiometer frame of reference and the Cartesian frame of reference. The potentiometer frame of reference is chosen as the base of the physical specimen in this example. Next, the total lengths of the potentiometers are formulated per Eq. (5.4) and linearized about the equilibrium position to obtain the $\boldsymbol{J}_2$ matrix. This process is repeated for the LVDT to Cartesian frames of reference to obtain the *Force Transform* labeled as $\boldsymbol{J}_1$ matrix. Both Jacobian matrices $\boldsymbol{J}_1$ and $\boldsymbol{J}_2$ formulated for use in the *Force Transform* and *Potentiometer FKT* processes are presented below

$$\boldsymbol{J}_1 = \begin{bmatrix} -1.00 & 0.02 & -0.01 & 0.06 & 3.85 & 0.50 \\ -1.00 & 0.02 & 0.00 & -0.06 & -3.85 & 0.50 \\ 0.00 & 0.07 & 1.00 & 1.85 & 1.69 & -0.13 \\ -0.02 & 1.00 & 0.01 & 0.00 & 0.04 & -3.54 \\ -0.05 & 1.00 & 0.01 & 3.38 & 0.10 & 5.01 \\ -0.04 & 1.00 & -0.04 & -2.84 & 0.07 & 4.83 \end{bmatrix} \quad \boldsymbol{J}_2 = \begin{bmatrix} -0.94 & -0.32 & 0.11 & -0.82 & 2.18 & -0.60 \\ -0.92 & -0.32 & 0.19 & 0.44 & -1.64 & -0.59 \\ -0.01 & -0.24 & 0.97 & -1.99 & -0.66 & -0.18 \\ -0.11 & -0.99 & 0.05 & -0.06 & 0.09 & 1.64 \\ -0.02 & -0.98 & 0.20 & -2.53 & -0.61 & -3.31 \\ -0.02 & -0.99 & 0.11 & 2.19 & -0.43 & -3.35 \end{bmatrix} \tag{5.9}$$

The elements of the Jacobian $\boldsymbol{J}_1$ describe the relationship between the actuator forces and the Cartesian forces. Meanwhile, the Jacobian $\boldsymbol{J}_2$ represents the correspondence between the potentiometer strokes and the Cartesian motion. These Jacobians are not symmetric because the positions of the actuators and the potentiometers with reference to the physical specimen are not symmetric. The translational and rotational elements in $\boldsymbol{J}_1$ and $\boldsymbol{J}_2$ are in units of mm and radians, respectively.

5.4 Experimental Verifications

This section aims to verify the proposed maRTHS development through an illustrative example involving a steel moment frame in Fig. 5.7.

5.4.1 Deformation of reaction wall and LBCB fixture

The target displacements may be different than the displacements imposed on the specimen due to deformations of the reaction wall and LBCB, which can negatively affect the hybrid simulation. Reaction wall deflections were observed in prior hybrid simulation experiments conducted on the large-scale facility described in Section 5.2 (Chang et al. 2014). To test the magnitude of these deflections on the small-scale MUST-SIM facility, LED markers are installed on the reaction wall and the 1/5th-scale LBCB frame. The locations of the LED markers are illustrated in Fig. 5.10. The blue markers are intended for measurements of the LBCB frame and orange markers are intended for the reaction wall.

In this study, a Krypton K600 camera is used to measure the displacements of the LED markers in Cartesian space with an accuracy of ± 0.02mm. An maRTHS experiment with a 30% El Centro earthquake is executed, and the deformations indicated by the LEDs are recorded. The vertical deformation in blue marker #2 and out-of-plane deformations in the orange marker #6 are presented in Fig. 5.11. The maximum deflections in the orange markers are obtained and plotted in Fig. 5.12. The blue dashed lines represent the extrapolations of the lateral deformations to the base of the reaction wall.

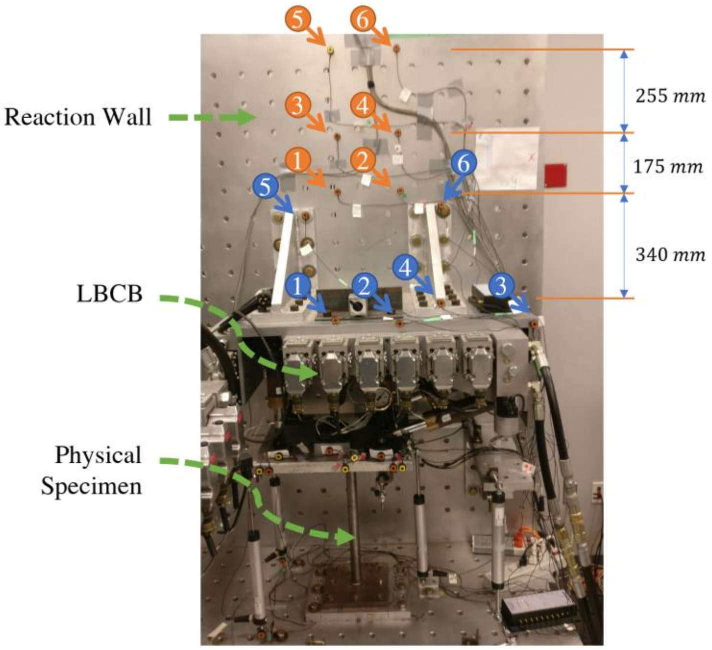

Figure 5.10 Configuration of the LED markers

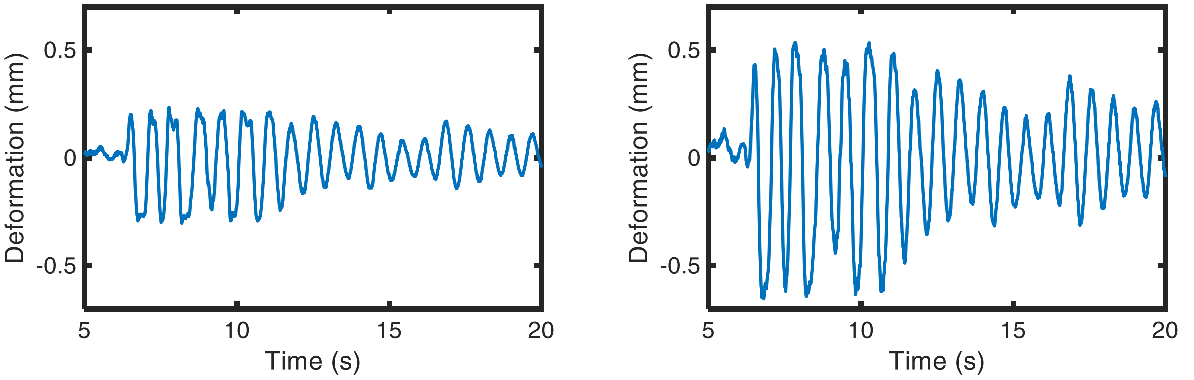

(a) Vertical deformation of blue LED #2

(b) Out-of-plane deformation of orange LED #6

Figure 5.11 Displacements of in blue LED #2 and orange LED #6

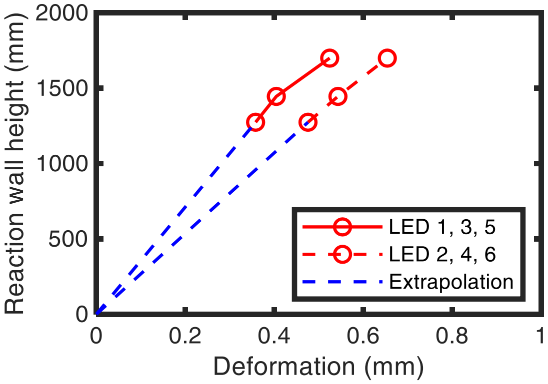

Figure 5.12 Maximum out-of-plane deformation in orange LED markers

These deformations are deemed significant as a ratio of the physical specimen deformations. To avoid measurement inaccuracies induced by LBCB and reaction wall deformations, external potentiometers are provisioned and used to measure the displacements of the moving platform. These potentiometers are connected to the moving platform of the LBCB at one end, and the fixed floor of the experimental setup, at the other end. The potentiometer deformations are converted to Cartesian measurements via $Potentiometer\ FKT$ and then converted to corrected LVDT measurements via $Actuator\ IKT$.

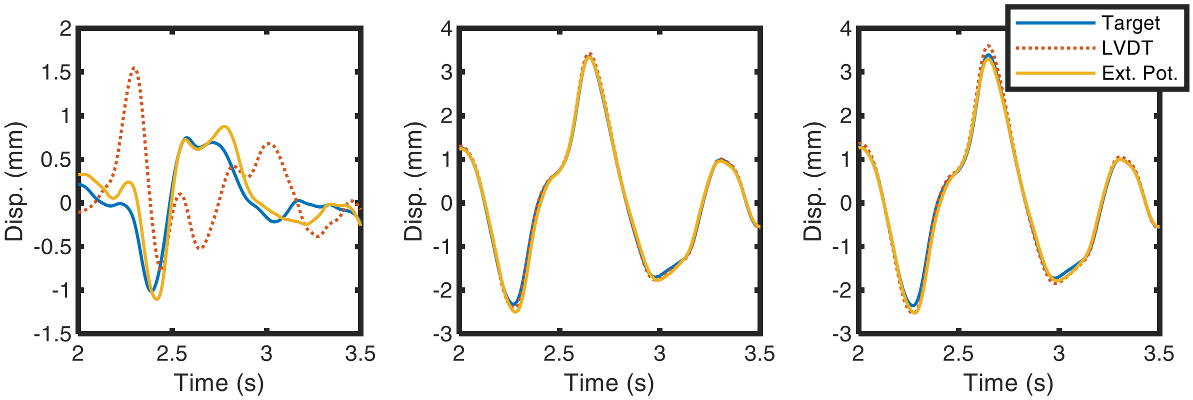

(a) Y_1 actuator (b) Y_2 actuator (c) Y_3 actuator

Figure 5.13 LVDT and Potentiometer measurements of the vertical (Y-axis) actuators

Fig. 5.13 demonstrates the target, LVDT and external potentiometer measurements. The LVDT measurement from actuator Y_1 points to a noticeably larger displacement than the potentiometer measurement. This observation highlights the incorporation of LBCB frame and reaction wall deformations to the LVDT measurements. The external potentiometers provide more accurate measurements since LBCB frame and reaction wall deformations are avoided. Another important observation is that actuator Y_1 is confronted with the high axial stiffness, due to its close proximity with the steel column. As a result, a larger lag is observed between the target and external potentiometer signals for this actuator. An actuator with a higher force capacity, or a physical specimen with a smaller axial stiffness can overcome the observed lag and result in a more accurate Y_1 tracking.

Lastly, the potentiometer measurements converted to Cartesian coordinates are validated via comparisons to reference measurements from a Krypton camera. The camera is directed at the front face of the LBCB and LEDs are installed on the moving platform of the LBCB. The moving platform executes sinusoidal translations in the X- and Z-axes, respectively, and rotation about the Z-axis. Next, Cartesian deformations are calculated from external potentiometer readings and compared to Krypton measurements. The results for the X-translation and Z-rotation presented in Fig. 5.14(a)-(b) demonstrate accurate tracking. The Z-translation results shown in Fig. 5.14(c) suffer from inaccuracies due to the nonuniform vertical translation as a result of the flexural deformations in the moving platform during experiments. The

Jacobians discussed earlier assume that the moving platform is rigid and does not undergo flexural deformation. Therefore, the use of the Jacobians to calculate Cartesian motion will result in minor errors in the Y translation calculations, when the flexural deformation in the moving platform is large.

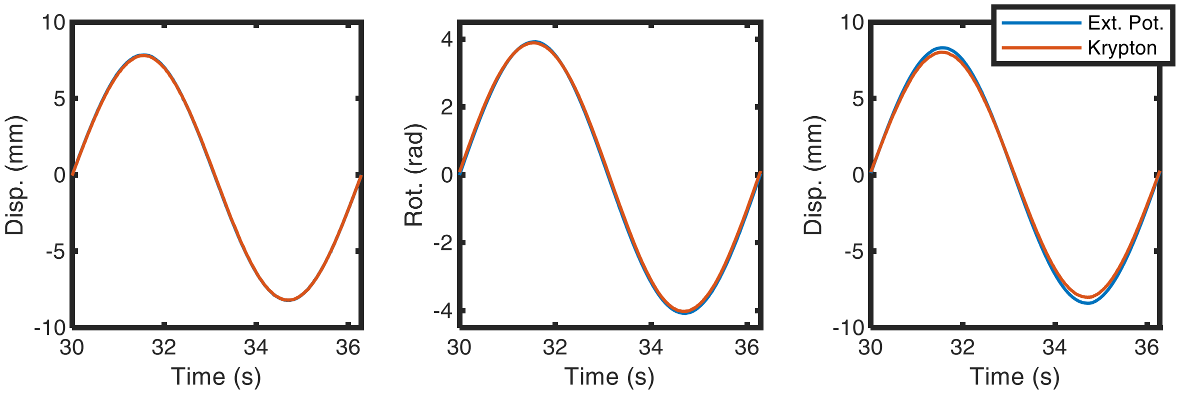

(a) X Translation (b) Z Rotation (c) Y Translation

Figure 5.14 Potentiometer and Krypton camera measurements

5.4.2 Tracking performance of compensation techniques

This section assesses the tracking performance of the mMBC compensator proposed in the previous sections, which is critical to ensuring the integrity of the maRTHS. Three compensation scenarios are considered for comparison: (i) no control, (ii) feedforward (FF) control, and (iii) mMBC. Next, open-loop maRTHS experiments are conducted and the tracking ability of each controller is assessed. The *open-loop* execution implies that restoring forces are set to zero and stability is assured while the tracking performance of each compensation scenario is considered.

Two evaluation criteria are used for assessment of the tracking performance of each compensation scenario: the normalized root-mean-square error ($RMSE$) and normalized maximum error ($MAXE$) per Eqs. (3.21) and (3.22), respectively. These criteria should be minimized for a better tracking performance.

Following open-loop executions of the maRTHS with a 10% PGA-scaled El Centro earthquake, the tracking performance of the compensation scenarios are listed in Tables 5.2–5.4. Inclusion of an FF compensator results in better tracking performance compared to the uncontrolled scenario. Addition of the feedback controller to formulate the mMBC compensator, further minimizes the evaluation criteria. Tracking in the Z actuator appears to be poor, however, the displacement of this actuator is quite small (~ 0.1 mm). Thus, even small errors are amplified by the tracking criteria. Fig. 5.15 illustrates the synchronization plots in Cartesian coordinates for DOFs 1 and 2, identified in Fig. 5.7. A $1:1$ diagonal line in these figures implies perfect tracking. Use of the FF and mMBC compensators reduces the area in the tracking loop, thereby reducing negative damping that can render a closed-loop RTHS unstable (Horiuchi et al. 2000). These results show that although feedback control serves in improving tracking, most of the compensation is brought about by the FF controller.

Table 5.2 RMSE tracking performance of actuators

Compensation scenario	$RMSE$					
	X_1	X_2	Y_1	Y_2	Y_3	Z
No control	0.159	0.198	0.242	0.168	0.198	3.623
FF	0.102	0.148	0.086	0.110	0.113	3.534
mMBC	0.095	0.137	0.083	0.098	0.099	3.221

Table 5.3 MAXE tracking performance of actuators

Compensation scenario	$MAXE$					
	X_1	X_2	Y_1	Y_2	Y_3	Z
No control	0.173	0.186	0.215	0.151	0.152	3.843
FF	0.111	0.126	0.101	0.109	0.127	3.608
mMBC	0.101	0.113	0.093	0.104	0.119	3.077

Table 5.4 Tracking performance in Cartesian coordinates

Compensation scenario	$RMSE$		$MAXE$	
	DOF 1	DOF 2	DOF 1	DOF 2
No control	0.195	0.214	0.190	0.184
FF	0.155	0.109	0.130	0.144
mMBC	0.115	0.098	0.099	0.142

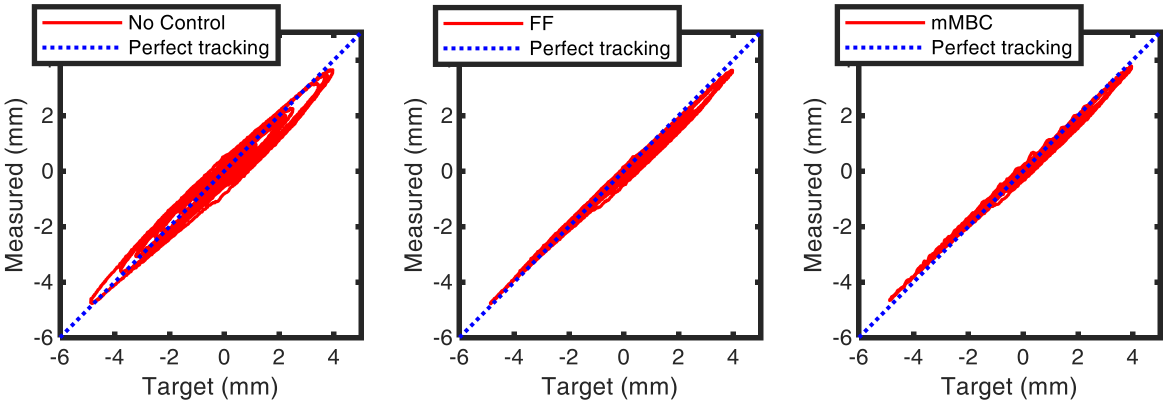

(a) DOF 1 (No Control) (c) DOF 1 (FF) (e) DOF 1 (mMBC)

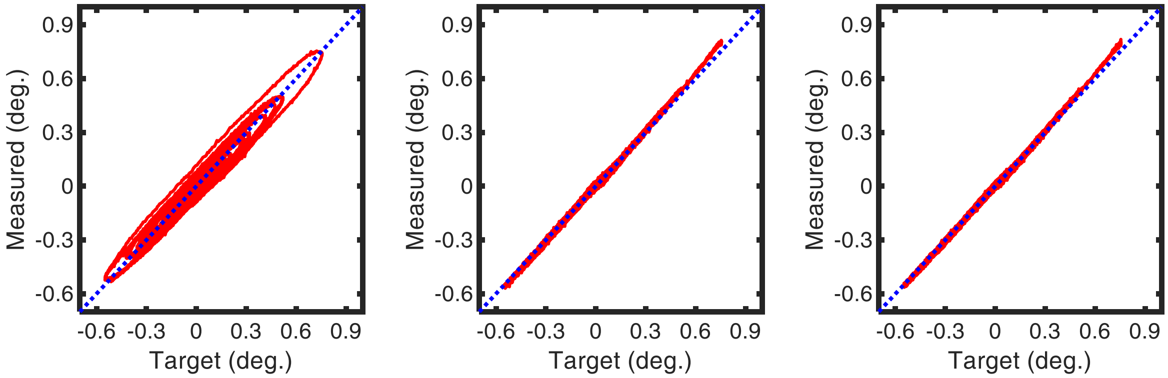

(b) DOF 2 (No Control) (d) DOF 2 (FF) (f) DOF 2 (mMBC)

Figure 5.15 Tracking performance of compensation scenarios for Cartesian coordinates – 10% El Centro

5.4.3 maRTHS results

Next, the maRTHS loop is closed (i.e., the feedback forces are returned to the numerical model) to enable maRTHS execution. The behavior of DOFs 1–3 of the steel moment frame are used for evaluation in this section. DOFs 1, 2 and 3 represent the horizontal translation of the beam in the X-direction, rotation at the top-right beam-column attachment about the Z-axis, and the rotation at the top-left beam-column attachment about the Z-axis, respectively, as shown in Fig. 5.7. A numerical model of the whole (reference) structure is first used for comparison and validation of the maRTHS test. This comparison is conducted in the linear elastic range for a 10% El Centro excitation.

In the linear elastic range, the results of the maRTHS test of the moment frame are compared to predicted response from a numerical model. A PGA-scaled El Centro at 10% excitation is introduced to the moment frame structure and the responses of DOFs 1–3 are presented in Fig. 5.16. The performance of the maRTHS experiment is observed to be closely matching that of the numerical simulation, thereby verifying the accuracy of the maRTHS results in the linear range. The differences observed in DOF 2, as shown in Fig. 5.16(b), may be associated to the imperfections in the compensation action of the boundary condition.

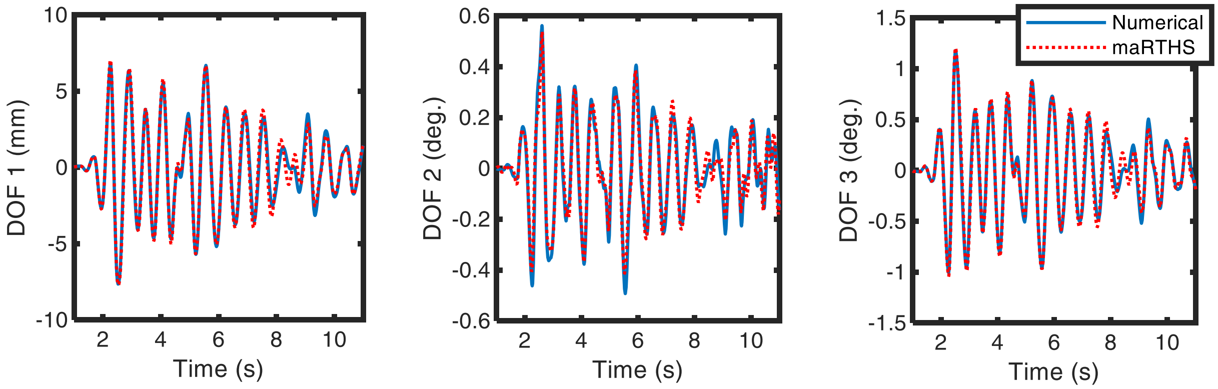

(a) DOF 1 (b) DOF 2 (c) DOF 3

Figure 5.16 Numerical simulation and maRTHS of the steel moment frame – 10% El Centro

A 30% El Centro excitation is used to push the moment frame structure into the nonlinear range. The results for the performance of DOFS 1–3 for this nonlinear maRTHS experiment are provided in Fig. 5.17. The hysteretic (i.e., force-displacement) responses of DOFs 1 and 2 are presented in Fig. 5.18. The results presented describe the evolution of the deformation parameters U_X and R_Z, and force parameters F_X and M_Z as demonstrated in Fig. 5.7.

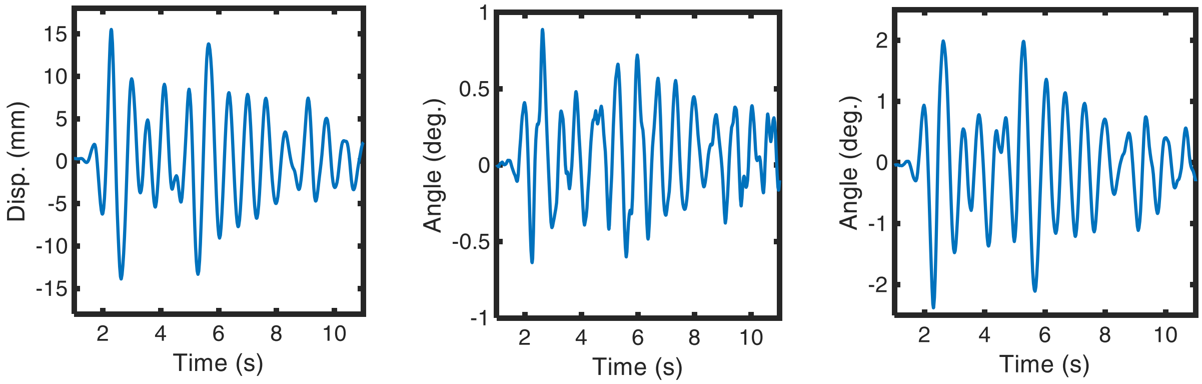

(a) DOF 1 (b) DOF 2 (c) DOF 3

Figure 5.17 maRTHS behavior of the steel moment frame – 30% El Centro

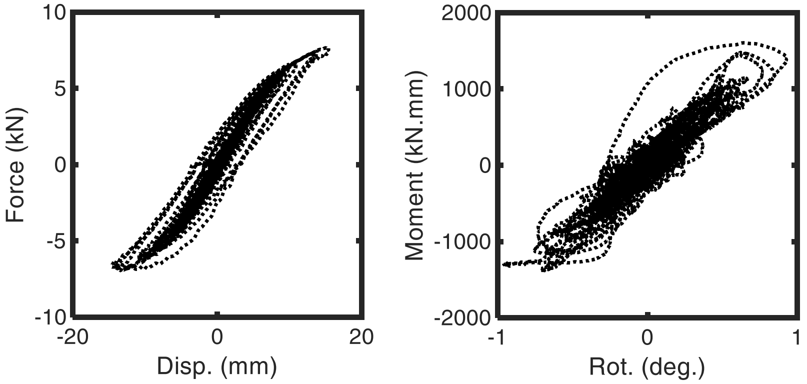

(a) F_X vs. U_X (DOF 1) (b) M_Z vs. R_Z (DOF 2)

Figure 5.18 Hysteretic responses at DOFs 1 and 2 – 30% El Centro

5.4.4 Damping ratio study

Closed-loop delays in RTHS can be interpreted as negative damping which can render experiments unstable. Instability may ensue unless the combined damping in the numerical and physical substructures is large enough. Therefore, delay compensation is an important feature of any RTHS implementation. The damping ratio of the numerical substructure has been set to 5% up to this point. To explore the effectiveness of the delay compensation action, the damping of the numerical substructure is varied from $\zeta = 2 - 10\%$, where ζ is the damping ratio. The corresponding maRTHS results are presented in Fig. 5.19. The boundary condition translation along the X-axis and rotation around the Z-axis, pertaining to DOF 1 and 2 are displayed. These results demonstrate a smooth and stable performance for the specified range of damping ratios. With the inclusion of the mMBC compensator in the maRTHS loop, the closed-loop delays and negative damping effects are reduced.

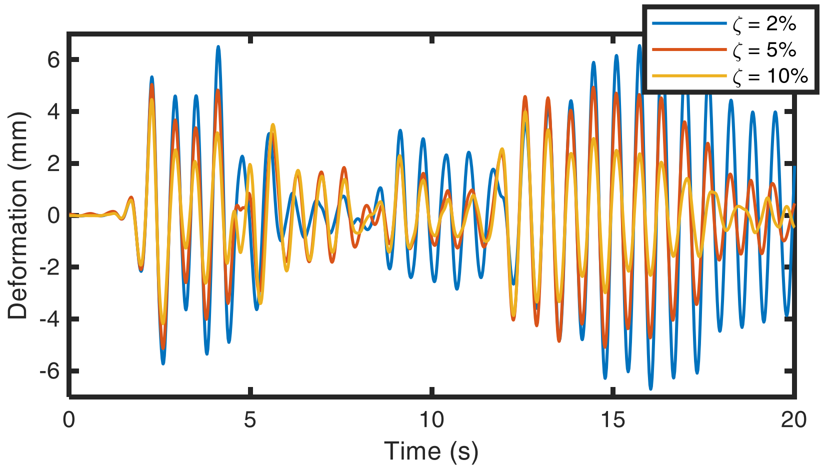

(a) Translation along X-axis (DOF 1)

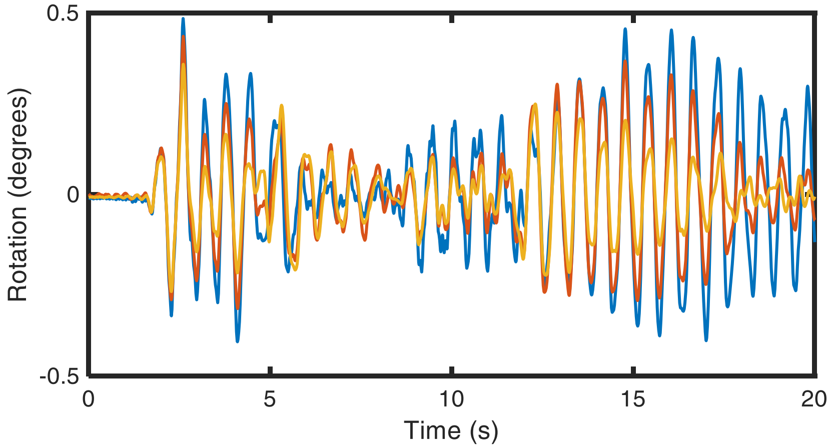

(b) Rotation along Z-axis (DOF 2)

Figure 5.19 maRTHS results under different damping scenarios – 10% El Centro

These results illustrate improvements over the previous development discussed in (Fermandois and Spencer 2017). The stability of the rotational DOF 2, at the top of the physical column, was discovered to be highly sensitive in the previous development and the decision was made to neglect it. This DOF however was included with the proposed maRTHS implementation, thus providing a more realistic substructuring selection. The previous development also condensed out the Y-translation controller, as the Cartesian feedforward controller was numerically singular due to the high axial stiffness of the physical specimen. None of the Cartesian directions are condensed out in this approach. Lastly, good tracking and stability are displayed by the maRTHS framework, even when the physical specimen is pushed into the nonlinear response region.

5.5 Summary

A novel framework for multi-axial real-time hybrid simulation (maRTHS) testing is proposed in this chapter. This development aims to provide a viable alternative to shake table and hybrid simulation with realistic dynamic and three-dimensional characteristics. This framework is divided into four steps, namely: (i) numerical substructure; (ii) numerical to physical ($N2P$) transformation; (iii) physical substructure; and (iv) physical to numerical ($P2N$) transformation. The 1/5th-scale Load and Boundary Condition Box (LBCB) device at the University of Illinois at Urbana-Champaign is used for experimental verification of the proposed framework.

The experimental verification is comprised of a steel moment frame, which is partitioned into physical and numerical substructures and evaluated via the proposed maRTHS algorithm. At every time step, the response of a beam-column model is numerically evaluated on a microcontroller for a given ground excitation. The $N2P$ transforms the Cartesian target boundary conditions (i.e., displacements and rotations) from the numerical substructure to actuator control signals for the LBCB to execute. This process involves several layers of kinematic transformations and a decoupled actuator compensation scheme. Once control signal has been executed, feedback forces measured by the loadcells in-line with the actuators are transformed via the $P2N$ transformation to Cartesian restoring forces and returned to the numerical substructure.

The actuator compensation in this framework is conducted in a decoupled manner, with each actuator channel compensated independently. The decoupled control scheme creates ease of design and enables utilization of SISO type controllers, like the modified model-based compensator (mMBC), which has good tracking and robustness behaviors. Three compensation scenarios are studied experimentally: (i) no control; (ii) feedforward; and (iii) mMBC. By comparison, the latter demonstrates the best tracking performance. A range of damping values were assigned to the numerical substructure to ensure that the compensation is robust, and instability caused by closed-loop delays are prevented. The results from the maRTHS test conducted in the linear range are compared to a numerical simulation for verification. Lastly, results from the maRTHS test with the physical specimen pushed into the nonlinear range demonstrate successful and stable implementation of the proposed maRTHS framework.

CHAPTER 6 MULTI-BOUNDARY INTERFACE REAL-TIME HYBRID SIMULATION

6.1 Problem Statement

For many practical engineering and research applications, maRTHS with more than one boundary interface and physical substructure may be necessary. In this Chapter, a framework for multi-axial real-time hybrid simulation employing substructuring at multiple boundary points is proposed; the framework also enables simulation of systems with multiple physical substructures. Out-of-plane physical realizations which vastly increase the mechanical coupling between the actuators of an LBCB will also be considered herein. After substructuring the reference structure, kinematic and force transformation, and actuator compensation algorithms are introduced to connect each physical element with the numerical model. The mathematical and analytical basis for the proposed maRTHS framework are first presented, addressing the following: (i) scalability for higher degrees-of-freedom (DOFs); (ii) multiple physical boundary points; (iii) decoupled compensation for dynamics and mechanical couplings between interacting actuators; and (iv) out-of-plane boundary condition motions and forces. The maRTHS framework is subsequently applied to a multi-span curved bridge structure with two LBCBs testing the physical piers. The bridge under consideration is a four-span, curved deck, and asymmetric structure loaded via a bi-directional ground motion. Steel physical substructures are employed herein for ease of analysis and repeatability. The inertial effects of LBCBs on the measurement feedback forces are also considered and shown to be negligible.

6.2 Multi-Boundary Multi-Axis Real-Time Hybrid Simulation

In most RTHS implementations to date, only a single boundary interface and a single physical specimen have been the subject of the study. In many applications however, physical testing of multiple boundary interfaces and specimen may be of interest. Several multi-axial boundary point devices, comprised of actuators and sensors, are required for such simulations. The goal here is to extend the maRTHS framework proposed in Najafi et al. (2020) for simulations with multiple physical substructures.

In seismic applications of maRTHS, with each integration time step, a ground acceleration $\ddot{x}_g(t)$ serves as the input excitation into the test. As the numerical substructure is excited, the deformation values at the boundary point with where the physical substructure would be positioned in the reference structure are computed and termed as the *target*. The target boundary condition $\boldsymbol{w}_i(t)$ for the i^{th} physical substructure is obtained in a Cartesian coordinate from the finite element model. Steps involving kinematic transformations and actuator compensation next prepare the target signal for execution in the physical substructure.

A transformation $N2P_i$ is responsible for converting target boundary condition to actuator control signal $\boldsymbol{u}(t)$. After physical execution (i.e., deformation of physical specimen by actuators), loadcells record actuator forced $\boldsymbol{F}^{act}(t)$. A transformation $P2N_i$ converts actuator forces to Cartesian feedback forces $\boldsymbol{F}^{crt}(t)$ for use in the numerical substructure. In addition, relevant physical data $\boldsymbol{x}_P$, $\dot{\boldsymbol{x}}_P$, and $\ddot{\boldsymbol{x}}_P$ are recorded from the experimental setup. A schematic of the proposed maRTHS framework for multiple physical substructures is presented in Fig. 6.1. In some experiments, the physical substructures may directly interact (e.g., one physical specimen with multiple boundary interfaces), while in others the physical interaction is through coupling in the numerical substructure (e.g., separate physical specimen and boundary interfaces).

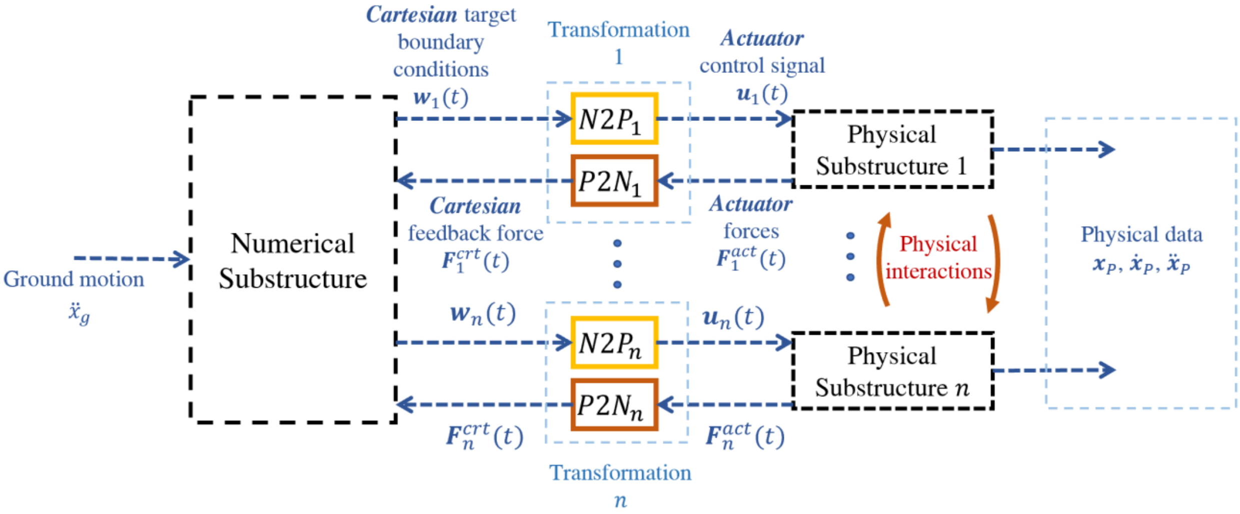

Figure 6.1 Proposed multi-boundary interface maRTHS framework

6.3 Experimental Setup Requirements

Multi-axial simulations are typically realized with actuated devices such as the LBCBs at the MUST-SIM laboratory at the University of Illinois at Urbana-Champaign, per Fig. 5.2. Each box can be used together or individually, and configured at different orientations, per Fig. 6.2.

To measure forces, six loadcells are necessary, installed in-line with the axis of the actuators. To measure the executed deformations, displacement transducers in the form of six linear potentiometers are used. To allow for the input/output (I/O) peripherical devices (e.g., loadcells), embedded systems (e.g., servocontroller and microcontroller) must have sufficient I/O channels for connectivity. Each actuator control channel requires a digital-to-analog (DA) channel from the microcontroller to the servocontroller, and from the servocontroller to the actuator for execution. The displacement transducer and loadcells each require an analog-to-digital (AD) channel from the microcontroller to the servocontroller, and from the servocontroller to the actuator for measurements.

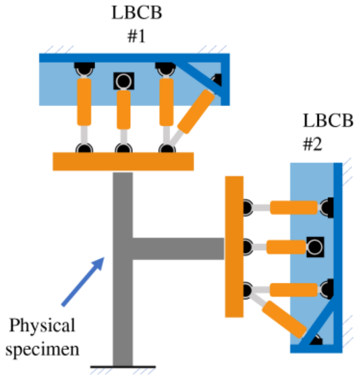

Figure 6.2 Two LBCBs used on a shared physical specimen

For an maRTHS test with n boundary interfaces, the peripheral device requirements are: $6n$ loadcells, $6n$ displacement transducers (LVDT or linear potentiometer), and $6n$ actuator command channels. The servocontroller and microcontroller must have the I/O connectivity interface for $6n$ DA channels and $12n$ AD channels.

6.4 Reference Model Development

A multi-span curved bridge is selected as the reference structure for the experimental verification of the proposed maRTHS framework. This selection is made as a natural extension to the developments made in the multi-axial slow-speed hybrid simulation testing done as part of the CABER program at the MUST-SIM facility at the University of Illinois at Urbana-Champaign (Abdelnaby et al. 2012; Chang et al. 2014; Elnashai et al. 2005; Frankie et al. 2013).

6.4.1 Multi-span curved bridge

An asymmetric four-span reinforced concrete curved-bridge is partitioned into a numerical deck and physical piers for slow-speed hybrid simulation. The numerical component is modeled via finite element analysis in Zeus-NL (Abdelnaby et al. 2012). The two outer physical piers are tested at a 1:3 scale using the full-scale LBCBs, while the inner pier is tested at a 1:20 scale using the 1/5$^{\text{th}}$-scale LBCB. Details of the abutments, input excitation, and restraints are also modeled numerically (Frankie 2013). The simulation coordinator integrating the numerical and physical substructures together is the UI SIMCOR (Kwon et al. 2005).

The reference structure discussed in the CABER program is a 400 ft long curved bridge with a curvature of 1/660 ft. The four-spans are 75 ft (22.9 m), 150 ft (45.7 m), 100 ft (30.5 m), and 75 ft (22.9 m), respectively. The piers of the bridge are 28.5 ft (8.7 m), 37.5 ft (11.4 m), and 22.5 ft (6.9 m), respectively. The piers are designed at 48 in. (1220 mm) round reinforced concrete elements with 28 #10 reinforcement bars, and #5 stirrups. The deck is idealized as a 60 in. (1.52 m) by 81 in. (2.06 m) transverse beam.

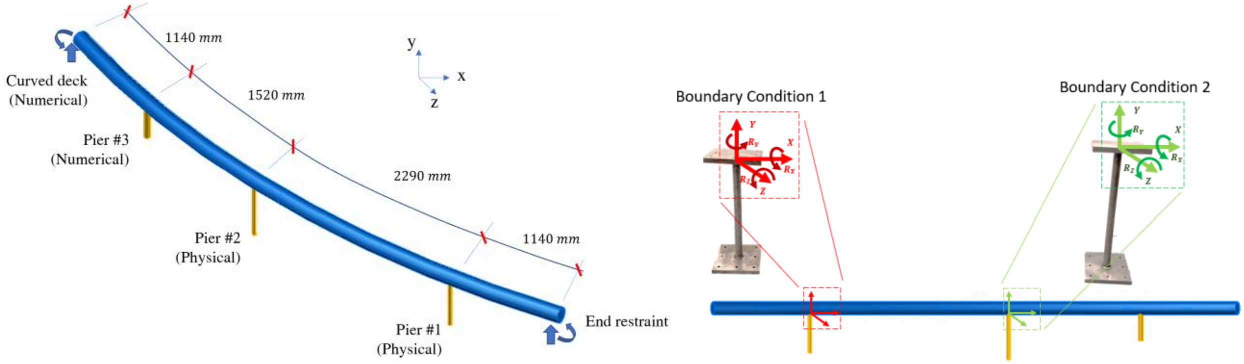

(a) Reference structure (b) Real-time substructuring

Figure 6.3 Illustrative curved bridge example

In this study, a reference structure is envisioned with similar geometry to the structure studied previously. Structural steel is used instead of reinforced concrete for repeatability and since this is a proof-of-concept study. The new reference structure is designed with a scale of 1:20 compared to the original CABER bridge. The new bridge is 20 ft (6.1 m) long with a curvature of 1/33 ft (1/10.1 m), as illustrated in Fig. 6.3(a). For ease of modeling and construction, round sections are appropriated for all numerical and physical components. The bridge deck is modeled as a round steel section with a diameter of 2.8 in. (71 mm). The supports at both ends of the curved deck, restrain the bridge in the rotational and the Y-direction. The piers are dimensioned per Table 6.1. Fig. 6.3(b) provides an illustration of the real-time substructuring of the reference bridge into numerical and physical substructures, and two multi-axial boundary interfaces.

Table 6.1 Bridge pier dimensions

Pier	Simulation	Diameter (in. / mm)	Length (in. / mm)
1	Physical	1.25 / 31.75	18.0 / 457.2
2	Physical	1.25 / 31.75	21.5 / 546.1
3	Numerical	2.00 / 50.80	13.5 / 342.9

6.4.2 Model development

A three-dimensional finite element model (FEM) of the reference structure is first formulated in MATLAB. The curved deck of the bridge is idealized via 16 linearized segments per Fig. 6.4. Development of a MATLAB-based numerical model is critical to the maRTHS implementation, as well-established FEM tools such as Abaqus and SAP2000 are not integrable with real-time testing hardware. Development of an accurate numerical model for the reference structure is a challenging task, due to the three-dimensional nature of the bridge and coupling present between out-of-plane and torsional moments in the curved deck.

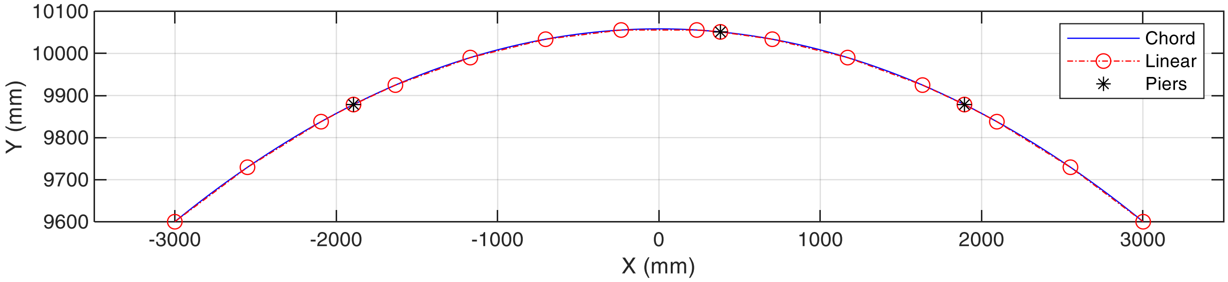

Figure 6.4 Linearized segments of the curved deck

The SAP2000 software was selected for verification of the MATLAB-based numerical model. Table 6.2 lists the dominant eigen modes, and natural frequencies identified in the SAP2000 and MATLAB models. Due to the out-of-plane flexibility of the curved bridge, most of the dominant eigen modes are lateral and vertical vibration modes. Fig. 6.5 compares a total of 30 eigen modes and the corresponding identified natural frequencies. Fig. 6.6 illustrates the first six mode shapes for the curved bridge structure. In this figure, the wireframe and the color-coded frame indicate the at-rest position and mode shape of the bridge. Results indicate that the MATLAB-based numerical model is similar to the SAP2000 model in dynamic performance.

Table 6.2 List of dominant eigen modes and natural frequencies

Natural Frequency (Hz)	1	2	3	4	5	6	7	8	9
Mode	Lateral	Lateral	Lateral	Lateral	Vertical	Vertical	Lateral	Vertical	Lateral
SAP2000	0.5235	0.6536	1.1027	1.2616	1.3312	1.4644	2.1894	3.0756	3.1976
Numerical Model	0.5260	0.6545	1.0919	1.2581	1.3270	1.4650	2.1864	3.0048	3.327

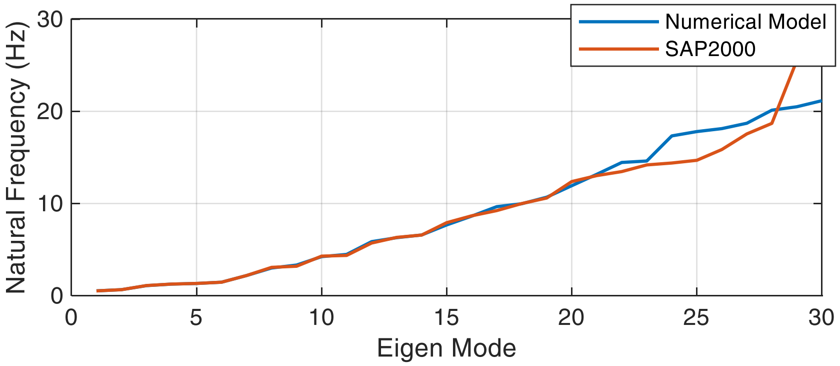

Figure 6.5 Comparison of 30 eigen modes

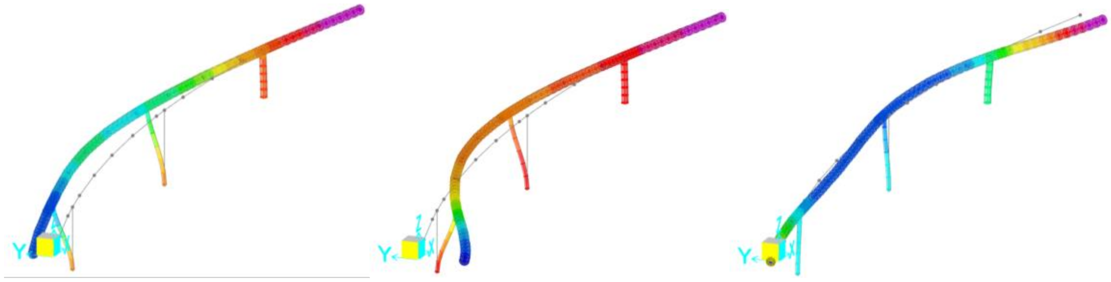

(a) Mode 1: lateral 0.5235 Hz (b) Mode 2: lateral 0.6536 Hz (c) Mode 3: lateral 0.9067 Hz

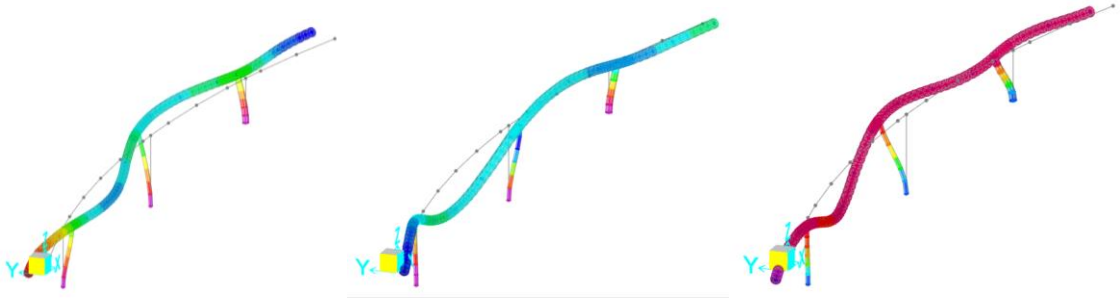

(d) Mode 4: lateral 0.7927 Hz (e) Mode 5: vertical 1.3312 Hz (f) Mode 6: vertical 1.4644 Hz

Figure 6.6 Mode shapes

6.5 Experimental Validation

In this section, the proposed multi-boundary interface maRTHS framework is validated by simulating the illustrative example involving the multi-span curved bridge structure. Following an introduction of the experimental platforms and hardware used, the structure is subjected to a bi-directional ground motion. The results for the elastic range are first compared to numerical simulation results. The amplitude of the ground motion is next increased until nonlinear behavior is achieved in the physical substructure.

6.5.1 Experimental setup

The numerical substructure and compensation algorithm are programmed in the real-time MATLAB-Simulink programming environment, on a host PC. Upon compilation, the MATLAB program is converted into a C-language source code and sent to a microcontroller. The graphical user interface based on the Simulink environment are displayed in Appendix A. The Speedgoat performance real-time target machine with a 4.20 GHz processor is the microcontroller of choice in this implementation. Appropriate I/O driver block interface for Simulink real-time are provided by the Speedgoat software library. For the I/O peripherals, two Speedgoat IO133 modules are installed on the performance real-time target machine, each with 68 pins. Two 1/5th-scale LBCBs are used in this study. Operation of each LBCB requires 17 pins which include 6 analog outputs for commanding the actuators, and 13 analog inputs (six loadcells, six external potentiometers, one reference potentiometer). The two LBCBs used herein are labeled LBCB #1 and LBCB #2.

Two Shore Western servo-controllers handles the operations of the two LBCBs and the corresponding Moog G631 2-stage servo valves and hydraulic actuators. A proportional controller programmed in the servo-controller ensures the stability of all actuators. The stroke limits and force capacities of the actuators are discussed in Najafi et al. (2020). The Speedgoat microcontroller and Shore Western servo-controllers communicate via analog I/O terminal boards. Fig. 6.7 provides a schematic of the experimental hardware used for this study.

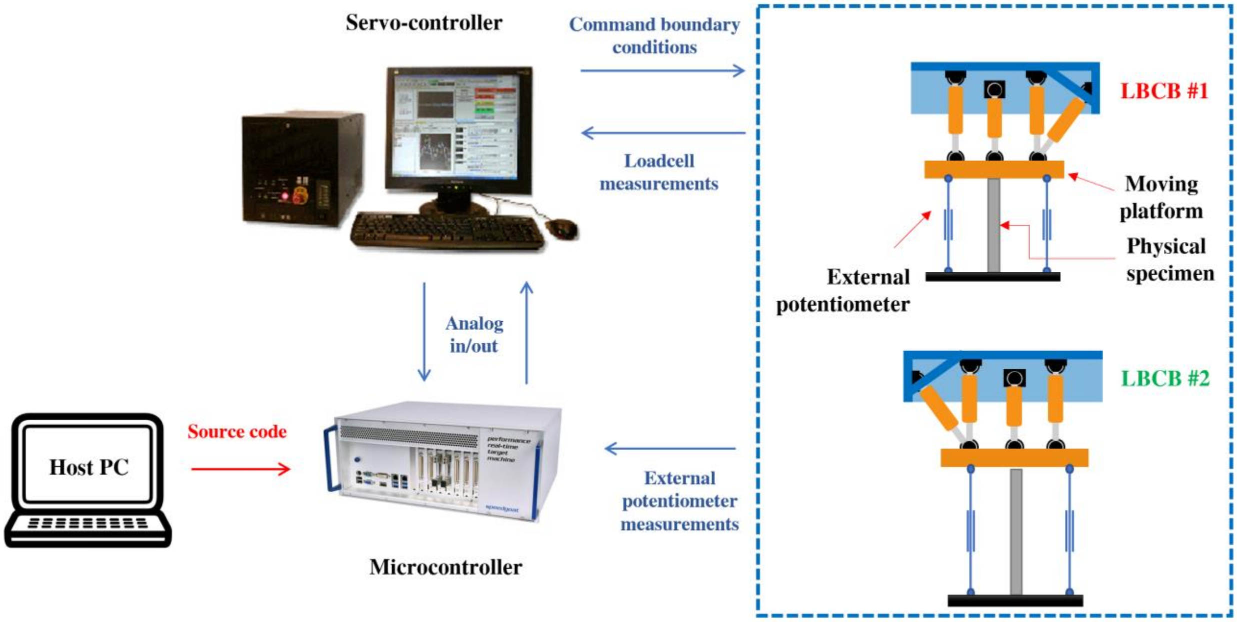

Figure 6.7 Experimental hardware used for maRTHS study

Each actuator onboard the LBCB possesses an inline displacement transducer in the form of LVDTs. However, as demonstrated Najafi et al. (2020) and discussed in Chapter 5, the deformations in the reaction wall and frame of the LBCB result in displacement measurements from LVDTs to be skewed. Therefore, external potentiometers are installed between the top of the physical specimen and base of the reaction wall to ensure more accurate displacement measurements. LBCB #1 uses Celesco CLWG-150-MC4 potentiometers, while LBCB #2 uses Celesco CLP-200 Potentiometers.

The Interface WMC-3000 loadcells are used with each actuator axis. Each loadcell has a capacity of 3 kips. The capacity of the loadcells to measure forces in the Y-direction is about 9 kips. For the steel piers to axially deform by 1 mm, a force of 77.9 kips is required. Therefore, to avoid damaging the loadcells, the Y-direction displacements are truncated out of the model at the locations of the boundary points.

6.5.2 System identification

The updated maRTHS framework uses a model-based control technique to compensate for the dynamics of the actuators. Because of the decoupled nature of the controller, each actuator is compensated independent of the other actuators. A system identification procedure is also necessary to obtain the nominal actuator model necessary for the development of the model-based controller.

A single-input single-output (SISO) identification procedure is employed here, where each of the six actuators onboard an LBCB are subjected to BLWN signal with a 0 – 50 Hz bandwidth, and an rms amplitude of 2 mm. The system identification procedure involves sending a BLWN target signal to actuator i, while the displacements of actuator j is recorded. Each time domain input-output pair r_i and y_j is converted to frequency domain to obtain $R(\Omega)$ and $Y(\Omega)$ at frequency Ω, respectively. The FRF of the input-output pair is obtained per Eq. (2.40).

Data acquisition is completed at a sampling rate of 1000 Hz, NFFT of 8192, and a Hanning window with 50% overlap. The frequency domain fitting tool MFDID is next employed for fitting transfer function models to the FRFs identified (Kim et al. 2005). A six-pole transfer function model is used to describe the FRFs given by Eq. (5.8). Figs. 6.8 and 6.9 summarize the amplitude and phase plots for the six-by-six FRF systems of the two LBCBs used in this study. The off-diagonal terms or coupling between the actuators are deemed to be small and ignored for the purposes of system identification. Hence, the MFDID tool is only used for the on-diagonal terms. Tables 6.3 and 6.4 describe the coefficients of the numerators and denominators of the nominal transfer function models fitted to the FRF plots. The coefficients for the transfer function of actuator $\boldsymbol{P}_{X_1}$ of LBCB #1 are presented in Tables 6.3 and 6.4 and illustrated schematically in the top-left block of Figs. 6.8 and 6.9.

The coupling between the LBCB actuators can be significant when the physical specimen attached to the LBCB is extremely stiff. The off-diagonal terms and the coupling between the actuators should not be ignored in such instances. MIMO or coupled compensators can be useful in addressing the compensation of LBCB setups with very stiff physical specimen.

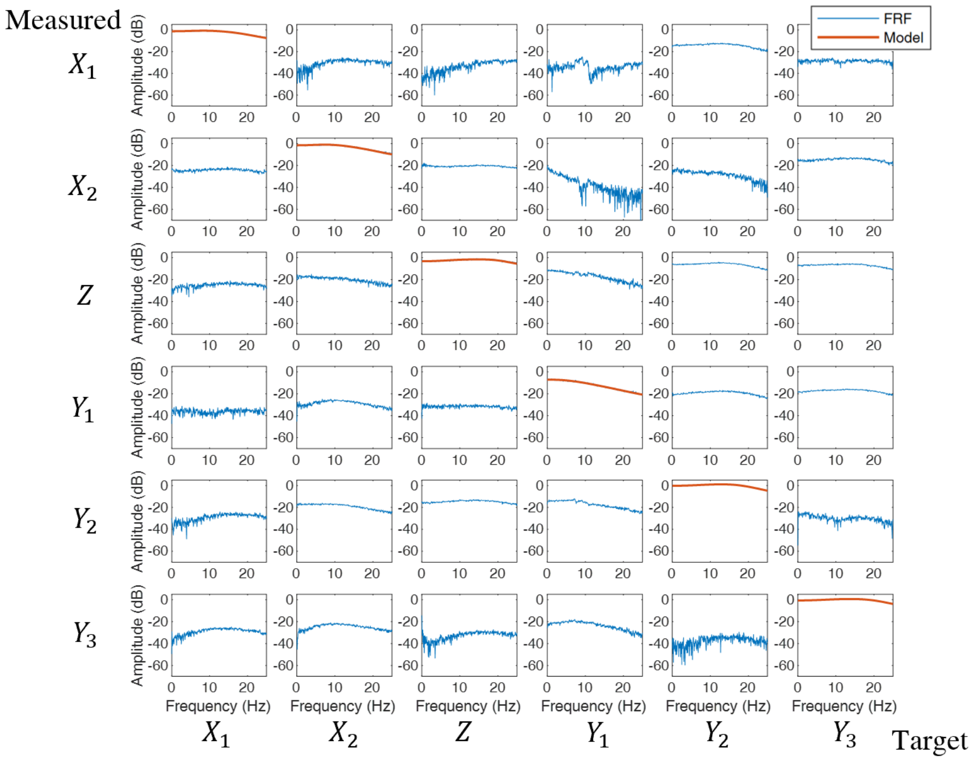

(a) Amplitude

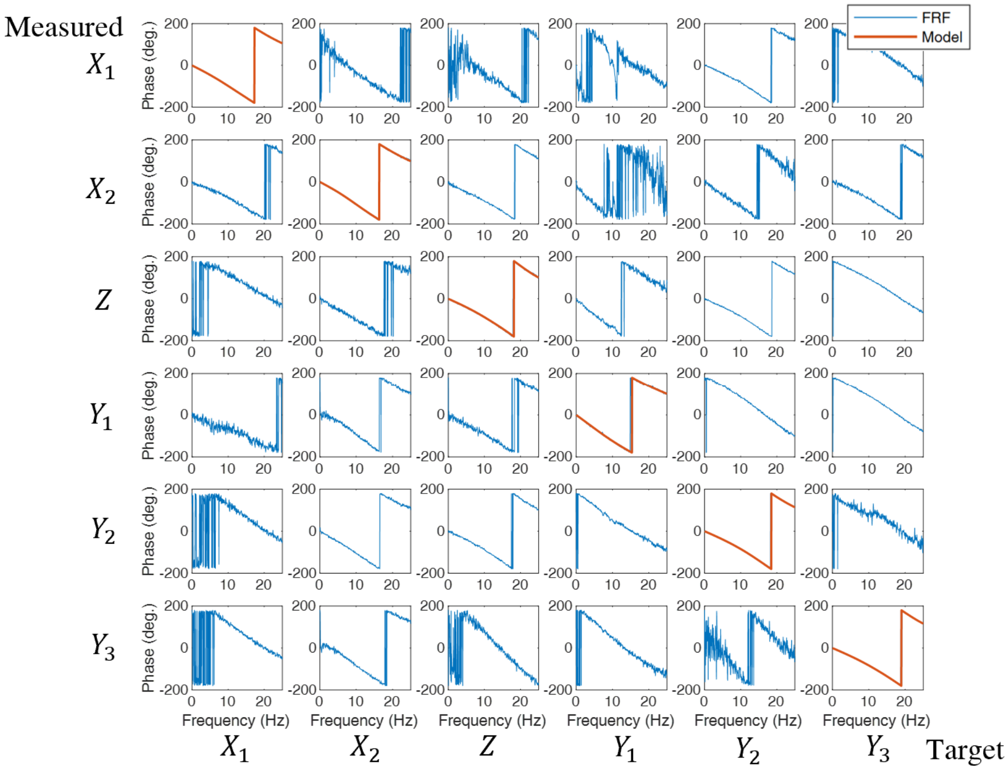

(b) Phase

Figure 6.8 System of FRFs for an LBCB #1 device

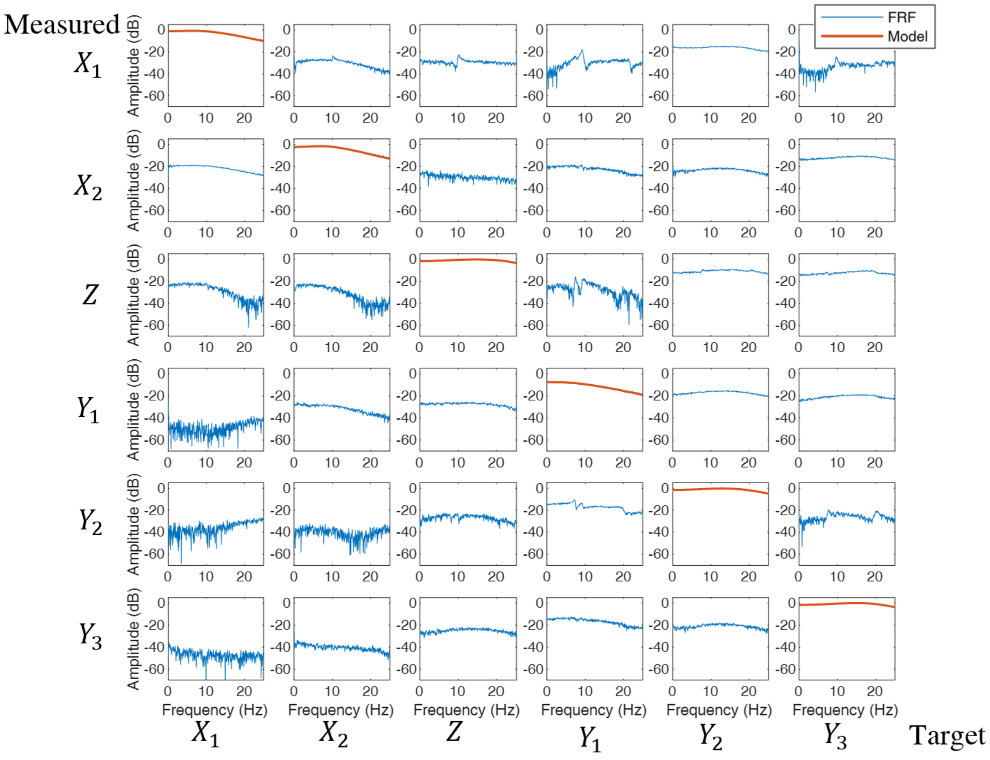

(a) Amplitude

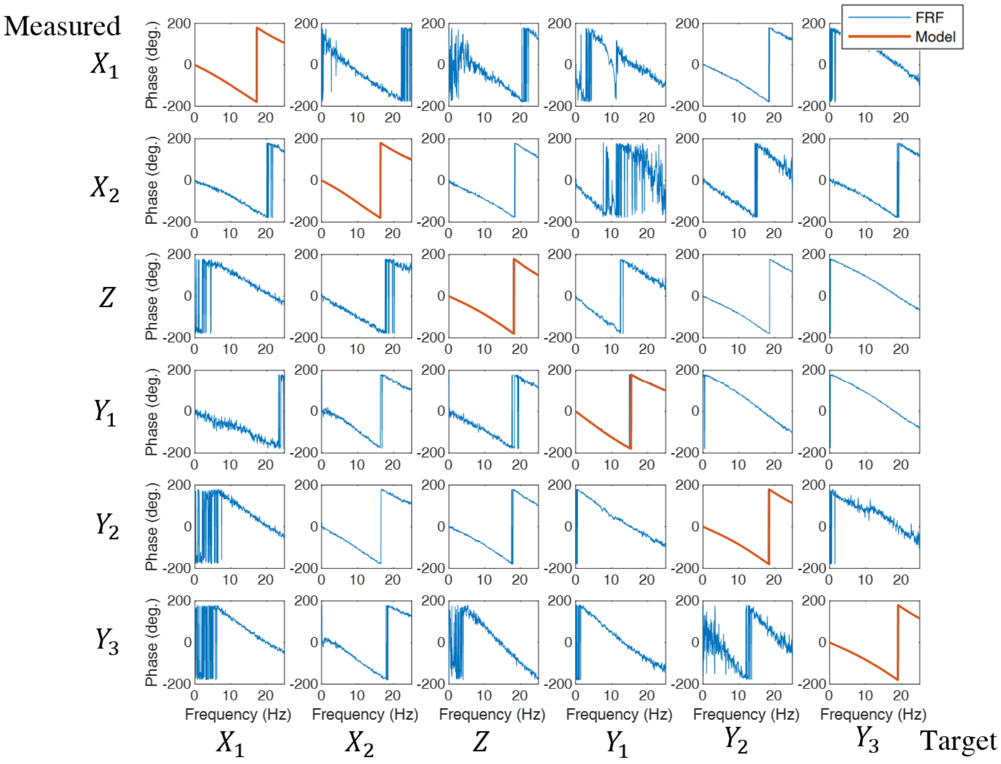

(b) Phase

Figure 6.9 System of FRFs for an LBCB #2 device

Table 6.3 Numerator and denominator coefficient of the transfer function - LBCB #1

Actuator ID	$\alpha_{0,i}$	$\beta_{0,i}$	$\beta_{1,i}$	$\beta_{2,i}$	$\beta_{3,i}$	$\beta_{4,i}$	$\beta_{5,i}$
$\boldsymbol{G}_{X_1}$	$5.403E12$	$6.264E12$	$1.536E11$	$2.175E9$	$1.631E7$	$9.685E4$	279.2
$\boldsymbol{G}_{X_2}$	$4.340E12$	$5.220E12$	$1.344E11$	$2.057E9$	$1.562E7$	$9.612E4$	272.5
$\boldsymbol{G}_{Y}$	$4.291E12$	$6.244E12$	$1.340E11$	$1.851E9$	$1.346E7$	$8.694E4$	242.7
$\boldsymbol{G}_{Z_1}$	$2.004E12$	$4.522E12$	$1.599E11$	$2.498E9$	$2.020E7$	$1.120E5$	332.2
$\boldsymbol{G}_{Z_2}$	$1.191E13$	$1.222E13$	$2.597E11$	$3.330E9$	$2.405E7$	$1.261E5$	352.0
$\boldsymbol{G}_{Z_3}$	$1.036E13$	$1.123E13$	$2.343E11$	$2.972E9$	$2.090E7$	$1.151E5$	310.1

Table 6.4 Numerator and denominator coefficient of the transfer function - LBCB #2

Actuator ID	$\alpha_{0,i}$	$\beta_{0,i}$	$\beta_{1,i}$	$\beta_{2,i}$	$\beta_{3,i}$	$\beta_{4,i}$	$\beta_{5,i}$
$\boldsymbol{G}_{X_1}$	$4.375E12$	$4.992E12$	$1.328E11$	$2.041E9$	$1.579E7$	$9.690E4$	278.2
$\boldsymbol{G}_{X_2}$	$2.710E12$	$3.543E12$	$9.736E10$	$1.659E9$	$1.330E7$	$8.847E4$	253.4
$\boldsymbol{G}_{Y}$	$8.595E12$	$1.060E13$	$2.125E11$	$2.688E9$	$1.815E7$	$1.050E5$	273.1
$\boldsymbol{G}_{Z_1}$	$2.194E12$	$5.201E12$	$1.623E11$	$2.461E9$	$1.898E7$	$1.098E5$	303.1
$\boldsymbol{G}_{Z_2}$	$1.149E13$	$1.374E13$	$2.779E11$	$3.468E9$	$2.341E7$	$1.233E5$	321.5
$\boldsymbol{G}_{Z_3}$	$1.153E13$	$1.406E13$	$2.755E11$	$3.359E9$	$2.269E7$	$1.207E5$	316.5

6.5.3 Kinematic transformations

The Jacobian matrices $\boldsymbol{J}_d$ and $\boldsymbol{J}_\delta$ for the *Force Transform* and *Potentiometer FKT* processes are identified for LBCB #1 and #2, from the linearization of the nonlinear functions in Eqs. (6.1) and (6.2). Elements of the Jacobian $\boldsymbol{J}_d$ describe the linearized relationship between the forces in actuator coordinates to forces in Cartesian coordinates. Elements of Jacobian $\boldsymbol{J}_\delta$ described the linearized relationship between the potentiometer strokes and Cartesian displacements and rotations. The units for these Jacobians are mm for the displacement terms and rad for the rotational terms.

$$\boldsymbol{J}_{d,1} = \begin{bmatrix} -1.00 & 0.02 & -0.01 & 0.06 & 3.85 & 0.50 \\ -1.00 & 0.02 & 0.00 & -0.06 & -3.85 & 0.50 \\ 0.00 & 0.07 & 1.00 & 1.85 & 1.69 & -0.13 \\ -0.02 & 1.00 & 0.01 & 0.00 & 0.04 & -3.54 \\ -0.05 & 1.00 & 0.01 & 3.38 & 0.10 & 5.01 \\ -0.04 & 1.00 & -0.04 & -2.84 & 0.07 & 4.83 \end{bmatrix} \boldsymbol{J}_{\delta,1} = \begin{bmatrix} -0.94 & -0.32 & 0.11 & -0.82 & 2.18 & -0.60 \\ -0.92 & -0.32 & 0.19 & 0.44 & -1.64 & -0.59 \\ -0.01 & -0.24 & 0.97 & -1.99 & -0.66 & -0.18 \\ -0.11 & -0.99 & 0.05 & -0.06 & 0.09 & 1.64 \\ -0.02 & -0.98 & 0.20 & -2.53 & -0.61 & -3.31 \\ -0.02 & -0.99 & 0.11 & 2.19 & -0.43 & -3.35 \end{bmatrix} \quad (6.1)$$

$$\boldsymbol{J}_{d,2}=\begin{bmatrix} 0.94 & -0.34 & 0.03 & -0.75 & -2.05 & 0.82 \\ 0.94 & -0.34 & 0.04 & 0.65 & 1.93 & 0.82 \\ 0.00 & -0.31 & 0.95 & -2.46 & 0.67 & 0.21 \\ -0.01 & -1.00 & 0.05 & -0.08 & -0.09 & -1.86 \\ 0.00 & -1.00 & 0.04 & -2.18 & 0.15 & 3.33 \\ 0.00 & -1.00 & 0.04 & 2.05 & 0.14 & 3.33 \end{bmatrix} \quad \boldsymbol{J}_{\delta,2}=\begin{bmatrix} 1.00 & 0.06 & 0.04 & 0.27 & -3.73 & -1.15 \\ 0.99 & 0.10 & 0.06 & -0.20 & 2.57 & -0.99 \\ -0.01 & 0.10 & 1.00 & 1.32 & 2.45 & -0.23 \\ -0.01 & 1.00 & -0.02 & 0.15 & 0.06 & 3.90 \\ -0.03 & 1.00 & -0.02 & 2.85 & -0.01 & -5.04 \\ -0.02 & 1.00 & -0.02 & -2.90 & -0.18 & -5.20 \end{bmatrix} \tag{6.2}$$

6.5.4 Multi-boundary maRTHS results

The 1940 El Centro earthquake acceleration record is applied bi-directionally as the ground excitation to the multi-span curved bridge structure. The ground accelerations are applied in the X and Z directions and are illustrated in Fig. 6.10. Scales of 5% and 2.5% is applied to the acceleration records in the X and Z directions, respectively, for the initial elastic range study and numerical verification. The scales are next set to 20% and 2.5% in the X and Z directions, respectively, to push the physical specimen into the nonlinear hysteresis range. The amplitude in the Z direction is limited to 2.5% to prevent large amplitude actuation in the Z direction.

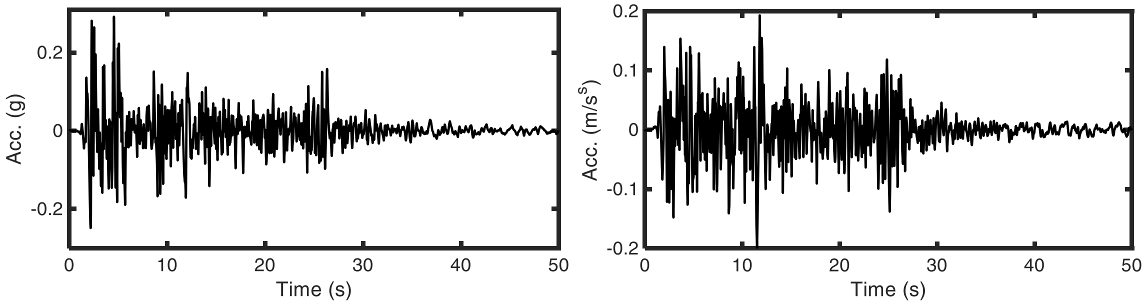

(a) X direction (b) Z direction

Figure 6.10 1940 El Centro ground acceleration

The results presented herein focus on the hysteretic and tracking behavior of the boundary conditions. The hysteretic study focuses on the force-deformation relationship in the structural element of interest. A tracking study assesses how accurately the actuated setup is able to replicate the prescribed trajectory without major delays. The boundary points as illustrated schematically in Fig. 6.3(b) are at the column caps of the physical piers.

To check the quality of the actuator target displacement tracking during the LBCB executions, the two evaluation criteria *RMSE* and *MAXE* per Eqs. (3.21) and (3.22) are used, respectively. Table 6.6 summarizes the tracking performance of the LBCB execution in Cartesian coordinates. Three compensation scenarios are considered: (i) No control, (ii) Feedforward, and (iii) mMBC. For this comparison, the maRTHS loop is left open with feedback forces set to zero. This step is necessary as the no control scenario leads to an unstable execution in the closed-loop maRTHS. Results demonstrate that feedforward and mMBC compensation can drastically reduce the tracking error. The rotational DOF R_Y corresponds to the torsional DOF of the physical specimen, inclusion of compensation worsens the tracking behavior. The torsional DOF is very stiff and difficult to control and compensation methods introduce noise in this channel. The largest errors are observed in the R_X channel of LBCB #1. Tracking errors and noise as a ratio to the small amplitude rotations in this channel (± 0.05 degrees), result in large tracking performance criteria.

Table 6.5 Tracking performance in Cartesian coordinates

	LBCB	LBCB #1					LBCB #2				
	Channel	U_X	U_Z	R_X	R_y	R_Z	U_X	U_Z	R_X	R_Y	R_Z
No Control	RMSE	0.231	0.310	2.436	0.871	0.568	0.251	0.158	0.587	0.551	0.337
	MAXE	0.198	0.297	2.460	0.616	0.520	0.200	0.117	0.411	0.462	0.360
Feedforward	RMSE	0.162	0.175	1.932	0.937	0.370	0.121	0.130	0.611	0.601	0.258
	MAXE	0.130	0.174	2.184	0.723	0.370	0.074	0.120	0.391	0.547	0.291
mMBC	RMSE	0.153	0.107	2.030	0.940	0.336	0.112	0.127	0.588	0.573	0.262
	MAXE	0.122	0.108	2.428	0.737	0.314	0.076	0.115	0.434	0.567	0.254

Figs. 6.11-6.16, demonstrate the tracking synchronization plots for the DOFs for LBCB #1 and LBCB #2. A 1:1 line is illustrative of perfect tracking in this figure. Incorporation of the mMBC generally results in better tracking performance.

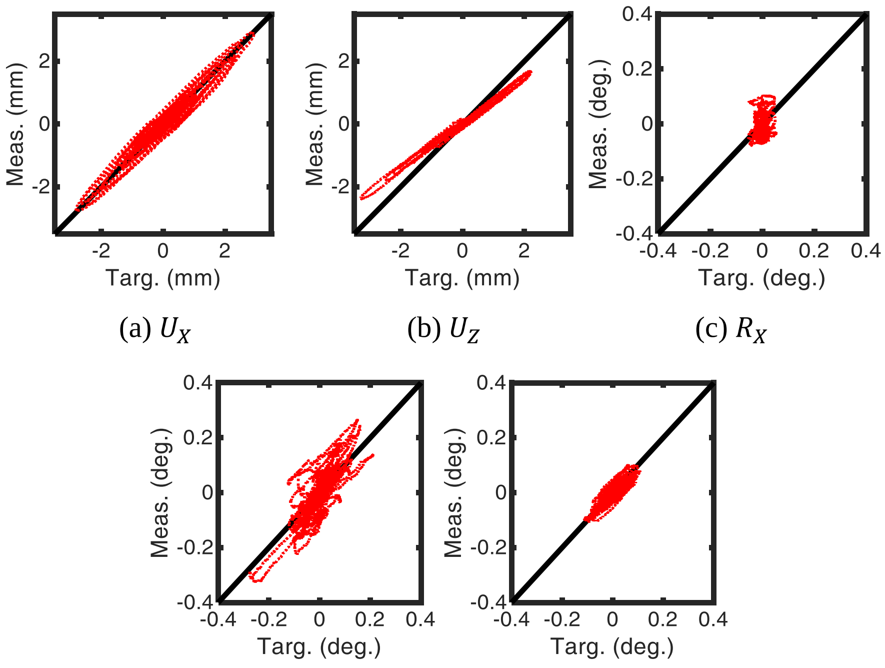

(a) U_X (b) U_Z (c) R_X

(d) R_Y (e) R_Z

Figure 6.11 Tracking synchronization plots for LBCB #1 – No Control

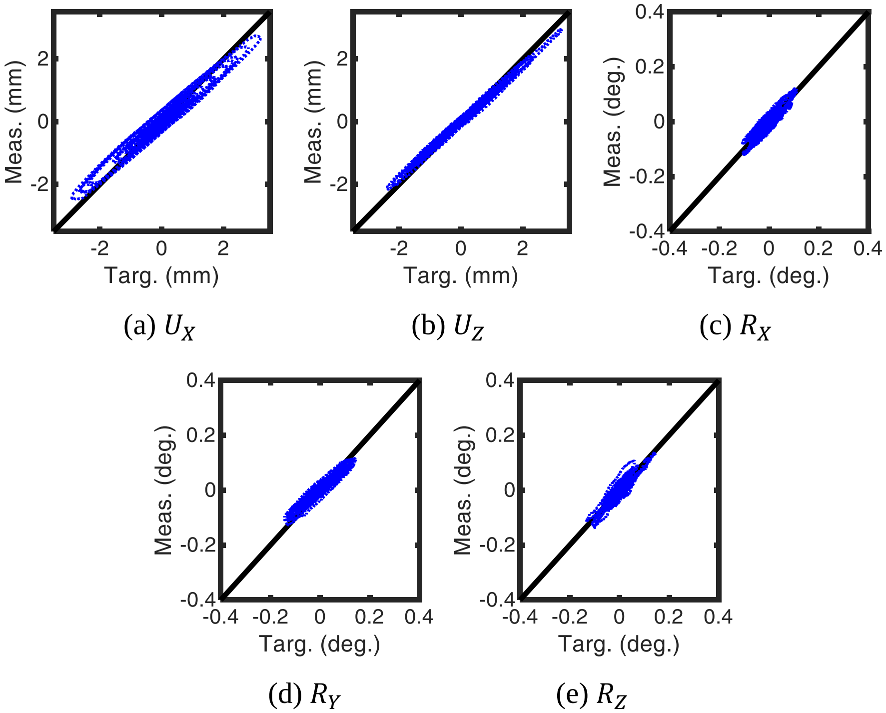

(a) U_X (b) U_Z (c) R_X

(d) R_Y (e) R_Z

Figure 6.12 Tracking synchronization plots for LBCB #2 – No Control

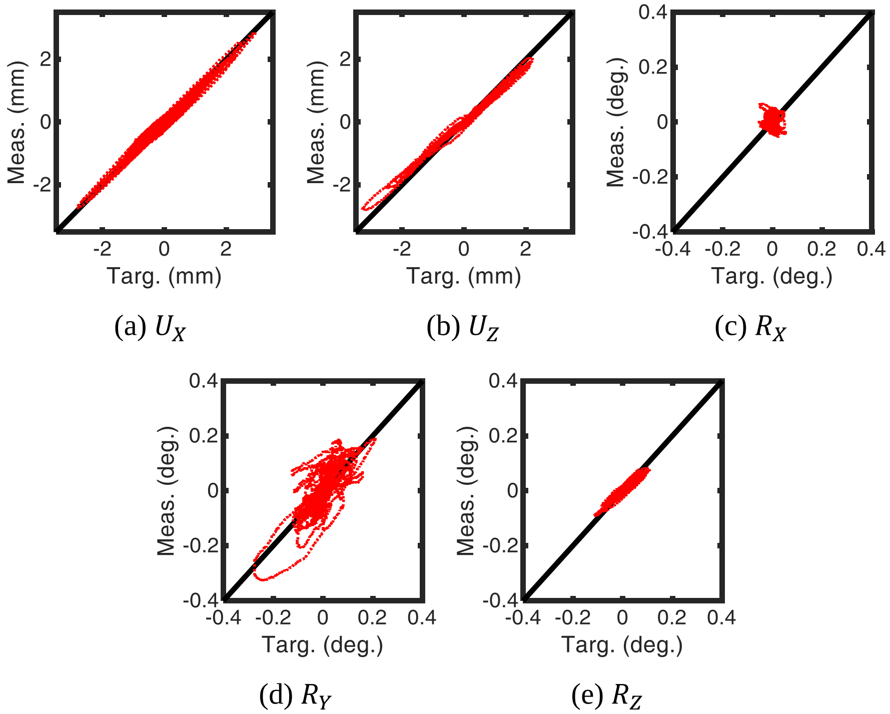

(a) U_X (b) U_Z (c) R_X

(d) R_Y (e) R_Z

Figure 6.13 Tracking synchronization plots for LBCB #1 – Feedforward

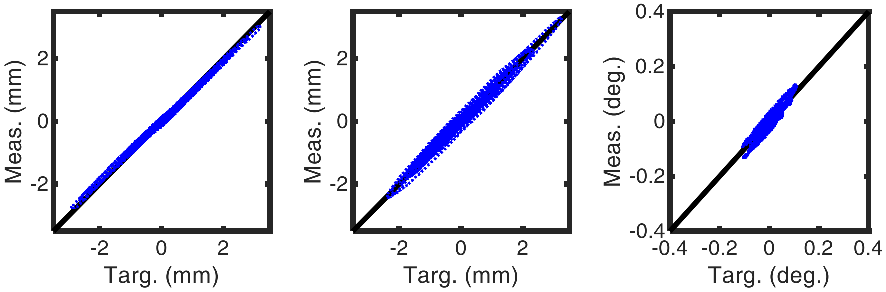

(a) U_X (b) U_Z (c) R_X

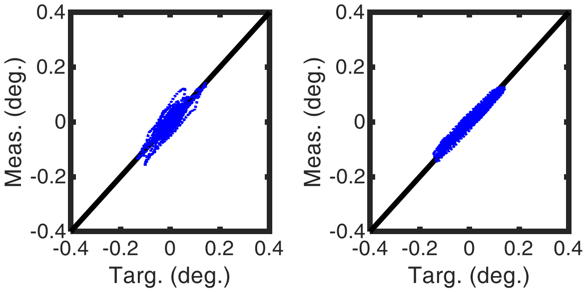

(d) R_Y (e) R_Z

Figure 6.14 Tracking synchronization plots for LBCB #2 – Feedforward

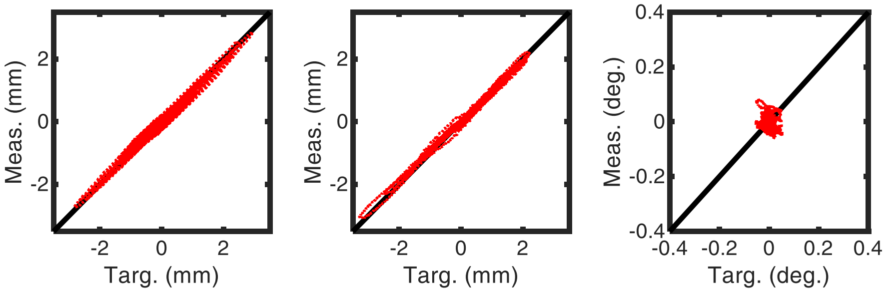

(a) U_X (b) U_Z (c) R_X

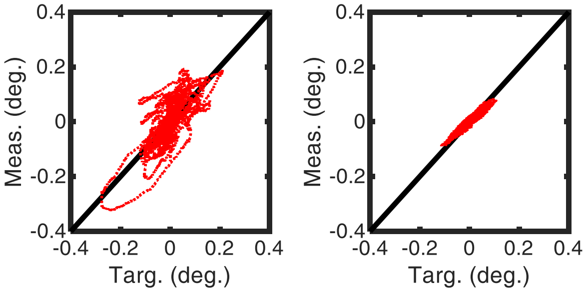

(d) R_Y (e) R_Z

Figure 6.15 Tracking synchronization plots for LBCB #1 – mMBC

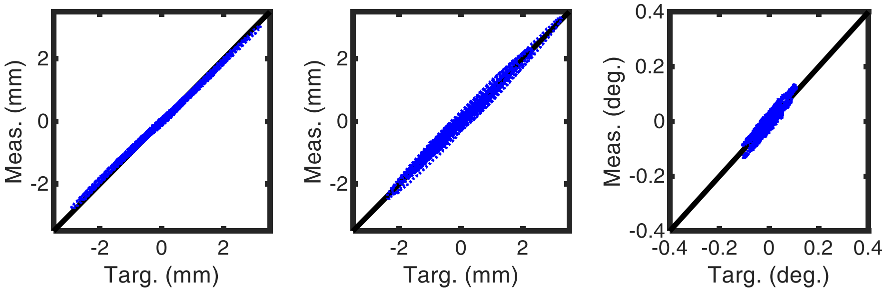

(a) U_X (b) U_Z (c) R_X

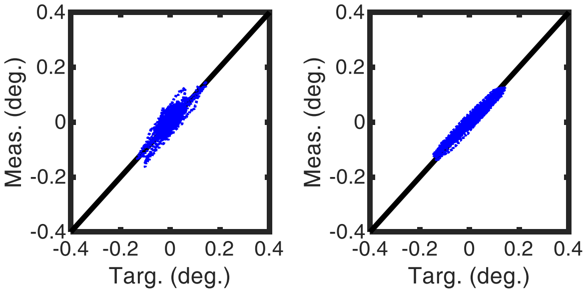

(d) R_Y (e) R_Z

Figure 6.16 Tracking synchronization plots for LBCB #2 – mMBC

Fig. 6.17–6.20 illustrate the deformation and force results of numerical simulation and maRTHS tests in the 5 directions for both LBCBs. The small amplitude ground motions are used for this comparison to ensure that the physical testing stays in the elastic range. The mMBC algorithm is employed for this implementation. By comparing maRTHS results to the numerical simulations, the accuracy of the execution proposed maRTHS framework is verified.

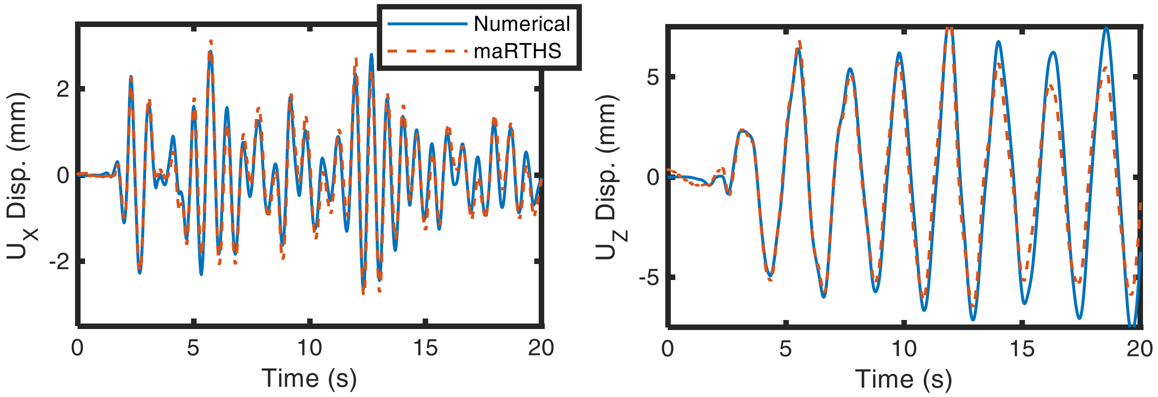

(a) U_X (b) U_Z

Figure 6.17 Numerical simulation and maRTHS of the multi-span curved bridge, LBCB #1 DOFs

Figure 6.17 (continued)

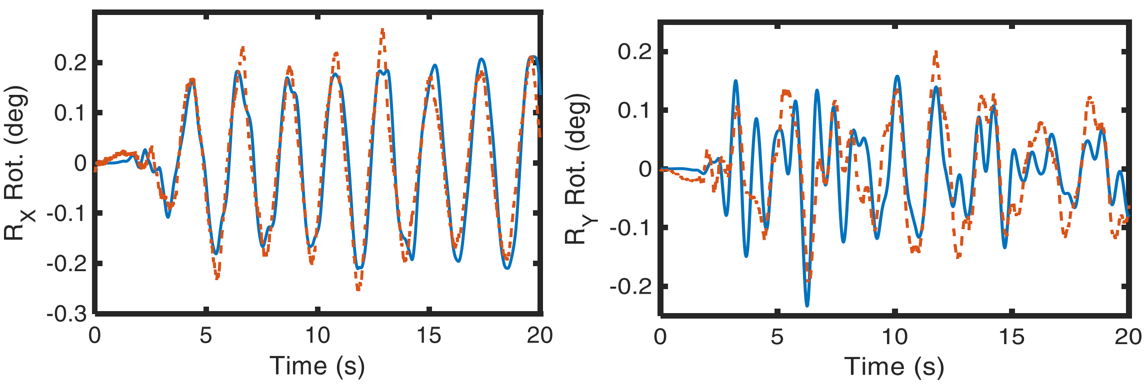

(c) R_X (d) R_Y

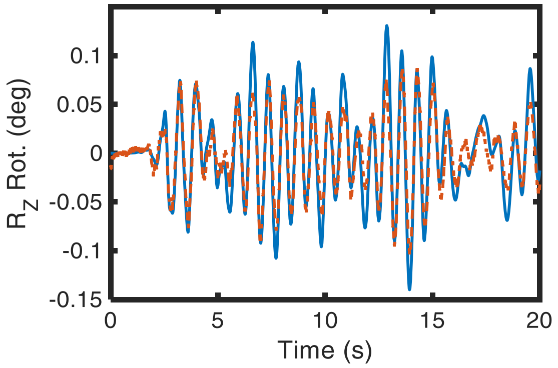

(e) R_Z

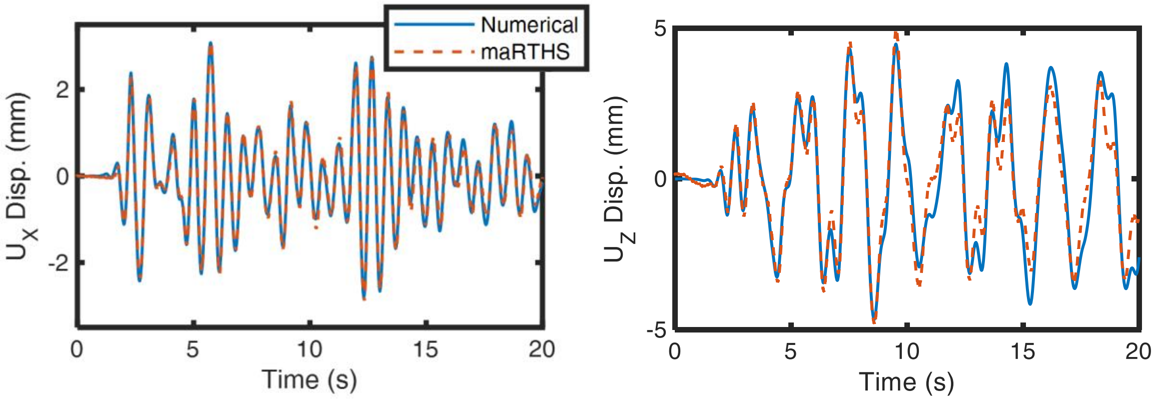

(a) U_X (b) U_Z

Figure 6.18 Numerical simulation and maRTHS of the multi-span curved bridge, LBCB #2 DOFs

Figure 6.18 (continued)

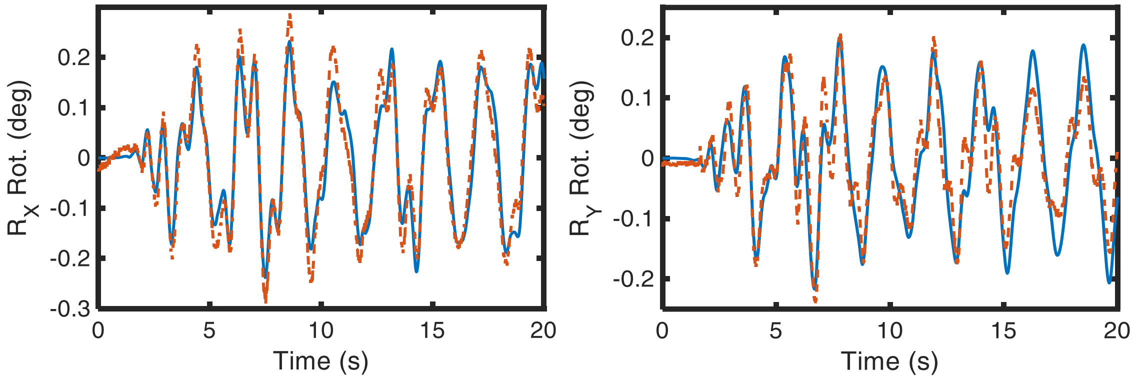

(c) R_X (d) R_Y

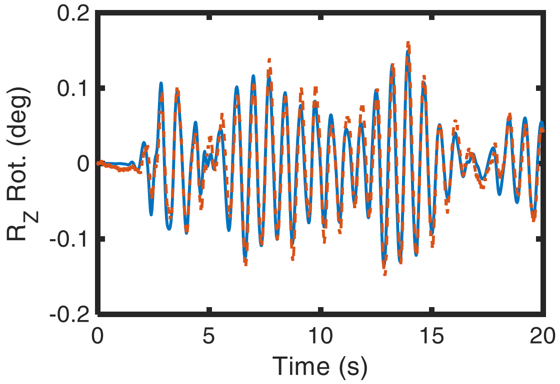

(e) R_Z

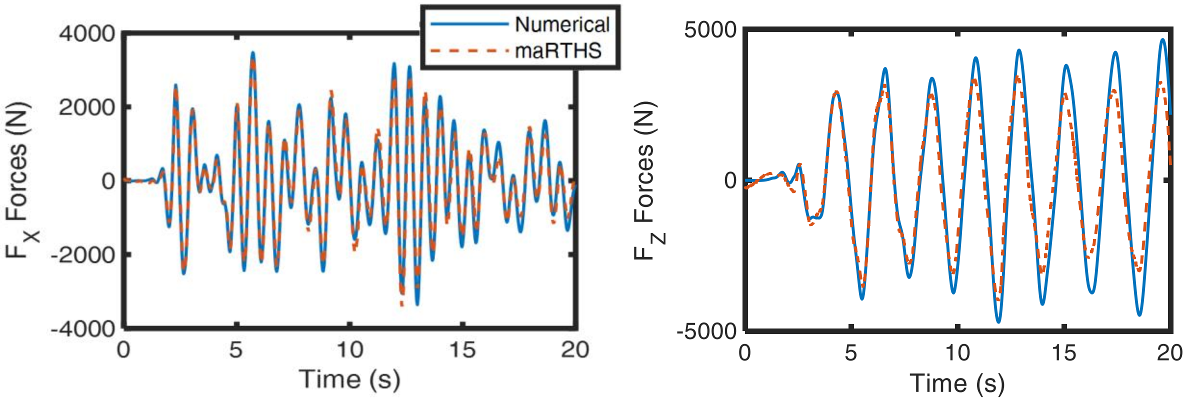

(a) F_X (b) F_Z

Figure 6.19 Numerical simulation and maRTHS of the multi-span curved bridge, LBCB #1 forces

Figure 6.19 (continued)

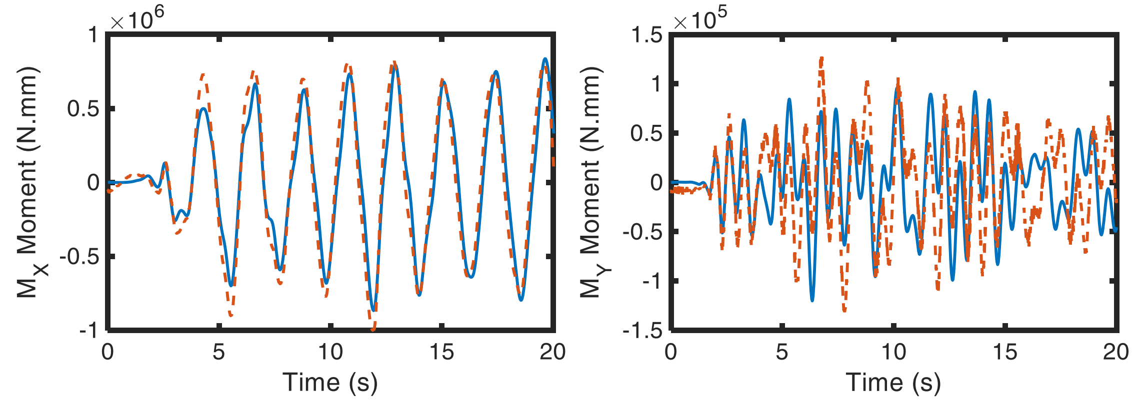

(c) M_X (d) M_Y

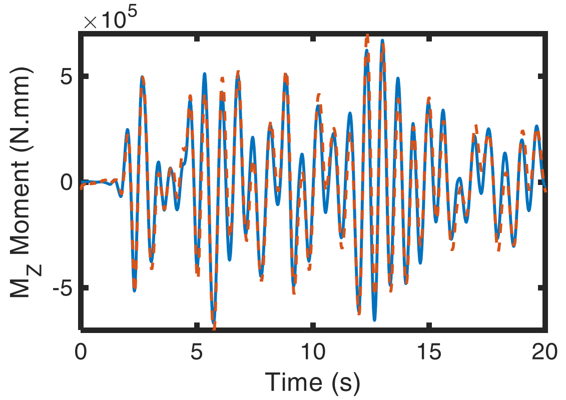

(e) M_Z

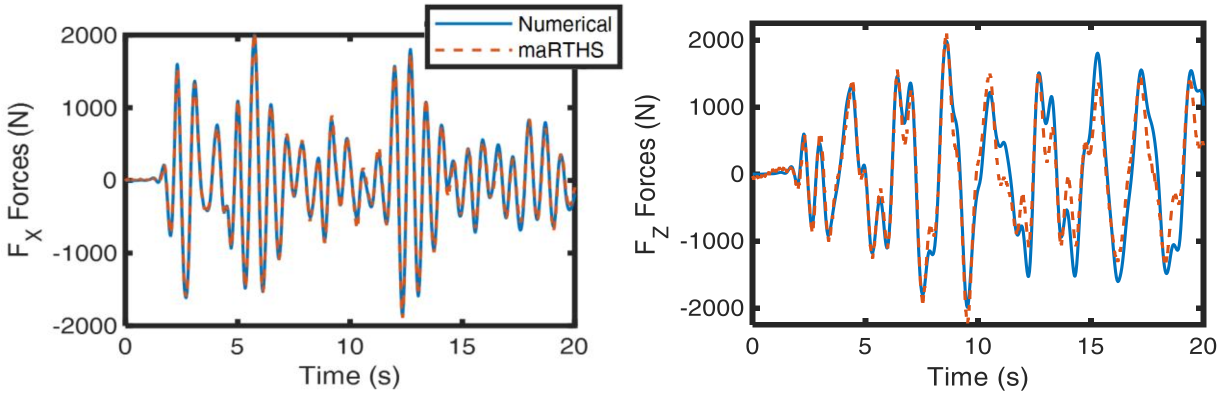

(a) F_X (b) F_Z

Figure 6.20 Numerical simulation and maRTHS of the multi-span curved bridge, LBCB #2 forces

Figure 6.20 (continued)

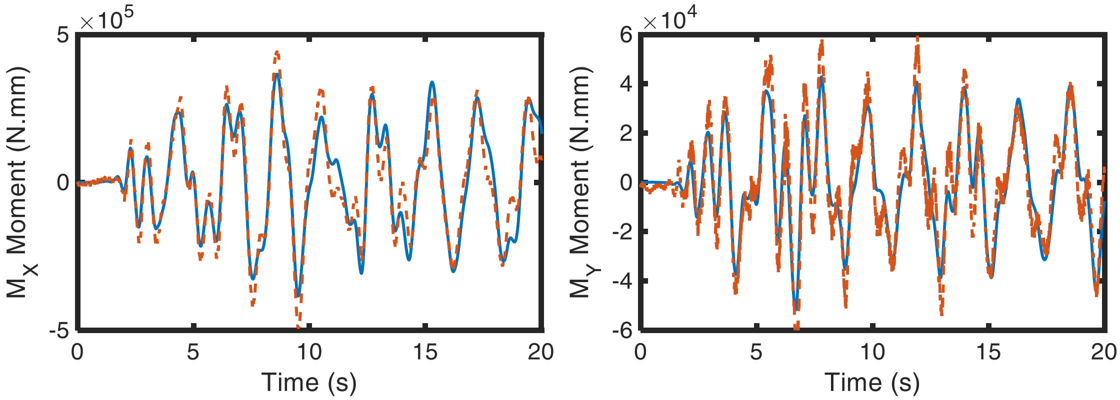

(c) M_X (d) M_Y

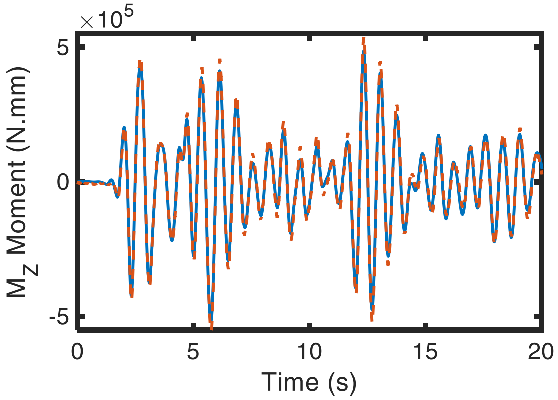

(e) M_Z

Fig. 6.21–6.22 illustrate the hysteretic behaviors of the physical piers connected to LBCB #1 and LBCB #2. The amplitude of the bi-axial ground motion is increased to ensure that nonlinearity is achieved in the physical piers. The proposed maRTHS framework is capable of handling sophisticated nonlinear dynamical behaviors as demonstrated in Fig. 6.21–6.22 and may be attractive for a variety of experimental tests and simulations.

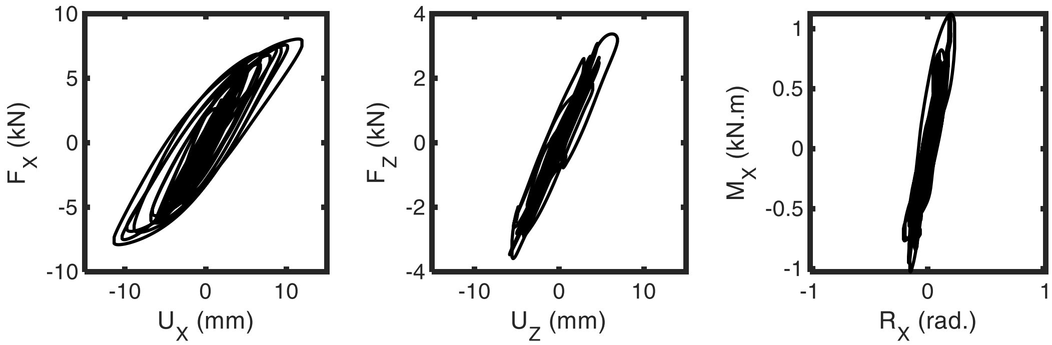

(a) $U_X - F_X$ (b) $U_Z - F_Z$ (c) $R_X - M_X$

Figure 6.21 Hysteretic behaviors of LBCB #1

Figure 6.21 (continued)

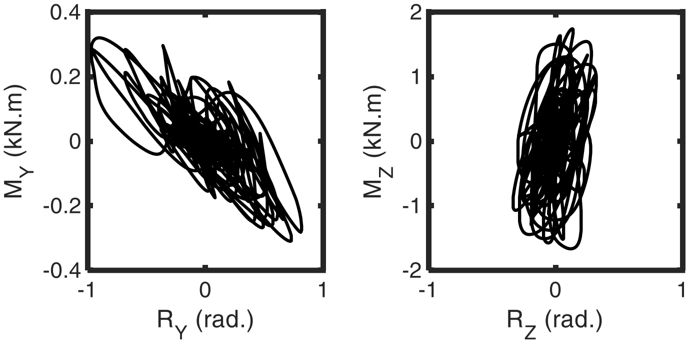

(d) $R_Y - M_Y$ (e) $R_Z - M_Z$

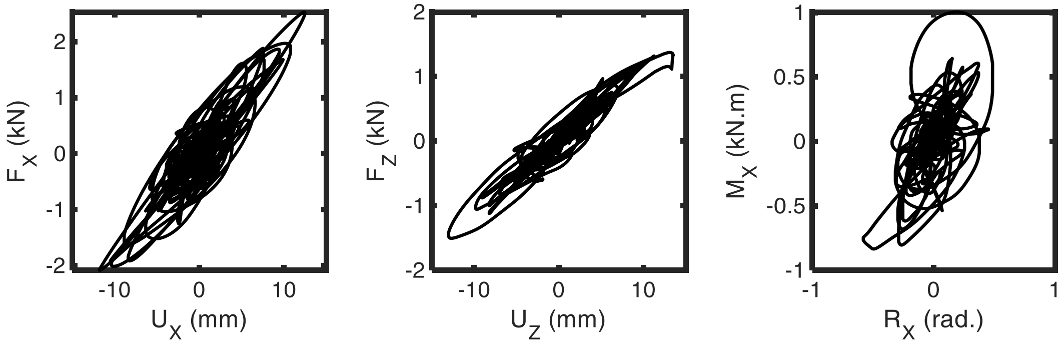

(a) $U_X - F_X$ (b) $U_Z - F_Z$ (c) $R_X - M_X$

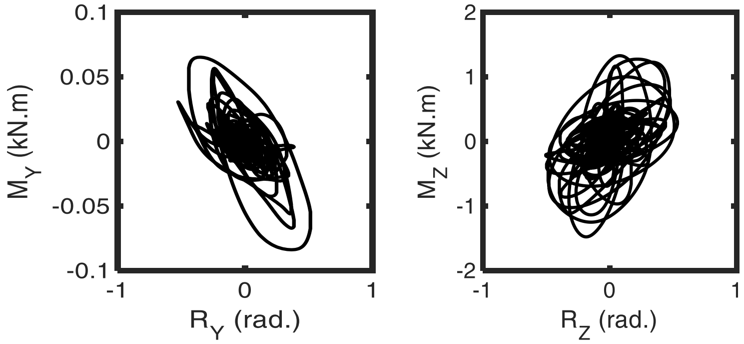

(d) $R_Y - M_Y$ (e) $R_Z - M_Z$

Figure 6.22 Hysteretic behaviors of LBCB #2

The inertial effects of the mass of the moving platform are next studied. The physical specimen attached to LBCB #1 is removed to avoid measuring of the specimen restoring forces. The small-amplitude El Centro ground motion scales of 5% and 2.5% in the X and Z directions, respectively, are imposed on the substructured system. The measured forces in LBCB #1 without a physical specimen are compared to the case where the physical specimen is included. The measured force for the case without the physical specimen includes the inertial force of the moving platform and some friction forces that exist as a result of the swivel joints. Table 4 summarizes the peak forces in each case and evaluates the effect of the inertial force as a percentage of the total force measured for the RTHS scenario where the physical specimen is attached to LBCB #1. Fig. 19 presents the hysteretic behavior of the inertial effects in the X and Z directions. Based on the results presented, the inertial effects of the moving platform are deemed to be negligible.

6.6 Effects of Inertia on Measured Force

The inertial effects of the mass of the moving platform are next studied. The physical specimen attached to LBCB #1 is removed to avoid measuring of the specimen restoring forces. The small-amplitude El Centro ground motion scales of 5% and 2.5% in the X and Z directions, respectively, are imposed on the substructured system. The measured forces in LBCB #1 without a physical specimen are compared to the case where the physical specimen is included. The measured force for the case without the physical specimen includes the inertial force of the moving platform and some friction forces that exist as a result of the swivel joints. Table 6.6 summarizes the peak forces in each case and evaluates the effect of the inertial force as a percentage of the total force measured for the RTHS scenario where the physical specimen is attached to LBCB #1. Fig. 6.23 presents the hysteretic behavior of the inertial effects in the X and Z directions. Based on the results presented, the inertial effects of the moving platform are deemed to be negligible.

Table 6.6 Inertial forces study in LBCB #1

Force (kN)	with specimen	without specimen	% of inertial component
F_X	3.295	0.017	0.51
F_Z	2.135	0.016	0.75

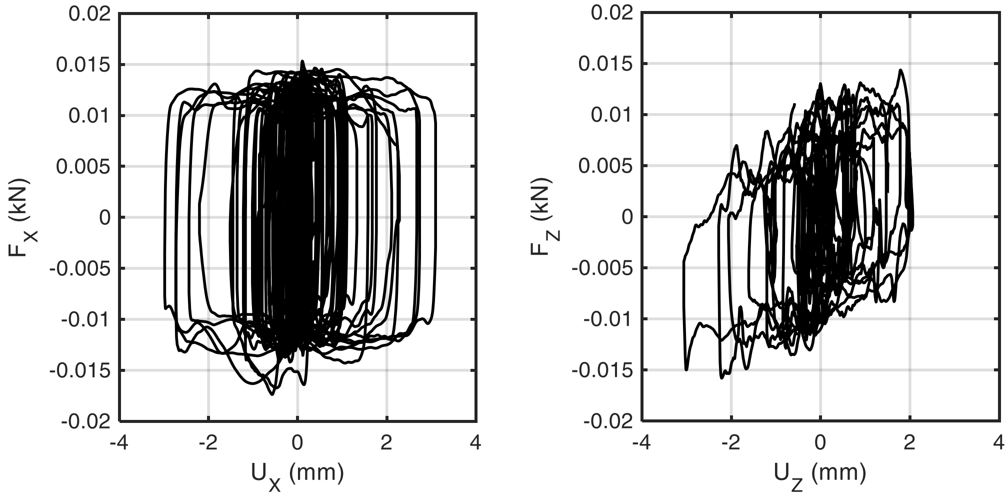

(a) $F_X - U_X$ (b) $F_Z - U_Z$

Figure 6.23 Hysteretic behavior in the X and Z directions for LBCB #1 without a physical specimen

6.7 Summary

A multi-axial real-time hybrid simulation (maRTHS) framework was proposed for use with multiple boundary interfaces and physical substructures. In the previous developments, out-of-plane dynamical behaviors were not considered, and hence this study was an opportunity to introduce higher degrees of freedom and out-of-plane motions to ensure that the maRTHS methodology is capable handling increased dynamical sophistications. A decoupled control algorithm was introduced which successfully compensated for the physical coupling between the actuators and the numerical coupling due to the hybrid simulation.

A multi-span curved bridge structure was then studied to validate the framework. The deck and one of the bridge piers were modeled numerically, while two piers are tested physically. Steel is used as the material for the physical and numerical substructures for ease of design and repeatability. Several studies were conducted including an actuator tracking study in the Cartesian frame of reference, maRTHS versus pure numerical simulation while the structure remains in the elastic range, and final a nonlinear dynamic test. The proposed maRTHS framework proved to be successful in capturing realistic nonlinear dynamic behavior of structural systems.

CHAPTER 7 CONCLUSIONS AND FUTURE STUDIES

7.1 Conclusions

In this dissertation, key algorithms were presented as part of a multi-axial real-time hybrid simulation (maRTHS) framework with substructuring at multiple boundary points, for nonlinear dynamic testing of structural systems. The proposed framework allows the acquisition of the three-dimensional behaviors of structures, execution at real speeds of natural hazard excitations, and substructuring of reference structures into numerical and physical components for flexibility, cost and space savings. The developments presented included compensation approaches for reducing unwanted dynamics of actuators, system identification strategies, kinematic transformations for converting in-axis actuator forces and strokes to Cartesian conditions, and computational resources and laboratory requirements for successful implementation of maRTHS framework. These algorithms were all experimentally verified.

On path towards the development of a compensation strategy for the maRTHS framework, a modified Model-Based Control (mMBC) actuator compensation strategy was proposed with excellent tracking and stability properties. Following system identification of the physical setup (i.e., actuator and physical specimen), feedforward and feedback controllers are developed and tuned for optimal tracking performance and stability. In the new modified framework, the feedforward controller is moved into the feedback loop, and the feedback compensator is designed based on the combined action of the feedforward controller and plant dynamics. The small-gain theorem was used to demonstrate the predictability and enhanced stability of the mMBC strategy. The mMBC was next incorporated in single-axis real-time hybrid simulation and shake table test demonstrations for validation.

The mMBC was next augmented with an adaptive law to create the adaptive Model Reference Control (aMRC). In this development, a reference model is designed as a lowpass filter. The mMBC tries follow the trajectory predicted by the reference model. Whenever the mMBC prediction is not matching the reference model, the adaptive feature kicks in to compensate. An integral control adaptive law with projection algorithm was proposed for rapid adaptation and prevention of drifting. The aMRC was incorporated into a virtual RTHS benchmark problem and evaluated against several other compensation strategies.

A one-boundary point maRTHS framework was next developed. In this framework, actuator and Cartesian signals measured in the physical substructure and calculated by the numerical substructure are related via forward and inverse kinematic processes. The actuator compensation takes place in actuator coordinates in a decoupled manner, where each actuator is compensated independent of the others. The mMBC algorithm was used for actuator coordinate compensation. Decoupled compensators are considerably easier to tune and optimize than multi-input multi-output coupled compensators. Actuator and sensor measurements and commands were converted to Cartesian coordinates via several kinematic transformation steps. Inverse kinematics converted Cartesian signals to actuator signals, and forward kinematics converted actuator and displacement transducer signals to Cartesian signals. Force kinematics converted in-axis loadcell measurements to Cartesian forces and moments. This framework was executed on a steel moment frame structure where one column of the frame is physically tested, while the remainder of the structure is numerically modeled. In this experiment, out-of-plane excitations were not considered.

Finally, the maRTHS framework was augmented to incorporated multiple boundary interfaces and multiple physical specimens. In this augmented framework, each boundary interface has its own kinematic transformation and decoupled actuator control steps. The experimental setups necessary for conducting maRTHS with high DOFs are also noted. For the validation of the multi-boundary point maRTHS, a multi-span curved bridge structure was selected. Two piers were tested physically while the remainder of the structure remained nonlinear. The maRTHS framework with multiple boundary points is a promising experimental technique for examining the nonlinear dynamical behavior of structures and is useful for studying structural behavior under natural hazard excitation.

7.2 Future Studies

7.2.1 Mixed-mode control

In section 3.2, the concept of setpoint tracking was introduced with a focus on displacement and acceleration signals for RTHS applications. In some RTHS experiments, such as the effective force testing method, the setpoint is a force signal that needs to be tracked. In many structural engineering experimental applications however, displacement and force need to be tracked at the same time. An example of such application is observed in earthquake engineering applications where a lateral load is applied on the physical specimen of the interest, while a gravitational downward force is needed to simulate the self-weight of the structure. Future research should focus on efficient methods for incorporating deformation and force signals into a combined mixed-mode control strategy.

7.2.2 Kinematic transformation algorithms

In section 2.6, 5.2, and 6.5, the forward and inverse kinematic transformations for parallel manipulators were listed. In such devices, it was mentioned that the forward kinematic transformation computation is challenging task, and hence linearization was made about the equilibrium position. Linearized approximations can deviate from the true solution of the nonlinear system of equations as the states of the manipulator deviate farther from the equilibrium position. Future research should consider higher-order approximations of the nonlinear system of equations or solve the system of equations in a computationally efficient manner.

7.2.3 Machine learning uses in hybrid simulation

Machine learning algorithms are computational tools that learn and improve through experience. Training data are used to program and optimize models of systems. The predictive abilities of machine learning algorithms have proven very attractive in the recent years. Machine learning algorithms have huge untapped potentials in the RTHS domain and can be used for efficiently and rapidly modeling of nonlinear systems. With applications in nonlinear actuator compensation, nonlinear finite element modeling, and real-time system identification of nonlinear physical system, machine learning can help solve nontrivial dynamical problems.

7.2.4 Stability guarantees studies

Instability problems are a common occurrence when dealing with actuated setups and dynamical speeds. Real-time hybrid simulation in particular is prone to many different forms of instabilities as a result of closed-loop delays. Therefore, in the recent years many researchers have used mathematical theorems from control theory such as the small-gain theory, like in Section 3.4, and phase and gain margin analyses to try and predict the stability behavior of a closed-loop RTHS system. However, because many of these RTHS systems are nonlinear and hard to model, stability predictors are not always successful. Future studies should identify newer and more complete ways of designing RTHS systems that are stable.

7.2.5 Nonlinear dynamic studies

Many of the existing RTHS frameworks involve linearized system identification, compensation, and other transformations. Because of the linear architecture of this frameworks, it is unclear to what extent the physical behavior can be pushed into the nonlinear range. Future studies should focus on studying the nonlinearity range that the linearized RTHS system can explore and continue to produce realistic results.

REFERENCES

Abdelnaby, A. E., Frankie, T. M., and Elnashai, A. S. (2012). "Numerical Hybrid Simulation Modeling Verification for a Curved 3-Pier Bridge (Investigation of Combined Actions on Reinforced Concrete Bridge Piers (CABER) Project)." *The 3rd International Multi-Conference on Complexity, Informatics and Cybernetics*, International Institute of Informatics and Systemics, IIIS, Orlando, 48–51.

Ahmadizadeh, M., Mosqueda, G., and Reinhorn, A. M. (2008). "Compensation of actuator delay and dynamics for real-time hybrid structural simulation." *Earthquake Engineering & Structural Dynamics*, 37(1), 21–42.

Asai, T., Chang, C., Phillips, B. M., and Jr, B. F. S. (2013). "Real-time hybrid simulation of a smart outrigger damping system for high-rise buildings." *Engineering Structures*, Elsevier Ltd, 57, 177–188.

Ashasi-Sorkhabi, A., Malekghasemi, H., and Mercan, O. (2015). "Implementation and verification of real-time hybrid simulation (RTHS) using a shake table for research and education." *Journal of Vibration and Control*, 21(8), 1459–1472.

Ashter, S. A. (2014). *Thermoforming of Single and Multilayer Laminates: Plastic Films Technologies, Testing, and Applications*. Elsevier.

Berndat, J. S., and Piersol, A. G. (2010). *Random data: analysis and measurement procedure*. Wiley, Hoboken.

Blakeborough, B. A., Williams, M. S., Darby, A. P., and Williams, D. M. (2001). "The development of real-time substructure testing." *Philosophical Transactions of the Royal Society of London. Series A: Mathematical, Physical and Engineering Sciences*, 359(1786), 1869–1891.

Bonnet, P. A., Lim, C. N., Williams, M. S., Blakeborough, A., Neild, S. A., Stoten, D. P., and Taylor, C. A. (2007). "Real-time hybrid experiments with Newmark integration , MCSmd outer-loop control and multi-tasking strategies." *Earthquake Engineering & Structural Dynamics*, 36(1), 119–141.

Campbell, J. D. (1954). "The yield of mild steel under impact loading." *Journal of the Mechanics and Physics of Solids*, 3(1), 54–62.

Cao, C., and Hovakimyan, N. (2009). "L1 adaptive output feedback controller for non strictly positive real Multi-input Multi-output systems in the presence of unknown nonlinearities." *American Control Conference*, St. Louis, 5138–5143.

Carrion, J. E., and Spencer, Jr., B. F. (2007). *Model-based Strategies for Real-time Hybrid Testing*. Urbana.

Carrion, J. E., Spencer Jr., B. F., and Phillips, B. M. (2009). "Real-time hybrid simulation for structural control performance assessment." *Earthquake Engineering & Engineering Vibration*, 8(4), 481–492.

Chae, Y., Kazemibidokhti, K., and Ricles, J. M. (2013). "Adaptive time series compensator for delay compensation of servo-hydraulic actuator systems for real-time hybrid simulation." *Earthquake Engineering & Structural Dynamics*, 42(11), 1697–1715.

Chae, Y., Park, M., Kim, C., and Suk, Y. (2017). "Experimental study on the rate-dependency of reinforced concrete structures using slow and real-time hybrid simulations." *Engineering Structures*, Elsevier Ltd, 132, 648–658.

Chae, Y., Ricles, J. M., and Sause, R. (2014). "Large-scale real-time hybrid simulation of a three-story steel frame building with magneto-rheological dampers." *Earthquake Engineering & Structural Dynamics*, 43(13), 1915–1933.

Chang, C. M., Frankie, T. M., Spencer, B. F., and Kuchma, D. A. (2014). "Multiple degrees of freedom positioning correction for hybrid simulation." *Journal of Earthquake Engineering*, Informa UK Limited, 19(2), 277–296.

Chang, K.-C., and Lee, G. C. (1987). "Strain Rate Effect on Structural Steel under Cyclic Loading." *Journal of Engineering Mechanics*, 113(9), 1292–1301.

Chang, K. C., Sugiura, K., and Lee, G. C. (1989). "Rate-Dependent Material Model for Structural Steel." *Journal of Engineering Mechanics*, 115(3), 465–474.

Changhai, L., and Hongzhou, J. (2014). "A seventh-order model for dynamic response of an electro-hydraulic servo valve." *Chinese Journal of Aeronautics*, Chinese Society of Aeronautics and Astronautics, 27(6), 1605–1611.

Chen, C.-T. (1999). *Linear System Theory and Design*. (A. S. Sedra and M. R. Lightner, eds.), Oxford University Press, New York.

Chen, C., and Ricles, J. M. (2010). "Tracking Error-Based Servohydraulic Actuator Adaptive Compensation for Real-Time Hybrid Simulation." *Journal of Structural Engineering*, 136(4), 432–440.

Chen, P.-C., Chang, C.-M., Spencer, Jr., B. F., and Tsai, K.-C. (2015). "Adaptive model-based tracking control for real-time hybrid simulation." *Bulletin of Earthquake Engineering*, 13(6), 1633–1653.

Chen, X., Wu, S., Zhou, J., Chen, Y., and Qin, A. (2013). "Effect of testing method and strain rate on stress-strain behavior of concrete." *Journal of Materials in Civil Engineering*, 25(11), 1752–1761.

Chopra, A. K. (2011). *Dynamics of Structures: Theory and Applications to Earthquake Engineering*. Prentice Hall.

Craig, R. R., and Kurdila, A. J. (2006). *Fundamentals of Structural Dynamics*. Wiley.

Cristescu, N. D. (1967). *Dynamic Plasticity*.

Darby, A. P., Williams, M. S., and Blakeborough, A. (2002). "Stability and delay compensation for real-time substructure testing." *Journal of Engineering Mechanics*, 128(12), 1276–1284.

Datta, B. N. (2003). *Numerical Methods for Linear Control Systems*. Academic Press.

Dermitzakis, S. N., and Mahin, S. A. (1985). *Development of substructuring techniques for on-line computer controlled seismic performance testing*. Berkeley.

Dimig, J., Shield, C., French, C., Bailey, F., and Clark, A. (1999). “Effective Force Testing: A Method of Seismic Simulation for Structural Testing.” *Journal of Structural Engineering*, 125(9), 1028–1037.

Dormand, J. R., El_Mikkawy, M. E. A., and Prince, P. J. (1987). “High-Order Embedded Runge-Kutta-Nystrom Formulae.” *Journal of Numerical Analysis*, 7, 423–430.

Drazin, P. L., and Govindjee, S. (2017). “Hybrid simulation theory for a classical nonlinear dynamical system.” *Journal of Sound and Vibration*, Elsevier, 392(3), 240–259.

Dullerud, G. E., and Paganini, F. (2000). *A Course in Robust Control Theory - A Convex Approach*. (J. E. Marsden, L. Sirovich, and S. S. Antman, eds.), Springer.

Dyke, S. J., and Caicedo, J. M. (2002). “The University Consortium on Instructional Shake Tables.” *Proceedings of the ICANCEER Conference*, Harbin.

Dyke, S. J., Spencer, Jr., B. F., Quast, P., and Sain, M. K. (1995). “Role of Control-Structure Interaction in Protective System Design.” *Journal of Engineering Mechanics*, 121(2), 322–338.

Elnashai, A. S., Spencer, B. F., Kuchma, D. A., Yang, G., Carrion, J., Gan, Q., and Kim, S. J. (2005). “The multi-axial full-scale sub-structured testing and simulation (MUST-SIM) facility at the University of Illinois at Urbana-Champaign.” *Advances in Earthquake Engineering for Urban Risk Reduction*, Springer, Istanbul, Turkey, 245–260.

Esparza, C., Núñez, R., and González, F. (2013). “Model Reference Adaptive Position Controller with Smith Predictor for Shaking-Table in Two Axes.” *Mexican International Conference on Artifical Intelligence*, Springer-Verlag Berlin, 271–282.

Fan, G., Song, Y., and Wang, L. (2014). “Experimental study on the seismic behavior of reinforced concrete beam-column joints under various strain rates.” *Journal of Reinforced Plastics & Composites*, 33(7), 601–618.

Fermandois, G. A., and Spencer, Jr., B. F. (2018). “Development and implementation of a multi-axial real-time hybrid simulation framework.” University of Illinois at Urbana-Champaign, Urbana.

Fermandois, G. A., and Spencer, B. F. (2017). “Model-based framework for multi-axial real-time hybrid simulation testing.” *Earthquake Engineering and Engineering Vibration*, 16(4), 671–691.

Fletcher, J. N. (1990). “Global Simulation: New Technique for Multiaxis Test Control.” *Sound and Vibration*, 24(11), 26–33.

Frankie, T., Abdelnaby, A., Silva, P., Sanders, D., Elnashai, A., Kuchma, D., and Chang, C. (2013). “Hybrid simulation of curved four-span bridge.” *Structures Congress*, ASCE, Pittsburgh, 721–732.

Frankie, T. M. (2013). “Impact of Complex System Behavior on Seismic Assessment of RC Bridges.” University of Illinois at Urbana-Champaign, Urbana.

French, C. W., Schultz, A. E., Hajjar, J. F., Shield, C. K., Ernie, D. W., Dexter, R. J., Du, D. H.-C., Olson, S. A., Daugherty, D. J., and Wan, C. P. (2004). “Multi-axial subassemblage testing (MAST) system: description and capabilities.” *13th World Conference on Earthquake Engineering*, Vancouver.

Friedman, A., Dyke, S. J., Phillips, B., Ahn, R., Dong, B., Chae, Y., Castaneda, N., Jiang, Z., Zhang, J., Cha, Y., Ozdagli, A. I., Ricles, J., Christenson, R., Agrawal, A., and Sause, R. (2015). “Large-Scale Real-Time Hybrid Simulation for Evaluation of Advanced Damping System Performance.” *Journal of Structural Engineering*, 141(6).

Friedman, A. J., Zhang, J., Phillips, B., Jiang, Z., Agrawal, A., Dyke, S. J., Ricles, J., Spencer, B., Sause, R., and Christenson, R. (2010). “Accommodating MR Damper Dynamics for Control of Large Scale Structural Systems.” *5th World Conference on Structural Control and Monitoring*, Tokyo, 1–15.

Gao, X., Castaneda, N., and Dyke, S. J. (2011). *Development and Validation of a Robust Actuator Motion Controller for Real-time Hybrid Simulation*. West Lafayette.

Gao, X., Castaneda, N., and Dyke, S. J. (2012). “Real time hybrid simulation: from dynamic system, motion control to experimental error.” *Earthquake Engineering & Structural Dynamics*, 42(6), 815–832.

Ghannoum, W., Saouma, V., Haussmann, G., Polkinghorne, K., Eck, M., and Kang, D.-H. (2012). “Experimental Investigations of Loading Rate Effects in Reinforced Concrete Columns.” *Journal of Structural Engineering*, 138(8), 1032–1041.

Goldsmith, W. (1960). *Impact: the Theory and Physical Behaviour of Colliding Solids*. Edward Arnold Publishers Ltd.

Hakuno, M., Shidawara, M., and Hara, T. (1969). “Dynamic destructive test of a cantilever beam, controlled by an analog-computer.” *Trans. Japan Society of Civil Engineers*, 171, 1–9.

Hanson, R. D., and McClamroch, N. H. (1984). “Pseudo dynamic test method for inelastic building response.” *Proceedings of the 8th World Conference on Earthquake Engineering*, San Francisco, 123–134.

Hashemi, M. J., Al-Ogaidi, Y., Al-Mahaidi, R., Kalfat, R., Tsang, H.-H., and Wilson, J. L. (2017). “Application of Hybrid Simulation for Collapse Assessment of Post-Earthquake CFRP-Repaired RC Columns.” *Journal of Structural Engineering*, 143(1).

He, S., and Sepehri, N. (1999). “Modeling and Prediction of Hydraulic Servo Actuators with Neural Networks.” *Proceedings of the American Control Conference*, San Diego.

Horiuchi, T., Inoue, M., and Konno, T. (2000). “Development of a real-time hybrid experimental system using a shaking table.” *12th World Conference on Earthquake Engineering*, New Zealand Society for Earthquake Engineering, Auckland, 1–8.

Horiuchi, T., Inoue, M., Konno, T., and Namita, Y. (1999). “Real-time hybrid experimental system with actuator delay compensation and its application to piping system with energy absorber.” *Earthquake*

Engineering & Structural Dynamics, 28(10), 1121–1141.

Horiuchi, T., Nakagawa, M., Sugano, M., and Konno, T. (1996). “Development of a Real-time Hybrid Experimental System with Actuator Delay Compensation.” *Proc. of 11th World Conf. Earthquake Engineering*, Pergamon, Acapulco.

Jelali, M., and Kroll, A. (2004). *Hydraulic Servo-systems: Modelling, Identification, and Control*. (M. J. Grimble and M. A. Johnson, eds.), Springer-Verlag London Ltd.

Juang, J., and Pappa, R. S. (1985). “An Eigensystem Realization Algorithm for Modal Parameter Identification and Model Reduction.” *Journal of Guidance, Control, and Dynamics*, 8(5), 620–627.

Jung, R., Shing, P. B., Stauffer, E., and Thoen, B. (2007). “Performance of a real-time pseudodynamic test system considering nonlinear structural response.” *Earthquake Engineering & Structural Dynamics*, 36(12), 1785–1809.

Kennedy, J., and Eberhart, R. (1995). “Particle Swarm Optimization.” *Proceedings of the Internatinal Conference on Neural Networks*, IEEE, Perth, 1942–1948.

Kim, D. H., and Tsau, T.-C. (2000). “A Linearized Electrohydraulic Servovalve Model for Valve Dynamics Sensitivity Analysis and Control System Design.” *Jounral of Dynamic Systems, Measurements, and Control*, 122(1), 179–187.

Kim, S. B., Spencer, Jr., B. F., and Yun, C. (2005). “Frequency Domain Identification of Multi-Input, Multi-Output Systems Considering Physical Relationships between Measured Variables.” *Journal of Engineering Mechanics*, 131(5), 461–472.

Kim, S. J., Holub, C. J., and Elnashai, A. S. (2011). “Experimental investigation of the behavior of RC bridge piers subjected to horizontal and vertical earthquake motion.” *Engineering Structures*, Elsevier Ltd, 33(7), 2221–2235.

Kwon, O., Elnashai, A. S., and Spencer, Jr., B. F. (2005). “A framework for multi-site distributed simulation and application to complex structural systems.” *Journal of Earthquake Engineering*, 9(5), 741–753.

Lamarche, C. P., Tremblay, R., Leger, P., Leclerc, M., and Bursi, O. S. (2010). “Comparison between real-time dynamic substructuring and shake table testing techniques for nonlinear seismic applications.” *Earthquake Engineering and Structural Dynamics*, 39(12), 1299–1320.

Li, M., and Li, H. (2012). “Effects of Loading Rate on Reinforced Concrete Beams.” *17th World Conference on Earthquake Engineering*, Lisbon.

Luco, J. E., Ozcelik, O., and Conte, J. P. (2010). “Acceleration Tracking Performance of the UCSD-NEES Shake Table.” *Journal of Structural Engineering*, 136(5), 481–490.

Maghareh, A., Dyke, S. J., and Bunting, G. B. (2013). “Establishing a predictive performance indicator for real-time hybrid simulation.” *Earthquake Engineering & Structural Dynamics*, 42(6), 815–832.

Mahin, S. A., and Shing, P. B. (1985). “Pseudodynamic method for seismic testing.” *Journal of Structural*

Engineering, 111(7), 1482–1503.

Mahmoud, H. N., Elnashai, A. S., Spencer, Jr., B. F., Kwon, O.-S., and Bennier, D. J. (2013). “Hybrid Simulation for Earthquake Response of Semirigid Partial-Strength Steel Frames.” *Journal of Structural Engineering*, 139(7), 1134–1148.

Malvar, L. J., and Ross, C. A. (1998). “Review of Strain Rate Effects for Concrete in Tension.” *ACI Materials Journal*, 95(6), 735–739.

MathWorks. (2020). “Solver.” *The MathWorks, Inc.*, <https://www.mathworks.com/help/simulink/gui/solver.html> (May 27, 2020).

Mercan, O., and Ricles, J. M. (2009). “Experimental studies on real-time testing of structures with elastomeric dampers.” *Journal of Structural Engineering*, 135(9), 1124–1133.

Merritt, H. E. (1967). “Hydraulic control systems.” John Wiley & Sons, Inc.

Moni, M., Hwang, Y., Kwon, O., Kim, H., and Jeong, U. Y. (2020). “Real-Time Aeroelastic Hybrid Simulation of a Base-Pivoting Building Model in a Wind Tunnel.” *Computational Methods in Structural Engineering*, 6(September), 1–16.

Mosqueda, G., Stojadinovic, B., and Mahin, S. A. (2004). “Geographically distributed continuous hybrid simulation.” *13th World Conference on Earthquake Engineering*, Vancouver.

Mu, D., and Li, C. (2011). “A New Mathematical Model of Twin Flapper-nozzle Servo Valve Based on Input-output Linearization Approach.” *2nd International Conference on Artificial Intelligence, Management Science and Electronic Commerce*, IEEE, Dengleng, 3662–3666.

Murray, J. A., and Sasani, M. (2016). “Near-collapse response of existing RC building under severe pulse-type ground motion using hybrid simulation.” *Earthquake Engineering & Structural Dynamics*, 45(7), 1109–1127.

Murray, M. P., Rowell, S. P., and Thornton, T. A. (2014). *Effects of High Strain Rates on ASTM A992 and A572 Grade 50 Steel*.

Najafi, A., Fermandois, G. A., and Spencer, Jr., B. F. (2020). “Decoupled Model-Based Real-Time Hybrid Simulation with Multi-Axial Load and Boundary Condition Boxes.” *Engineering Structures*.

Najafi, A., and Spencer, Jr., B. F. (2020). “Modified model-based control of shake tables for online acceleration tracking.” *Earthquake Engineering & Structural Dynamics*.

Najafi, A., and Spencer, B. F. (2019). “Adaptive model reference control method for real-time hybrid simulation.” *Mechanical Systems and Signal Processing*, Elsevier Ltd, 132, 183–193.

Nakashima, M. (2020). “Hybrid simulation : An early history.” *Earthquake Engineering & Structural Dynamics*, 49(10), 949–962.

Nakashima, M., Ishida, M., and Ando, K. (1990). “Integration techniques for substructure pseudo dynamic test.” *Journal of Structures and Construction Engineering*, 417.

Nakashima, M., and Kato, H. (1987). "Experimental error growth behavior and error growth control in on-line computer test control method." *Building Research Institute, Ministry of Construction*, No. 123.

Nakashima, M., Kato, H., and Takaoka, E. (1992). "Development of real-time pseudo dynamic testing." *Earthquake Engineering and Structural Dynamics*, 21(1), 79–92.

Nakata, N. (2010). "Acceleration trajectory tracking control for earthquake simulators." *Engineering Structures*, 32(8), 2229–2236.

Nakata, N., Erb, R., and Stehman, M. (2019). "Mixed Force and Displacement Control for Testing Base-Isolated Bearings in Real-Time Hybrid Simulation Mixed Force and Displacement Control for Testing Base-Isolated." *Journal of Earthquake Engineering*, Taylor & Francis, 23(6), 1055–1071.

Nakata, N., Spencer, Jr., B. F., and Elnashai, A. S. (2010). "Sensitivity-Based External Calibration of Multiaxial Loading System." *Journal of Engineering Mechanics*, 136(2), 189–198.

Ohtani, K., Ogawa, N., Katayama, T., and Shibata, H. (2004). "Construction of E-Defense (3-D Full-scale Earthquake Testing Facility)." *13th World Conference on Earthquake Engineering*, Canadian Association for Earthquake Engineering, Vancouver.

Ou, G., Ozdagli, A. I., Dyke, S. J., and Wu, B. (2015). "Robust integrated actuator control: experimental verification and real-time hybrid-simulation implementation." *Earthquake Engineering & Structural Dynamics*, 44(3), 441–460.

Peeters, B., and Roeck, G. De. (1999). "Reference-based stochastic subspace identification for output-only modal analysis." *Mechanical Systems and Signal Processing*, 13(6), 855–878.

Phillips, B. M., and Spencer, B. F. (2013). "Model-Based Multiactuator Control for Real-Time Hybrid Simulation." *Journal of Engineering Mechanics*, 139(2), 219–228.

Phillips, B. M., Wierschem, N. E., and Spencer, Jr., B. F. (2014). "Model-based multi-metric control of uniaxial shake tables." *Earthquake Engineering & Structural Dynamics*, 43(5), 681–699.

Qian, Y., Ou, G., Maghareh, A., and Dyke, S. J. (2014). "Parametric identification of a servo-hydraulic actuator for real-time hybrid simulation." *Mechanical Systems and Signal Processing*, 48(1–2), 260–273.

Rea, D., Abedi-Hayati, S., and Takahashi, Y. (1977). *Dynamic Analysis of Electrohydraulic Shaking Tables*. Berkeley.

Reinhorn, A. M., Bruneau, M., Whittaker, A. S., Constantinou, M. C., Thevanayagam, S., Sivaselvan, M., Shao, X., Hanley, J., Pitman, M. C., and Albrechcinski, T. (2004). "The UB-NEES Versitile High Pefromance Testing Facility." *13th World Conference on Earthquake Engineering*, Canadian Association for Earthquake Engineering, Vancouver.

Reinhorn, A. M., Sivaselvan, M. V, Liang, Z., Shao, X., and Weinreber, S. (2003). "Large scale real time dynamic hybrid testing technique – Shake tables substructure testing." *Proc. of ASCE Structures*

Congress Seattle WA, 587(c), 457–464.

Sadeghian, V., Kwon, O., and Vecchio, F. (2017). “Small-scale multi-axial hybrid simulation of a shear-critical reinforced concrete frame.” *Earthquake Engineering and Engineering Vibration*, 16(4), 727–743.

Severn, R. T. (2011). “The development of shaking tables – A historical note.” *Earthquake Engineering & Structural Dynamics*, 40(2), 195–213.

Severn, R. T., Stoten, D. P., and Tagawa, Y. (2012). “The Contribution Of Shaking Tables To Earthquake Engineering.” *Proc. of 15th World Conference on Earthquake Engineering*, Lisbon.

Shao, X., Reinhorn, A. M., and Sivaselvan, M. V. (2011). “Real-Time Hybrid Simulation Using Shake Tables and Dynamic Actuators.” *Journal of Structural Engineering*, 137(7), 748–760.

Shing, P. B., and Mahin, S. A. (1983). *Experimental error propagation in pseudodynamic testing*. Berkeley.

Shing, P. B., and Mahin, S. A. (1988). “Rate-of-Loading Effects on Pseudodynamic Tests.” *Journal of Structural Engineering*, 114(11), 2403–2420.

Shing, P. B., Vannan, M. T., and Cater, E. (1991). “Implicit time integration for pseudodynamic tests.” *Earthquake Engineering and Engineering Vibration*, 20(6), 551–576.

Silva, C. E., Gomez, D., Maghareh, A., Dyke, S. J., and Spencer Jr., B. F. (2020). “Benchmark control problem for real-time hybrid simulation.” *Mechanical Systems and Signal Processing*, Elsevier Ltd, 135.

Singh, M., Sood, D., Gupta, R. K., Kumar, R., Gautam, P. C., Sewak, B., Sharma, A. C., and Mathew, T. (2008). “Dynamic Yield Strength of Mild Steel under Impact Loading.” *Defence Science Journal*, 58(2), 275–284.

Spencer, B. F., and Yang, G. (1998). “Earthquake Simulator Control by Transfer Function Iteration.” *Proceedings of the 12th ASCE engineering mechanics conference*.

Spong, M. W., Hutchinson, S., and Vidyasagar, M. (2005). *Robot Modeling and Control*. Wiley.

Stathas, N., Skafida, S., Bousias, S. N., Fardis, M. N., Digenis, S., and Palios, X. (2017). “Hybrid simulation of bridge pier uplifting.” *Bulletin of Earthquake Engineering*, Springer Netherlands, 15(8), 3385–3398.

Stoten, D. P., and Shimizu, N. (2007). “The feedforward minimal control synthesis algorithm and its application to the control of shaking-tables.” *Journal of Systems and Control Engineering*, 221(3), 423–444.

Takanashi, K., and Ohi, K. (1983). “Earthquake response analysis of steel structures by rapid computer-actuator on-line system.” *Bulletin of Earthquake Engineering*, 16, 103–109.

Takanashi, K., Udagawa, K., Seki, M., Okada, T., and Tanaka, T. (1975). “Non-linear earthquake response analysis of structures by a computer-actuator on-line system (details of the system).” *Architectural*

Institute of Japan Transactions, 229, 77–83.

Tell, S., Andersson, A., Karoumi, R., Najafi, A., and Spencer, B. F. (2019). "Real-time hybrid simulation of a bridge-damper system." *Proceedings of the 7th International Conference on Structural Engineering*, Mechanics and Computation, Cape Town, 1810–1813.

Thewalt, C. R., and Mahin, S. A. (1987). *Hybrid solution techniques for generalized pseudodynamic testing*. Berkeley.

Tidwell, T., Gao, X., Huang, H., Lu, C., Dyke, S., and Gill, C. (2009). "Towards Configurable Real-Time Hybrid Structural Testing : A Cyber-Physical Systems Approach." *IEEE International Symposium on Object/Component/Service-Oriented Real-Time Distributed Computing*, IEEE, Tokyo, 37–44.

Tsai, L.-W. (1999). *Robot Analysis: The Mechanics of Serial and Parallel Manipulators*. Wiley-Interscience.

Tsai, M.-C., and Gu, D.-W. (2014). *Robust and Optimal Control: A Two-port Framework Appraoch*. (M. J. Grimble and M. A. Johnson, eds.), Springer-Verlag London, London.

Twitchell, B. S., and Symans, M. D. (2003). "Analytical Modeling, System Identification, and Tracking Performance of Uniaxial Seismic Simulators." *Journal of Engineering Mechanics*, 129(12), 1485–1488.

Wallace, M. I., Wagg, D. J., and Neild, S. A. (2005). "An adaptive polynomial based forward prediction algorithm for multi-actuator real-time dynamic substructuring." *Proceedings of The Royal Society*, 461(2064), 3807–3826.

Wang, J. F., Lin, C. C., and Chen, B. L. (2003). "Vibration suppression for high-speed railway bridges using tuned mass dampers." *International Journal of Solids and Structures*, 40, 465–491.

Wang, J., Wierschem, N. E., Spencer, Jr., B. F., and Lu, X. (2015). "Experimental study of track nonlinear energy sinks for seismic reduction." *Engineering Structures*, 94, 9–15.

Wu, B., Xu, G., Wang, Q., and Williams, M. S. (2006). "Operator-splitting method for real-time substructure testing." *Earthquake Engineering & Structural Dynamics*, 35(3), 293–314.

Zhang, R., Phillips, B. M., Taniguchi, S., Ikenaga, M., and Ikago, K. (2017). "Shake table real-time hybrid simulation techniques for the performance evaluation of buildings with inter-story isolation." *Structural Control and Health Monitoring*, 24(10), 1–19.

Zhao, J., Shield, C., French, C., and Posbergh, T. (2005). "Nonlinear System Modeling and Velocity Feedback Compensation for Effective Force Testing." *Journal of Engineering Mechanics*, 131(3), 244–253.

Zhou, X. Q., and Hao, H. (2008). "Modelling of compressive behavior of concrete-like materials at high strain rate." *International Journal of Solids and Structures*, 45(17), 4648–4661.

Zhu, F., Wang, J.-T., Jin, F., and Lu, L.-Q. (2017). "Real-time hybrid simulation of full-scale tuned liquid column dampers to control multi-order modal responses of structures." *Engineering Structures*, 138, 74–90.

APPENDIX A GRAPHICAL USER INTERFACE

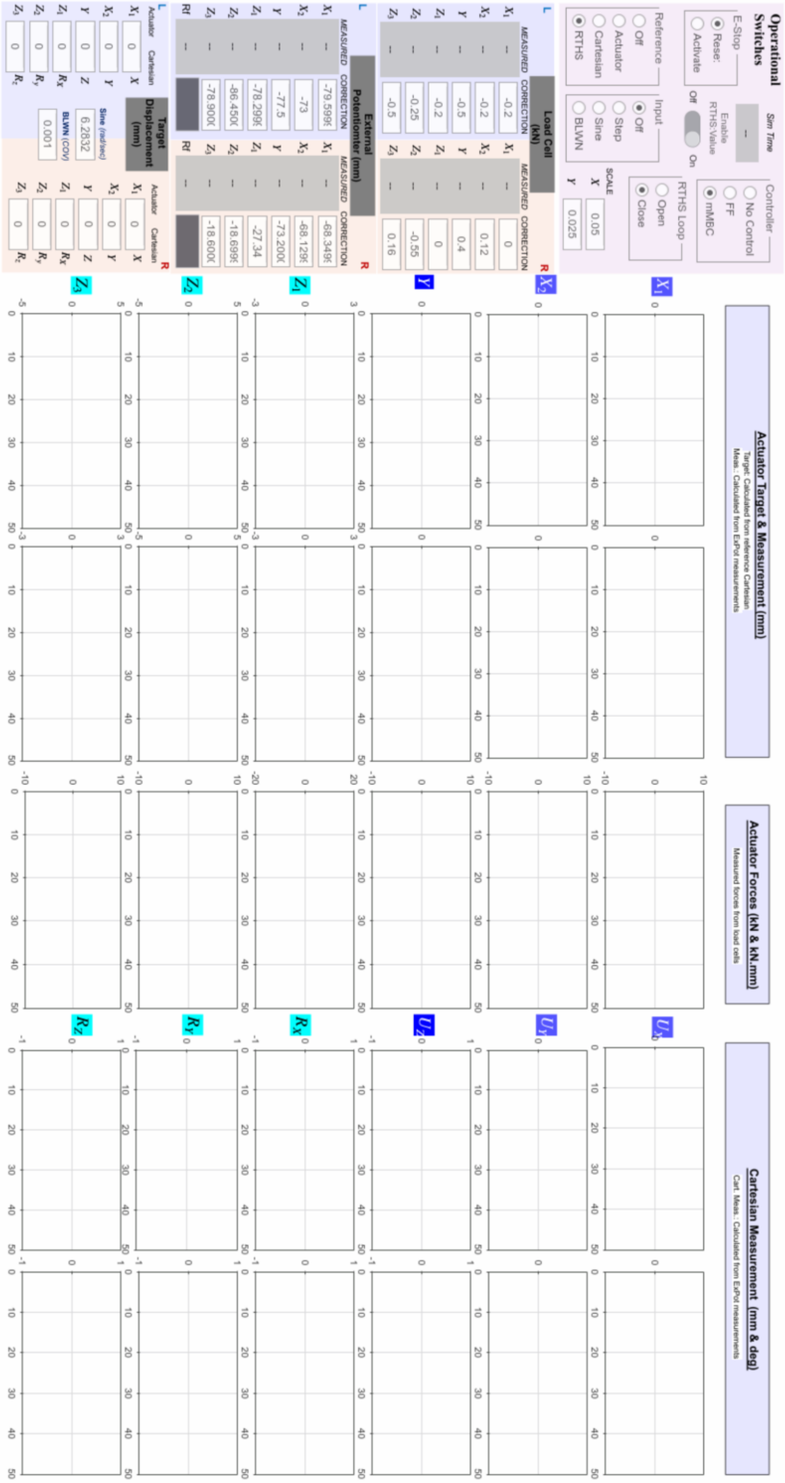

E-Stop: ● Reset ○ Activate

Reference: ○ Off ○ Actuator ○ Cartesian ● RTHS

Input: ● Off ○ Step ○ Sine ○ BLWN

Controller: ○ No Control ○ FF ● mMBC

RTHS Loop: ○ Open ● Close

SCALE X 0.05

SCALE Y 0.025

Sine (rad/sec) 6.2832

BLWN (COV) 0.001

Figure A.1 Graphical user interface (dashboard) for execution of experiments

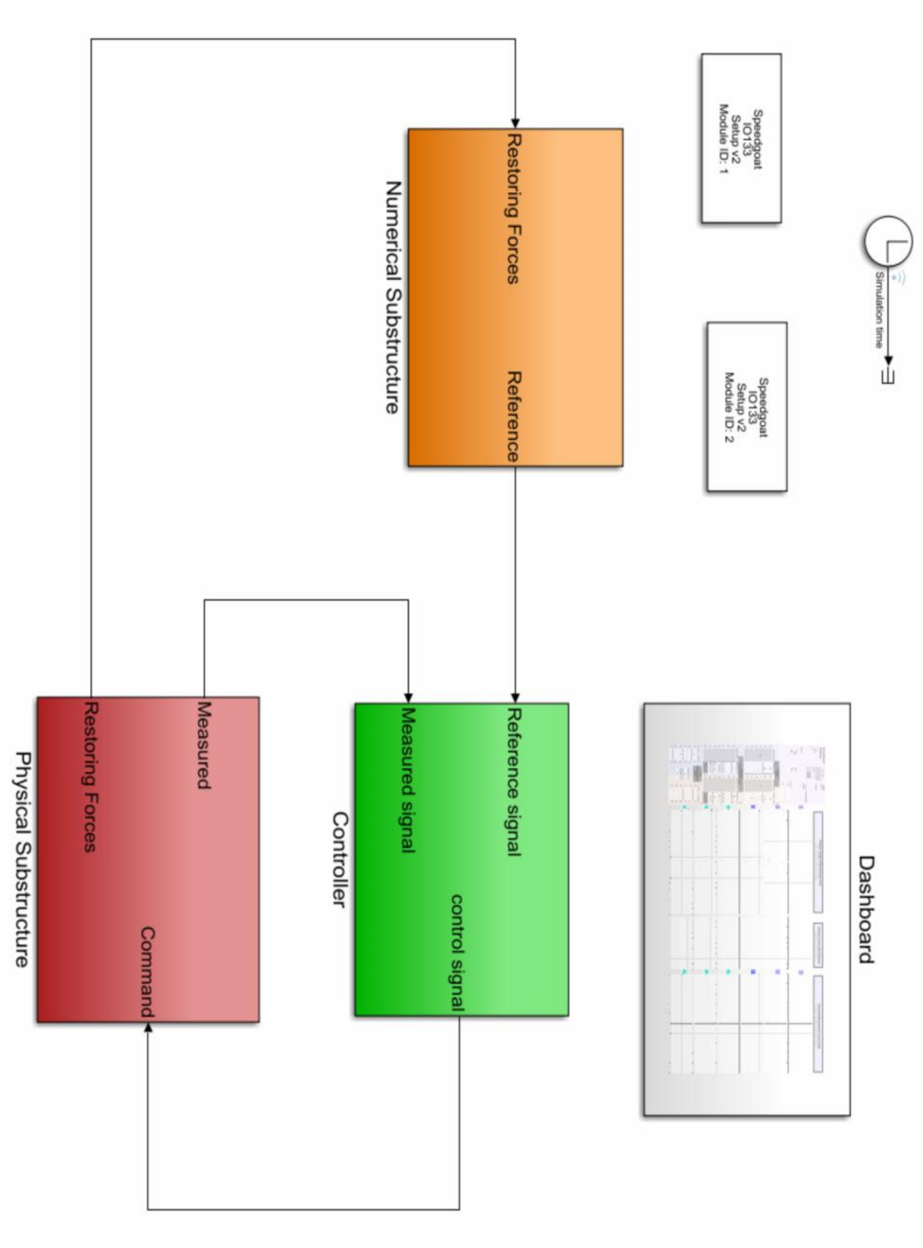

Figure A.2 Closed-loop real-time hybrid simulation program

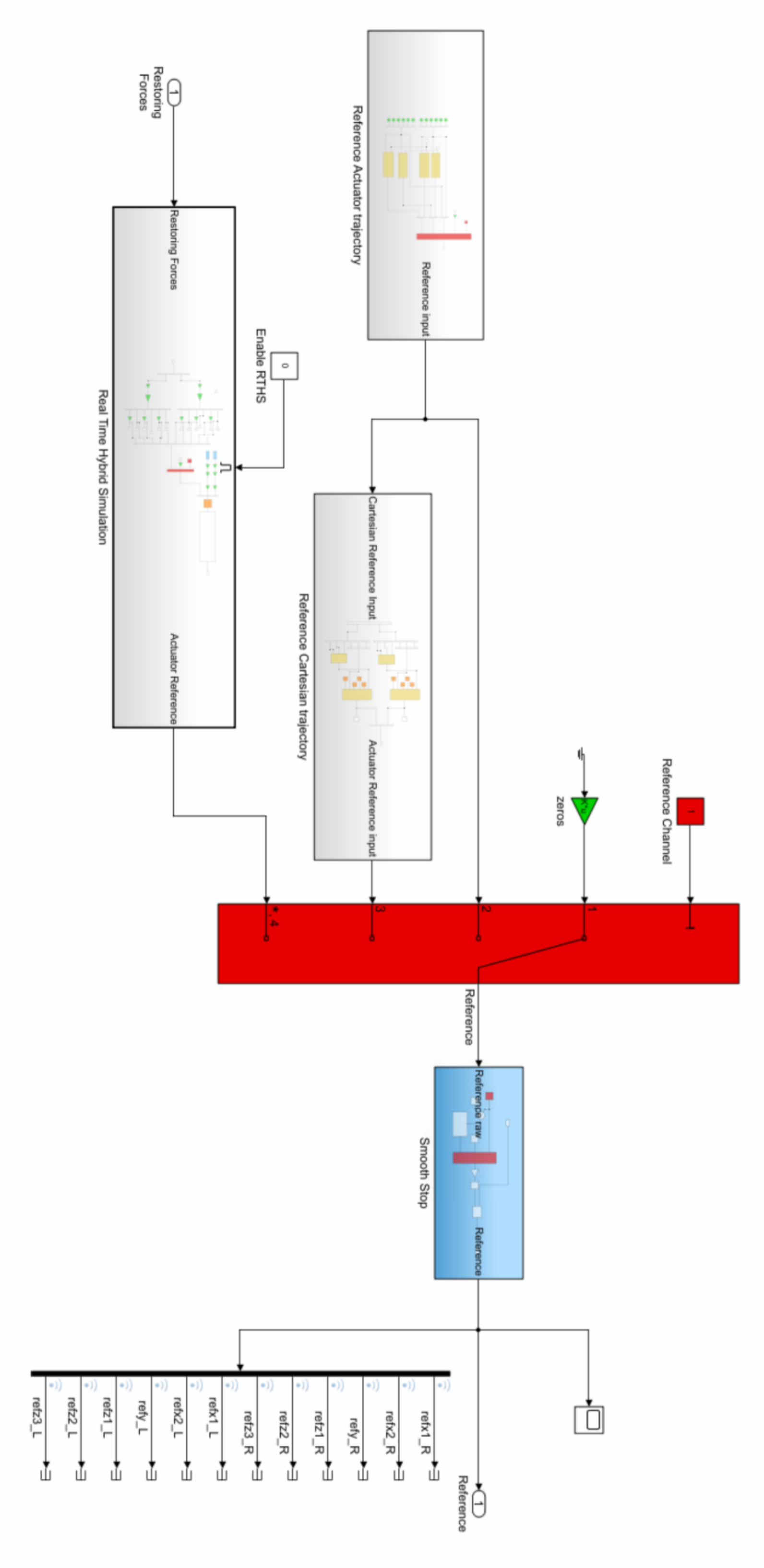

Figure A.3 Numerical substructure

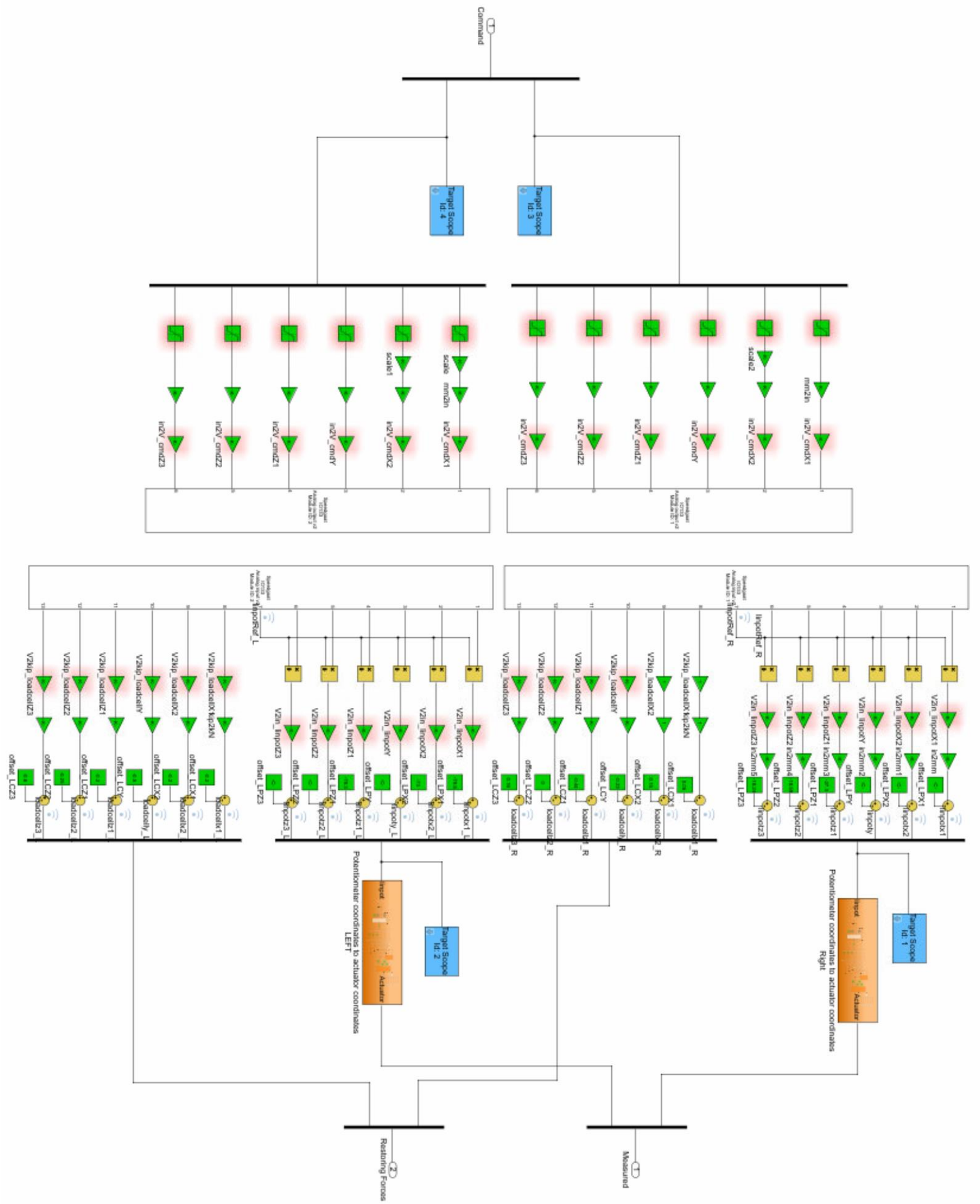

Figure A.4 Physical substructure including input-output channels

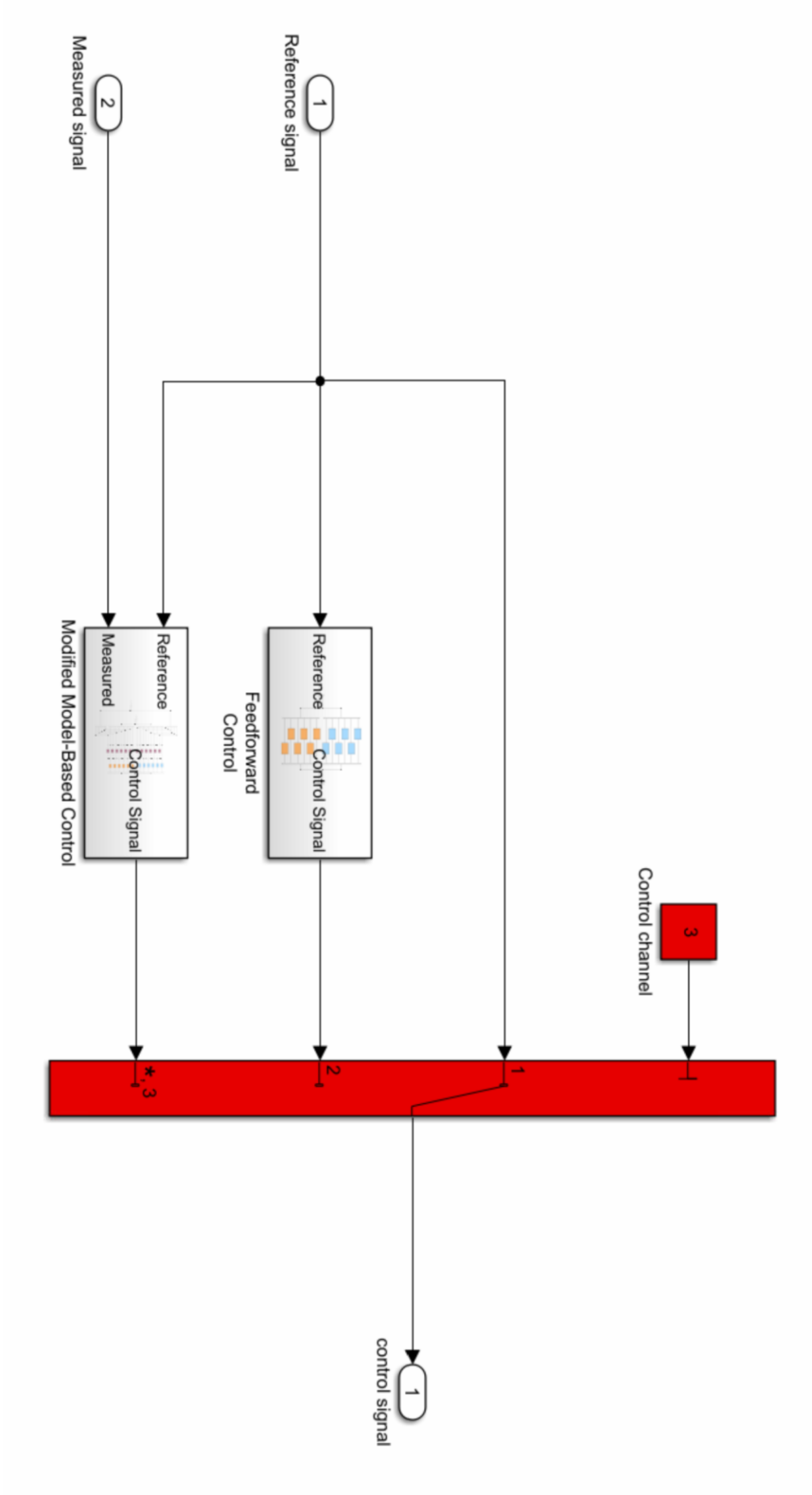

Figure A.5 Compensation options

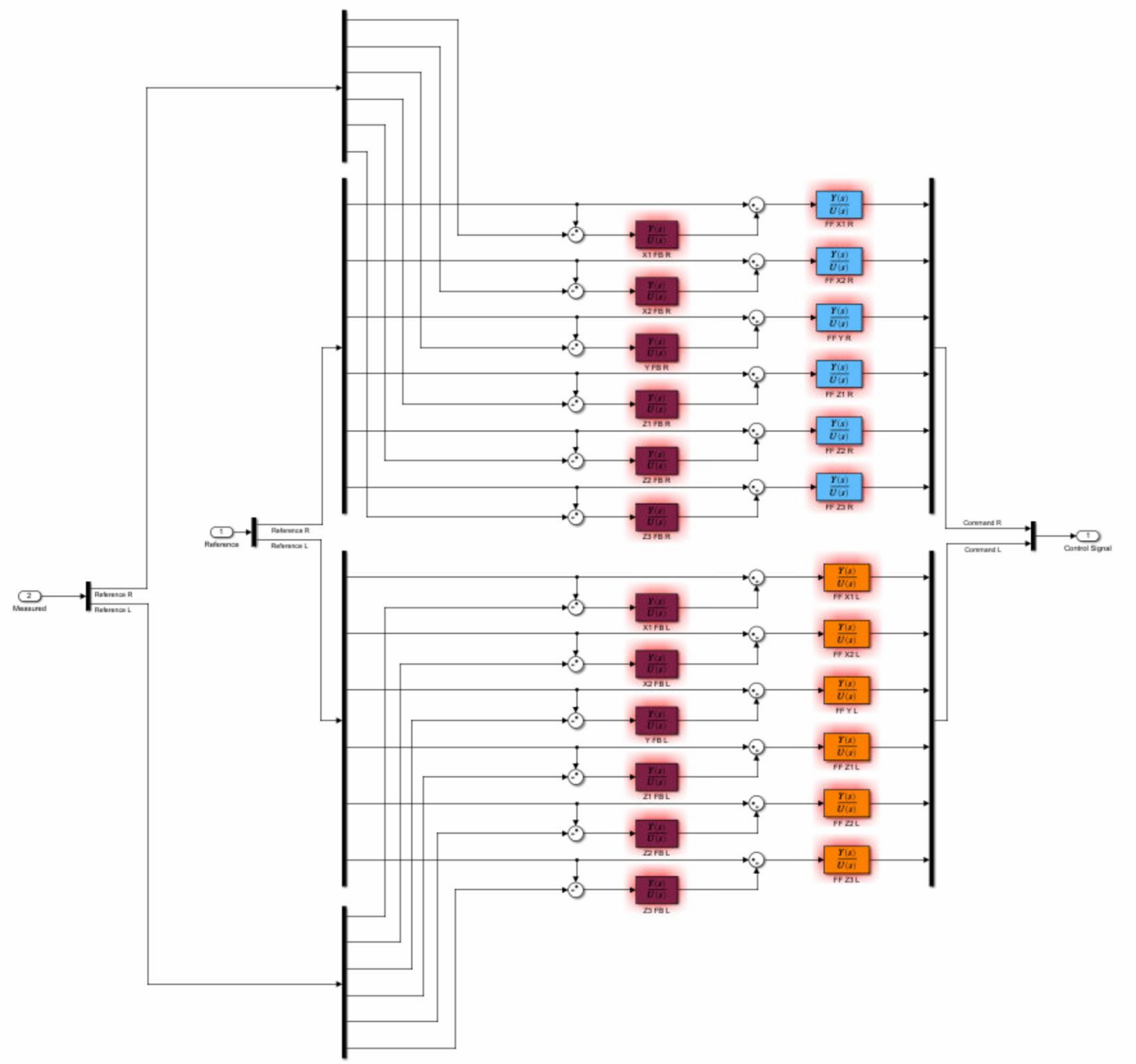

Figure A.6 Modified Model-Based Control (mMBC) compensation

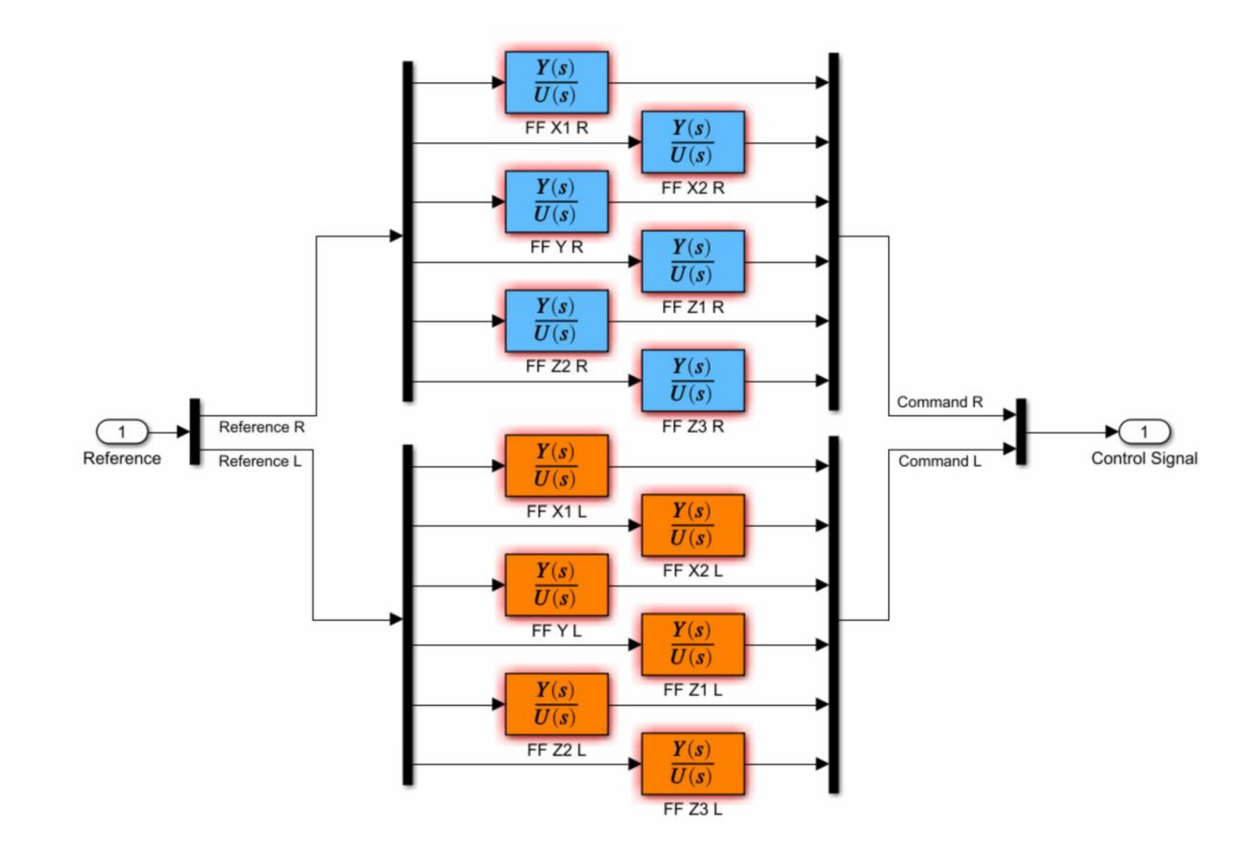

Figure A.7 Feedforward compensation

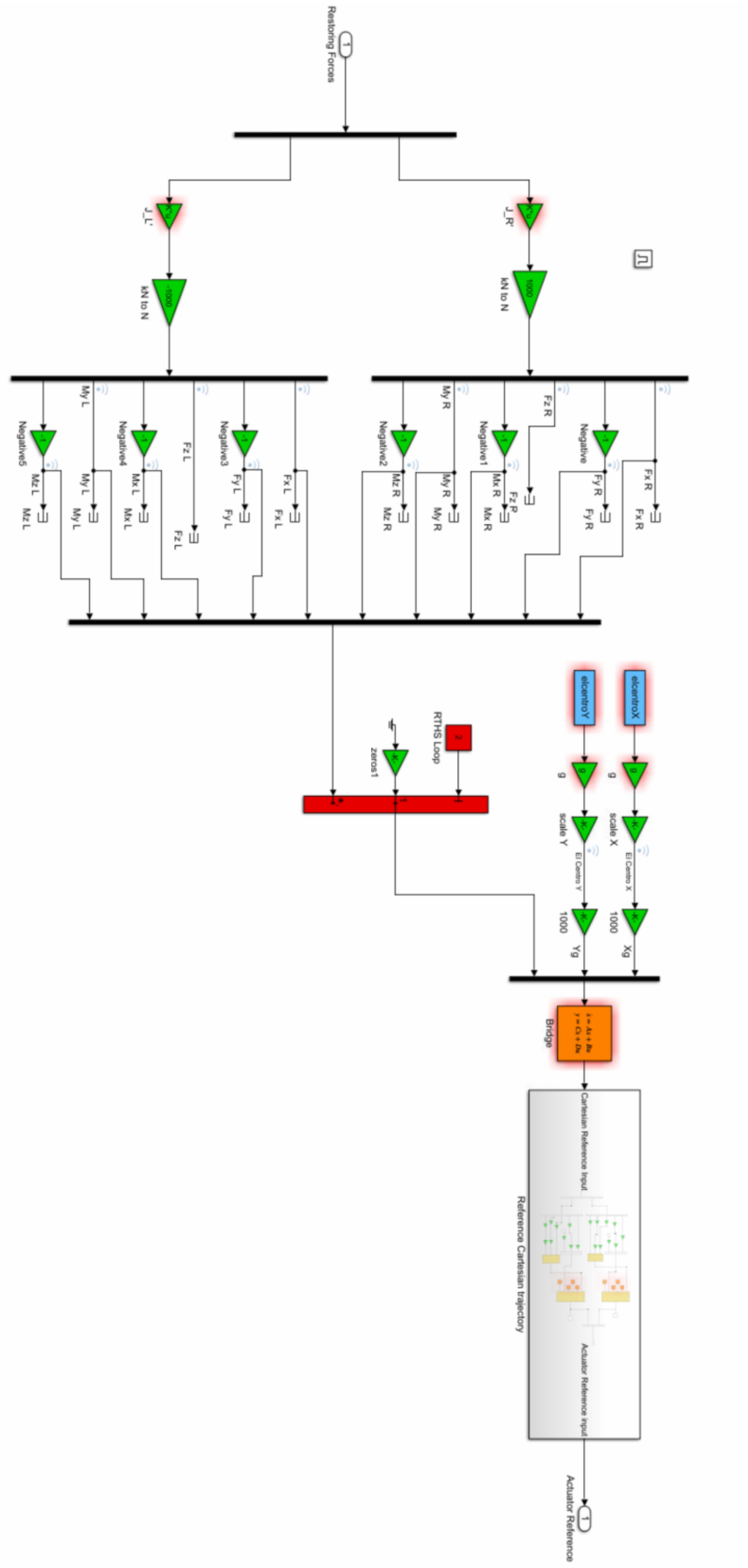

Figure A.8 Earthquake excitation and state-space model

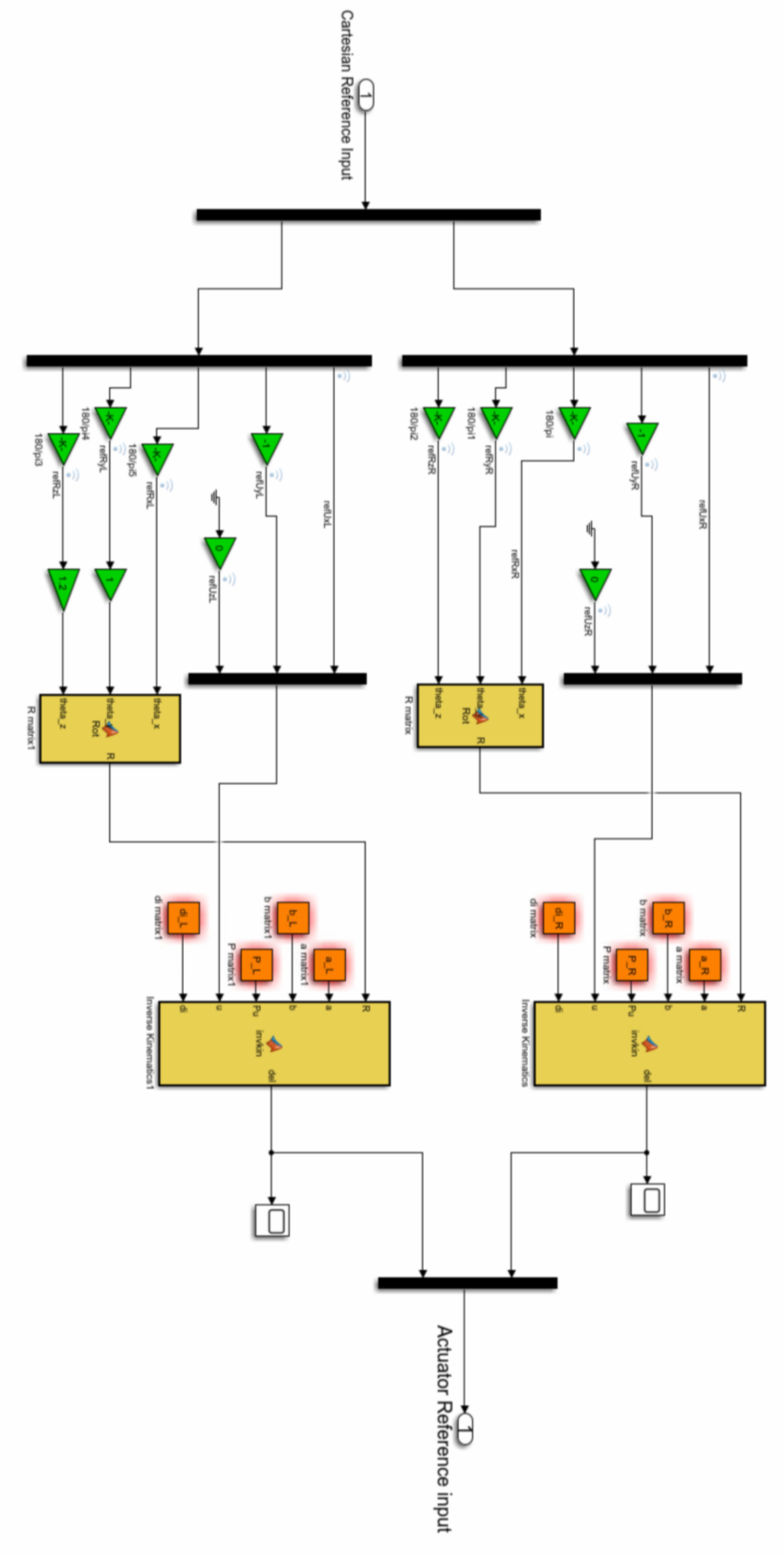

Figure A.9 Kinematic transformation for Cartesian target signals

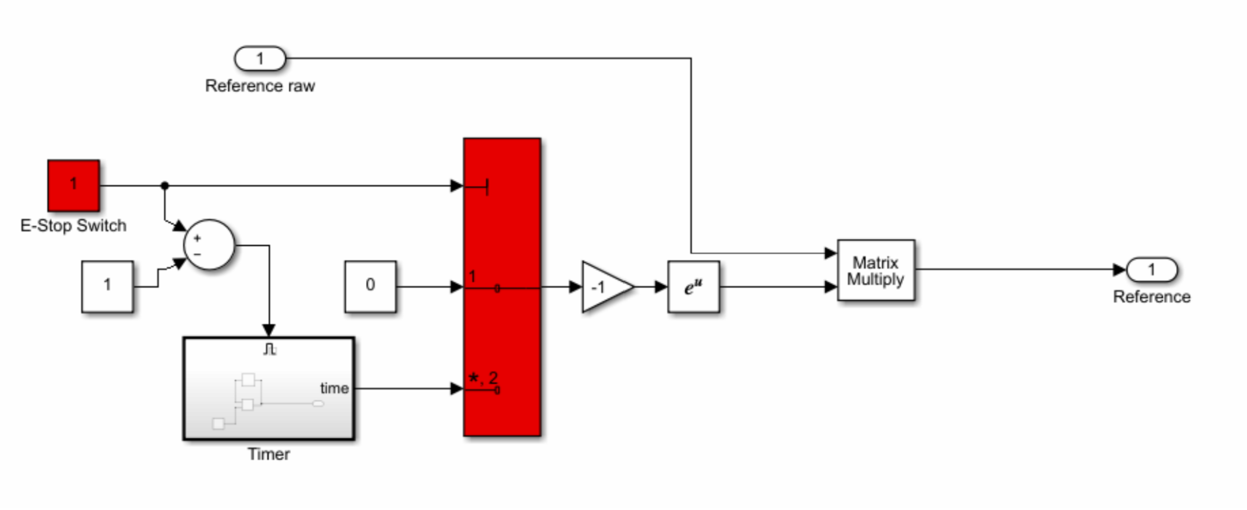

Figure A.10 Smooth-stop for emergency stops